



## Demonstration and validation of new control concepts by dedicated and scaled turbine experiments

Agreement n.:	308974
Duration	November 2012 – October 2017
Co-ordinator:	DTU Wind



The research leading to these results has received funding from the European Community's Seventh Framework Programme FP7-ENERGY-2012-1-2STAGE under grant agreement No. 308974 (INNWIND.EU).

---

### PROPRIETARY RIGHTS STATEMENT

This document contains information, which is proprietary to the "INNWIND.EU" Consortium. Neither this document nor the information contained herein shall be used, duplicated or communicated by any means to any third party, in whole or in parts, except with prior written consent of the "INNWIND.EU" consortium.

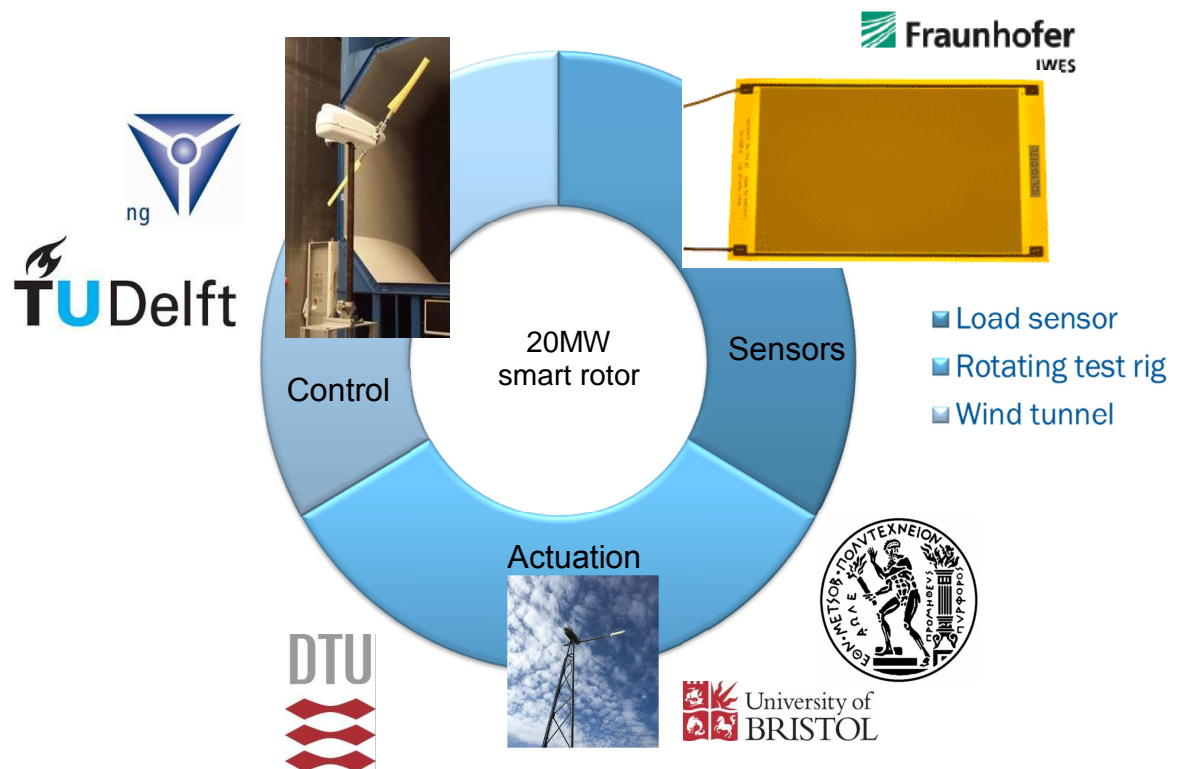
---

# Document information

<b>Document Name:</b>	Demonstration and validation of new control concepts by dedicated and scaled turbine experiments
<b>Document Number:</b>	
<b>Author:</b>	Joeri Frederik (TUD), Sachin Navalkar (TUD), Jan-Willem van Wingerden (TUD), Thanasis Barlas (DTU), Helge Aagaard Madsen (DTU), Tom Løgstrup Andersen (DTU), Anders Smærup Olsen (DTU), Lars Kröger (OL), Vasilis Riziotis (NTUA), Qing Ai (Bristol), Paul Weaver (Bristol), Leonardo Bergami (SE Blades), Jannes Kloepper (Fraunhofer)
<b>Document Type</b>	Report
<b>Dissemination level</b>	PU
<b>Review:</b>	Flemming Rasmussen
<b>Date:</b>	28-09-2017
<b>WP:</b>	2
<b>Task:</b>	3
<b>Approval:</b>	Approved by WP Leader

## EXECUTIVE SUMMARY

The general objective of INNWIND Work Package 2.3 is the evaluation of the technology-readiness level of advanced load control strategies primarily targeting the attenuation of rotor loads. In the previous deliverable, a preliminary analysis of various load control techniques was done, and the trailing edge flap control mechanism was down selected as the most promising and technically feasible solution. The integration of this mechanism with conventional rotor design is evaluated in terms of its load reduction potential using different numerical tools. Since the proof of the pudding is in the eating the objective of this deliverable is on the experimental proof-of-concept of the trailing-edge control concept. Dedicated experiments are performed to test the actuators, the sensors and the control systems. These different elements are tested during wind tunnel, field and laboratory experiments.



### Novel Load Sensor

For feedback control the loads have to be measured. Through the experimental investigation of piezoelectric patches on a laboratory scale blade, the feasibility of using those types of sensors as load sensor has been proven. Especially the low frequency range down to 0.1Hz has not been investigated in a systematic manner before. By appropriate selection of sensor dimension and effect type (d31, d33) along with careful design of sensor signal conditioning, quasi-static load measurements down to 0.1 Hz could be achieved in a laboratorial setting.

The same type of sensors are used during the **wind tunnel test** where three new elements are introduced: 1) the free floating flap, 2) an active grid, 3) an adaptive control scheme.

## Wind tunnel experiments

**Free-floating flaps** were designed for the first time for the application of wind turbine load control. Numerical aeroelastic analysis concluded that such flaps show significant control authority in the desired frequency band (2P and beyond). However, the additional degree of freedom couples aerodynamically with the flapwise flexible mode of the blade and causes flutter at low wind speeds, just outside the design envelope. Using a data-driven feedback controller, the blade can be stabilized in the post-flutter region. Both of these results were validated experimentally in the wind tunnel (see Fig. 1).

The experiment is conducted in the wind tunnel of the university of Oldenburg. The wind tunnel has a cross section of  $3 \times 3 \text{ m}^2$  and a test section of 30 m. Wind speeds up to 30 m/s could be achieved. The inflow of the wind tunnel gets modulated by an active grid which is mounted to the wind tunnel inlet. The **active grid** is used to generate customized turbulence for wind tunnel applications. The used active grid is divides the cross section by 80 horizontal and vertical rods, resulting in a mesh width of about 0,14m. Each of its axes is connected to a servomotor in a such manner that each can be controlled individually by a real time system. Mounted on the rods are square flaps which are, depending on the orientation with respect to the inflow, blocking and deflecting the wind. Dynamic changes of the angle of attack of the flaps to the flow are in the following described as an excitation protocol. The excitation protocol defines the dynamics of the generated turbulence.



Figure 1, Wind tunnel experiments in Oldenburg with the active grid and a scaled innovative two-bladed wind turbine.

During the wind tunnel tests, the concept of **Subspace Predictive Repetitive Control (SPRC)**, a dedicated data-driven control technique, was used to achieve blade load reductions. The pitch control action was composed of a superposition of 1P and 2P sinusoidal basis functions where the gains are automatically adapted to the time-varying wind conditions. It was shown that significant rejection of 1P and 2P loads in the blade load spectrum could be achieved with combined pitch and flap control (see Fig. 2).

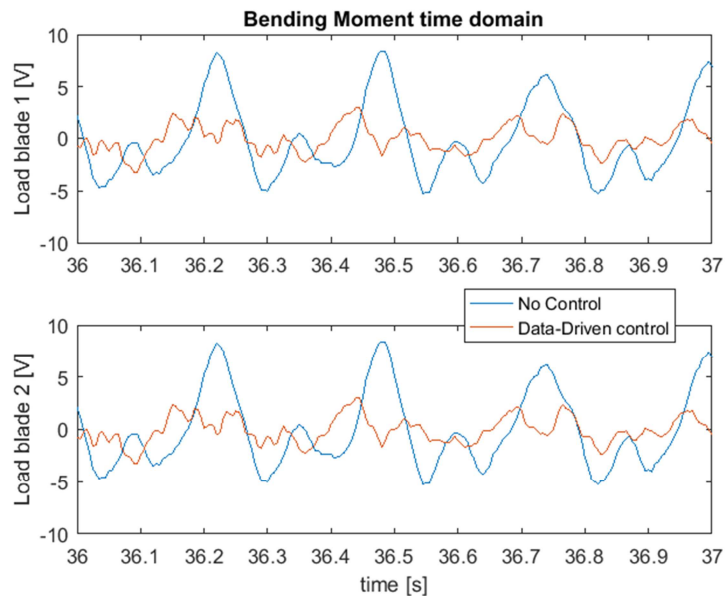


Figure 2, A typical result of the wind tunnel experiments using an advanced data-driven feedback controller that mitigates the loads. Turbulence intensity 3%.

### Rotating Test Rig

A morphing trailing edge (MTE) flap has been developed for the alleviation of unsteady loads within Task 2.3. It consists of an inner, printed cell structure which allows a deflection of the flap. On the suction side, the flap is covered with a Carbon Fiber Reinforced Polyester (CFRP) skin and on the pressure side with a pre-stressed silicone skin. The flap is actuated with a carbon rod attached to the trailing edge of the flap (see Figure 3 (right)).

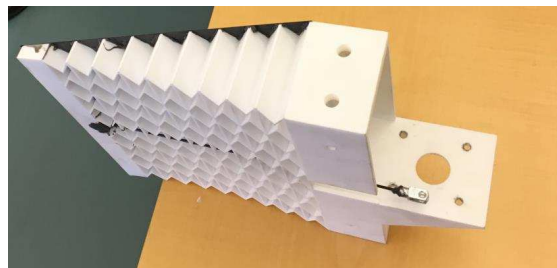


Figure 3, (Left) Rotating test-rig at DTU, Campus Risoe. (Right) A flap prototype. The silicone skin on the pressure side is not glued on at this stage. The actuation rod is visible at the lower part of the flap.

The flap is tested under realistic conditions on a rotating test rig, developed previously in a National Danish project INDUFLAP in the period from 2011-2014. It is a test facility based on a 100 kW turbine platform where the rotor has been taken down and instead a 10m long boom is mounted with at the end a 2m blade section. The flap system is integrated on this blade section and then tests can be run with the boom rotating,

simulating conditions close to the ones on a full scale turbine. The boom can be pitched, which means that combined pitch and flap actuation can be performed.

A new blade section for testing the flap system on the rotating test rig has been manufactured using the 30% airfoil, developed within the INNWIND.EU project. A comprehensive instrumentation comprising about 120 pressure tabs is appended so that the flap influence on the loading can be monitored in details. The flaps are manufactured in sections and resulting in eight sections that together constitute the flap spanning the total length of the 2m blade.

In the testing campaign utilizing DTU's rotating rig, the morphing trailing edge technology developed in collaboration with the University of Bristol has been evaluated and successfully demonstrated. It is shown that the morphing wing achieves good performance in terms of aerodynamic load response, close to numerical estimations. Moreover, simple controller implementations show promising results in terms of dynamic load alleviation. In addition, the aerodynamic performance of ECN's new airfoil has been evaluated in atmospheric conditions. Furthermore, the BEM-based codes from DTU and NTUA show good performance in the prediction of the unsteady force response with the flap activation.

After proof of the technical feasibility of the concept, the whole control system is tested on a 2MW commercial wind turbine, and on the 10MW INNWIND turbine using high-fidelity simulations.

#### Evaluation of trailing edge flaps on a commercial MW Suzlon wind turbine

The individual flap controller developed in the INNWIND project has been included in the aero-servo-elastic model of the Suzlon's wind turbine S111, and tuned to the turbine characteristics. Aeroelastic simulations of the turbine with and without Adaptive Trailing Edge Flaps (ATEF), and considering different flap control modes, are performed reproducing the IEC operational load cases (1.1 to 1.5) and the idling rotor case (1.6). The effects of the ATEF control are quantified in terms of fatigue and ultimate load variations, as well as the increase in the AEP.

Overall the flap control achieves its main objective of alleviating the blade root flapwise fatigue loads with 9%, whereas the power increase control mode yields a 1.7% increase in AEP, which, given the observed increase of both fatigue and ultimate loads, is probably not sufficient to justify. A more carefully tuned control system, or maybe a more sophisticated control algorithm, would probably allow to achieve higher load reductions with the ATEF, especially considering the ultimate loads.

Whether the load alleviations achieved with the flaps in the simulated cases would ultimately be sufficient to justify the increase in complexity for a class III A turbine remains an open question. The answer would require a redesign of the rotor considering the modification to the load constraints given by the active flaps, as well as an estimation of the costs of the rotor, other turbine components, and also of the flap system.

#### Evaluation of trailing edge flaps on the 10 and 20 MW INNWIND turbine

Fatigue and extreme load reduction capabilities of IPC and IPC&IFC are assessed on the 10 MW and 20 MW Innwind.EU RWT. Blade flapwise fatigue load reductions of about 25% are attained with both control strategies tested in the present study (i.e. IPC and

combined IPC&IFC), independent of the turbine size. Overall, tower fatigue loads slightly increase for both turbine sizes and both control strategies. A slightly higher increase is noted on the fatigue loads of the up-scaled 20 MW turbine. This is because the proposed control loops have only been designed for the alleviation of the blade loads while they are not aiming at tower loads. The effect on ultimate loads by both control concepts is minor. As a result of the combined application of IPC and IFC, a 6% reduction of the blade extreme flapwise load is obtained on the 20MW turbine. The combined application of IPC&IFC, while resulting in the same blade load reduction as IPC, considerably reduces the pitch mechanism duty cycle. For the 20MW turbine, the increase in the standard deviation of the pitch motion exceeds 100%. This is reduced to about 10% when IFC is activated.

The main conclusion of this deliverable is that trailing edge flaps provide another degree of freedom to the wind turbine designers which make it possible to distribute the evitable structural loading over all the wind turbine components. Performing field experiments on a MW rotor is the next big step towards large scale implementation.

## TABLE OF CONTENTS

<b>EXECUTIVE SUMMARY</b> .....	3
TABLE OF CONTENTS .....	8
<b>1 INTRODUCTION</b> .....	10
<b>2 NOVEL LOAD SENSOR (FRAUNHOFER)</b> .....	13
2.1 Introduction .....	13
2.2 State-of-the-art overview.....	13
2.3 Experimental investigation of the piezoelectric load sensor .....	15
2.4 Sensor-Network Platform.....	36
2.5 Conclusion .....	38
2.6 References .....	39
<b>3 SCALED 2 BLADED ROTOR WITH FREE-FLOATING FLAPS [TUD]</b> .....	40
3.1 Introduction .....	40
3.2 Blade design and manufacturing.....	41
3.3 Aeroelastic blade analysis .....	45
3.4 Testing Environment .....	47
3.5 Iterative Feedforward Tuning for combined Pitch and Flap control .....	49
3.6 Results.....	50
3.7 Conclusions .....	57
3.8 References .....	58
<b>4 ACTIVE GRID [OLDENBURG]</b> .....	60
4.1 Introduction .....	60
4.2 Methods.....	61
4.3 Results and discussion.....	63
4.4 Conclusions .....	69
4.5 References .....	69
<b>5 WIND TUNNEL EXPERIMENTS [TUD+OLDENBURG]</b> .....	71
5.1 Introduction .....	71
5.2 Inflow Conditions.....	72
5.3 1P and 2P Individual Pitch Control .....	74
5.4 2P Individual Flap Control .....	80
5.5 Results.....	81
5.6 Conclusions .....	97
5.7 References .....	98

6	DESIGN OF A MORPHING WING [BRISTOL]	100
6.1	Introduction	100
6.2	Background	100
6.3	Morphing flap design	101
6.4	Building and al testing of the demonstrator	103
6.5	Conclusion	105
6.6	References	106
7	ROTATING RIG EXPERIMENTS AND ANALYSIS [DTU+NTUA]	108
7.1	Introduction	108
7.2	Description of the rotating rig	108
7.3	Development of the blade section	110
7.4	Test cases	111
7.5	Test results	114
7.6	Rotating rig simulations cases	119
7.7	Simulation results	119
7.8	Conclusions	122
7.9	References	123
8	TRAILING EDGE FLAPS ON THE 20MW TURBINE [NTUA]	125
8.1	Introduction	125
8.2	Camber line morphing	125
8.3	Controller description	127
8.4	Results and discussion	128
8.5	Conclusions	142
8.6	References	142
9	ADAPTIVE TRAILING EDGE FLAPS (ATEF) ON A 2.1 MW COMMERCIAL TURBINE [SE BLADES]	143
9.1	Executive Summary	143
9.2	Introduction	144
9.3	Flap Setup	146
9.4	Flap Control Tuning	148
9.5	Aeroelastic Simulations	151
9.6	Conclusion	157
9.7	References	158
10	CONCLUSIONS	160

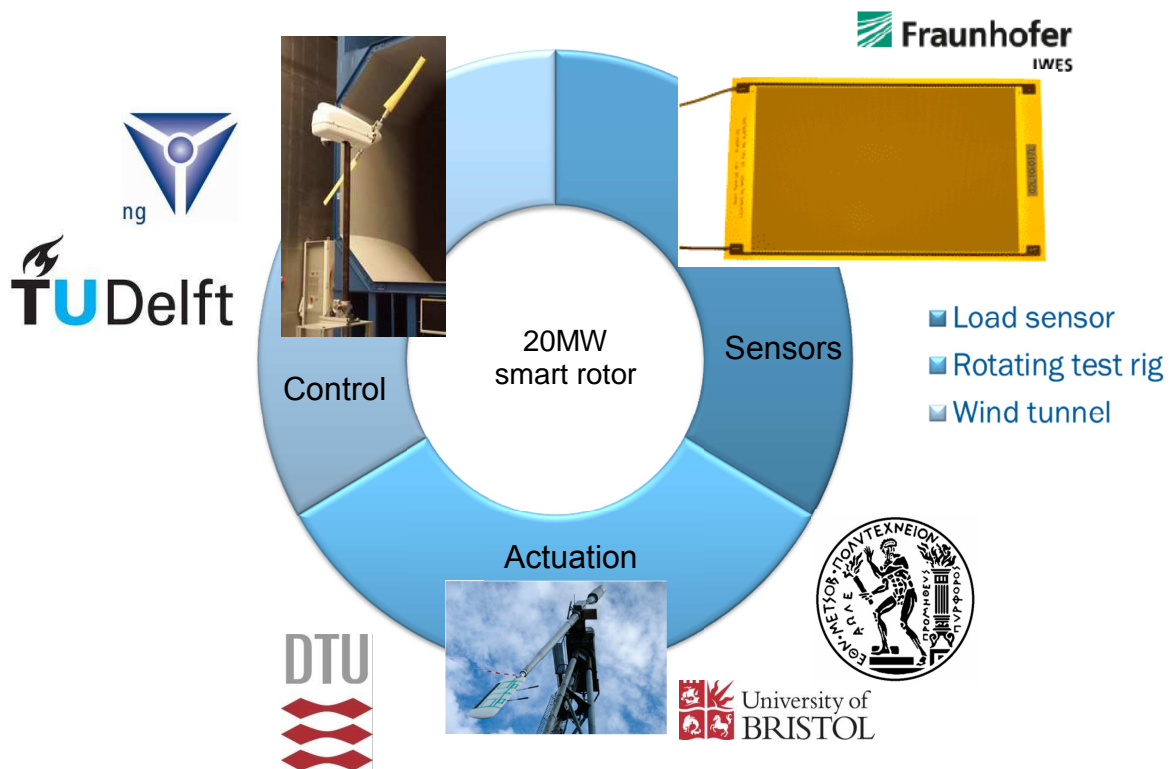
# 1 INTRODUCTION

## 1.1 Background

The need for reducing the cost of wind energy, especially in the resource-rich offshore locations, has been a driving factor in the increasing size of modern wind turbines. However, an increased turbine size also increases the component loading, especially dynamic (fatigue) loading, pushing it to beyond the limits of engineering experience. It is the objective of the INN WIND program to investigate innovations in wind technology that can allow for an increase in the rating of turbines while circumventing an exponential increase in the turbine loads and their concomitant material costs.

One of the primary cost drivers in wind turbines is the rotor design. The rotor blades themselves, on account of the complex aerostructural design and glass-fibre/carbon-fibre composition, form an important part of turbine costs that is sought to be minimised by limiting dynamic blade loads. Further, the blade loads cascade down through the entire structure, as such, blade load attenuation can prove beneficial in reducing total turbine costs, in terms of initial outlay as well as maintenance cost. Therefore, the objective of INN WIND Task 2 is the investigation of rotor design concepts that can alleviate blade loads in a passive (structural) or active (aeroservoelastic) manner.

INN WIND Task 2.3 devotes its attention to the control implications of these concepts. In the previous deliverable, several different rotor (re)design concepts for blade load reduction were explored in terms of advantages and limitations. The focus of the deliverable was on the technical feasibility and readiness level of various technologies for their implementation in the field. It was concluded that active trailing edge flaps, that can modify aerofoil camber in response to varying wind loads, show the highest technology-readiness level. Other concepts, namely passive trailing-



edge flaps and material/geometric coupling, need further validation in the simulation and experimental environment.

Since the proof of the pudding is in the eating the objective of this deliverable is on the experimental proof-of-concept of the trailing-edge control concept. Dedicated experiments will be performed to test the actuators, the sensors and the control systems. These different elements will be tested during wind tunnel, field and laboratory experiments.

## PART 1: Wind tunnel experiments

## 2 NOVEL LOAD SENSOR (FRAUNHOFER)

### 2.1 Introduction

As mentioned in [1] previous work has demonstrated that significant reductions in fatigue loading on a wind turbine can be achieved by using individual pitch control, in which the pitch of each blade is adjusted individually, in response to measured loads.

In order to control the loads along the rotor blades knowledge of the loads is essential, which can be measured by several sensor concepts. A huge number of sensor concepts have been investigated in the last years and the following chapter should give a brief overview about these different principles.

As one can see in [2] sensor failures belongs with 11% to the third biggest total numbers of failures.

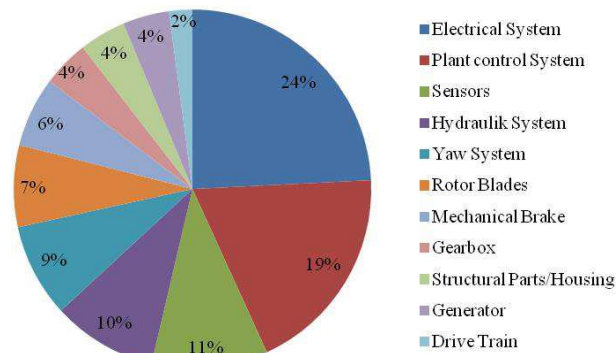


Figure 4: Share of the main components of the total number of failures, [2]

From this it is apparent that a higher reliability of the sensor systems is crucial and therefore novel sensor systems needs to be investigated.

The main focus of these chapter will be the strain sensors, in particular the piezoelectric based sensors, because of their multifunctional characteristics, which makes them ideal for application in smart structures. For the sake of completeness also different measurements principles like accelerometers and inflow measurements will be presented as a brief overview.

### 2.2 State-of-the-art overview

#### Accelerometers

Accelerations can be a possible measure for load reduction control strategies. They can be measured by different sensor principles.

The most common used accelerometers use the piezoelectric effect to measure vibrations. They are characterized by a high signal quality but due to their high invest prices they are not suitable for a widespread industrial application. Furthermore they usually behave like a high pass, so they cannot be used for measuring the low frequency vibrations of the rotor blades.

An alternative are micro electro-mechanical systems (MEMS) -based sensors that achieve poorer signal quality compared to the laboratory sensors, but show considerable advantages in price.

Application in [3] indicates that cost effective MEMS-type accelerometer's shows sufficient performance in an industrial application for health monitoring of shock absorbers and can easily be integrated in tailored housings which are produced with a selective laser melting (SLM) process.

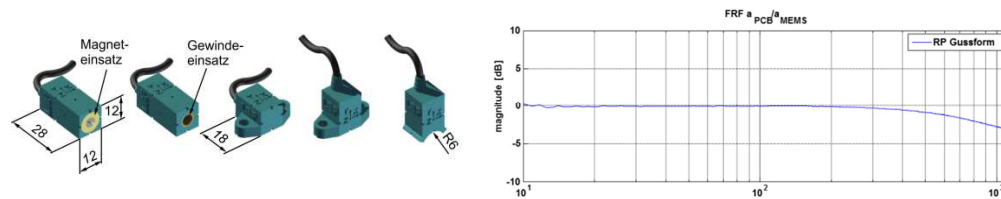


**Figure 1: MEMS accelerometers with tailored housings<sup>1</sup> and Back-to-back frequency response with piezoelectric accelerometer**

In contrast to the piezoelectric-based sensors, those sensors can also measure static accelerations like gravity, which makes them suitable for application on wind turbines.

#### Inflow Measurements

As discussed in [4] and [5] inflow measurement should be considered for pitch and yaw control to increase the power capture and to reduce the load variations on the turbine. There are different devices for inflow measurements in the focus of recent research, which are shortly summarized in the following sections. Uncertainties that are associated with inflow measurements were presented and discussed by [4].

#### Pitot tubes

Pitot tubes are small cylindrical devices, which are capable to measure the pressure and thus the inflow velocity. This is achieved by measuring the pressure in distributed pressure holes in the cylinder. Those pitot tubes are mounted on the leading edge of the blades and because of the small distance in front of the blade, the measurement is acquired with a slight preview to the incoming wind. [6] A successful demonstration of pitot tubes has been performed in the DANAERO experiment. [7], [4]

#### Spinner anemometer

Spinner anemometers can be used for inflow speed and directions estimation. Those devices consist in three sonic anemometers which are placed on a spinner. To estimate speed and direction a precise calibration based on computational fluid dynamics is required. [4]

<sup>1</sup> <http://www.isys-as.de/>

### Laser anemometer (LiDAR)

A Spinner mounted light detection and ranging (LiDAR) sensor can be used to measure the inflow velocity parallel to an emitted laser light. By reflection of the light due to particles and dust in the air, the inflow can be estimated by utilizing the Doppler theory. [6] Those anemometers can be subdivided into pulsed and continuous wave LiDAR sensors. Their differences are described in [8] and [4].

### Strain sensors

Strain-based measurements at the blade roots can be directly related to an applied load and are a recommended method for load measurements on a wind turbine. [9] Several types of strain sensors have been investigated in the last years, which can be subdivided into electrical-, piezoelectric- and optical strain sensors.

#### Electrical

Especially the electrical-type sensors, which can be further subdivided into resistance-, capacitance-, photoelectric and semiconductor strain gauges, are well known and they have been used intensely for laboratory tests or prototypes of wind turbines. On the one hand they seem suitable as sensors for load reduction controllers in terms of measurement range, time- and frequency response but on the other hand none of those sensors are a robust solution in terms of lifetime compared to a wind turbine. [5]

#### Optical

From the different types of optical sensor, which are photoelastic strain gauges, moire interferometry strain gauges, holographic interferometry strain gauges and fiber optics strain gauges only the last mentioned shows is suitable for load monitoring because of the complexity of the former mentioned. The main type of fiber optics, which is already in use for blade monitoring is the fiber bragg grating (FBG) sensor. Another type which is investigated is the microbend strain sensor. Those optical methods show outstanding performance in terms of reliability, sensitivity, electrical interference, size and weight. But also the main drawbacks, which are the high invest cost for this technology and their high sensitivity to temperature changes has to be mentioned. [5]

## 2.3 Experimental investigation of the piezoelectric load sensor

Another strain sensor type is based on the piezoelectric effect. Under mechanical stress charge displacement in the piezoelectric crystal is generated which can be measured as a voltage across the electrodes [10].

Several studies ([11], [12], [13], [14],[15]) have investigated those sensors as strain sensors and has shown their excellent potential as low power, low cost and reliable strain sensor. Especially their high reliability which was investigated by [16] and [15] makes them an interesting alternative to conventional metal foil strain gauges.

Furthermore they belong to the multifunctional materials, thus sensing and actuating is possible. This makes them an ideal candidate for application in wind turbines where they can be used as load sensor, but also as actuator for structural health monitoring methods like Acousto ultrasonic ([17]).

The main drawback of those piezoelectric elements is their strong high-pass behavior as they exhibit capacitive source impedance. Without further techniques the measurement of signals with  $f_{\text{MIN}} \leq 0.5$  Hz is usually not possible [10]. Thus direct application as blade root strain sensor is not possible.

For further investigation of the piezoelectric patches as strain gauges, a four-point bending test was performed as pretest.

The sensor patch which was chosen for further investigation is macro fiber composite (MFC) of manufacturer Smart Material. It consists of piezoelectric rods which are embedded between layers of adhesive, electrodes and polyamide film<sup>2</sup>. Compared to traditional lead zirconate titanate (PZT) piezoceramic those MFCs are superior because of their flexibility whereby they can be applied on curved structures and even embedded. The manufacturer provides two different types of MFC which differ in terms of operational mode. The operating principle of MFC type P1 is based on piezoelectric longitudinal effect ( $d_{33}$ -mode) whereby MFC of type P2 operates using piezoelectric transversal effect ( $d_{31}$ -mode). Related to the operational mode, the assembly of MFC is subject to different consideration. For MFC of type P1 it can be assumed that it consists of interdigitated electrodes and can be approached as multiple capacitors in parallel. The assembly of MFC type P2 can be treated as a single capacitor with two parallel plate electrodes. According to the recommendations of the manufacturer, P1-patches are suitable for sensor applications due to higher sensitivity. But typically an assembly consisting of interdigitated electrodes results in an inhomogeneous electric field and low capacity. Furthermore P2-patches are preferred for actuator applications in respect to higher output signal due to specifications of the assembly.

The strain formulation valid for piezoelectric transducers equivalent to a single capacitor, such as MFC type 2 is presented in detail in [10], [12] and [13].

According to this the strain can be calculated by:

$$\varepsilon = \frac{V_C C_S}{K_p K_s d_{31} Y_C l_1 l_2}, C_S = \varepsilon_{33}^T \varepsilon_0 \frac{l_1 l_2}{l_3}$$

Where  $V_C$  is the voltage across the electrodes,  $C_S$  is the capacity of the MFC,  $K_p$  is a correction factor due to Poisson's effect,  $K_s$  is a correction factor to account for shear lag effect,  $Y_C$  is the Young's modulus, and  $l_1$ ,  $l_2$  and  $l_3$  are the dimension of the patch. The development of the corrections factors for strain calculation was discussed in [18], [12], [13], [19].

For piezo patch of type P1, different approaches have been developed to approximate the electromechanical parameters in case of charge displacement. In [25], [26] an approach for interdigitated assembly is presented. The capacity of each pair of electrode has to be calculated and multiplied by the number of electrode pairs since these are equivalent to capacitors in parallel. This approach constitutes a less accurate solution than numerical simulation and is not described in detail at this point.

---

<sup>2</sup> <http://www.smart-material.com/index.html>

### Pretest

Because of the above mentioned drawbacks further investigation needs to be performed to assure that MFCs can be used as sensor input to advanced blade control algorithms.

In a first test-setup the mentioned sensors (M0714-P2, P-878.SP1 and 1-LY11-6/120) were mounted with HARDMAN® Extra-Fast Setting Epoxy (Royal Adhesives and Sealants, LLC) along the longitudinal axis on a metal beam with dimension of 0.35 m x 0.09m x 0.002m. This specimen was then arranged in a 4-point bending test rig in a climate chamber according to Figure 5. The excitation of the specimen was performed with an electrodynamic shaker (V2664-DSA4-20k, Gearing & Watson Electronics Ltd).

For comparison conventional metal film strain gauges (1-LY11-6/120, HBM) are applied to the test specimen.

Given the rectangular cross-section of the beam the strain on the top in between the two supports will be equal in magnitude.

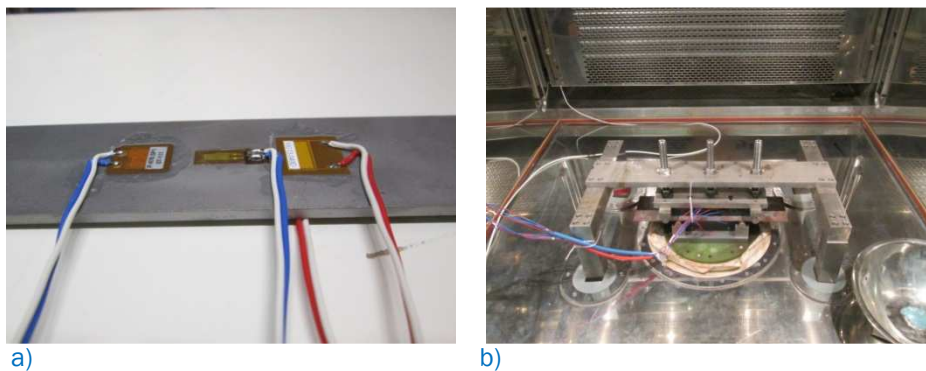


Figure 5: a) Probe with mounted sensor elements, b) four-point bending test setup in climate chamber

After the pretest have approved the compliance between measurement performances of strain gauges and piezo patches for a temperature range of -10 °C to +65 °C, influence of rel. humidity, excitation frequency and strain is investigated in further steps. The correlation to sensor patch dimension and operating mode is also considered as objectives in further investigations (Figure 6).

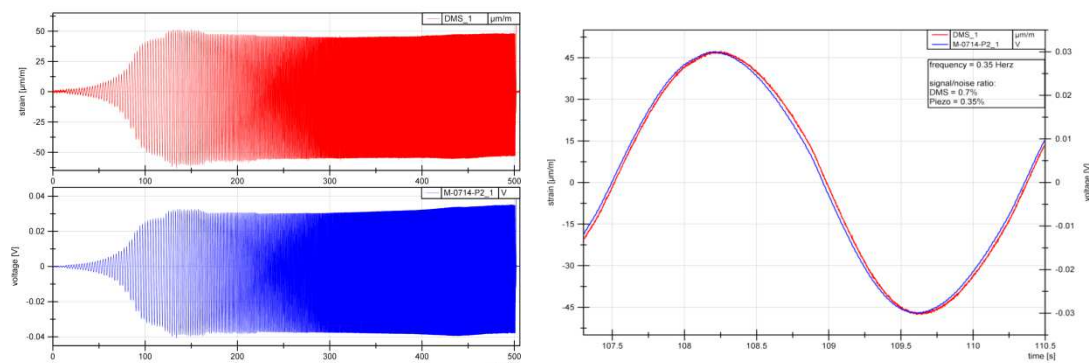
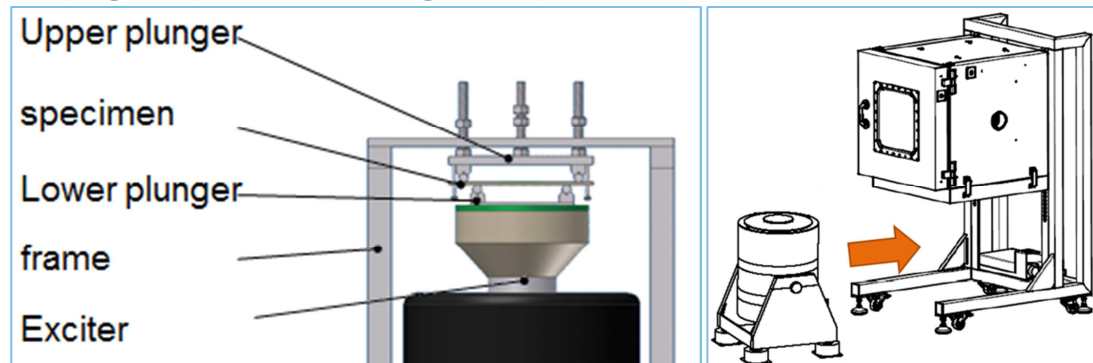


Figure 6: Output signal of strain gauges and piezo patch M0714-P2 in compliance. Left: Time signal of strain gauges (red) in comparison to time signal of M0714-P2. Right: Both signals at a frequency of 0.35 Hz.

**Main Test with multiple parameters**

At the beginning of the main test, appropriate assumptions have to be determined to meet requirements which have to be fulfilled for characterization of sensor patch performance. As test set-up for further investigation, the set-up used in pretest is modified. The four-point bending test is performed to simulate flapwise bending of a rotor blade as simplified approach and to generate uniaxial strain along the longitudinal axis to excite piezoelectric sensors. The test set-up consists mainly of an upper and plunger clamping test specimen of rectangular shape as illustrated in Figure 7.



**Figure 7: Illustration of four-point-bending test set up (left) and assembly consisting of the exciter and climate chamber (right)**

Mechanical properties which concern strain measurement on rotor blades have been calculated by means of the software BECAS (Beam Cross Section Analysis Software). Beside properties of force and torque which occur for an arbitrary operational mode and axis of rotor blade, it is possible to determine the elastic modulus of any location of the rotor blade which differs along the horizontal axis due to anisotropy of material. Assuming that strain sensors are located on rotor blade roots, respective uniaxial strain values for loads on rotor blades generated by air speed up to 21 m/s are calculated in Table 1. According to this table, the upper limit of strain measuring range need to be at least at approx. 1487  $\mu\text{m}/\text{m}$ . Another parameter which has to be considered is elastic modulus of the rotor blade. The elastic modulus at the blade root is determined to 41.63 GPa along the horizontal axis while in perpendicular direction the elastic modulus is 14.93 GPa. This parameter is important in regard to strain transmission of host structure to sensor structure. Both structures should exhibit same or similar values of elastic modulus.

**Table 1: Strain in relation to air speed**

Air speed	Strain
5 m/s	770 $\mu\text{m}/\text{m}$
9 m/s	1327 $\mu\text{m}/\text{m}$
13 m/s	1897 $\mu\text{m}/\text{m}$
21 m/s	1487 $\mu\text{m}/\text{m}$

To match climatic conditions of a wind energy plant, the four-point bending test is carried out in the climate chamber VCS 7018-5. According to [24] load sensors for wind turbine applications have to withstand temperatures of -30 °C to +60 °C and rel. humidity of 10 % to 98 %. In regard to given specification of climate chamber rel. humidity of 10 % to 98 % can only be generated for a temperature range of +10 °C to +95 °C whereby without simulating rel. humidity a minimum temperature of -70 °C and maximum temperature of +180 °C can be set. Thus temperature of -30 °C will be investigated separately. Furthermore relevant frequency range for wind turbine application is denoted as 0.1 Hz

to 8 Hz in [24]. The mechanical excitation of the test set-up within this frequency range is performed with shaker TV 54216-130 of TIRA. Relating to mechanical excitation, the specimen is strained between 50  $\mu\text{m}/\text{m}$  and 100  $\mu\text{m}/\text{m}$ . Inducing of higher strain than 100  $\mu\text{m}/\text{m}$  is restricted by constructional aspects and size of the test set up. Within the scope of feasible test parameters resumed in Table 2, a Design of experiments (DoE) is elaborated to carry out the main test.

**Table 2: Feasible test parameters**

Parameter	Minimum value	Maximum value
Temperature	+10 °C	+60 °C
Rel. Humidity	10 %	90 %
Strain	50 $\mu\text{m}/\text{m}$	100 $\mu\text{m}/\text{m}$
Frequency	0.1 Hz	8 Hz

The MFC show the best matching properties for wind turbine applications among available piezoelectric sensor patches and are appropriate test objects for the main test. To investigate the influence of patch dimension and operating mode, four different patches have been chosen as test objects. Two patches of same size but different operational mode, M8507-P1 and M8507-P2 have been selected to evaluate the influence of operational mode. Furthermore sensor patch of both operational mode with different dimension than of M8507 patches are chosen to investigate the influence of dimension. These sensor patches are M2814-P1 in  $d_{33}$ -mode and M0714-P2 in  $d_{31}$ -mode. The parameters of the chosen MFC correspond to values in Table 3

**Table 3: Parameters of chosen MFC**

Sensor Patch	Material	Capacity in nF	Young's Modulus in GPa	$d_{31}$ or $d_{33}$ in pC/N	Dimension in $\text{mm}^3$	Rel. Permittivity
M8507-P1	PZT 5A1	1.76	30.34	400	85x7x0.3	1850
M8507-P2	PZT 5A1	49.84	30.34	-170	85x7x0.3	1850
M2814-P1	PZT 5A1	1.15	30.34	400	28x14x0.3	1850
M0714-P2	PZT 5A1	7.89	30.34	-170	7x14x0.3	1850

Test specimens with dimension of 0.3 m x 0.04 m x 0.002 m serve as a host structure for the selected piezoelectric patches. These test specimen are manufactured of stainless steel and glass-fiber reinforced plastic (GFRK). By means of specimen of two different materials, the influence of an anisotropic and isotropic host structure will be compared. As reference sensor for piezoelectric sensors conventional metal film strain gauges (1-LY11-6/120, HBM) are applied in a half-bridge configuration to the test specimen. On the top side of the specimen, which elongates during the four-point bending test and generates strain on the surface, P1-patches are mounted. P2-patches which measure strain as contractors are attached on the bottom side (Figure 8).

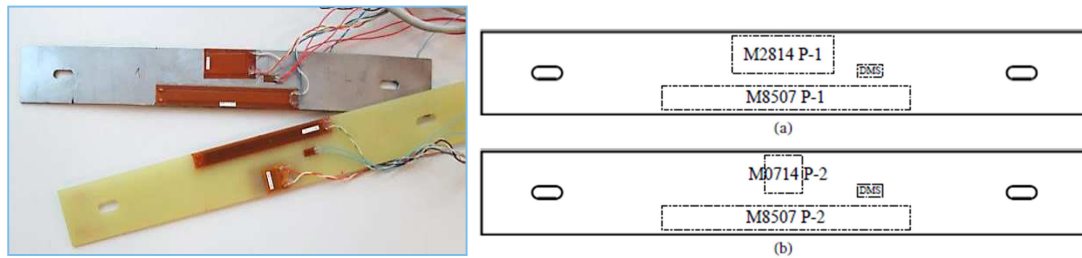


Figure 8: Right: Test specimen made of stainless-steel and GFRK. Left: a) Top-side and b) bottom-side of a specimen with denoted mounting-positions of MFC

### Test procedure

The test procedure begins with setting of the climate chamber. According to the elaborated design of experiment, the desired values of temperature and rel. humidity are chosen. After the climatic conditions are reached, a specimen is put into the climate chamber and is preloaded by the test set up. Since the temperature of the specimen has to be equivalent to the ambient temperature, the thermal time constant of the given specimen is calculated to estimate the waiting time until the ambient temperature is reached. After this step, the zero-point adjustment of the strain gauges is implemented to eliminate the offset signal which is caused by preloading. The signal conditioning of strain gauges is carried out by PICAS carrier frequency amplifier of Peekel Instruments. The bending of the specimen is measured by laser rangefinder LD 1605-50 of Micro-Epsilon which determines the distance of the maximum bending point to the laser source. This parameter is required to verify the calculated mechanical parameters of the test set up in comparison with measured values. The charge as output signal of the four different piezo patches attached to the specimen is amplified by a commercial charge amplifier of type 5015A of Kistler. The climate data acquisition is realized by serial communication between the climate chamber and control computer. The control computer is linked to a target PC and utilizes the software Simulink Realtime for acquisition of all measurement parameters. The hardware of the system provides multiple channels to measure various parameters simultaneously. Besides of data acquisition, the mechanical excitation of the specimen by means of the shaker is controlled by the software.



Figure 9: Four-point bending test set up

### Design of Experiment

By means of a design of experiment, effects of input variables on an output variable can be analyzed. The input variables are referred to as factors and the output variable to as response. Within the scope of current investigation, sensor patch dimension (factor A),

climatic condition (factor B), excitation frequency (factor C) and strain (factor D) are considered as factors. The magnitude gain which can be extracted from the transfer function between piezo patch and strain gauges is the response of the elaborated DoE. The effects of given factors on the magnitude are investigated in a 2-level factorial design. In this design, each factor is set to two different levels to identify the change of the response due to investigated factor. Furthermore, main effects and interactions of factors have to be distinguished in such kind of a factorial design. Main effects can be determined for one or more factors and are illustrated in a main effect diagram which determines if different levels of one factor affect the response. The response of each factor level is connected by a line in the diagram while the x-axis demonstrates the factor level and the y-axis represents the magnitude. If one factor level causes an effect on the response different to the effect of the other level, the connecting line will be not parallel to the horizontal axis. If the effects of both factor levels are equal, the connecting line will proceed along the horizontal axis.

The effects of 2-way interactions are determined for at least four factors. An interaction is characterized by the fact that the effect of one factor depends on the level of the other factor. If the response caused by one factor level is overlapped by response of the other factor level, no interaction is present. An interaction is denoted by different responses corresponding to different factor levels.

In general, the main effect diagram helps to identify the trend of the response without regarding interactions. If there would be no interactions between factors, a main effect diagram would be sufficient for analysis. A significant interaction would affect the diagram of the main effects so that an analysis of interactions is necessary to interpret main effects properly. By means of the diagram for 2-way interactions, it is determined which combination of factors affects the response mostly.

The gain of magnitude was chosen as output variable respectively as response for the assessment of different piezo patches by means of an equal criterion. Due to the specific dimension of each sensor patch, the generated charge as output signal is not equal even under same test condition and the sensor patches are not comparable. For this reason, the transfer function between strain and charge is determined while measurement data in time domain has been normalized to the each maximum amplitude. The transfer function  $H$  is described by equation  $H(j\omega) = \frac{C(S)}{U(S)}$ , whereby  $C$  is charge generated by piezo patches and  $U$  is the output voltage of strain gauges. Both variables represented normalized measurement data and are related to uniaxial strain  $S$  of the applied specimen. An inconsistency of charge magnitude caused by a factor is quantified as a drift distinct from 0 dB for each sensor patch. This approach enables the comparison of the performance of different piezo patches according to performance of strain gauges.

In the course of the current investigation, factor A is interesting for reason of the influence of the active sensor patch area on strain measurement. The level factors are chosen to 'S' for short and 'L' for long. So 'S' denotes "short" sensor patches as M2814-P1 (L/B = 2<sup>3</sup>) and M0714-P2 (L/B = 0.5) and 'L' denotes "long" sensor patches as M8507-P1 and M8507-P2 (L/B = 12.14).

Factor B was chosen with regard to the fact that temperatures up to +60 °C and rel. humidity of maximum 90 % occur during measurement on a rotor blade. Temperature and rel. humidity are considered separately as factor. According to the specifications of

---

<sup>3</sup> L/B = Length-to-Width Ratio

the climatic chamber utilized in this investigation, the minimum level of temperature is determined to +10 °C and the maximum level to +60 °C. The minimum level of rel. humidity is 10 % and the maximum level is 90 %. Since the point of the investigation is the suitability of piezoelectric sensors in quasi-static frequency range, the excitation frequency as factor C constitutes an importance factor of the DoE. The value of minimum excitation frequency is at 0.1 Hz while the maximum value is 8 Hz. The dependence on measured strain is investigated by means of factor D. To ensure constant operation of sensor patches on rotor blades for strains higher than 1000  $\mu\text{m}/\text{m}$  it is examined which sensor patch is suitable for this purpose. With respect to mechanical restrictions given by the test set up for four point bending test, the strain is varied between 50  $\mu\text{m}/\text{m}$  and 100  $\mu\text{m}/\text{m}$ . The different piezoelectric operational mode is not accounted as a factor but measurements with same parameters are carried out for the two given types of MFC for comparison. All available combinations of four factors are presented in Table 4.

**Table 4: Available combinations for four factors**

	<b>A</b>	<b>B</b>	<b>C</b>	<b>D</b>
A	-	A*B	A*C	A*D
B	B*A	-	B*C	B*D
C	C*A	C*B	-	
D	D*A	D*B	D*C	-

Due to the characteristics of a 2-level factorial design, just a partial quantity is analyzed so that main effects and interactions cannot be distinguished in some cases. For this reason interactions which can be identified in a 2-level factorial design correspond to the first line of table 3 and are denoted as A\*B, A\*C and A\*D.

In regard to the available factors, measurement series have been elaborated for different test conditions. Measurement series which deal with interactions of factors are termed as measurement series no. 2 and no. 3 in the following. Measurement series no. 1 and no. 4 illustrate main effects of three different factors.

The DoE concerns short time measurements of 4 min. For long time measurement of 4 h, performances under extreme conditions are investigated.

#### Measurement series no. 1

Measurement series no. 1 deals with sensor patch performance under normal conditions, i.e. temperature value of +23 °C and rel. humidity value of 50 %. Since the climatic conditions remain constant, effects of three factors described in Table 5 are investigated by means of a main effect diagram. The minimum factor level is denoted by '(-)'-symbol and the maximum factor level by '(+)'-symbol.

**Table 5: Test parameters for measurement series no. 1**

<b>Variable</b>	<b>Factor</b>	<b>-</b>	<b>+</b>
A	Dimension	S	L
C	Frequency	0.1 Hz	8 Hz
D	Strain	50 $\mu\text{m}/\text{m}$	100 $\mu\text{m}/\text{m}$

Transfer-functions of MFC type 1 corresponding to measurement series no. 1 carried out with excitation of 50  $\mu\text{m}/\text{m}$  are illustrated in Figure 10 and Figure 11. It can be observed that the magnitude decreases slightly with increased frequency for both sensor patches whereby the decrease of M2814-P1 is higher than of M8507-P2. If the excitation is increased to 100  $\mu\text{m}/\text{m}$  it is observed that the magnitude gain of M8507-P1 decreases more than with an excitation of 50  $\mu\text{m}/\text{m}$  at frequency of 8 Hz. The decrease can be

caused by the effect of higher strain but also an interaction between frequency and strain is possible.

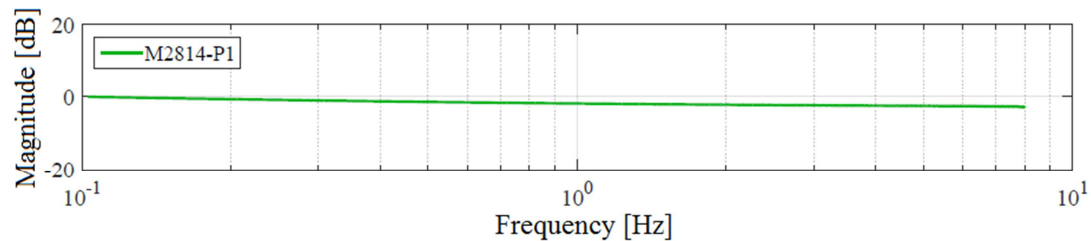


Figure 10: Transfer-function of M2814-P1 under normal conditions (excitation: 50  $\mu\text{m/m}$ )

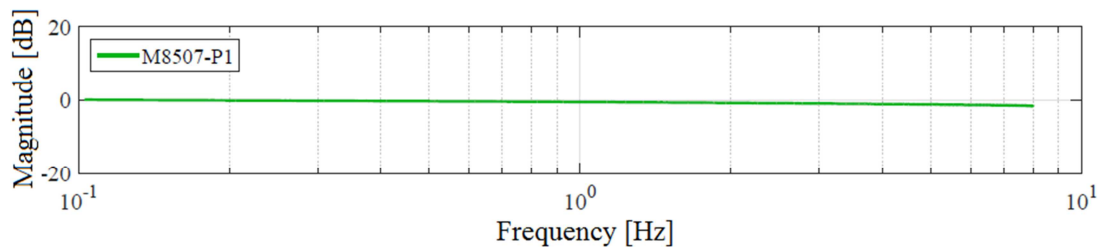


Figure 11: Transfer-function of M8507-P1 under normal conditions (excitation: 50  $\mu\text{m/m}$ )

These results are reflected in the main effect diagram which follows below. The main effect diagram considers also measurements carried out with an excitation of 100  $\mu\text{m/m}$  of which transfer-functions are not presented as figures for reasons of clarity. The main effect diagram depicted in Figure 12 visualizes the effects of factors dimension, frequency and strain. The highest change of magnitude  $A_M$  is approved for the factor frequency by the steepest slope connecting the magnitude of each factor level. The steepness of slope indicates that MFC of type P1 are highly dependent on excitation frequency. The factors dimension and strain affect the performance just slightly, in equal scale.

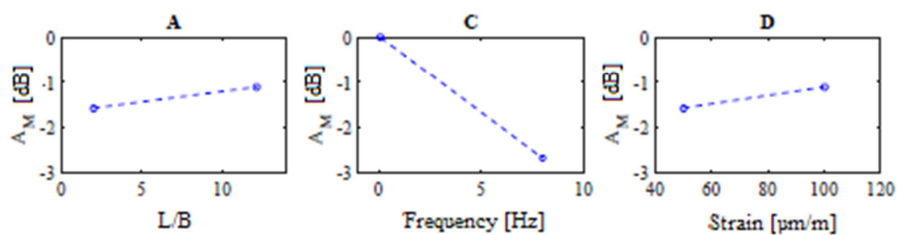


Figure 12: Main effects on response of MFC P1

The transfer-functions of MFC type P2 are characterized by another trend. The magnitude of M0714-P2 is increased at a frequency of 8 Hz while the magnitude of M8507-P2 has not changed (Figure 13, Figure 14).

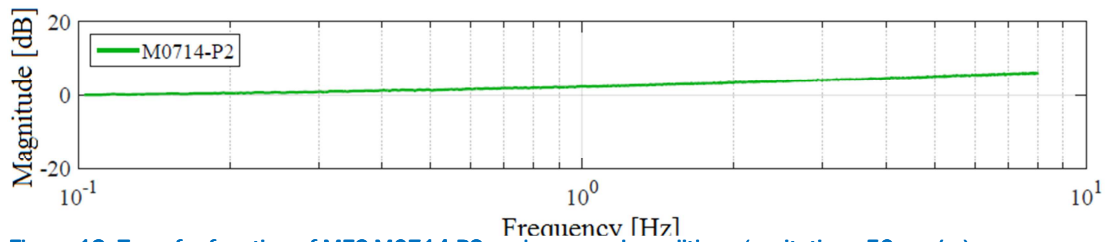


Figure 13: Transfer-function of MFC M0714-P2 under normal conditions (excitation: 50  $\mu\text{m/m}$ )

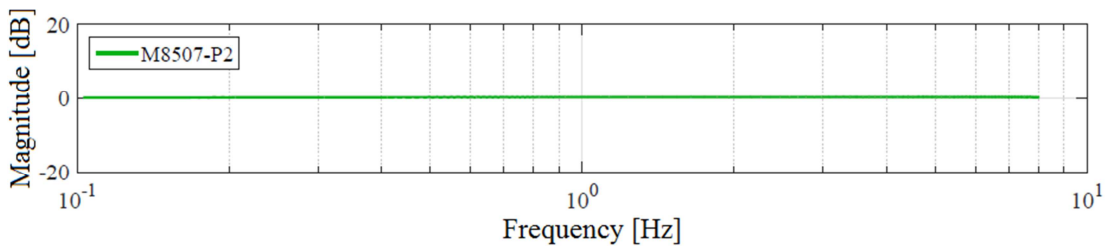


Figure 14: Transfer-function of M8507-P2 under normal conditions (excitation: 50  $\mu\text{m/m}$ )

The main effect diagram of MFC of type P2 (Figure 15) demonstrates different characteristics in comparison to MFC of type P1. At first sight, MFC of type P2 seem to be highly dependent on each investigated factor as steep slopes between the magnitudes of factor levels are illustrated in the diagram. In regard to the interaction between the factors in the following chapters, it should be considered that the main effect diagram shows up the trend but can be influenced by interactions of factors.

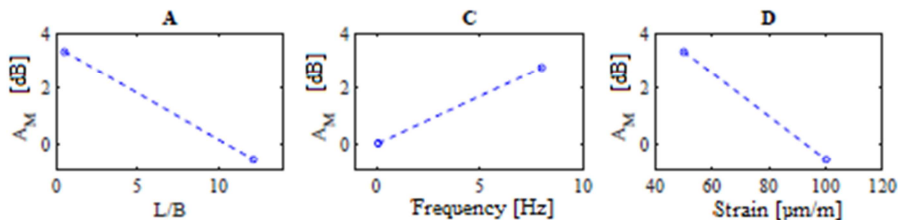


Figure 15: Main effects on response of MFC P2

## Measurement series no. 2

The measurement series no. 2 investigates the effects of factors for constant rel. humidity of 50 %. While rel. humidity remains constant, temperature is varied between two factor levels (Table 6). Since four different factors are affecting the measurement, a main effect diagram and an interaction diagram is generated for measurement series no. 2.

Table 6: Test parameters for measurement series no. 2

Variable	Factor	-	+
A	Dimension	S	L
B	Temperature	+10 °C	+60 °C
C	Frequency	0.1 Hz	8 Hz
D	Strain	50 $\mu\text{m/m}$	100 $\mu\text{m/m}$

Transfer-functions of measurement series no. 2 with excitation of 50  $\mu\text{m/m}$  are illustrated in Figure 16 and Figure 17. In measurement series no. 1, the decreasing trend of MFC type P1 sensors was identified whereby the effect was larger for M2814-P1 than M8507-P1. At test conditions of measurement series no. 2, the decrease of magnitude is higher for M8507-P1. In particular it is remarkable that at temperature of +10 °C, the decrease of magnitude is even higher than at +60 °C. This indicates that the decrease must be mostly caused by frequency dependence or that there is an interaction which results as an unexpected effect.

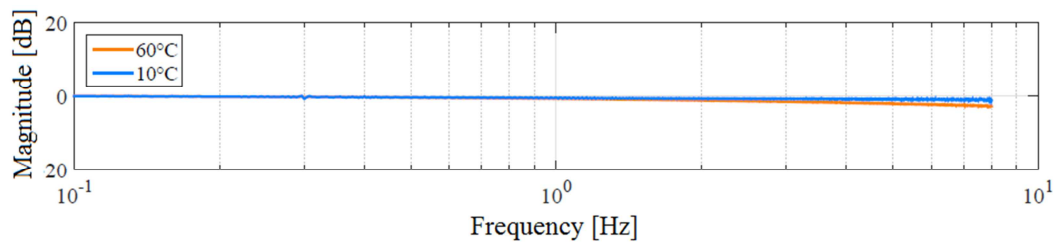


Figure 16: Transfer-function of M2814-P1 for measurement series no. 2 (excitation: 50  $\mu\text{m/m}$ )

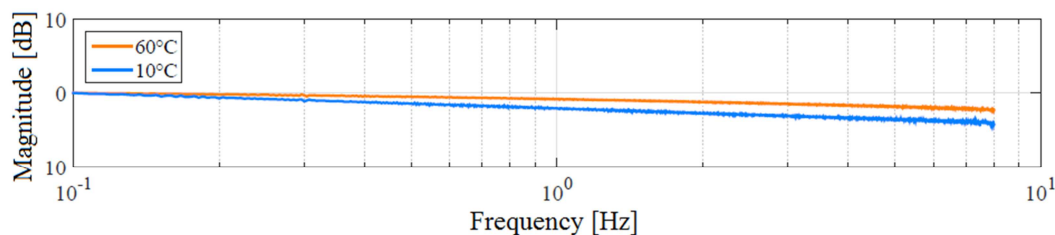


Figure 17: Transfer-function of M8507-P1 for measurement series no. 2 (excitation: 50  $\mu\text{m/m}$ )

The main effect diagram of MFC type P1 (Figure 18) indicates that the most remarkable effect is caused by the excitation frequency under condition of constant rel. humidity.

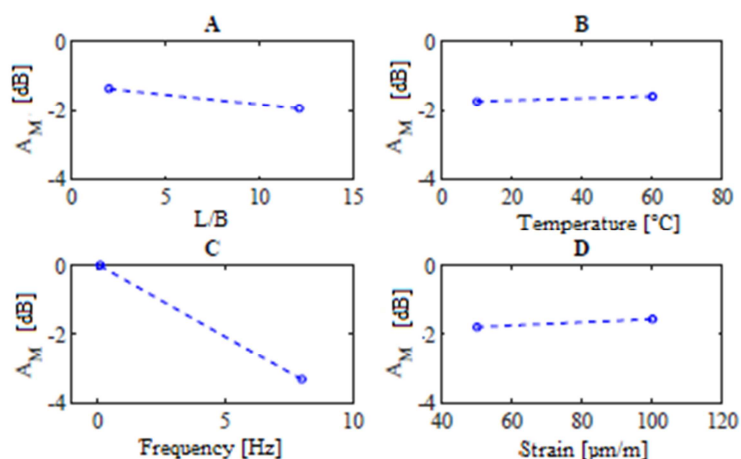


Figure 18: Main effects for a constant rel. humidity of 50 % for sensor type P1

In Figure 19, Figure 20 and Figure 21 effects of the investigated factors are analyzed in detail due to interactions between the factors. The interaction between temperature and sensor dimension is depicted in Figure 19. While the magnitude of M2814-P1 remains at same value for +10 °C and +60 °C, the magnitude of M8507-P1 changes due to the variation of temperature.

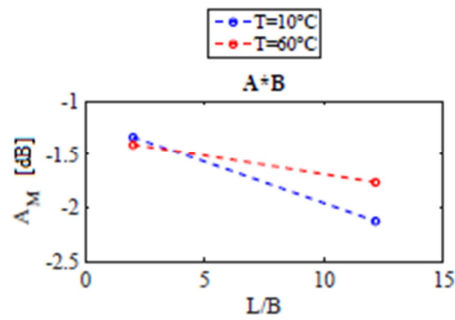


Figure 19: Interaction between sensor dimension and temperature for sensor type P1

As opposed to the interaction with temperature, MFC P1 of both dimensions interacts with the excitation frequency (Figure 20). The increase of frequency causes a decrease of magnitude for each factor level. The high frequency dependence as depicted in the main effect diagram can be approved.

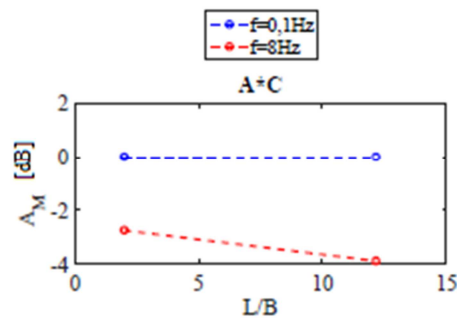


Figure 20: Interaction between sensor dimension and frequency for sensor type P1

The interaction between sensor dimension and strain is equal to the interaction between sensor dimension and temperature. The effect of interaction affects the magnitude of MFC M8507-P1 higher than the magnitude of MFC M2814-P1 (Figure 21).

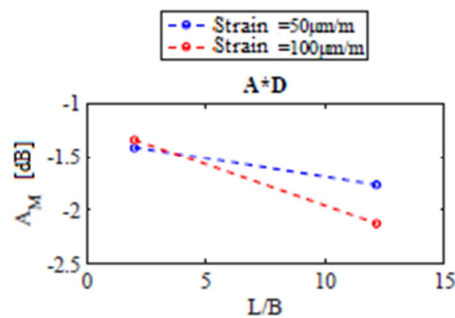


Figure 21: Interaction between sensor dimension and strain for sensor type P1

The transfer-function of MFC M0714-P2 in Figure 22 demonstrates also that the effect on magnitude is higher at +10 °C than at +60 °C. In comparison, the transfer-function of M8507-P2 in Figure 23 is not disturbed by any effect at 0 dB level.

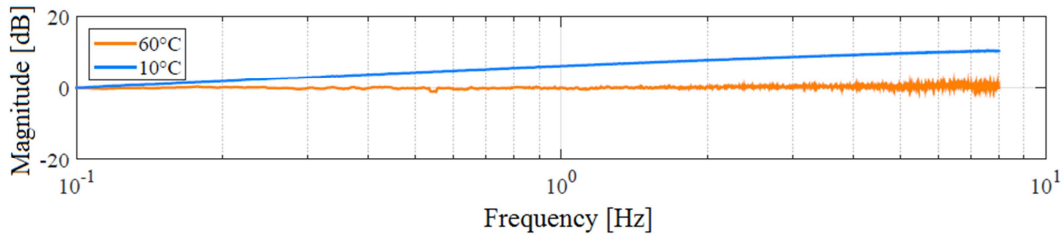


Figure 22: Transfer-function of M0714-P2 for measurement series no. 2 (excitation: 50  $\mu\text{m/m}$ )

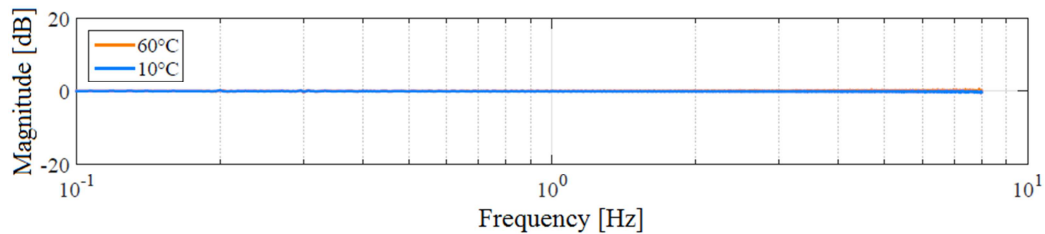


Figure 23: Transfer-function of M8507-P2 for measurement series no. 2 (excitation: 50  $\mu\text{m/m}$ )

The main effect diagram of MFC type P2 in Figure 24 illustrates a different trend than the main effect diagram of MFC P1 in Figure 18. The effect of each factor is designated with a steep slope. In particular sensor dimension and excitation frequency induce the most remarkable change of magnitude.

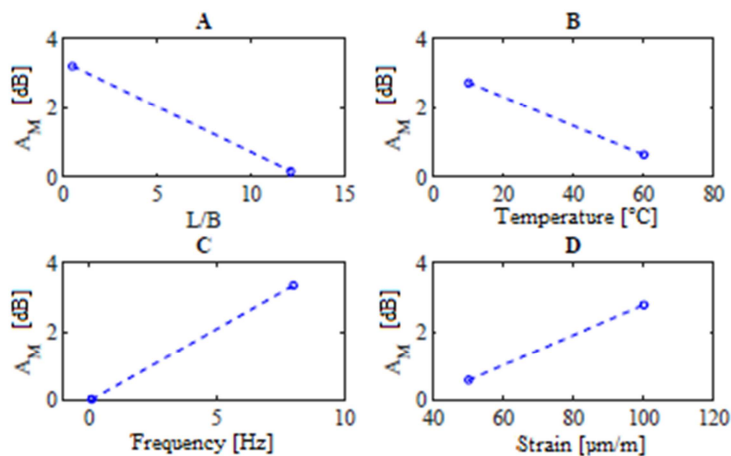


Figure 24: Main effects for a constant rel. humidity of 50 % for sensor type P2

In the diagrams illustrating the interactions the high dependence of “short” sensor patch M0714-P2 on all factors is identified (Figure 25). The magnitude increases up to +6 dB

affected by interaction between two factors while the magnitude of “long” sensor patch M8507-P2 remains at same value irrespective of measurement conditions. The interaction of temperature and strain with sensor patch dimension is influencing the magnitude at the same way (Figure 26, Figure 27).

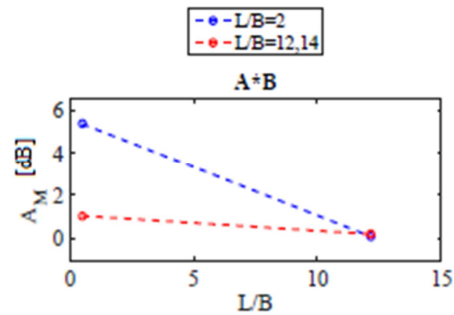


Figure 25: Interaction between sensor dimension and temperature for sensor type P2

The highest influence is caused by excitation frequency. A frequency of 8 Hz increases the magnitude of M0714-P2 to a level of +6 dB.

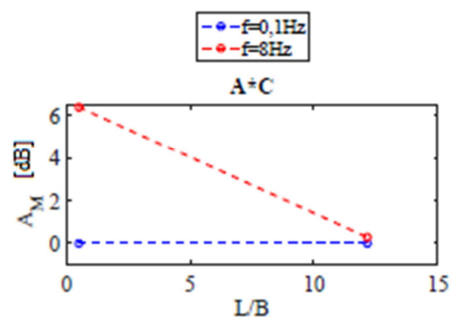


Figure 26: Interaction between sensor dimension and frequency for sensor type P2

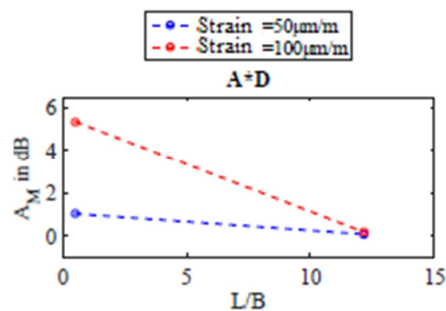


Figure 27: Interaction between sensor dimension and strain for sensor type P2

The interaction of factors influences the analysis of the main effect diagram. The main effect diagram helps to understand the trend of two different sensor types P1 and P2 but to know which factor effects which one of each sensor type, interaction need to be examined.

Measurement series no. 3

To carry out measurement series no. 3, the factor level of temperature is at a constant of value of +23 °C. While temperature value remains at same level, rel. humidity, dimension, frequency and strain are varied (Table 7).

Table 7: Test parameters for measurement series no. 3

Variable	Factor	-	+
A	Dimension	S	L
B	Rel. humidity	10 %	90 %
C	Frequency	0.1 Hz	8 Hz
D	Strain	50 $\mu\text{m}/\text{m}$	100 $\mu\text{m}/\text{m}$

As designated in the main effect diagram for MFC of type P1 in Figure 28, just excitation frequency can be considered as a main effect since the influence of other factors is marginal. Excitation frequency of 8 Hz can cause a decrease of magnitude to -2 dB.

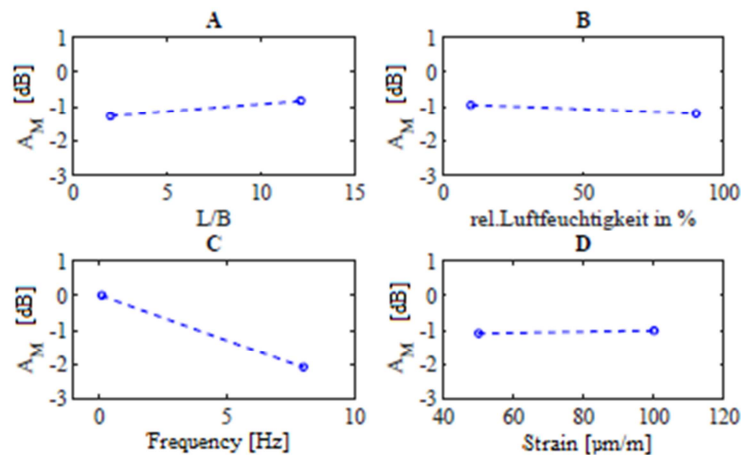


Figure 28: Main effects for a constant temperature of +23 °C for sensor type P1

In regard to Figure 29, an interaction of patch size and rel. humidity exists for MFC M2814-P1. For MFC M8507-P1 no change of magnitude is detected.

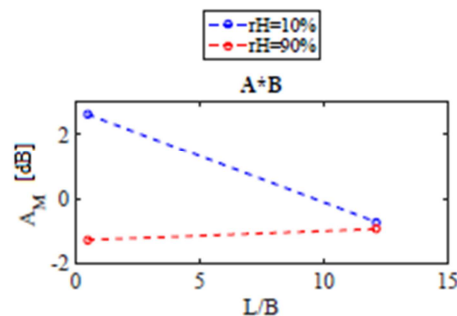


Figure 29: Interaction between sensor dimension and rel. humidity for sensor type P1

Figure 30 demonstrates opposite trend of M2814-P1 and MFC M8507-P1 for interaction with excitation frequency. The change of magnitude of each sensor patch is same according to amount but while the magnitude of M2814-P1 increases with higher frequency, the magnitude of M8507-P1 decreases. In comparison to Figure 20 it is

interesting that for constant rel. humidity, the magnitude of both sensors changed in the same direction while for constant temperature the direction is opposite to each other.

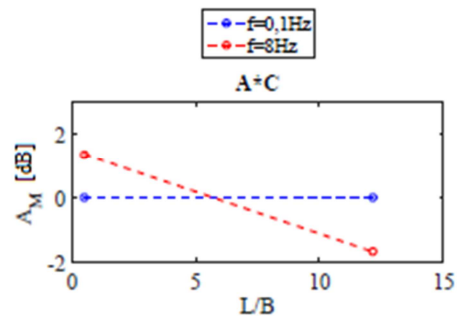


Figure 30: Interaction between sensor dimension and frequency for sensor type P1

The interaction between sensor patch dimension and strain cause an increase of the magnitude of M2814-P1. The magnitude of M8507-P1 does not change (Figure 31).

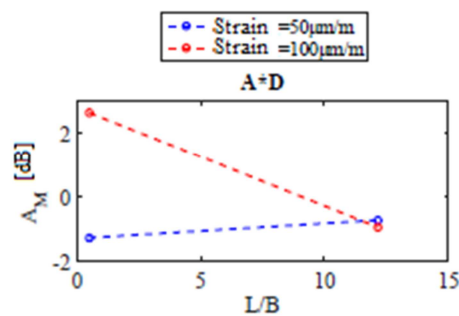


Figure 31: Interaction between sensor dimension and strain for sensor type P1

The main effect diagram for sensor patches of type P2 in Figure 32 characterizes sensor patch dimension and excitation frequency as main effects. The change of magnitude is equal to the change in the main effect diagram of measurement series no. 1 which is carried out under laboratory conditions.

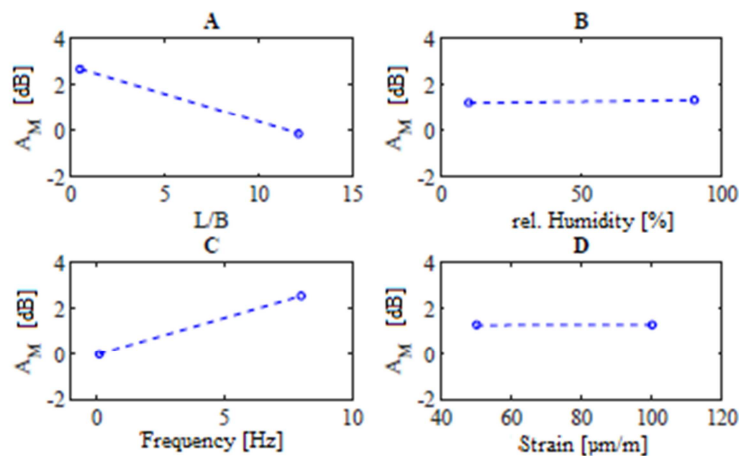


Figure 32: Main effects for a constant temperature of +23 °C for sensor type P2

Figure 33 indicates that there is no interaction between rel. humidity and sensor patch dimension. The variation of factor level does not affect the magnitude of both sensor patches.

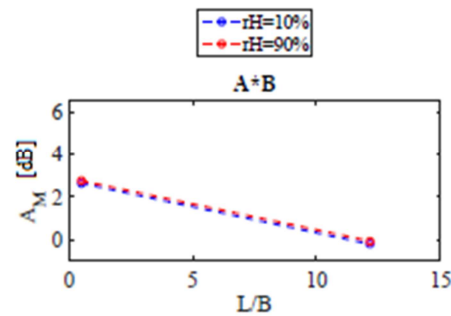


Figure 33: Interaction between sensor dimension and rel. humidity for sensor type P2

The change of level of frequency causes a shift of +6 dB of the magnitude of M0714-P2 (Figure 34). The effect of frequency is the most remarkable effect among the investigated factors.

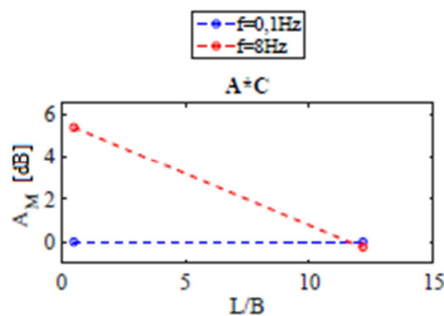


Figure 34: Interaction between sensor dimension and frequency for sensor type P2

The interaction between sensor patch dimension and strain (Figure 35) is equal to the interaction with rel. humidity.

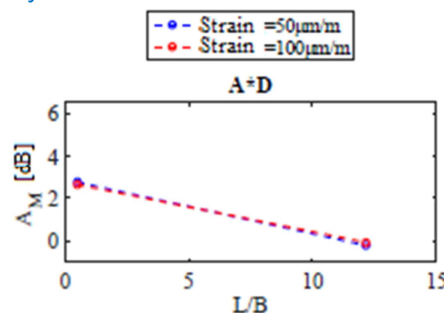


Figure 35: Interaction between sensor dimension and strain for sensor type P2

The measurement and analysis with DoE leads to the recognition that the magnitude of M8507-P2 remains at a level of 0 dB under any condition.

#### Measurement series no. 4

The measurement series no. 4 deals with temperature conditions of -30 °C. The factor levels are varied as described in Table 8. Due to three existing factors which affect the measurement, a main effect diagram is examined.

Table 8: Test parameters for measurement series no. 4

Variable	Factor	-	+
A	Dimension	S	L
C	Frequency	0.1 Hz	8 Hz
D	Strain	50 $\mu\text{m/m}$	100 $\mu\text{m/m}$

In regard to the main effect diagram for MFC of type P1 (Figure 36) it is significant that the influence of excitation frequency shows same behavior for temperature condition of  $-30\text{ }^{\circ}\text{C}$  as of  $+23\text{ }^{\circ}\text{C}$ . Furthermore the increasing magnitudes for higher factor level in measurement series no. 1 are decreasing in measurement series no. 4.

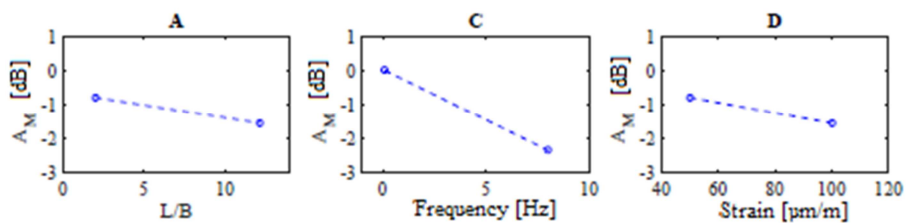


Figure 36: Main effects for a constant temperature of  $-30\text{ }^{\circ}\text{C}$  for sensor type P1

The performances of MFC of type P2 (Figure 37) demonstrate the same trend as in measurement series no. 1 beside the fact, that the slope of each factor is less steep. The decrease of the slopes indicates that the influence of main effects is less for temperature condition of  $-30\text{ }^{\circ}\text{C}$  than of  $+23\text{ }^{\circ}\text{C}$ .

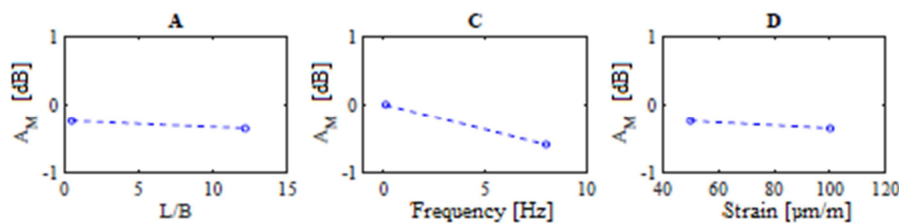


Figure 37: Main effects for a constant temperature of  $-30\text{ }^{\circ}\text{C}$  for sensor type P2

#### Results of measurement series no. 1 to no. 4

In regard to the magnitude gain of transfer-functions corresponding to measurement-series no. 1 to no. 4, P1-patches are not suitable as strain sensors contrary to the specification given by the manufacturer. The performances of MFC type P1 are characterized by high frequency dependence which increases with the patch dimension. Also influences of temperature, rel. humidity and excitation were remarkable in the magnitude and increased also with the patch dimension. The maximum drift of the magnitude of M2814-P1 is about  $-3\text{ dB}$  whereby the magnitude of M8507-P1 drifted up to  $-4\text{ dB}$ . The performance of P2-patches has shown the opposite result. The M0714-P2 is highly dependent on the investigated influences and the maximum drift of the magnitude is  $+6\text{ dB}$ . The piezo patch M8507-P2 shows the best performance for strain measurement among the investigated sensor patches. The drift of the magnitude of M8507-P2 is around  $0\text{ dB}$  at all events caused by simulated influences. An absolute shift of the amplitude in due to the climate is remarkable during strain measurement with piezoelectric patches but this shift is reproducible and can be compensated.

No remarkable difference was identified according to two different host structures for MFC of type P2.

**Table 9: Resumed results of measurement series no. 1 to no. 4**

	No. 1	No. 2	No. 3	No. 4
MFC	Magnitude	Magnitude	Magnitude	Magnitude
M8507-P1	-1.10 dB	-1.37 dB	-0.83 dB	-1.57 dB
M2814-P1	-1.57 dB	-1.94 dB	0.68 dB	-0.8 dB
M8507-P2	-0.6 dB	0.14 dB	-0.13 dB	-0.35 dB
M0714-P2	3.36 dB	3.32 dB	2.68 dB	-0.24 dB

### Results of long-time measurements

Beside Short Time measurement series, long-time measurement series have been carried out. Long-time measurement series investigate the magnitude consistency of sensor patches for extreme environmental conditions within 4 hours. These conditions comprise the combination of maximum temperature value with minimum rel. humidity value, combination of maximum rel. humidity value with minimum temperature and combination of maximum values of both parameters. To eliminate effects of other factors than temperature and rel. humidity, specimens have been excited by constant frequency. For long-time measurements, the correlation of strain and charge was determined (Table 10). The consistency of charge signal amplitude for investigated environmental conditions is illustrated in Figure 38.

**Table 10: Correlation coefficient for long-time measurements**

	I	II	III
Sensor patch	+60 °C and 10 % rel. humidity	+23 °C and 90 % rel. humidity	+60 °C and 90 % rel. humidity
M8507-P1	0,9561	0,9954	0,9921
M2814-P1	0,9962	0,9706	0,9998
M8507-P2	0,9925	0,9905	0,9931
M0714-P2	0,9895	0,9921	0,9892

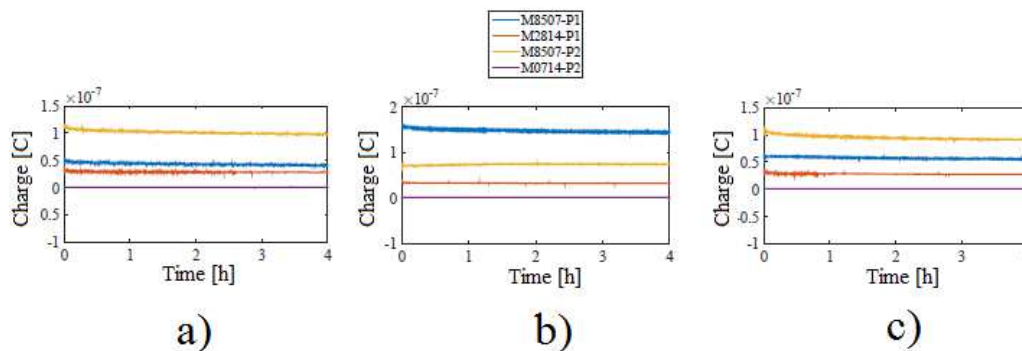


**Figure 38: Consistency of charge signal amplitude: a) condition I, b) condition II and c) condition III according to Table 13.**

### Signal Conditioning

The common used technique to improve the low frequency behavior of piezoelectric based strain sensors is a simple charge amplifier circuit which presents high input impedance to the piezoelectric sensor and is capable to measure the charge which is generated by the piezoelectric sensor due to induced stress. As discussed above, this corresponds to measure the strain.

In the following a charge amplifier in voltage mode corresponding to Figure 39 is investigated.

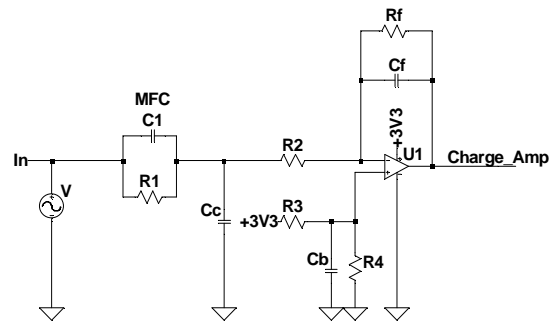


Figure 39: Voltage mode charge amplifier circuit

The time constant of the circuit is given by  $R_f C_f$  and can be selected to match the desired lower cut-off frequency. Due to the presence of a finite leakage resistance in the electrical parts there is always a physical limit for adjusting the lower cut-off frequency, so that there is no possibility to measure static conditions with this circuit [12]. Even if very large values for  $R_f C_f$  are selected, the output voltage will tend to drift after a while. Furthermore values for  $R_f \geq 100 \text{ M}\Omega$  can cause problems like thermal noise. Figure 40 indicates how different values for  $R_f$  effect the lower cut-off frequency of the amplifier circuit. Even if there are very large values for surface mount resistors available, the desired dynamic range from 0.2 Hz - 5 Hz cannot covered with this conventional conditioning circuit.

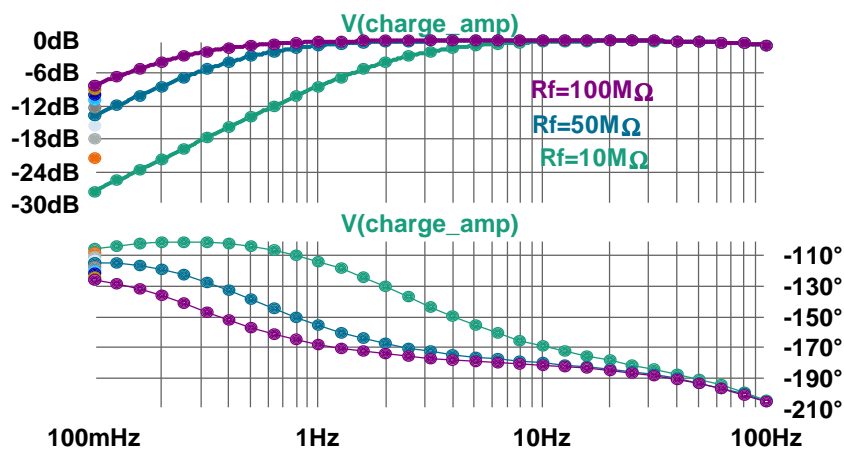


Figure 40: frequency response of the charge amplifier for different values for  $R_f$

In [27] it is proposed to assume  $R_f$  as the insulation resistance of the capacitor. Related to the material of the capacitor, the insulation resistance is at least 10 MΩ while the

maximum value is conventionally not a given specification. Furthermore the input resistance of the charge amplifier is pointed out as one of the most important specifications since leakage current of the input accounts for signal drift. With respect to this matter of fact, a charge amplifier is realized in the course of investigation regarding signal conditioning for quasi-static measurements.

As a high-input-resistance operational amplifier, OPA657 of the manufacturer Texas Instruments is chosen. This amplifier consists of a JFET input stage, which is a recommended architecture for charge amplifier applications. According to datasheet OPA 657 provides an input resistance of  $1\text{ T}\Omega$  and has an input leakage current of  $2\text{ pA}$ . The feedback capacitor  $C_f$  has a value of  $1\mu\text{F}$  whereby a switch is set in parallel. The switch is necessary to shortcut  $C_f$  for discharge. If the capacitor would not be shortcut, remaining charges would disturb further measurements with the charge amplifier. To avoid drift current, the switch also needs a high insulation resistance in opened state. Electromechanical relays are suitable for this task, since transistors exhibit leakage current in not conducting state. Therefore miniature relay G6K-2F of the manufacturer Omron is chosen.

The developed charge amplifier is designed for a power supply voltage of  $+5\text{ V}$  with respect to data acquisition with a microcontroller platform. The output signal refers to an offset voltage of  $2.5\text{ V}$ . To adopt the output signal at the input of the analog-to-digital-converter of the microcontroller, the end stage of the charge amplifier amplifies the signal with a gain factor of  $0.66$ . Thus the maximum amplitude of the signal at the input will be steadily at  $3.3\text{ V}$ .

With respect to creating a sensor-network, the charge amplifier is realized as a shield for XMC 4800 development platform of Infineon (Figure 41).

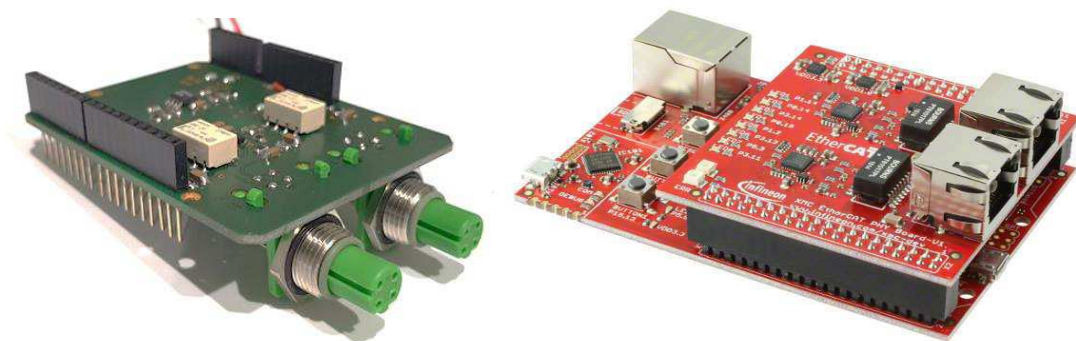


**Figure 41:** Left: developed charge amplifier shield, right: XMC 4800 development platform of Infineon

Measurement data with the developed shield are shown in Figure 42 and Figure 43 whereby output signal of strain gauges serve as reference values. The output signal of the charge amplifier is in compliance with the reference values assured by coherence and transfer-function.

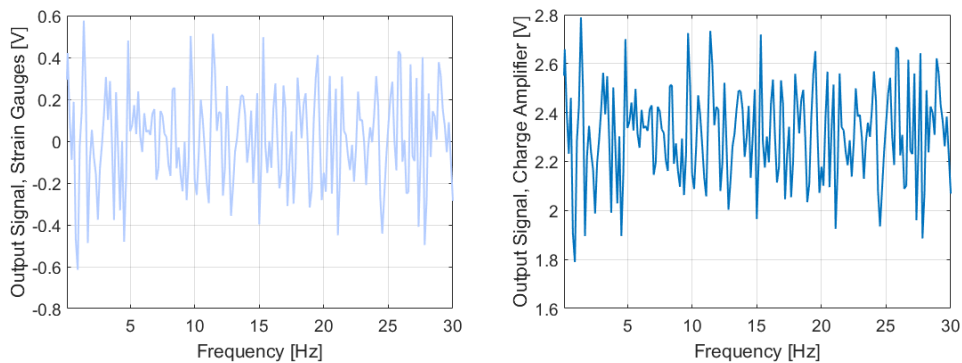


Figure 42: Left: output signal of strain gauges, right: output signal of charge amplifier

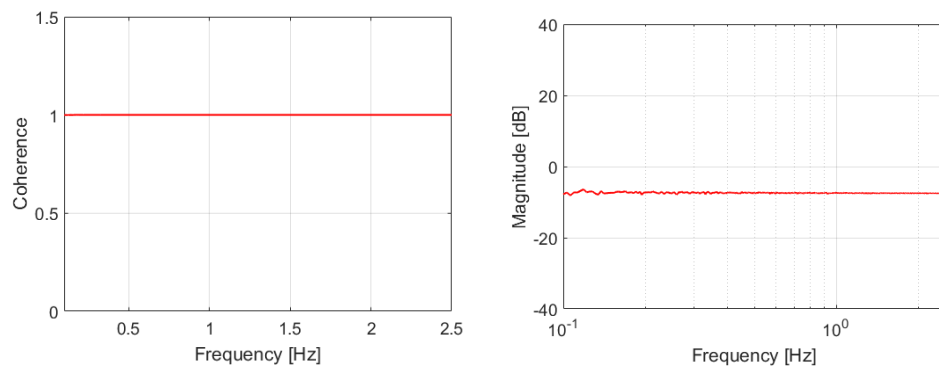


Figure 43: coherence (left) and transfer-function (right) between both output signals

## 2.4 Sensor-Network Platform

Finally based on the former investigations a signal conditioning unit for the piezoelectric load sensor has been developed along with an appropriate data acquisition, signal-processing and data communication system. Each load sensor mote consists of the developed signal conditioning circuit, which is capable to interface two MFC patches. In addition a XMC 4800 Development platform from Infineon<sup>4</sup> has been taken for data acquisition, signal processing and data transmission.

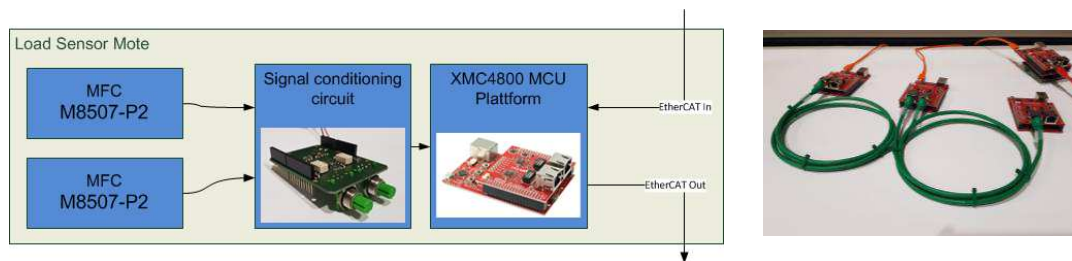
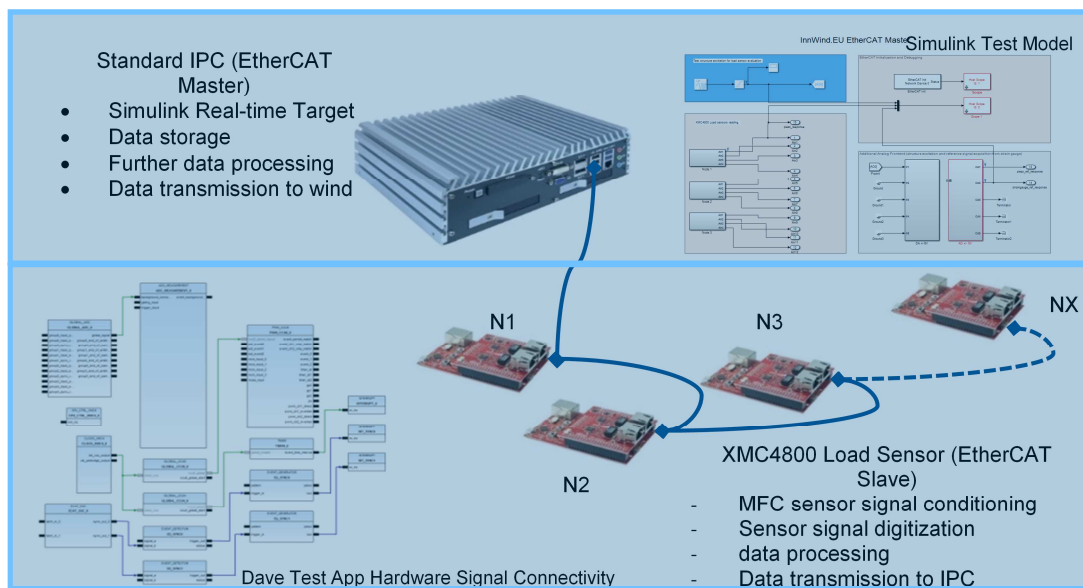


Figure 44: Load sensor Electronics and 4 Mote test configuration

The XMC4800 Microcontroller from Infineon consists of an ARM Cortex M4 MCU which has an integrated EtherCAT Node, so multiple (theoretically up to 65535 devices per network segment) of those Motes can be connected to distributed network of sensors. The decision for EtherCAT as

<sup>4</sup> [https://www.infineon.com/cms/en/product/promopages/xmc4300\\_4800-EtherCAT/](https://www.infineon.com/cms/en/product/promopages/xmc4300_4800-EtherCAT/)

communication bus has been made because of several performance benefits compared to other bus systems. Especially the tight synchronization mechanism of the EtherCAT slaves (load sensor motes) down to  $1\mu\text{s}$ , flexible topologies of the network (Line, Star, Tree) as well as long possible distances between slaves (100m for copper cable, 2km Optical fiber) makes EtherCAT an ideal candidate as powerful bus system for the aforementioned application. Since EtherCAT is based on Ethernet, commercial of the shelf Ethernet components and Industrial PCs (IPCs) can be used to build up a Sensor network. In case of installation of a line topology network along the rotor blade, 100Base-FX (optical fiber) can be used instead of 100Base-TX (copper cable) as transport medium to enhance lightning protection. A test topology that has been build up can be seen in Figure 45.



**Figure 45: Sensor network test topology and test application implementation in Simulink and Dave (Eclipse-based IDE from Infineon)**

On large rotor blades or towers the topology is scalable by plug and play extension of additional motes, e.g. distributed along the rotor blades or the tower for local load assessment, modal analysis and structural health monitoring (see Figure 46).

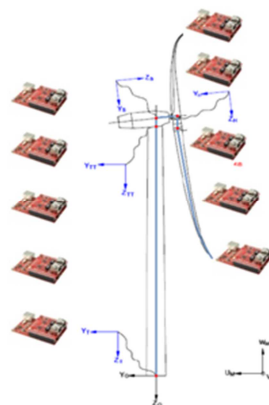


**Figure 46: Example for distribution of multiple load sensor motes along the wind turbine**

## 2.5 Conclusion

Through the experimental investigation of piezoelectric patches on a laboratory scale, the feasibility of using those types of sensors as load sensor has been proven. Especially the low frequency range down to 0.1 Hz has not been investigated in a systematic manner (DoE) before. By appropriate selection of sensor dimension and effect type ( $d_{31}$ ,  $d_{33}$ ) along with careful design of sensor signal conditioning, quasi-static load measurements down to 0.1 Hz could be achieved in our experiments.

According to the measurement results, the piezoelectric sensor patch M8507-P2 is approved to be suitable for SHM application of wind turbines and is able to operate in quasi-static frequency range by means of appropriate signal conditioning. Since the sensor performance of MFC type P2 was improved by increased sensor patch dimension, the findings in this investigation also provide an outlook for further piezoelectric sensors of bigger dimension which operate in  $d_{33}$ -mode for SHM applications on wind turbines. With regard to rotating components of a wind turbine, feasibility of wireless signal conditioning and data acquisition of the sensor principle is an important issue. Within the scope of the given investigation, it was shown that piezoelectric sensors are suitable to realize a sensor network for monitoring systems especially because piezoelectric sensors do not require external power supply and the effort of creating of a network will be highly reduced in comparison to strain gauges. Beside this specification, superior durability of piezoelectric patch sensors has been approved in [16] and higher sensitivity than of strain gauges is provided by piezoelectric sensors. Furthermore the principle of piezoelectric methodology enables structure health monitoring based on acousto ultrasonics (electromechanical impedance method) so that one further measurement principle beside charge measurement is feasible by means of piezoelectric sensors. In this context, the performance of electromechanical impedance method can be characterized for wind turbines and future applications in prospect.

**Table 11: Comparison of strain gauges and piezoelectric sensors**

Specification	Strain gauges	Piezoelectric sensor
Sensitivity	1 $\mu\text{m}/\text{m}$	$10^{-4}$ $\mu\text{m}/\text{m}$
Operating frequency range	$\geq 10^{-3}$	Quasi-static with appropriate signal conditioning, dynamic operating possible
Durability	Below life span of a wind energy plant	Higher durability and fatigue life
External Power	Power supply required	No need of power supply
Functionality	Non multi-functional	Multi-functional, EMI method realizable

## 2.6 References

- [1] E. A. Bossanyi, "Further load reductions with individual pitch control," *Wind Energy*, vol. 8, no. 4, pp. 481–485, <http://dx.doi.org/10.1002/we.166>, 2005.
- [2] P. Tchakoua, R. Wamkeue, M. Ouhrouche, F. Slaoui-Hasnaoui, T. A. Tameghe, and G. Ekemb, "Wind Turbine Condition Monitoring: State-of-the-Art Review, New Trends, and Future Challenges," *Energies*, vol. 7, no. 4, pp. 2595–2630, <http://www.mdpi.com/1996-1073/7/4/2595>, 2014.
- [3] H. Buff, J. Kloepfer, and J. Hansmann, "Automatic Damage Detection in Vehicle's Shock Absorbers," in *Proceedings of the Int. Conf. on Structural Engineering Dynamics*, 2013.
- [4] K. A. Kragh, *Performance enhancement and load reduction on wind turbines using inflow measurements*. Kgs. Lyngby: DTU Vindenergi, 2013.
- [5] T.K. Barlas and G.A.M. van Kuik, "Review of state of the art in smart rotor control research for wind turbines," *Progress in Aerospace Sciences*, vol. 46, no. 1, pp. 1–27, <http://www.sciencedirect.com/science/article/pii/S0376042109000293>, 2010.
- [6] K. A. Kragh, M. H. Hansen, and L. C. Henriksen, "Sensor comparison study for load alleviating wind turbine pitch control," *Wind Energ*, pp. n/a, 2013.
- [7] H. Aagaard Madsen and A. Fischer, "Wind shear and turbulence characteristics from inflow measurements on the rotating blade of a wind turbine rotor," in *EWECE 2009 Scientific proceedings: EWECE, 2009*, pp. 53–58.
- [8] A. Peña, C. B. Hasager, J. Lange, J. Anger, M. Badger, F. Bingöl, O. Bischoff, J.-P. Cariou, F. Dunne, S. Emeis, M. Harris, M. Hofsäss, I. Karagali, J. Laks, S. E. Larsen, J. Mann, T. Mikkelsen, L. Y. Pao, M. Pitter, A. Rettenmeier, A. Sathe, F. Scanzani, D. Schlipf, E. Simley, C. Slinger, R. Wagner, and I. Würth, *Remote Sensing for Wind Energy: DTU Wind Energy*, 2013.
- [9] K. Argyriadis (GL), and M. Capellaro (USTUTT) et al, *PROcedures for TESTing and measuring wind energy systems: Deliverable D1: State-of-the-Art-Report (2014, Aug. 05)*.
- [10] G. Gautschi, *Piezoelectric sensorics: Force, strain, pressure, acceleration and acoustic emission sensors, materials and amplifiers*. Berlin, New York: Springer, 2002.
- [11] J. Zayas, J. Paquette, and R. Werlink, "Evaluation of NASA PZT Sensor/Actuator for Structural Health Monitoring of a Wind Turbine Blade," in *45th AIAA Aerospace Sciences Meeting and Exhibit*
- [12] J. SIROHI and I. CHOPRA, "Fundamental Understanding of Piezoelectric Strain Sensors," *Journal of Intelligent Material Systems and Structures*, vol. 11, no. 4, pp. 246–257, 2000.
- [13] M. D. Todd and J. R. Wait, *Validation of Macro Fiber Composites as Strain Sensors*.
- [14] J. Rausch, C. Hatzfeld, R. Karsten, R. Kraus, J. Millitzer, and R. Werthschützky, "Strain measurement on stiff structures: experimental evaluation of three integrated measurement principles," *Smart Mater. Struct.*, vol. 21, no. 6, p. 064008, 2012.
- [15] M. Gall, "Experimentelle und numerische Untersuchungen zur Lebensdauer von flächigen piezokeramischen Sensor - / Aktor - Modulen," Universität Karlsruhe, 2012.
- [16] K. Wolf, J. Nuffer, A. Schönecker, B. Brückner, D. Kohlrantz, P. Michelis, and O. Adarraga, "Reliability Investigation of Piezoelectric Macro Fibre Composite (MFC) Actuators," in *ISPA 2007 International Symposium on Piezocomposite Applications*, 2007.
- [17] E. Schulze, L. Schubert, and B. Frankenstein, "Monitoring of a wind turbine rotor blade with Acousto Ultrasonics and acoustic emission techniques during a full scale fatigue test," in *Proceedings of the fifth European Workshop on Structural Health Monitoring 2010*, F. Casciati and M. Giordano, Eds, Lancaster, Pa.: DEStech Publications, 2010, pp. 1229–1234.
- [18] E. F. CRAWLEY and J. de LUIS, "Use of piezoelectric actuators as elements of intelligent structures," *AIAA Journal*, vol. 25, no. 10, pp. 1373–1385, 1987.
- [19] S. Bhalla, "Electromechanical Impedance Modeling for Adhesively Bonded Piezo-Transducers," *Journal of Intelligent Material Systems and Structures*, vol. 15, no. 12, pp. 955–972, 2004.
- [20] A. Laskovski, Moheimani, S O R, and M. R. Yuce, "Note: Piezoelectric strain voltage sensing at ultra-low frequencies," (eng), *Rev Sci Instrum*, vol. 82, no. 8, p. 086113, 2011.
- [21] A. N. Laskovski, M. R. Yuce, and S. O. R. Moheimani, "Ultra low frequency FM sensing of piezoelectric strain voltage," in *2012 IEEE Sensors*, pp. 1–4.
- [22] Anthony N. Laskovski, Mehmet R. Yuce, and S.O. Reza Moheimani, "FM-based piezoelectric strain voltage sensor at ultra-low frequencies with wireless capability," *Sensors and Actuators A: Physical*, vol. 199, no. 0, pp. 49–55, <http://www.sciencedirect.com/science/article/pii/S0924424713001982>, 2013.
- [23] U. Tietze, C. Schenk, and E. Gamm, *Halbleiter-Schaltungstechnik*, 12th ed. Berlin [u.a.]: Springer, 2002.

### 3 SCALED 2 BLADED ROTOR WITH FREE-FLOATING FLAPS [TUD]

This chapter is a slightly modified version of the following paper:

*Navalkar, Sachin T and Bernhammer, Lars O and Sodja, Jurij and van Solingen, Edwin and van Kuik, Gijs AM and van Wingerden, Jan-Willem , 'Wind tunnel tests with combined pitch and free-floating flap control: data-driven iterative feedforward controller tuning', Wind Energy Science, 1, 2, 2016*

#### 3.1 Introduction

The increasing size and flexibility of wind turbines demand that attention be devoted towards the active and passive control of rotor loads in order to limit the costs related to both the construction as well as maintenance of the turbine blades and the support structure. The dominant dynamic loading of turbine components occurs at 1P (rotor speed), and its harmonics. One of the most interesting and readily accessible methods of blade load control is Individual Pitch Control (IPC) Bossanyi (2003), whereby each blade is pitched along its longitudinal axis independently to counteract the variation in wind loading. Numerous references can be found in literature which prove the efficacy of IPC in load control of wind turbines, both in the simulation environment Selvam et al. (2009), Bottasso et al. (2013), as well as experimentally Bossanyi et al. (2013). In these references, with ordinary levels of turbulence, it has been observed that IPC can achieve up to 30% reduction in the standard deviation of blade loads. Previous experimental studies conducted by the authors Navalkar et al. (2015) show that in a controlled, wind tunnel environment, wind turbine blade load reductions up to 70% can be reached, since the blade loading under these circumstances is almost entirely deterministic. However, in all the references mentioned, the target of IPC has been to reduce low-frequency loads, primarily around the 1P (rotor frequency). While IPC can herewith address a large part of load spectrum, the emphasis on low frequencies is also a product of the low bandwidth that can be achieved with the full-span pitch control, which involves actuation of the large torsional inertia of the blades around their axes. As expected, IPC also leads to a substantial increase in pitch activity.

In an effort to reduce pitch actuator duty, target higher frequencies in the load spectrum, and address localised disturbances in the wind loading, recent literature has explored the concept of the 'smart' rotor Lackner and Van Kuik (2010): a rotor where the blades are instrumented with sensors and flow-modifying actuators at various radial locations. Reviews of such rotors Barlas and Van Kuik (2010) Bernhammer et al. (2012) invariably conclude that trailing-edge flaps give the best control authority for load alleviation. The load alleviation potential has been demonstrated in simulations Andersen et al. (2006) Bernhammer et al. (Article in Press) and experimentally in a wind tunnel Van Wingerden et al. (2011). Further, field tests of this concept have also been conducted Castaignet et al. (2013), although such a system is still not considered mature enough for incorporation in a commercial wind turbine. While these tests used conventional actuators, many references recommend the useage of smart actuators, such as piezoelectrics, in order to enhance bandwidth and achieve a high power-to-weight ratio. Such actuators unfortunately show low stroke and hence reduced control authority.

The concept of the free-floating flap Heinze and Karpel (2006) combines a trailing-edge flap that is free to rotate about its axis, with a small tab located on the flap, that can be actuated at a high speed to dynamically change flap camber. This concept was developed specifically to take advantage of aerodynamic levering to increase the low stroke of smart actuators. For a fixed wing instrumented with such a free-floating flap, it was experimentally shown Bernhammer et al. (2013) that it is possible to achieve enhanced control authority. Further, this study also demonstrated that such a flap could be completely autonomous in terms of energy consumption, and can be used as a plug-and-play device. This modularity shows promise for the construction and maintenance of future smart blade. However, this concept has not yet been demonstrated experimentally on a wind turbine.

Numerical and experimental investigations of the free-floating flap concept Heinze and Karpel (2006) Bernhammer et al. (2013) have shown that the additional degree of freedom adds

a rigid-body mode to the system, the dynamics of which are strongly dependent on the total air speed at operation. Aeroelastic coupling of this mode with the flexible blade mode induces flutter at low wind speeds, an instability that can lead to dangerously high vibrations and even structural failure. However, it has also been shown in the references that closed-loop control of the tab can ensure safe operation of a fixed wing, well into the unstable regime. A pitchable wind turbine blade instrumented with free-floating flaps thus poses several control challenges. Firstly, the nature of the flap implies that its dynamic response is not constant but varies strongly with the wind speed. Such a system cannot be described by a linear time-invariant (LTI) state-space realisation, but can possibly be expressed as a linear parameter-varying (LPV) system, where the time-varying parameter depends on the wind speed. Further, the presence of a stabilising closed-loop controller is mandatory. Finally, the uncertainties in flow and structure modelling imply that a robust controller may be unable to achieve the maximum possible load reductions. The advantage of using a data-driven control strategy would be that input-output data could be used to (locally) optimise a simple user-defined criterion. Further, if such a strategy is used to tune a feedforward controller, then the optimised controller cannot, in the steady state, destabilise the plant, and in the best case, it may be able to achieve load reductions that may not be attainable by a conservative, globally robust controller.

Data-driven control of wind turbine loads has been demonstrated experimentally in Navalkar et al. (2015), where online recursive system identification was combined with online controller synthesis for minimising the periodic turbine loads. However, such a controller would be required to retune itself at every instant the ambient wind conditions change. An alternative methodology for the data-driven alleviation of wind loads has been described in Navalkar and Van Wingerden (2015) which employs the iterative feedback tuning (IFT) Hjalmarsson (2002) methodology to tune the gains of a fixed structure controller, hereby optimising a (convex) performance criterion. While IFT controllers have been used in the industry, they have typically been implemented to converge to linear time invariant controller structures Gevers (2002). The use of IFT for tuning the gains of time-varying controllers, as required for the current application, has been described in literature Navalkar and Van Wingerden (2015) but not yet demonstrated in practice.

The contribution of this paper is thus threefold: firstly, scaled wind turbine blades instrumented with outboard free-floating flaps are designed and manufactured for wind tunnel testing. Secondly, the load alleviation potential of the free-floating flaps in combination with individual pitch control is demonstrated for the first time in an experimental sense. The load alleviation potential is investigated in both the stable and unstable (post-flutter) modes of operation, and the importance of collocated control will be highlighted. Finally, the setup will serve as a test bench for a novel iterative feedback tuning algorithm that automatically tunes a controller gain schedule for load alleviation in real-time variable wind speed operation.

The remainder of the chapter is organised as follows: Section 3.2 describes the design and manufacturing process for the wind turbine blades with free-floating flaps. Section 3.3 gives a brief description of the testing environment. The aeroelastic behaviour of the blades is studied in Section 3.4. The control algorithm used for load alleviation is formulated in Section 3.5. The results of the testing are laid out in Section 3.6, and conclusions are drawn from these results in the final section.

## **3.2 Blade design and manufacturing**

Since this paper reports on the first wind turbine implementation of free-floating flaps, first, the design of the experimental setup is discussed, and details regarding the materials, method of manufacture and assembly are provided. Primarily, the destabilising effect of the free-floating flap is studied in detail, and the parameters are tuned such that the blade is close to its 5 flutter point in order that maximal control authority is achieved. The design of the blades formed the most important part of the design process of the scaled turbine, since it had to form a reasonable approximation of a full-scale wind turbine blade while adhering to the constraints set by the wind tunnel capabilities. The primary scaling that was aimed to be achieved was maintaining the ratio

of blade first eigenfrequency to rotor speed ( $1P$ ), as is done in Van Wingerden et al. (2011). This ratio is typically around 3.5 for the modern turbines, Bak (2013).

#### Blade design

The overall aerodynamic and structural design of the blades follows the procedure described in Van Wingerden et al. (2011), since the blades were designed for similar wind tunnel testing conditions. Aerodynamic and structural details of the blade design can be found in Hulskamp et al. (2011). However, as the wind tunnel experiments will also incorporate blade pitch control, the torsional inertia of the blades was reduced by scaling down the root chord by 30%. The root chord thus measures 200 mm, tapering to a tip chord value of 120 mm over a blade length of 750 mm, with a total blade twist of 12 degrees.

Out of structural considerations, it was deemed necessary to minimise the weight of the blades, while ensuring adequate structural integrity to withstand the centrifugal and out-of-plane loading that the blade will be subject to during operation. An accurate aerodynamic shape of the blade was ensured by 3d printing the blade and then further reinforced with unidirectional carbon fibre spar caps, as shown in Figure 47. Small wind turbine blades have previously been manufactured in this manner by the University of Stuttgart Bauer et al. (2014), and a comparison of different additive manufacturing techniques can be found in Karutz (2015). These references specifically investigate 3D printing of blades in a set of sections that are bonded together. In order to avoid solid plastic-plastic joints, it was decided that the blades in the current case would be printed in one piece.

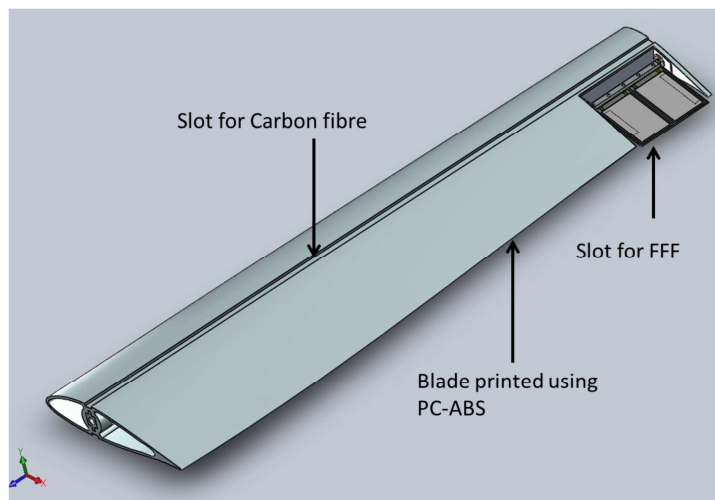


Figure 47, Blade CAD model



Figure 48, Photograph of Blade

Three different materials (ABS M30, PC-ABS and nylon), that can be used for 3D printing, were evaluated qua their ability to bond with carbon fibre. For each material, a rectangular sample of size 200 mm x 30 mm, of thickness 3 mm, was 3D printed. Subsequently, each sample was

bonded on the top and bottom with a single layer of unidirectional carbon fibres of thickness 0.14 mm, impregnated with epoxy resin. A four-point bending test to failure was then conducted with each of the samples. The distance between the supports was 140 mm, while the points of force application were 40 mm apart. The results of the test can be seen in Figure 49 and Figure 50. In Figure 49, the behaviour to failure in bending can be observed. For small loads, the response is linear. At higher loads, small kinks can be observed in each of the curves, these physically represent the snapping of individual carbon fibres in compression. Finally, there is a large drop in strength when delamination occurs in the materials ABS M30 and nylon. For the material PC-ABS, brittle fracture occurs before delamination, as such the bond between this material and the carbon fibre spar is the best for this material. Further, it also holds its strength over a larger range of deformation than the other materials. Since PC-ABS also shows good mechanical workability, the choice was made to 3D print the scaled blade using this material.

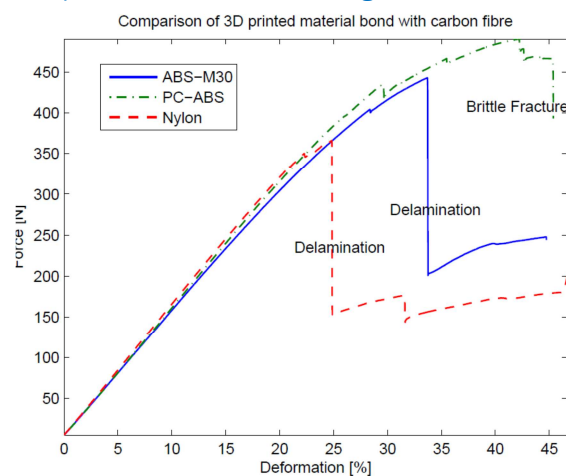


Figure 49, Structural behaviour of the bond between 3d printed substrate and carbon fibre spar



Figure 50, The grey rectangle on the top and the two black rectangles below it are the 3d printed samples post fracture, placed on a sandstone-coloured desktop that forms the background. Top: ABS M30, Middle: PC-ABS, Bottom: Nylon

The blade was printed as a 3 mm-thick shell, with an internal spar structure, using stereolithography techniques. In order to add structural stiffness to the blades, a spanwise slot was engraved at the spar cap location on both the top and bottom of the blade. This slot was filled with a 0.14 mm thick layer of unidirectional carbon fibre tow impregnated with epoxy resin. The slot was then aerodynamically faired using crushed glass fibre epoxy filler, which was then sanded down for a smooth finish. A Computer-Aided Design (CAD) model of the blade and a photograph of the finished blade are shown in Figure 47 and Figure 48. The CAD software Solidworks was used for designing the blade, with the blade material considered to be homogeneous and isotropic. The metal connection to the hub and the carbon fibre are modelled to be bonded to the blade ideally such that delamination is not possible. An ultimate loading case is simulated for a wind speed of 10 m/s, rotor speed of 400 rpm and a thrust coefficient of 1. For this extreme case, the stresses

in the plastic material are calculated to be less than the flexural strength of the material by a factor of safety of 1.3.

The designed static force-deflection curve, compared with the measured structural behaviour, is seen in Figure 51. It is interesting to note that the predicted stiffening effect of the carbon fibre layer is nearly identical. The tip deflection was calculated to be 17.2% lower with carbon fibre spars, while it was measured to be 16.6% lower after stiffening. A flexible mode analysis of the blade yields its first natural frequency as 16.43 Hz. Post manufacture, the blades are instrumented with piezoelectric strain sensors on the top and bottom, at the root of each blade. These sensors provide a measure of the blade loads that are sought to be minimised.

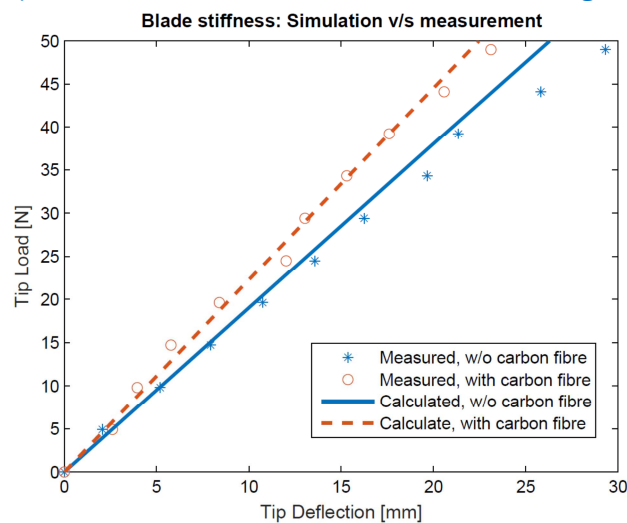


Figure 51, Calculated stiffness characteristics compared with measured stiffness characteristics

### Free-floating flap (FFF) design

The CAD design of the free-floating flaps is depicted in Figure 52. The leading edge is a continuation of the inboard portion of the blade, including the slot meant for carbon fibre stiffening. The hinge axis of the flap is mounted using bearings on an aluminium bracket just behind the spar; apart from the negligible bearing friction, it is entirely free to rotate. A T-section is connected to this axle, such that its interference with the mounting bracket provides limit stops for the rotation of the flap. The flap can hereby rotate freely through a maximum upward and downward deflection angle of 30 degrees. .

A metal plate (spring steel) of thickness 0.2 mm is sandwiched between the axle and the T-section. Two piezobenders (Macrofibre composite, type M8557-P1) are affixed rigidly to the top and the bottom, respectively, of this metal plate. The benders are electrically connected together in an antiparallel manner such that their piezoelectric effect reinforces each other and they produce the same magnitude but an opposite direction of strain in the substrate. A maximum voltage of +/- 500 V can be applied to the benders in order to emulate the behaviour of the trim tab from Heinze and Karpel (2006) and Bernhammer et al. (2013). Finally, an appropriate aerodynamic shape of the flap was achieved by embedding the instrumented metal plate into a highly compliant foam which was shaped according to the aerofoil geometry. The entire flap, from the angle-limiting T-section to the foam spacers, is covered with a fairing shroud. A contactless angle encoder is embedded into the tip section, which provides feedback on the flap angular position. This configuration causes a step change in the chordwise profile just aft of the spar, that produces undesirable aerodynamic behaviour, which is a well-known trade-off against the increase in the deformability of the trailing edge. In this experiment, to achieve a proof of concept for free-floating flaps, aerodynamic accuracy is sacrificed for control authority in the design of the flap.

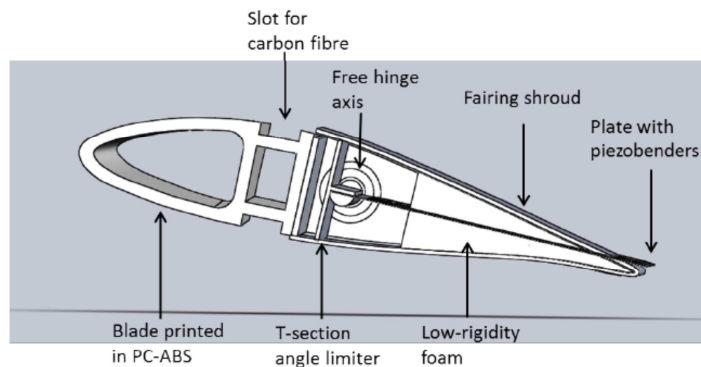


Figure 52, Flap cross-section: trim tabs replaced by chordwise

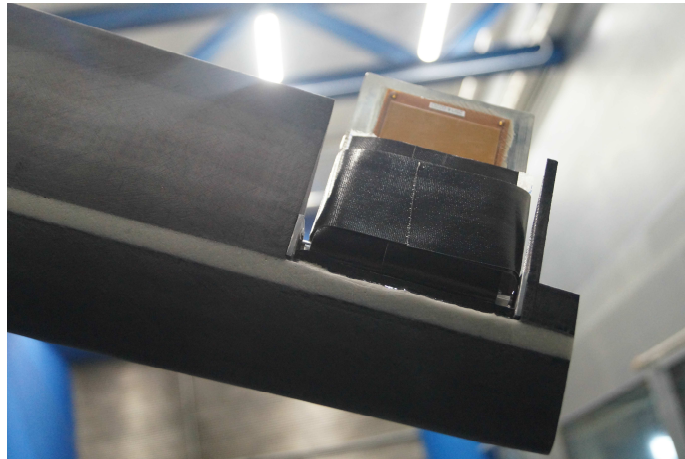


Figure 53, Photograph of flap

### 3.3 Aeroelastic blade analysis

While in the previous section it was ensured that the behaviour of the blade under the ultimate static structural load was acceptable, an aeroelastic analysis is required to determine the change in its structural response with increasing wind speed. The rigid-body mode of the free-floating flap is expected to couple with the first flexible mode of the system, giving rise to a low wind speed form of flutter. In order to analyse the aeroelastic behaviour of the blade instrumented with a free-floating flap, the blade is modelled in MSC/NASTRAN as a cantilever beam of non-uniform cross-section (CBAR elements). The various cross-sections of the modelled beam were taken at ten equidistant spanwise stations along the blade. Each element is rigidly connected to a flat plate aerodynamic panel of the corresponding chordwise length. The flap is modelled in a similar manner. First, a structural modal analysis of the blade is carried out, at zero wind speed. The calculated modes of the blade are given in Table 15 Test cases in the rotating rig experiments. The corresponding modal frequencies predicted by Solidworks are:

- 1st flapwise frequency: 18.97 Hz (Solidworks), 19.44 Hz (Nastran)
- 1st edgewise frequency: 78.37 Hz (Solidworks), 76.67 Hz (Nastran)
- 2nd flapwise frequency: 84.8 Hz (Solidworks), 87.88 Hz (Nastran).

It should be noted that these frequencies differ from the actual modal frequencies measured experimentally. This discrepancy arises because the experimental frequencies correspond to rotor modes, and hence also include the flexibility in the blade connection pieces, the motors and the hub and are hence necessarily lower than the blade modal frequencies. This difference between the calculated blade frequencies and the measured rotor frequencies can be considered modelling uncertainty, and forms powerful motivation for a data-driven controller that tunes itself in accordance with the true system parameters. It is most interesting to note that the lowest

flexible mode is the flapwise mode, with modal frequency 19.44 Hz. This is the mode most likely to couple unstably with the rigid body flap mode. The blade is significantly stiffer in both the lead-lag and torsional directions; these modes are hence unaffected by aerodynamic coupling. An actual turbine blade Bak (2013) is relatively softer in these directions, however even for such a blade, the flapwise mode is the most relevant one for load analysis and also possesses the lowest frequency. The current scaled blade design, with high lead-lag and torsional stiffness, allows us to study the low-speed flutter phenomenon with limited complexity.

**Table 12, Structural modes of the blade at zero total air speed**

Mode description	Modal frequency	Mode description	Modal frequency
Rigid-body flap mode	0 Hz	1 <sup>st</sup> Flapwise mode	19.44 Hz
1 <sup>st</sup> Lead-lag mode	76.67 Hz	2 <sup>nd</sup> Flapwise mode	87.88 Hz
3 <sup>rd</sup> Flapwise mode	223.9 Hz	2 <sup>nd</sup> Lead-lag mode	291.3 Hz
1 <sup>st</sup> Torsional mode	361.6 Hz	4 <sup>th</sup> Flapwise mode	449.6 Hz

The low-speed flutter phenomenon, as predicted by NASTRAN, can be seen in Figures 8 and 9. Here, the abscissæ correspond to total air speed, which is defined as the resultant of the inflow wind speed and turbine rotational speed at the blade tip. It should be noted that the speed regulation trajectory of the wind turbine is linear, such that rotor speed increases linearly with wind speed at the rate of 51.1 rpm/(m/s).

For the purpose of aeroelastic analysis, the blade has been considered to be held stationary, with inflow wind speed equal to the total air speed defined above. This assumption is not strictly valid, since the incident wind speed is lower at the inboard sections of the blade. However, since these sections undergo lower structural deformations, it is expected that the impact on the aeroelastic behaviour of the blade is also lower. Further, the blade is twisted such that the angle of attack along the span remains 20 more or less constant. Since the blade is non-rotating and subject to constant wind flow, the aerodynamic panels attached to each section maintain a constant angle along the blade span. With these simplifying assumptions, a first-order approximation of the flutter behaviour of the turbine blade is synthesised.

It can be directly observed that the frequency of the rigid body flap mode rises linearly with total air speed. Due to coupling of this mode with the first blade flexible mode, the blade mode becomes unstable at the onset of flutter. For the given physical configuration of the blade, flutter occurs at a total air speed of 36 m/s, which corresponds to a turbine rotor speed of 340 rpm, thus at a speed beyond the designed operational speed of the wind turbine (230 rpm).

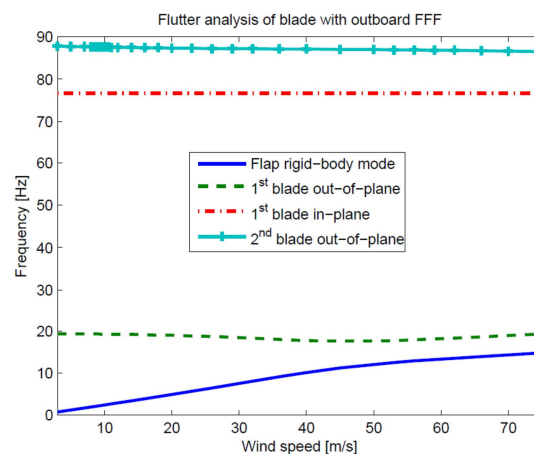


**Figure 54, Variation in modal frequency with total incident air speed**

The aeroelastic analysis served as a guideline for designing the kinematic parameters of the free-floating flap. A sensitivity analysis showed that the flutter speed depends strongly on the inertia of the flaps about the hinge axis. As seen in Figure 56, an increase in flap inertia increases the flutter speed. Since an increase in flutter speed is also associated with a decrease in control authority, the flap inertia is chosen such that flutter occurs at a speed just beyond the operational regime of the wind turbine. As such, the flap inertia is chosen to be 270 g-cm<sup>2</sup>, so that the flutter speed is 36 m/s, as described before. This aeroelastic analysis also served as a guideline for the design of the blades and for identifying the range of operation permissible in the experiments described in the sequel. Experimentally, it was observed that the onset of flutter occurred at 315 rpm. However, since this mode involves exponentially diverging vibrations in the blades, which cannot be physically limited, open-loop experiments in this unstable regime were not conducted out of safety considerations.

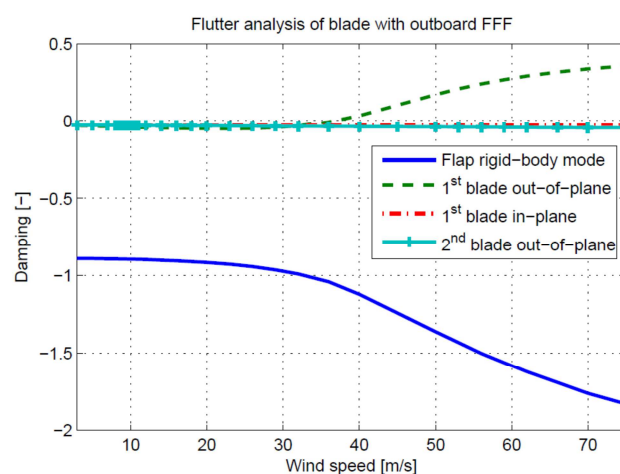
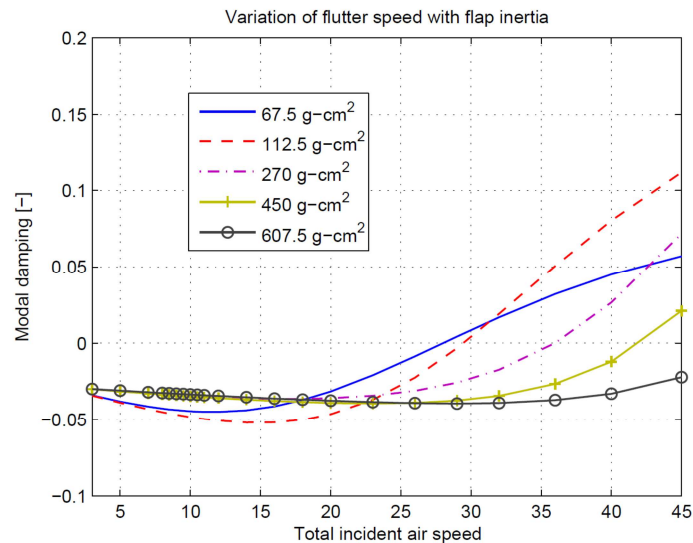


Figure 55, Variation in modal damping with total incident air

### 3.4 Testing Environment

The blades designed and analysed as above were mounted on the test turbine setup used previously in Navalkar et al. (2015). As described in this reference, the blades are connected to the hub through pitch servomotors. The hub is mounted on a shaft supported by two main bearings located in the nacelle. The electrical connections of the hub are transferred to the stationary part of the wind turbine via slip rings, rated at 500 V, which is also the maximum voltage that can be fed to the piezobenders located outboard on the blades. Further, the shaft is instrumented with a torque transducer and speed encoder, and connected mechanically with the generator. The turbine is direct-drive; the rotor speed is the same as the generator speed. The generator is in turn connected electrically in series with an adjustable dump load amenable to resistance control. Thus, in principle this setup can also provide torque control. However, in this series of tests, the resistance of the dump load is kept constant. This implies that the wind turbine is in constant torque operation, and its rotor speed rises linearly with the incoming wind speed. This form of control deviates from classical variable-speed variable-pitch turbine control, which utilises collective pitch to ensure constant speed regulation above rated wind speed. However, the variable-speed constant load operation of the scaled turbine serves three purposes: overspeed behaviour can be investigated, which may induce flutter, below-rated turbine behaviour can be emulated, and the use of adaptive control can be evaluated in terms of its ability to retune itself to adapt to changed operating conditions.



**Figure 56, Variation of flutter speed with flap inertia.**

speed encoder, and connected mechanically with the generator. The turbine is direct-drive; the rotor speed is the same as the generator speed. The generator is in turn connected electrically in series with an adjustable dump load amenable to resistance control. Thus, in principle this setup can also provide torque control. However, in this series of tests, the resistance of the dump load is kept constant. This implies that the wind turbine is in constant torque operation, and its rotor speed rises linearly with the incoming wind speed. This form of control deviates from classical variable-speed variable-pitch turbine control, which utilises collective pitch to ensure constant speed regulation above rated wind speed. However, the variable-speed constant load operation of the scaled turbine serves three purposes: overspeed behaviour can be investigated, which may induce flutter, below-rated turbine behaviour can be emulated, and the use of adaptive control can be evaluated in terms of its ability to retune itself to adapt to changed operating conditions.

The nacelle is connected rigidly to the top of a tower, mounted on bearings on its base. The tower (and hence the entire wind turbine) can yaw freely around its base. For this set of experiments, the tower is kept fixed such that the plane of the rotor is always perpendicular to the incoming wind speed. The entire assembly is mounted inside the Open Jet Facility of the Delft University of Technology, which is an open jet wind tunnel of 6 m test cross-section and 2.85 m equivalent open jet diameter. A photograph of the turbine can be seen in Figure 57. While wind speeds up to 35 m/s can be achieved in this wind tunnel, the operation of the wind turbine under the current settings requires no more than 6 m/s, with a rated wind speed of 4.5 m/s (and thus a tip speed ratio of 5.35). Data acquisition and online control is furnished at a sampling frequency of 2 kHz by a real-time PC, on which the controller is compiled using Matlab-Simulink xPCTarget. There are two primary sensing elements: the load sensors at the blade roots and the free-floating flap angle sensors. Further, there are two primary actuators: the piezobenders on the flaps and the pitch motors. The objective of the experiments is to use these sensing and actuating elements to achieve load control of the scaled wind turbine.

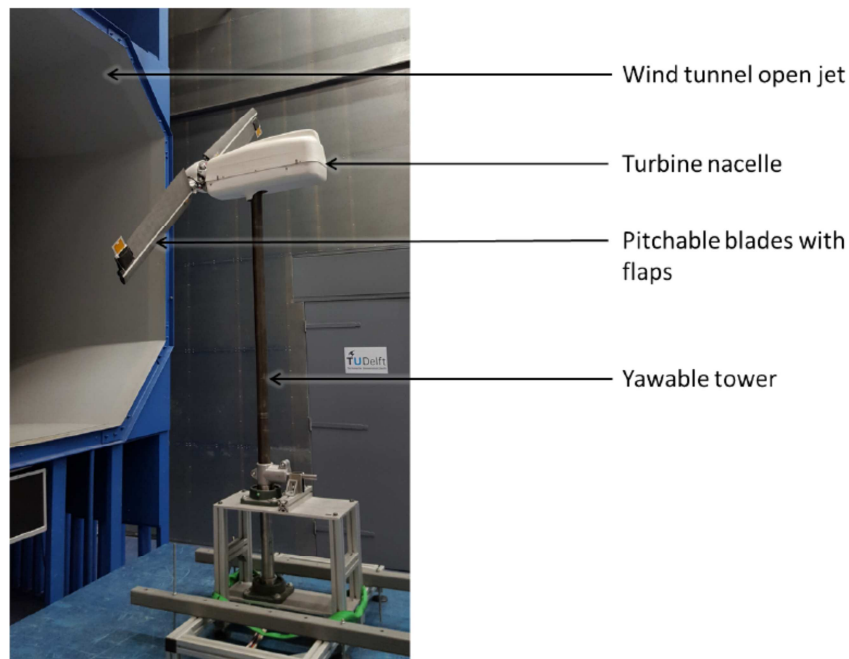


Figure 57, Photograph of the assembled turbine with pitch and flap control.

### 3.5 Iterative Feedforward Tuning for combined Pitch and Flap control

For a wind turbine in the field, the blade loads arise mainly out of wind shear, tower shadow, turbulence and its rotational sampling. As such, the blade load spectrum for a typical turbine shows dominant peaks at the rotor speed (1P) and its harmonics: for a two-bladed turbine at 2P, 4P, and so on, while for a three-bladed machine at 3P, 6P etc. The presence of turbulence broadens these peaks and adds energy in the high frequency region of the spectrum. In the wind tunnel environment, the levels of turbulence are low. The main cause of the blade loads is the tower passage, which leads to sharp peaks at 1P and its harmonics. The objective of the experiments is to demonstrate that these peaks can be attenuated by pitch and flap control, which by extension implies that a significant portion of the load spectrum of an in-field turbine can be addressed by these actuation and control methods. For achieving load control, Iterative Feedforward Tuning (IFT) of the pitch and flap controllers will be implemented. This technique specifically targets deterministic disturbances, as seen in the blade load spectrum of the turbine, with minimal control action. As long as there exists a nominally stabilising controller in the loop to avoid the unstable flutter region, the controllers tuned using IFT will not render the plant unstable. Further, IFT ensures that data-driven tuning of the controllers makes them converge to an optimal control action over a number of iterations. It should be noted that this optimality refers to the local optimum of the user-defined cost criterion, and is unrelated to global controller optimality. There are, at present, no global optimality proofs for IFT. Indeed, if a feedback controller is tuned using IFT for a poorly-designed performance criterion, it may yield an unstable closed loop. However, since this paper considers IFT for feedforward control, this issue is not relevant. Further, if the step size in the gradient descent algorithms is too large, the parameter tuning process may become unstable. These issues have been dealt with by Hjalmarsson (2002). The optimal controller parameters depend strongly on the incoming wind speed and hence demand a linear parameter varying (LPV) controller. LPV controller tuning using IFT has been explored and shown to work in the simulation environment Navalkar and Van Wingerden (2015). However, the computational burden and number of experiments required for tuning imply that this methodology is required to be modified to meet the demands of real-time control in the wind tunnel. Hence, a quasi-LPV approach will be followed in this section. Accordingly, while the plant remains LPV at all times, when the wind speed varies slowly in the wind tunnel and the plant is approximated as LTI for the duration of each set of IFT experiments.

As a consequence of this assumption of constant dynamics, IFT tunes controller parameters that are optimal only for one specific operating point, while being suboptimal for the rest of the operating range. It is for this reason that the ordinary IFT process has to be repeated for different constant wind speeds, or an IFT gain schedule has to be generated for a varying wind speed.

The details of this controller can be found in:

Navalkar, Sachin T and Bernhammer, Lars O and Sodja, Jurij and van Solingen, Edwin and van Kuik, Gijs AM and van Wingerden, Jan-Willem, 'Wind tunnel tests with combined pitch and free-floating flap control: data-driven iterative feedforward controller tuning', Wind Energy Science, 1, 2, 2016

### 3.6 Results

To recapitulate, the objective of the wind tunnel experiments was to achieve blade load control for the scaled wind turbine, using full-span pitch actuation and free-floating flap control, with Iterative Feedforward Tuning for optimal performance of the load controller. It should be noted that since experiments are conducted under constant load operation, the rotor speed varies linearly with wind speed. Thus, a rated wind speed of 4.5 m/s corresponds to a rotor speed of 230 rpm. The flutter speed of 6 m/s (total air speed 34 m/s) corresponds to a rotor speed of 315 rpm. In this section, operating conditions will be designated by the operating rotor speed.

#### System identification and stabilising controller

Initially, the response of the wind turbine blade to flap actuation is studied and compared with the simulations. Open-loop identification experiments are conducted in the pre-flutter regime, 200-300 rpm, with a zero-mean white noise (maximally +/- 500 V) imposed on the piezobenders. Predictor-based subspace identification (PBSID) Van der Veen et al. (2013) is performed using the acquired data to obtain the transfer function between the tab actuation and the flap angle and blade root load measurements. The transfer functions are depicted in Figure 58 and Figure 59. It can be observed that significant phase loss occurs in the transfer from the actuator to the blade root loads. This implies that stabilising the system using the measurements from the root loads poses a control challenge, and it may prove difficult in the case of uncertain systems to guarantee robust stability in the unstable post-flutter region. Further, it also motivates the use of local load sensors to enhance load attenuation capabilities. On the other hand, the phase loss in the transfer between the actuator and the flap angle measurement is minimal. This collocated sensor is hence ideal for system stabilisation in the post-flutter region. A simple classically tuned controller is used for stabilisation, it is not designed for load reduction, and is hence not optimal. It is described in continuous time as follows:

$$K = \underbrace{0.0001}_{\text{Static gain}} \underbrace{\frac{s/0.001 + 1}{s/10 + 1}}_{\text{High pass}} \underbrace{\frac{s^2 + 0.001s * 50/2\pi + (50/2\pi)^2}{s^2 + 0.1s * 50/2\pi + (50/2\pi)^2}}_{\text{notch for 50 Hz electrical back-coupling artefact}} \underbrace{\frac{1}{2\pi s/100 + 1}}_{\text{Low pass}}$$

This controller is now used in closed-loop for studying system behaviour beyond flutter. Closed-loop identification experiments are performed in a similar manner and the transfer functions are obtained using PBSID, also shown in Figure 58 and Figure 59. In all identification experiments, the variance accounted for (VAF) Van der Veen et al. (2013) values exceed 60%. The dynamic behaviour can be seen to follow the predicted aeroelastic response from Figures 8 and 9. The frequency of the blade flexible mode remains more or less constant, Figure 13, however the damping goes on reducing until it is unstable at 340 rpm, as indicated by the sharp peak at 74 rad/s (11.8 Hz). On the other hand, Figure 59 shows that the frequency of the rigid-body mode increases with wind speed, along with the damping, as predicted in NASTRAN. Finally, system identification shows that the control authority of the flaps is low at low frequencies, but increases substantially at and beyond 2P (8Hz), making it suitable for reducing 2P loads and loads induced by turbulence.

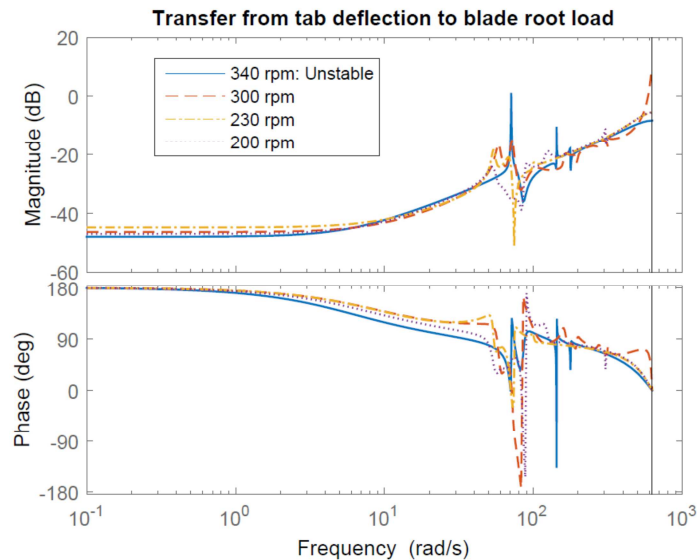


Figure 58, Transfer from piezobender actuators to blade root loads, different wind speeds

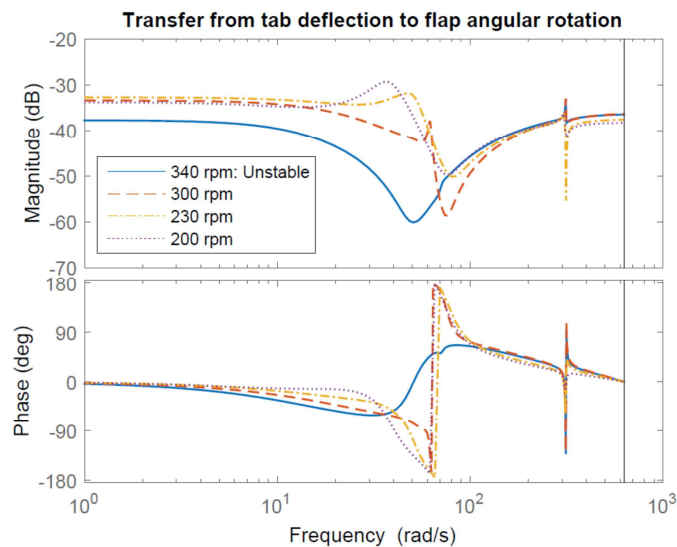


Figure 59, Transfer from piezobender actuators to free floating flap angle, different wind speeds

#### Optimal IFT for constant wind speeds: Pre-flutter

The next step was to study the effect of the IFT load controllers for combined pitch and flap control. The block diagram for the load controllers is shown in Figure 12. Accordingly, the pitch and flap actuation signals were combinations of 1P and 2P sinusoidal basis functions, respectively. The basis functions are scheduled on the azimuth and are hence phase-locked. IFT was used to train the amplitudes of these 5 basis functions; thus, with two basis functions for each frequency and each blade, for pitch and flap control both, a total of eight gains were required to be tuned.

The IFT process was first studied for a constant operational speed. Selected results, at an operational speed of 230 rpm, are presented here, although similar results were also observed throughout the operational range. The convergence of the controller gains and the IFT cost criterion can be seen in Figure 60 and Figure 61. It can be seen that, within ten minutes, the controller gains converge to their optimal values. The performance of the controller after convergence can be visualised in Figure 62 and Figure 63. The figures show that the actuation

demanded, both pitch and flap, is purely sinusoidal, as constrained by the respective basis functions. Further, the load components in the blade load spectrum at the frequencies 1P and 2P are almost entirely eliminated by the pitch and flap action respectively. Thus, IFT is successful in tuning the controllers as required. One final point of note is that the converged gains for the two blades are not exactly antisymmetric, this is especially pronounced for the flap actuation. The primary reason for this is a difference in the manufacture of the two blades. Specifically for the flap dynamics, for the scaled blade, a difference in the order of a few grams in its weight distribution can strongly alter system dynamics and even prepone the onset of flutter. Commercially manufactured blades are ideally expected to be identical; they would require antisymmetric pitch action and identical flap action for load attenuation, as produced by a conventional IPC controller Bossanyi (2003). Such a controller does not achieve optimal load reduction in the case there are discrepancies in blade manufacture or aging. The IFT controller designed above is thus shown capable of accounting for blade asymmetry and adjusting control action for maximising load reduction.

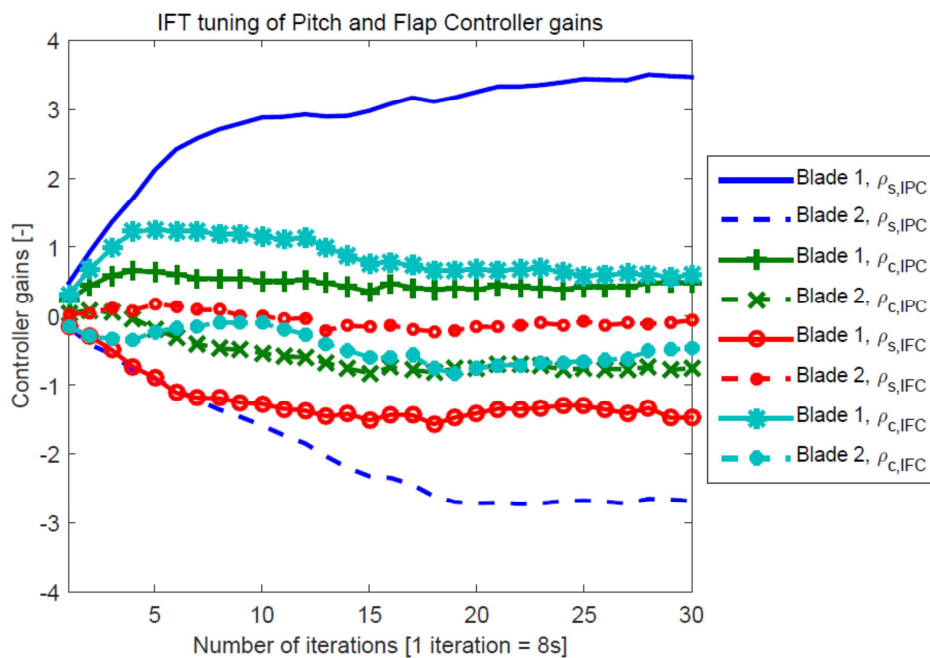


Figure 60, Convergence of controller gains over iterations

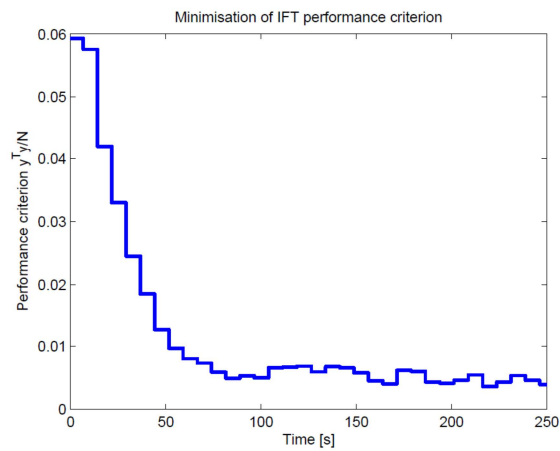


Figure 61, Minimisation of IFT cost criterion over iterations

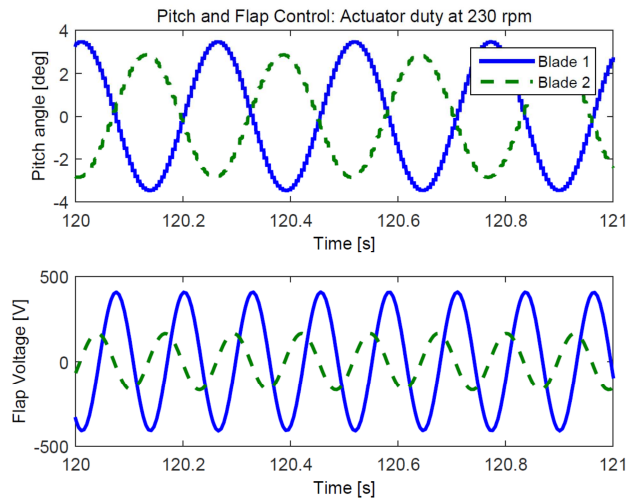
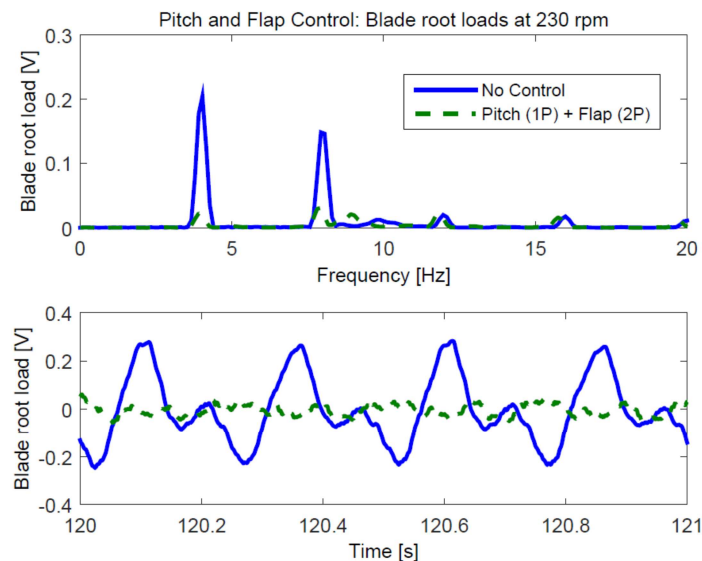


Figure 62, Actuator duty cycles of optimised controller (Pre-flutter)



**Figure 63, Load reductions achieved by optimised controller (Pre-flutter)**

Optimal IFT for constant wind speeds: Post-flutter

Next, the free-floating flap is connected in series with the stabilising PID controller described above and the wind turbine is run at an operational speed of 330 rpm, in the post-flutter region. Since it is not optimally tuned, this controller does not maximise load reductions. Hence, IFT is used to tune the feedforward load reducing pitch and flap controller gains in a manner similar to the previous 5 experiments; however in this case the underlying plant is the stabilised post-flutter wind turbine in closed-loop with the PID controller. From Figure 64 and Figure 65, it can be seen that the optimised IFT controller gains are still able to achieve load reduction even in this highly challenging unstable operational regime. The Figure 64 shows that the pitch controller no longer issues antisymmetric commands; a traditional IPC controller is no longer adequate in this region. Further, the flap command has already reached its maximum limits of +/- 500 V.

Optimal IFT gain-schedule for varying wind speeds

For an in-field wind turbine, controller gain optimisation cannot be implemented considering the wind speed to be constant. Hence, the gain scheduling approach described in the previous section is followed, where, instead of the absolute values of the controller gains, the coefficients of a gain schedule, are optimised based on the IFT experiments. This method is tested in the wind tunnel, with a varying operational speed profile as depicted in Figure 66. The convergence of the gain schedule coefficients can be seen in Figure 67 and Figure 68. It can be seen that in the first 100 seconds, since the wind speed is constant, a good gain schedule cannot be identified owing to a lack of persistency of excitation in the scheduling parameter. However, as the wind speed changes beyond this point in time, the gain schedule rapidly converges to an optimum. The gain schedule finally achieved is compared with the optimal controller gains obtained from the previous set of experiments in Figure 69 and Figure 70. It can be seen that for the pitch controller, the linear gain schedule obtained is a good fit to the optimal values obtained at constant wind speed. On the other hand, the flap controller optimal gains show a non-linear variation with wind speed and the linear gain schedule obtained achieves reduced goodness of fit.

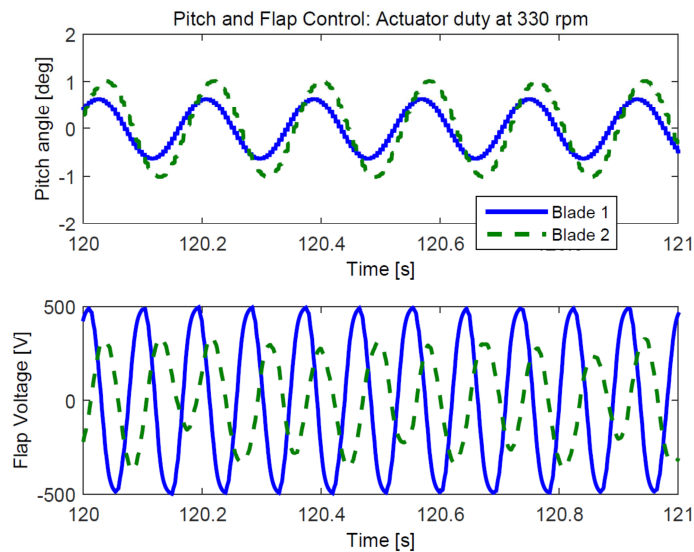


Figure 64, Actuator duty cycles of optimised controller (Post-flutter)

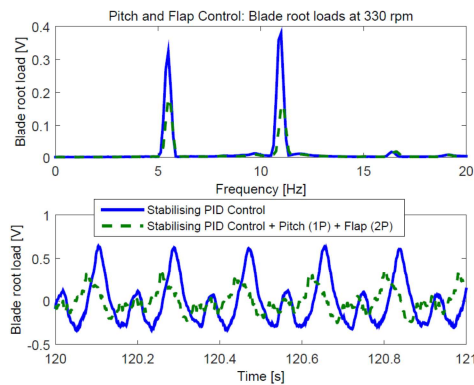


Figure 65, Load reductions achieved by optimised controller (Post-flutter)

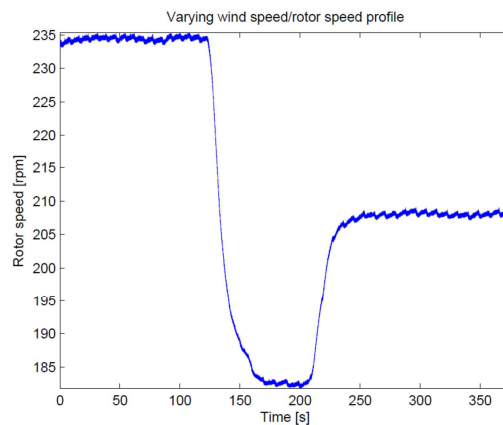


Figure 66, Varying operational speed for optimisation of gain schedule

Herewith, the combined pitch and flap controller has been shown to be able to reduce blade loads both in pre- and post-flutter conditions. Further, an optimal gain schedule for these controllers is automatically tuned online using IFT in varying wind conditions.

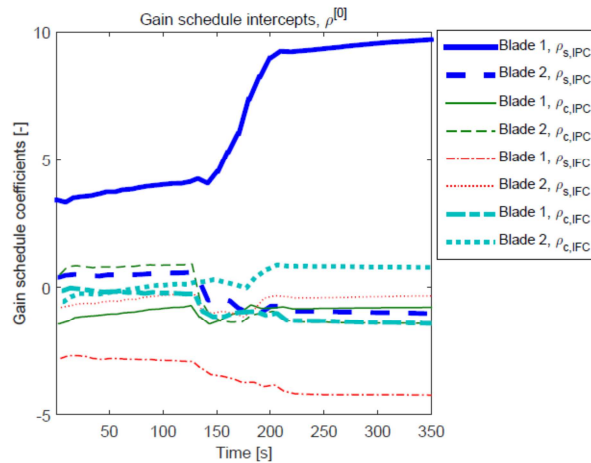


Figure 67, Optimisation of gain schedule intercepts for varying wind speed conditions

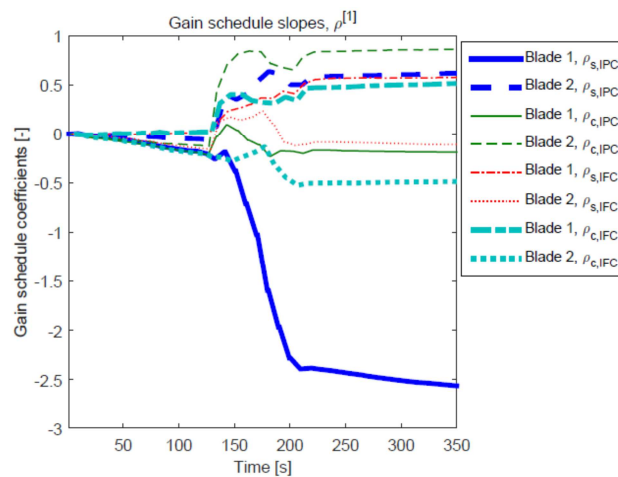


Figure 68, Optimisation of gain schedule slopes for varying wind speed conditions.

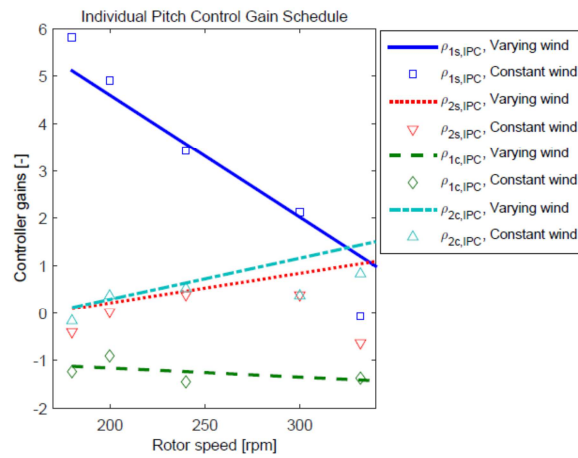


Figure 69, Gain schedule at varying wind speeds versus optimal gains at constant wind speed: Pitch Control.

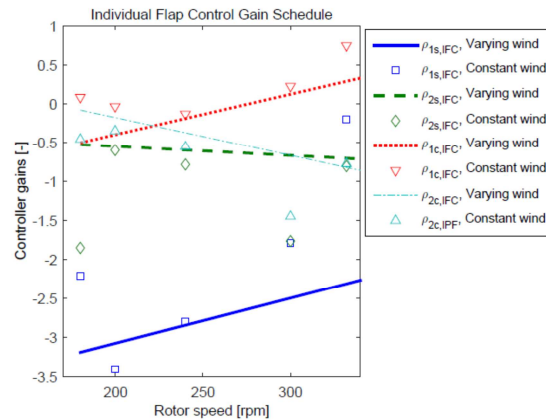


Figure 70, Gain schedule at varying wind speeds versus optimal gains at constant wind speed: Flap Control

### 3.7 Conclusions

A successful experimental proof of concept has hereby been achieved for the first time of free-floating flaps for wind turbines and of combined pitch and flap control for blade load mitigation. Free-floating flaps were designed for the first time for the application of wind turbine load control. Numerical aeroelastic analysis concluded that such 5 flaps show significant control authority in the desired frequency band (2P and beyond). However the additional degree of freedom couples aerodynamically with the flapwise flexible mode of the blade and causes flutter at low wind speeds, just outside the design envelope. Using a feedback controller, the blade can be stabilised in the post-flutter region. Both of these results were validated experimentally in the wind tunnel.

Blades were manufactured using the novel combination of 3D-printing with carbon fibre layup, and instrumented with free floating flaps close to the blade tip. The concept of Iterative Feedforward Tuning of the gains of phase-locked basis functions was used to achieve blade load reductions. The pitch control action was composed of a superposition of 1P sinusoidal basis functions, while for the flap control action, 2P sinusoidal basis functions were used. It was shown that, for a constant pre-flutter wind speed, ideal rejection of 1P and 2P loads in the blade load spectrum could be achieved with combined pitch and flap control. Further, at a post-flutter wind speed, the system was connected in closed-loop with a stabilising PID controller using collocated feedback. Iterative Feedforward Tuning was able to optimise, in this unstable regime, the load control gains of the pitch and flap control action for this closed-loop plant. Load rejection was also achieved in the challenging post-flutter regime, although the flap actuation duty reached close to its physical limits under these conditions. Finally, for the case of varying wind speed conditions, the IFT

methodology was able to autonomously synthesise an optimal linear gain schedule, in real time, for the combined pitch and flap controller. Such a gain schedule was found to be near-optimal for a large portion of the range of operation.

### 3.8 References

Andersen PB, Gaunaa M, Bak C, Buhl T (2006). Load alleviation on wind turbine blades using variable aerofoil geometry. Proc. of the EWEC, Brussels, Belgium.

Bak C (2013). Description of the DTU 10 MW reference turbine. DTU Wind Energy Tech. Rep. I-0092.

Barlas TK, Van Kuik GAM (2010). Review of 5 the state of the art in smart rotor control research for wind turbines. Progress in Aerospace Sciences 46:1-27.

Bauer S, Czakalla M, Göppele F, Grandy M, Hammer A, Hofmann L, Jenter T, Kaus S, Pullman T, Rahn A, Samol D, Schlesiger J, Schwenk J, Beyer F and Cheng PW(2014). Abschlussbericht Windenergieprojekt WS 13/14 -Windenergie aus dem 3D-Drucker. Universität Stuttgart.

Bernhammer LO, Van Kuik GAM, De Breuker R (2012). How far is smart rotor research and what steps need to be taken to build a full-scale 10 prototype? Journal of Physics: Conference Series 555 (1), 012008.

Bernhammer LO, De Breuker R, Karpel M, Van der Veen GJ (2013). Aeroelastic control using distributed floating flaps activated by piezoelectric tabs. Journal of Aircraft 50 (3): 732-740.

Bernhammer LO, Sodja J, Navalkar ST, De Breuker R, Karpel M (2015). Experimental and numerical investigation of an autonomous flap for load alleviation. Journal of Aircraft, Article in Press.

Bernhammer LO, De Breuker R, Van Kuik GAM. Fatigue and extreme load reduction of wind turbine components using smart rotors. Journal of Wind Engineering and Industrial Aerodynamics, Article in Press.

Bossanyi EA (2003). Individual blade pitch control for load reduction. Wind Energy 6 (2): 119-128.

Bossanyi EA, Fleming PA, Wright AD (2013). Validation of individual blade pitch control by field tests on two- and three-bladed wind turbines. IEEE Trans. Control Syst. Technol. 21 (4):1067-1078.

Bottasso CL, Croce A, Riboldi CED, Nam Y (2013). Multi-layer control architecture for the reduction of deterministic and non-deterministic loads on wind turbines. Renew. Energy 51:159-169.

Castaignet D, Barlas TK, Buhl T, Poulsen NK, Wedel-Heinen JJ, Olesen NA, Bak C, Kim T (2013). Full-scale test of trailing edge flaps on a Vestas V27 wind turbine: active load reduction and system identification. Wind Energy 17 (4):549-564.

Dunne F, Pao LY, Wright AD, Jonkman B, Kelley N (2011). Adding feedforward blade pitch control to standard feedback controllers for load mitigation in wind turbines. Mechatronics 682-690.

Gevers M (2002). A decade of progress in iterative process control design: from theory to practice. Journal of Process Control 12:519-531.

Heinze S, Karpel M (2006). Analysis and wind tunnel testing of a piezoelectric tab for aeroelastic control applications. Journal of Aircraft 43 (6):1799-1804.

Hjalmarsson H (2002). Iterative feedback tuning - an overview. *Journal of Adaptive Control and Signal Processing* 16:373-395.

Hulskamp AW, VanWingerden JW, Barlas TK, Champlaud H, Van Kuik GAM, Bersee HEN, Verhaegen M (2011). Design of a scaled wind turbine with a smart rotor for dynamic load control experiments. *Wind Energy* 14:339-354.

Karutz R. Untersuchung Generativer Fertigungsverfahren im Rotorblattbau von Kleinwindkraftanlagen. Universität Stuttgart Bachelor Thesis.

Lackner MA, Van Kuik GAM (2010). A comparison of smart rotor control approaches using trailing edge flaps and individual pitch control. *Wind Energy* 13:117-134.

Navalkar ST, Van Wingerden JW (2015). Iterative feedback tuning of an LPV feedforward controller for wind turbine load alleviation. The 1st IFAC LPV Systems Conference, Grenoble, France. 24

Navalkar ST, Van Solingen E, Van Wingerden JW (2015). Subspace predictive repetitive control for variable pitch wind turbines. *IEEE Trans. Control Syst. Technol.* 23 (6):2101-2116.

Selvam K, Kanev S, Van Wingerden JW, Van Engelen T, Verhaegen M (2009). Feedback-feedforward individual pitch control for wind turbine load reduction. *Int. J. Robust Nonlinear Control* 19 (1): 72-91.

Van der Veen GJ, Van Wingerden JW, Bergamasco M, Lovera M (2013). Closed-loop subspace identification methods: an overview. *Control Theory and Applications IET* 7 (10): 1339-1358.

Van Wingerden JW, Hulskamp AW, Barlas TK, Houtzager I, Bersee HEN, Van Kuik GAM, Verhaegen M (2011). Two-degree-of-freedom active vibration control of a prototyped 'smart' rotor. *IEEE Trans. Control Syst. Technol.* 19:284-296.

Van Wingerden JW (2008). Control of wind turbines with 'smart' rotors: proof of concept and LPV subspace identification. PhD Thesis, Delft University of Technology.

## 4 ACTIVE GRID [OLDENBURG]

### 4.1 Introduction

As wind turbines are mainly operating inside the turbulent atmospheric boundary layer, the performance of the turbine and the resulting structural loads are strongly influenced by the dominating highly intermittent wind fields as shown by Wächter et al.(2012). Regarding the chaotic nature of turbulence, high resolved measurements in situ are difficult to achieve especially in terms of reproducible events. Therefore wind tunnel experiments with repeatable and controllable turbulent inflow conditions are of increasing importance.

The most common way to introduce turbulence in wind tunnel experiments is the use of passive turbulence generators in front of the test section for example one or a combination of grids. Defined by the design turbulence with different kind of dynamics can be generated. Classical grids like bars and square meshes are generating very isotropic and homogenous turbulence. As the turbulence is introduced to the flow by the interactions of the bars with the bypassing flow, the largest structures introduced to the wind field are in the order of the mesh or bar width. Turbulence generated like this is decaying fast on the way downstream of the wind tunnel (Roach (1986)). Use of a fractal grid can introduce turbulence on multiple scales which are preserving better on the way downstream and is generating a quite special wake shown for example by Stresing et al. (2010) or Seoud et al. (2007). These grids are just influencing the wake in a passive way and are already described very well but are somewhat limited in their statistical features. Also the comparison of turbulence found in the atmospheric boundary layer to the one generated by such grids are showing major differences, for example it is not possible to generate fast appearing gusts within such a setup. To achieve realistic conditions in the wind tunnel comparable to the inflow conditions wind turbine in the open field are facing a dynamic approach to generate turbulence is needed.

A dynamic way to generate turbulence in the wind tunnel is a so called active grid firstly described by Makita (1991). Horizontal and vertical rods are dividing the cross section of the wind tunnel in front of the test section. To each of these rods a motor is connected which can be moved individually. Square flaps which are mounted on to the rods are leading to a changing blockage at the cross section of the wind tunnel nozzle as these axes are moving.

The most common way to move these active grid axes is in a random fashion changing the direction and speed of movements for every axis in predefined intervals for time and rotation speed. An active grid used in that way can generate homogenous and quasi isotropic turbulence with a high turbulent Reynolds number (Mydlarski et al. (1996)). Experiments have shown that it is also possible to replicate atmospheric like turbulence regarding specific statistical properties as intermittency, turbulence intensity and integral length as seen in Knebel et al. (2011). Further a given time series of wind data, for example measured atmospheric wind data, could be reproduced at a specific point in space in a wind tunnel behind the grid (Reinke (2016)). In this approach an excitation is designed consisting of a sequence of angle of attack changes between the inflowing wind and the active grid flaps over time. These excitation protocols can be designed to create turbulence with a wide variety in the statistical features and more importantly the sequence can be repeated. The possibility to repeat a turbulent time series would mean a great achievement for optimization processes in air foil and wind turbine design and also a perfect basis to develop new control strategies to increase power generation and increase the lifetime of a wind energy converter by decreasing the acting loads.

This work has two major objectives the first is to evaluate to what extend a time series generated by an active grid excitation protocol can be reproduced and the second objective is to determine the scalability of the generated wakes by active grids of different sizes to establish experiments with comparable inflow conditions in wind tunnel of different sizes. The first objective is motivated by the aim to test newly developed control algorithms for a model wind turbine to reduce the structural loads under turbulent conditions. The used model turbine and the control algorithms are developed by the TU Delft and described in an earlier chapter.

The second objective was caused by the fact that the active grid with fitting dimensions to test the model wind turbine (3 x 3 m<sup>2</sup>) had to be planned and constructed during the Innwind Project.

Causing that the protocols to generate the turbulent inflow conditions for the test cases had to be developed using the previously existing active grids.

In the following the experimental setup will be described, including a more detailed description of the used active grids and the used excitation protocol. The statistical tools used to determine the correlation of the reproduced active grids wakes will be introduced in the next section, followed by the discussion of the results and a conclusion leading to the follow up experiment in the project.

## 4.2 Methods

### Wind tunnel and active grids

The experiments were conducted in a low speed wind tunnel of the University of Oldenburg. The wind tunnel has an outlet size of 0.8 m times 1 m and was operated in an open test section configuration. The wind speeds can reach up to 50 m/s and the turbulence intensity is less than 0.3%.

For the experiments with turbulent inflow conditions two active grids were used, which were mounted at the nozzle of the wind tunnel. One with a cross section of 0.8 m times 1 m, containing 16 axes resulting in a mesh width of 0.11 m. This grid has a quite new design of the axes with a minimal blockage of the cross section below 5% when all the axes are open. The design is described in Reinke (2016). The second grid has a cross section of 0.25 m times 0.25 m, containing 10 axes with a mesh width of 0.05 m. The design of this grid is equal to the original one of Makita with a minimal blockage of nearly 20%. Photographs of both grids can be seen in figure 4-1. Every axis in this setup is driven by a stepping motor and can be moved individually.

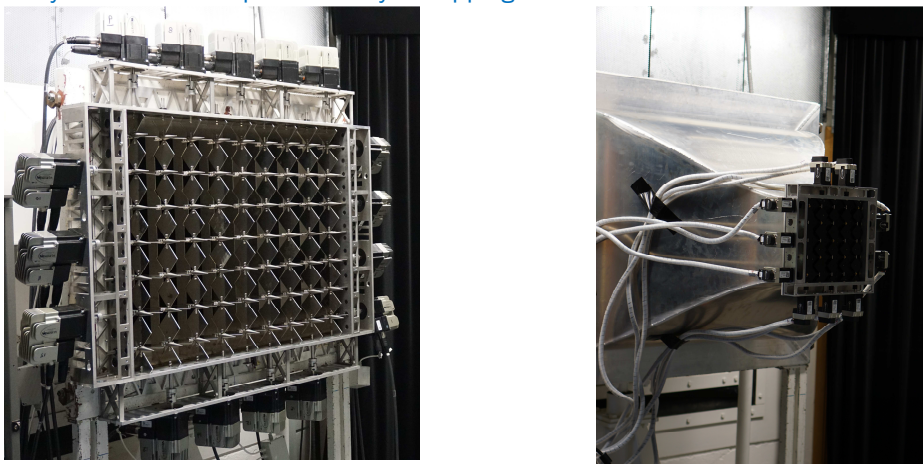


**Figure 4-1 Pictures of the used active grids. Left: 0.8 x 1 m<sup>2</sup> - 16 axes. Right: 0.25 x 0.25 m<sup>2</sup> - 10 axes. To mount the small active grid an additional nozzle had to be used.**

### Excitation protocol

The movement of the axes is defined by a so called excitation protocol which defines the angle between the flaps and the inflowing wind for every axis over time. Figure 4-2 is showing an exemplary excitation protocol for one axis. It is created based on a time series of measured atmospheric wind speeds by a Lidar system and is designed to be used at 15m/s. The creation of an excitation protocol which leads to a similar but scaled velocity time series at a certain point in space behind the active grid is a quite new process and the underlying theory is described in detail by Reinke (2016). An angle of 0° between the inflowing wind and the flap is defined as the position of minimal blockage and corresponding to that an angle of 90° describes maximum blockage. The movements of every motor are described by such a time series defining the resulting wake of the active grid.

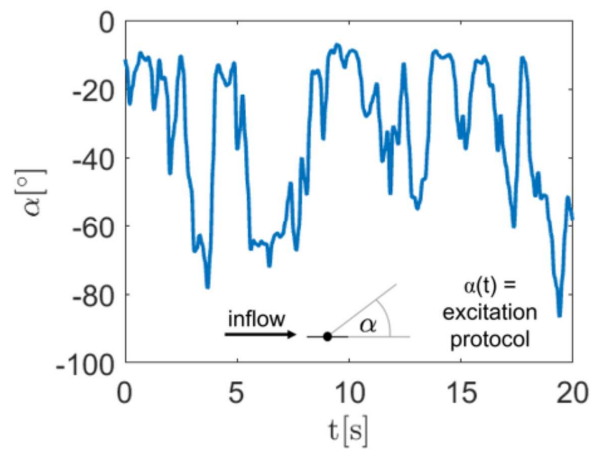


Figure 4-2 Example for the excitation of one axis of the active grid defined by the angle over time.

### Reproducibility

The first experiment had the objective to determine to what extent a wind speed time series can be reproduced using an active grid. To do that a hotwire was placed at a distance of 10 mesh widths downstream of the active grid in the centerline position. The wind speed was set to 15 m/s and the earlier described excitation protocol was then repeated for 50 times and the generated wake was acquired by the hotwire system. In this experiment only the active grid with the cross section of  $0.8 \times 1 \text{ m}^2$  was used. A sketch and a photograph of this setup can be seen in Figure 4-3.

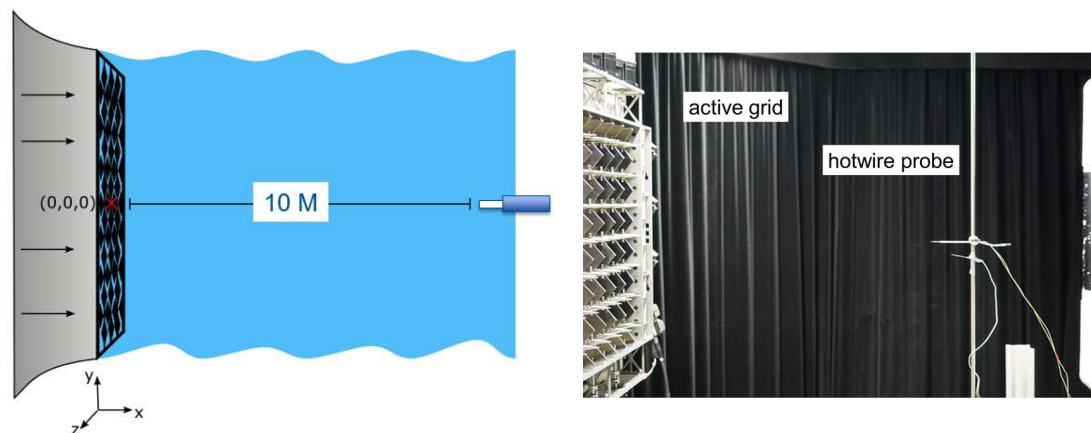
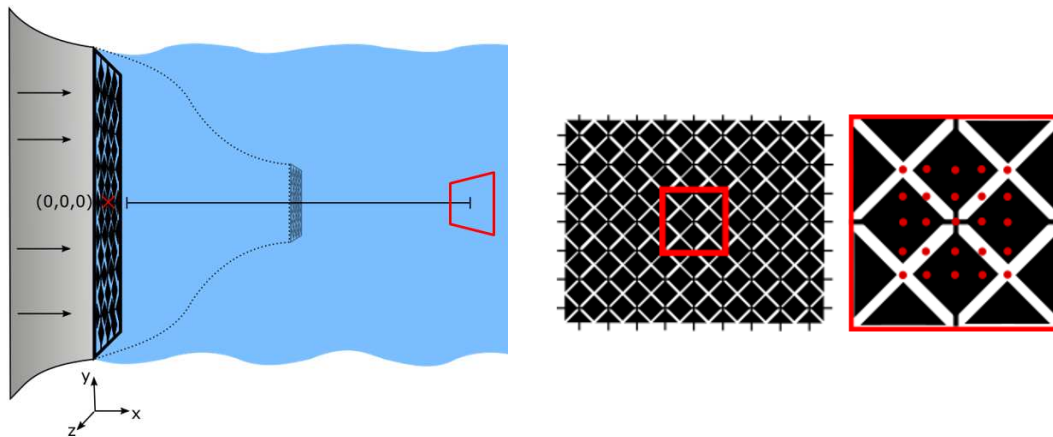


Figure 4-3 Left: Sketch of the experiment. 2D hotwire in 10 M distance of the active grid at the centerline. Right: Photograph of the setup.

### Scalability

To examine the scalability of an excitation protocol from one active grid to another of a different size and the possible modifications which have to be made to achieve a comparable wind field for experiments another setup was used. The 2D hotwire was mounted on a traversing unit to measure at different positions at a distance of 10 M downstream of the active grids. Figure 4-4 is showing a sketch of the setup and the mesh for the different measurements positions. The indicated measurement positions are exemplary as the measurements for both of the active grids were conducted in an analogical manner respecting the different mesh widths of the grids, respectively. The positions are chosen to investigate the generated wake behind different parts of the active grid.



**Figure 4-4** Left: Sketch of the scalability experiment. Wind tunnel nozzle with mounted active grid. Measurement plane (red) in 10 M distance. The dotted line refers to the second setup with additional nozzle and small active grid (light grey). Right: Location of the measurement plane from an upfront view and the distribution of measurement points.

First these measurements were performed behind the active grid with the cross section of 0.8 m times 1 m, then repeated for the smaller one.

#### Measurement system

The active grid wake was measured in all experiments with a 2D CTA hotwire system (Dantec Dynamics). An x-wire of type 55P51 was used and operated at a sampling rate of 20 kHz with a frequency low pass filter at 10 kHz. For the data acquisition an 18 bit National Instruments A/D converter was used (NI PXI DAQmx 6281). The start of the measurements were triggered at the start of the active grid excitation by a TTL signal.

### 4.3 Results and discussion

#### Reproducibility

The possibility to reproduce the generated active grid wake is strongly depending on the correlation of the excitation of the axes and the resulting flow field. Figure 4-5 is showing a comparison of the excitation of one axis and a measured velocity time series. Because the movements are the same for all axes just the movement of one axis is shown. A moving average filter was applied to the wind speed time series to allow a better illustration of the correlation. The moving average span is chosen that way that the time scale of the active grid excitation is bigger than the fluctuations which are averaged out. That way we can observe a good resemblance between the blockage variations of the axes and the resulting wind speed changes in the wake. An increase in the blockage of the wind tunnel nozzle leads to a decrease in the measured wind speed and an increase in wind speed is caused by a decrease in blockage.

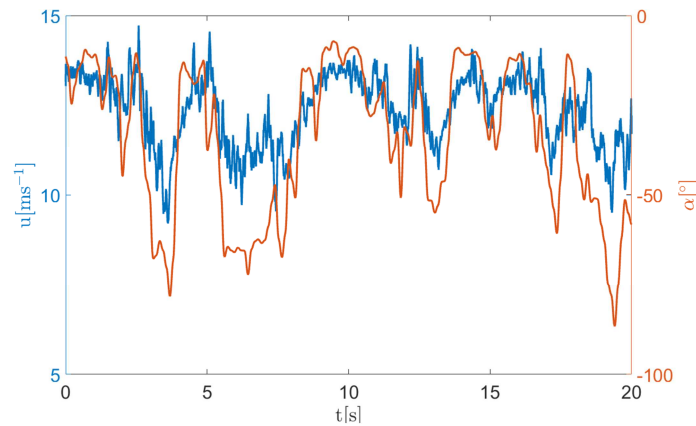


**Figure 4-5 Comparison of the active grid excitation (red) and resulting wind speed time series in 10 M distance at centerline position (blue)**

As a next step the wind speed time series of the active grid wake are analysed and compared in respect to each other. Figure 4-6 shows on the left three examples of the 50 acquired velocity time series. The data sampled with 20 kHz was filtered with a moving average over 1000 Samples. In light grey an unfiltered time series is shown. All filtered time series match very well. Thus the wind dynamics on the scale of about 50cm, which is the typical size of a model wind turbine in a wind tunnel, can be designed and repeated accurately. To quantify this resemblance the normalized cross covariance was calculated for every pair of the time series. As the measurements were triggered to a specific event in the used excitation protocol the cross covariance function should be maximal for a lag of zero between both time series which could be validated. The maximal cross covariance coefficient was then determined for every pair and saved in a diagonal symmetric matrix.

$$\rho_{xy} = \begin{bmatrix} \rho_{1,1} & \cdots & \rho_{1,50} \\ \vdots & \ddots & \vdots \\ \rho_{50,1} & \cdots & \rho_{50,50} \end{bmatrix}$$

As the original wind speed time series are turbulent and strongly fluctuating this was done for several different moving average spans  $\Delta t$  to determine which time scales of the flow can be reproduced to what extent. To quantify the resemblance the mean covariance coefficient  $\langle \rho_{xy}(\Delta t) \rangle$  and the standard deviation of every matrix was calculated and plotted over the corresponding moving average span. The result is shown in figure 4-6 on the right.

$$\langle \rho_{xy}(\Delta t) \rangle = \left\langle \begin{bmatrix} \rho_{1,1}(\Delta t) & \cdots & \rho_{1,50}(\Delta t) \\ \vdots & \ddots & \vdots \\ \rho_{50,1}(\Delta t) & \cdots & \rho_{50,50}(\Delta t) \end{bmatrix} \right\rangle$$

The comparison of the time series with the covariance function shows that even the unfiltered data are reaching a similarity between 50 and 60 per cent. The mean value of the coefficient increases to over 90% when the small time scales get averaged out.

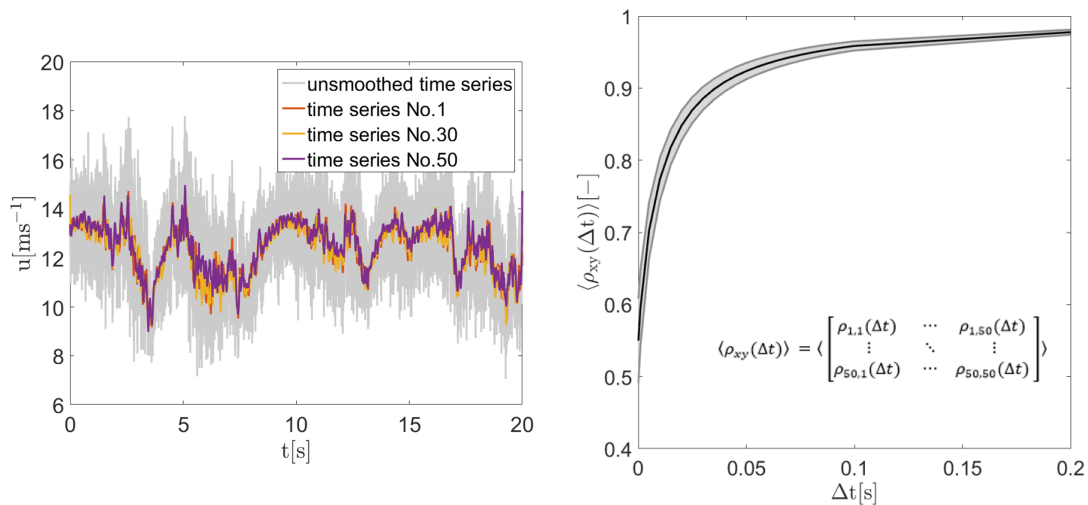


**Figure 4-6 Left:** Three exemplary wind speed time series with an applied moving average filter. In light grey an unsmoothed wind speed time series is shown. **Right:** The maximum cross covariance coefficient between every pair of the 50 measurements over different applied moving average spans. In black the mean value over the moving average span are shown. Grey is showing the standard deviation of the correlation values.

This leads to the conclusion that the bigger scales of the generated active grid wake are reproduced quite well while the smaller scales are varying for every iteration of the excitation protocol. As turbulence is a chaotic process driven by an energy cascade described by Richardson (1922) this was expected and is now pursued by a deeper analysis of the data using statistical methods to verify the results and identify possible reoccurring statistic properties. As a first method the power spectrum was used to identify the energy distribution in the frequency domain. Figure 4-7 shows in blue colour the spectra of all 50 measurements which are filtered by binning. The applied binning process is non-linear in respect to the logarithmic scale of the axes. In light grey an unfiltered exemplary power spectra is shown. All 50 power spectra are very similar and appear nearly as a single line. The distribution of the energy in the wake seems to be very equal for every protocol iteration, not just for the large time scales but especially for the small time scales respectively the high frequencies. To get a better understanding of the origin of the driving forces in the power spectra additionally the spectrum of the active grid dynamics (movements of the flaps) and the spectra of a wind speed time series measured behind a fully opened static active grid is shown in green and red. An assumption can be made that the larger scales of the power spectra are mainly defined by the dynamics of the active grid excitation (green line in Figure 4-7), referred to as production zone in the following. The smaller scales are primary defined by the natural decay of the turbulence as the straight dashed line following Kolmogorov's -5/3 law is suggesting. The natural decay on the lower scales is thereby driven by the decaying larger scales introduced by the active grid and the design of the grid in terms of the mesh width. The straight vertical line is referring to the time scale arising from the mesh width and the mean wind speed behind the active grid.

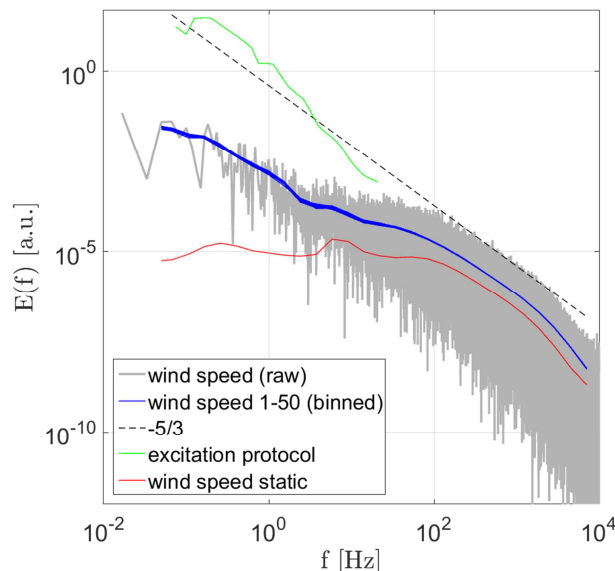


**Figure 4-7** Power spectra of all 50 measurements in blue. In red the power spectra for a fully opened active grid with no movement. In green the FFT of the movements performed by the active grid flaps. The vertical black line refers to the time scale resulting from the mean wind speed and the mesh width of the active grid.

For further investigation the dynamics of the active grid wake are analysed by two point statistics. Therefore the velocity increments are calculated. Velocity increments are defined as the following

$$\delta u(\tau) = u(t + \tau) - u(t)$$

Thus describing the fluctuations of the wind field. The distribution of the fluctuation on different time scales defined by the interval  $\tau$  are a specific property of the wind field generated and in respect to wind energy research of high importance as the fluctuations have a big impact on the loads a wind turbine has to face. To estimate the intermittency of the generated flow the shape parameter  $\lambda^2$  was used.

$$\lambda^2(u) = \frac{1}{4} \ln \left( \frac{\langle (u - \langle u \rangle)^4 \rangle}{3\sigma_u^4} \right)$$

A value of zero corresponds to a Gaussian distribution of the increments and for values above zero the distribution is showing intermittent behaviour.

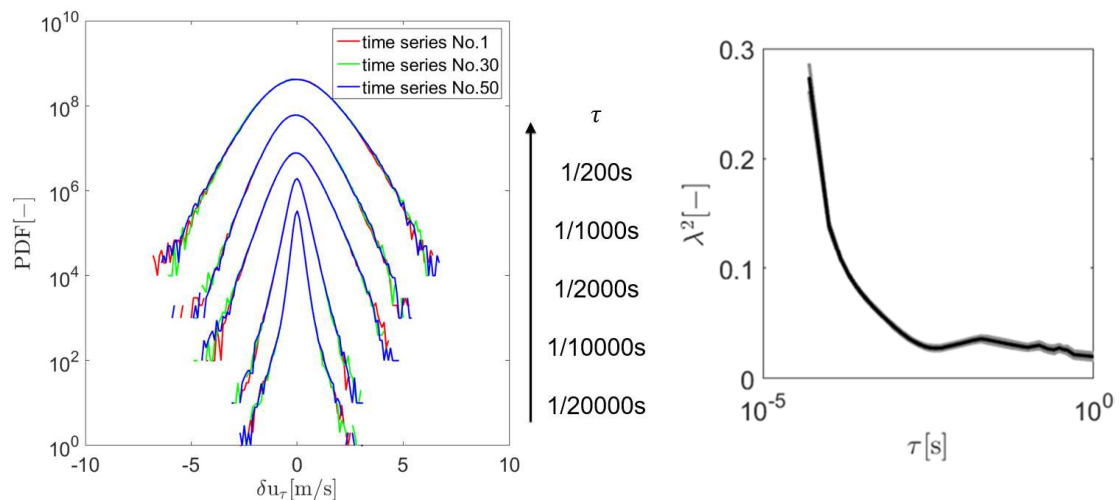


**Figure 4-8** Left: PDF of the velocity increments shifted for a better visualisation. Time scales beginning for the lowest plot (1/20000 s, 1/10000 s, 1/2000 s, 1/1000 s, 1/200 s) Right: Mean of shape parameter  $\lambda^2$  of all 50 measurements in black in light grey the standard deviation.

In Figure 4-8 on the left the histograms of the increments for three of the 50 time series are shown. The probability density functions (PDFs) were calculated for increments of five different time scales (1/20000 s, 1/10000 s, 1/2000 s, 1/1000 s, 1/200 s). For a better visualisation the histograms are shifted upwards for the larger scales. For larger time scales the distribution seems to be Gaussian distributed whereas the flow is more intermittent on the smaller scales. The trend for the exemplary increments PDFs are very similar on all scales except for the events which are occurring less than a hundred time in a time series of 1.2 million samples. We can again speak of a good agreement in terms of reproducibility. To determine the degree of intermittency and the agreement of all 50 measurements the shape parameter is calculated for 120 different increments. The mean of the shape parameter (in black) with the related standard deviation (in grey) is shown in figure 4-8 on the right. The low values of the standard deviation is showing that also in terms of intermittency the wind speed time series can be reproduced very well. The decrease of intermittency for larger increments can also be identified in the trend of the shape parameter  $\lambda^2$ . For large increments the distribution is nearly Gaussian.

### Scalability

The second objective is to show the scalability of such generated flow fields. To quantify that the acquired hotwire measurement behind the different active grids were analyzed and compared with the same tools used as for the previous experiments.

Figure 4-9 is showing the wind speed fluctuations of the first seconds of the time series at the centerline ten mesh sizes downstream of the two grids described in chapter 4.2. Because of the unsimilar minimal blockage of the two active grids the mean wind speed of the time series could not be matched ideally. Therefore the wind speed was disregarded from for the comparison. The moving average span over a thousand samples was chosen as in the previous experiment before.

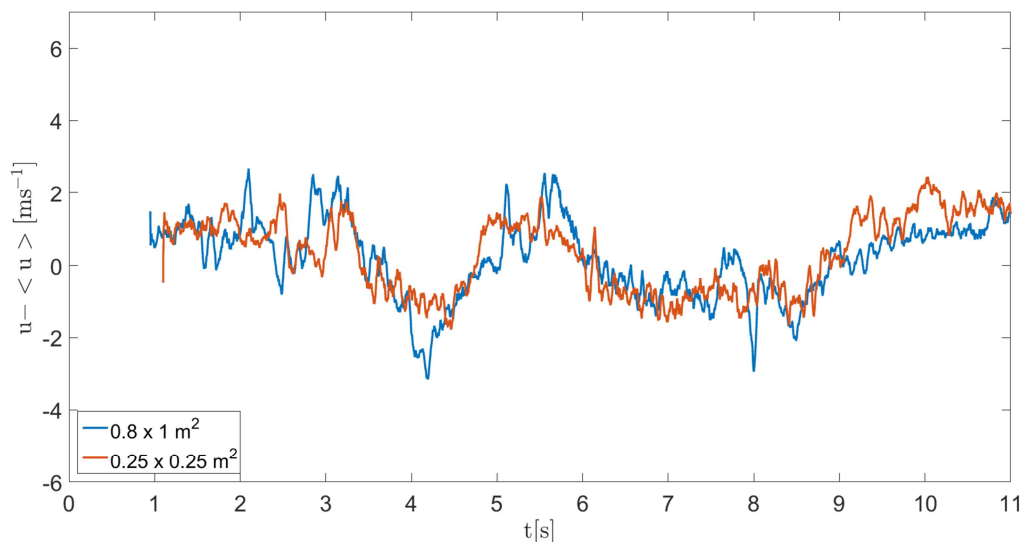


**Figure 4-9** Fluctuations of time series measured behind the two grids at the centerline in 10M distance.

The trend of both measurements are matching pretty well, but on smaller scales differences can be seen. The extend of the variations is again determined by the use of the cross covariance function. The evaluation of the covariance was done separately for every grid. To evaluate the spatial differences of the flow field.

Additionally as a comparison between the time series of the different grids. The comparison was done in respect to the spatial distribution of the measurements shown in figure 4-4. The centerline measurement of the bigger grid was compared to the centerline measurement of the small grid and so on, to show the differences in the flow field. The result is displayed in figure 4-10 on the left. The coefficients are showing an equal trend as in the previous experiments but are not reaching as high values which can be explained by the varying measurement points around the

centerline position. But both grids showing an equally good behavior reaching values between 80 and 90 per cent and showing a good resemblance of the flow field despite the spatial variation of the measurement positions behind the active grids.

The covariance coefficients of the two wakes generated by the different active grids is reaching values between 60 and 70%. Given the differences in the setup and the design this is a good result as the main features of the wind fields seem to be reconstructed. Further investigation of the time series is again accomplished using one and two point statistics.

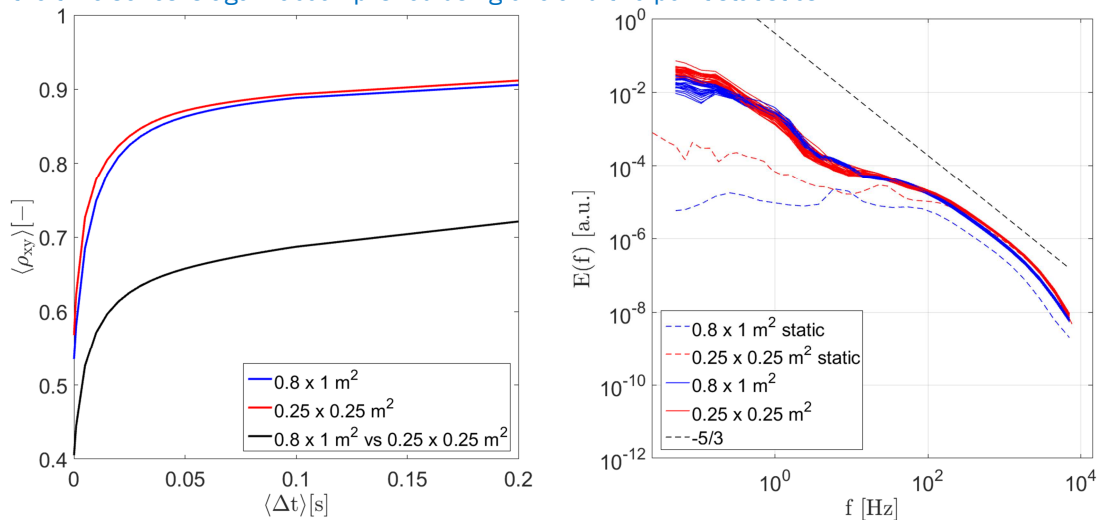


**Figure 4-10 Left: Mean cross covariance coefficient between the acquired wind speed time series in dependence of the moving average span for the different active grids. Right: Power spectra of the different measurement positions for both active grids. Power spectra for both fully opened active grid with no excitation**

The power spectra of the wind speeds measured at the 25 measurement positions behind both active grid are shown in figure 4-10 on the right. For high frequencies, which were identified earlier to be dominated by the natural decay of the turbulence, the spectra of the time series for both active grid wakes show similar behaviour. For a frequency range from 100 Hz to 10 kHz the dynamics of the wakes for both grids are following the  $-5/3$  law described by Kolmogorov. In this frequency region the different measurement positions do not have that big an influence on the spectra, as the base turbulence introduced by the mesh width is nearly isotropic at a distance of 10 M.

The biggest differences can be seen in the frequency region earlier described as the production region of the active grid wake defined by the motion of the axes. For both active grids the spectra of the wind speed time series are diverging as a result of the measurement position behind the active grids. This effect seems to be less for the smaller active grid, which can be caused by the higher background turbulence intensity of the smaller active grid as a result of the higher minimal blockage. Comparing the power spectra for the fully opened configurations the smaller active grid is also showing higher values for these frequencies. But as the structures are bigger than the mesh width of the small active grid they are probably induced by the wind tunnel itself. This could be induced by the nozzle which had to be installed to mount the small active grid resulting in a pumping of the fan.

The increment statistics of the wind speed time series are shown in figure 4-11 on the left. Again we can identify the fluctuations on the small scales as the most intermittent and becoming more Gaussian distributed for larger increments. The shape parameter  $\lambda^2$  is also showing the same trend for both grids.

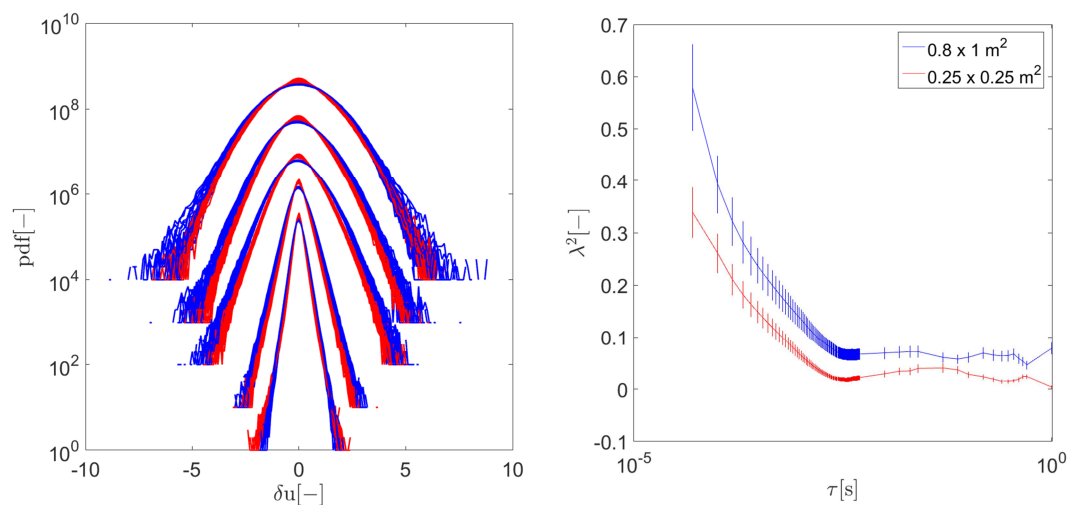


**Figure 4-11 Left: Probability density functions of the velocity increments (1/20000 s, 1/10000 s, 1/2000 s, 1/1000 s, 1/200 s) for both active grids. Shifted for better visualization.**

#### 4.4 Conclusions

The experiments have proven that it is possible to reproduce turbulent inflow in wind tunnel experiments to a certain extent. Especially the length scales in the range of model wind turbines are strongly dependent on the active grid excitation and therefore repeatable. The scalability of the generated wind fields by active grid of different dimensions could be shown with small restrictions. The comparison is showing good results as the main features of the generated flow could be achieved using the same active grid excitation. If the goal is to generate a flow field with certain dynamics and the possibility to reproduce this wake for certain time scales, previous work in terms of excitation protocol development can be directly applied. If the flow should be repeated as accurate as possible every protocol has to be designed for the specific active grid.

#### 4.5 References

M. Wächter, H. Heißelmann, M. Hölling, A. Morales, P. Milan, T. Mücke, J. Peinke, N. Reinke, and P. Rinn (2012). The turbulent nature of the atmospheric boundary layer and its impact on the wind energy conversion process. *Journal of Turbulence*, 13/26.

R. Stresing, J. Peinke, R. E. Seoud, and J. C. Vassilicos (2010). Defining a new class of turbulent flows. *Phys. Rev. Lett.*, 104:194501.

R. E. Seoud and J. C. Vassilicos (2007). Dissipation and decay of fractal-generated turbulence. *Physics of Fluids*, 19(10).

P.E.Roach (1987). The Generation of Nearly Isotropic Turbulence by Means of Grids. *International Journal of Heat and Fluid Flow*. 8. 82-92. 10.1016/0142-727X(87)90001-4.

H. Makita (1991). Realization of a large-scale turbulence field in a small wind tunnel. *Fluid Dynamics Research*, 8(1-4):53.

L. Mydlarski and Z. Warhaft (1996). On the onset of high-reynolds-number gridgenerated wind tunnel turbulence. *Journal of Fluid Mechanics*, 320:331–368, 8.

P. Knebel, A. Kittel, and J. Peinke (2011). Atmospheric wind field conditions generated by active grids. *Experiments in Fluids*, 51(2):471–481.



N. Reinke (2017), Application, Generation and Stochastic Analysis of Turbulent Flows, PhD Thesis, University of Oldenburg

L. F. Richardson (1922). Weather prediction by numerical process. Cambridge University Press.

## 5 WIND TUNNEL EXPERIMENTS [TUD+OLDENBURG]

### 5.1 Introduction

In this chapter, the results of the wind tunnel tests done with an active grid developed by the Universität Oldenburg, as evaluated in Chapter 4, will be discussed. The two-bladed wind turbine discussed in Chapter 3 is placed in this wind tunnel, as shown in Figure 12. Different individual pitch control (IPC) algorithms are implemented on this turbine. The goal of these control algorithms is to reduce the (periodical) loads on the blades of the turbine.



**Figure 12, The two-bladed TU Delft scaled wind turbine placed inside the open wind grid in Oldenburg.**

The operating conditions that have been studied, are with an inflow wind velocity of between 4 and 5 m/s. As a result, the rotor speed usually lies between 180 and 250 rpm. At these speeds, the bandwidth of the pitch actuators only allows alleviation of the first two harmonics, 1P and 2P. In normal operating conditions, these harmonics also cause the largest loads on the blades, making IPC a useful strategy for load alleviation.

Three different pitch control strategies will be studied: the well-known Conventional Individual Pitch control (CIPC) and Linear IPC (LIPC), as well as recently developed Subspace Predictive Repetitive Control (SPRC), *Navalkar e.a., 2014*. In this algorithm, subspace identification is used to get a model of the wind turbine in predictor form, which is used to determine the optimal repetitive control to reduce 1P and 2P loads. The performance of SPRC will be compared to CIPC and LIPC to evaluate the validity of this control strategy. We will also study the control authority of Individual Flap Control (IFC) in addition to LIPC.

These control algorithms will be tested on the mid-sized scaled wind presented in Chapter 3, in the open wind tunnel with active grid in Oldenburg that has been presented in Chapter 4. By means of this active grid, higher Turbulence Intensities (TI's) can be achieved. This makes the experiments done here unique: so far, SPRC has only been tested in low to zero TI conditions, but these experiments will show that it is also a viable control strategy in the more realistic case where turbulence is present in the wind.

In Section 5.2, the inflow conditions in the wind tunnel in Oldenburg with the active grid are presented, followed by a brief overview of the control algorithms in Section 5.3. Subsequently, the

results that have been obtained in these experiments will be presented in Section 5.4. Finally, Section 5.6 will give the conclusions that can be drawn from the results that have been obtained.

## 5.2 Inflow Conditions

To validate the new control concepts of the model wind turbine with turbulent boundary conditions it is necessary to firstly to characterize the flow field acting on the wind turbine. This was realized using a 2D hotwire system by Dantec Dynamics. An x-wire of the type 55P51 was used and operated at a sampling rate of 20 kHz with a low pass filter at 10 kHz. For the data acquisition an 18 bit National Instruments A/D converter was used. The hot wire was installed 3 m (20M) behind the active grid and at hub height of the model turbine which corresponds to the centreline. Additionally the hotwire was shifted 1m to the side to determine differences of the flow field in the range of the wind turbine radius.

The active grid was used in four different modes: Two static and two active cases. For the static cases the angle of attack of the active grid flaps was set to  $0^\circ$  and  $45^\circ$  and hold steady. In the active cases two excitation protocols were used. The first one is based on measured atmospheric wind data and creates a wind field with intermittent behaviour. The second one is creating a wind field with single gusts. All these modes were investigated for three different wind speeds of 4m/s, 4.5m/s and 5 m/s. In the following these inflow conditions are characterised in terms of reproducibility flow characteristics, turbulence intensity, dynamics and intermittency.

The reproducibility was again determined using the cross covariance function as described in chapter 4. The results for all different modes and wind speeds at the centreline position is shown in Figure 13. For the active modes a good resemblance for every protocol iteration can be observed. For the static modes this is not the case as the vortices introduced to the flow by the grid are random distributed. To determine the resemblance of the flow field at the position of the nacelle and the tip of the rotor, also the cross covariance coefficients between the acquired time series at this positions were analysed. Exemplary the result for the Lidar protocol at 5 m/s is shown in Figure 13 on the right as a reference the coefficients between the time series on the centreline are given. The values are slightly lower probably caused by the interaction of the free stream in the boundary regions.

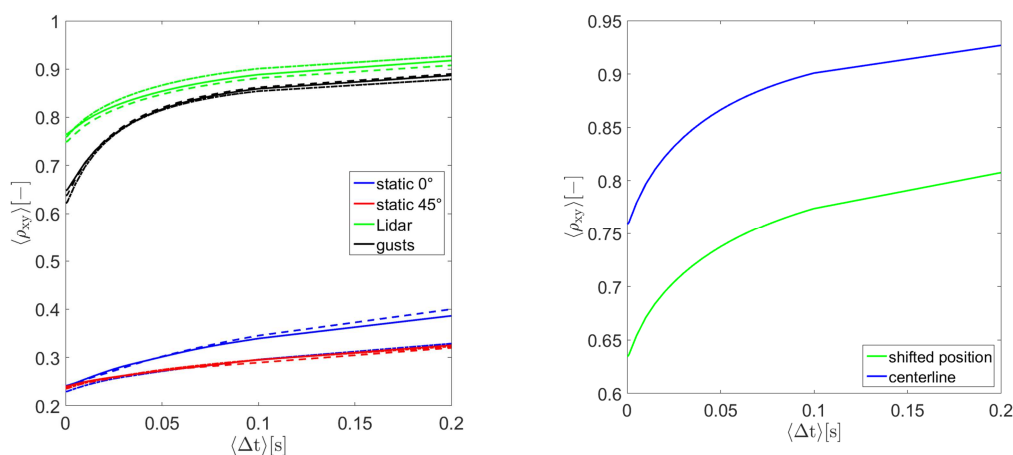


**Figure 13, Left: Cross covariance coefficient for all modes and wind speed: 4 m/s (solid line), 4.5 m/s (dashed line), 5 m/s (dashed-dotted line) Right: Cross covariance coefficient for centreline position as reference and for the comparison between centreline and shifted position.**

This influence can also be seen in the evaluation of the turbulence intensity. The values for the shifted position are always slightly higher than in the centre. The mean for the different wind speeds and the two different position is shown in Table 13. For the different wind speeds the turbulence intensity is changing less than 10 %.

**Table 13: Mean turbulence Intensity for the different working modes of the active grid for both examined positions behind the grid.**

Mode	TI/% (centreline)	TI / % (shifted)
Static 0°	2.5	2.7
Static 45°	3.7	5.1
Lidar	8.8	10.1
Gusts	4.2	7.2

In Figure 14, the power spectra for all working modes of the active grids are shown. The power spectra are not showing major differences for the different wind speeds. The two static cases are containing less energy as expected as no additional energy is transferred to the flow. The active grid excitation for the used protocols is driving the turbulence on larger scales thus introducing structures in the range of the model wind turbine rotor.

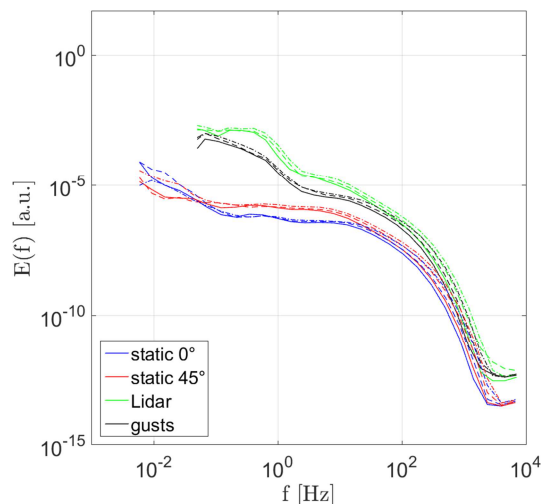


**Figure 14, Power spectra for all different active grid working modes 4 m/s (solid line), 4.5 m/s (dashed line), 5 m/s (dashed-dotted line)**

The intermittency is also lowest for the static cases as expected, this can be seen in the increment statistics as well as in the shape parameter. For all modes except the Lidar protocol the distribution of the increment are nearly Gaussian.

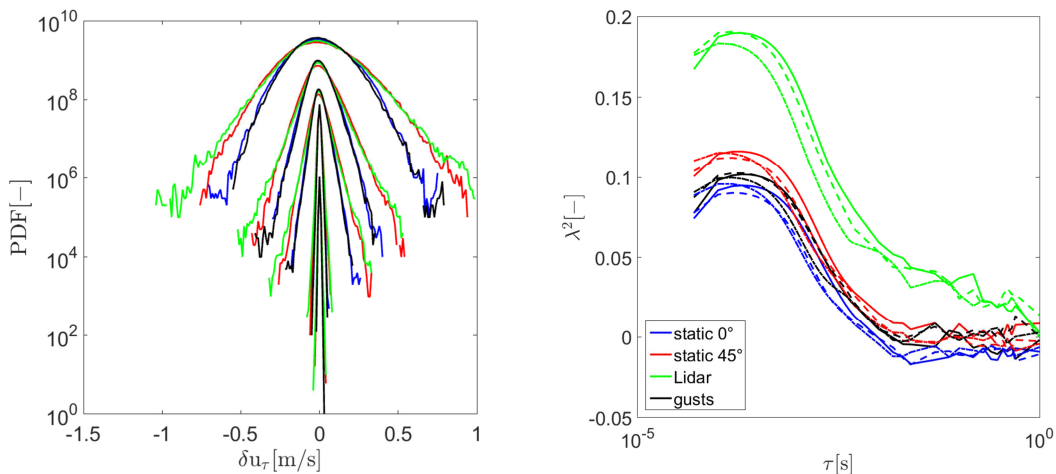


**Figure 15, The shape parameter (left) and intermittency (right) for the different active grid protocols.**

### 5.3 1P and 2P Individual Pitch Control

Two different algorithms have been implemented to reduce the loads on the blades at the rotational frequency (1P) of the turbine: Conventional Individual Pitch Control (CIPC) and Linear IPC (LIPC). In this section, these control methods will be explained.

#### Diagram of IPC on turbine

As depicted in Figure 16, the blade bending moments and the azimuth are fed into the individual pitch controller. Based on this information, the controller determines the demanded individual pitch angles of both blades, which are fed back to the wind turbine baseline system. The pitch motors, which are controlled by standard PID controllers, will then follow this reference signal. Both controllers are implemented within the IPC block of Figure 16.

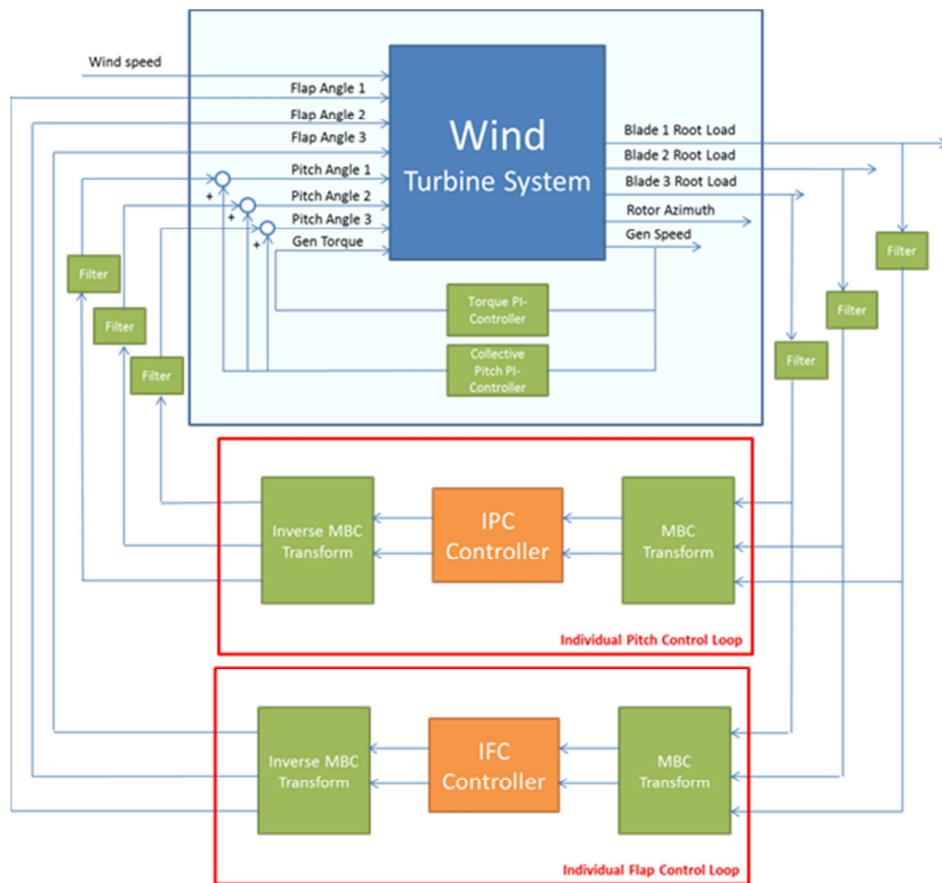


Figure 16, Control diagram of the IPC presented in this section.

#### Conventional IPC

In Conventional IPC, the Coleman Transformation is used to move from a rotating coordinate system to a static one. The Coleman Transformation determines the yaw and tilting moment of the blade forces by using the following equation:

$$M_{yaw} = M_1 \sin \varphi + M_2 \sin(\varphi + \pi)$$

$$M_{tilt} = M_1 \cos \varphi + M_2 \cos(\varphi + \pi)$$

CIPC then simply applies a notch and an integrator to filter out the 1P loads on the blades. The transfer function of the notch filter is given by

$$H_{notch} = \frac{s^2 + 2\beta_2\omega s + \omega^2}{s^2 + 2\beta_1\omega s + \omega^2}$$

where  $\omega$  is the rotational speed of the blades and  $\beta_1$  and  $\beta_2$  are tuning variables, as well as gain  $k$ . Subsequently, the inverse Coleman Transformation is applied to obtain the demanded individual pitch angles that are fed back to the wind turbine system.

#### Linear IPC

In Linear IPC, a different coordinate transformation is used. Here, the difference of the blade moments is used to determine the 1P load:

$$M_{1P} = M_1 - M_2$$

$$M_{2P} = M_1 + M_2$$

Subsequently, a notch filter is used to filter out these periodic load. For LIPC, this notch has the following transfer function:

$$H_{notch} = \frac{2\beta\omega s}{s^2 + 2\beta\omega s + \omega^2}$$

Since pitch control is only used to alleviate the 1P loads, the notch on the 2P moment is not used. After applying the reverse coordinate transformation, the demanded individual pitch angles are obtained. These two simple control algorithms are used as a benchmark for the Subspace Predictive Repetitive Control (SPRC) algorithm that will be discussed in the next section.

#### SPRC

In this section, the SPRC control methodology for IPC will be explained. The wind turbine system will first be identified online using Markov parameters, and this identified system will then be used to establish a repetitive control law using basis functions. This method is similar to the one presented in *Navalkar e.a., 2015*, although modifications have been made to improve performance.

The wind turbine system is assumed to be represented by a discrete linear time-invariant (LTI) system with unknown periodic disturbances, *Houtzager e.a., 2013*:

$$\begin{aligned} x_{k+1} &= Ax_k + Bu_k + Ed_k + Ke_k \\ y_k &= Cx_k + Fd_k + e_k \end{aligned}$$

where  $x_k \in \mathbb{R}^n$  is the state vector,  $u_k \in \mathbb{R}^r$  the input vector; in this case the pitch angles of both blades. The output vector  $y_k \in \mathbb{R}^l$  contains the blade loads as measured by the piezo's mounted on the blades. Disturbance  $d_k \in \mathbb{R}^m$  represents the periodic component on the load of the blades, and  $e_k \in \mathbb{R}^l$  the aperiodic component. If we rewrite these equations in innovation form, the following state-space equations are obtained:

$$\begin{aligned} x_{k+1} &= \tilde{A}x_k + Bu_k + \tilde{E}d_k + Ky_k \\ y_k &= Cx_k + Fd_k + e_k \end{aligned}$$

with  $\tilde{A} = A - KC$ ,  $\tilde{E} = E - KF$ . Furthermore, it is known that  $d_k$  is a periodic disturbance. By defining the difference operator  $\delta$ , we obtain:

$$\delta d_k = d_k - d_{k-p} = 0$$

since the disturbance  $d$  has a period  $P$ . Applying the  $\delta$ -notation on the innovation system, will yield a representation where  $d$  disappears:

$$\begin{aligned} \delta x_{k+1} &= \tilde{A}\delta x_k + B\delta u_k + \tilde{K}\delta y_k \\ \delta y_k &= C\delta x_k + \delta e_k \end{aligned}$$

Next, the stacked vectors  $\delta U_k^{(s)}$  are defined:

$$\delta U_k^{(s)} = \begin{bmatrix} u_k - u_{k-p} \\ \vdots \\ u_{k+s-1} - u_{k+s-1-p} \end{bmatrix}$$

and similarly  $\delta Y_k^{(s)}$ . As a result, the state  $\delta x_{k+p}$  for a certain past window  $p$  can be written as:

$$\delta x_{k+p} = \tilde{A}^p \delta x_k + \begin{bmatrix} \kappa_u^{(p)} & \kappa_y^{(p)} \end{bmatrix} \begin{bmatrix} \delta U_k^{(p)} \\ \delta Y_k^{(p)} \end{bmatrix}$$

with:

$$\begin{aligned} \kappa_u^{(p)} &= [\tilde{A}^{p-1}\tilde{B} \quad \tilde{A}^{p-2}B \quad \dots \quad B] \\ \kappa_y^{(p)} &= [\tilde{A}^{p-1}\tilde{K} \quad \tilde{A}^{p-2}\tilde{K} \quad \dots \quad \tilde{K}] \end{aligned}$$

It is important to select  $p$  sufficiently large, such that  $\tilde{A}^j \approx 0$  for all  $j \geq p$ , *Chiuso, 2007*. For such  $p$ , the equation above can be simplified to:

$$\delta x_{k+p} \approx \begin{bmatrix} \kappa_u^{(p)} & \kappa_y^{(p)} \end{bmatrix} \begin{bmatrix} \delta U_k^{(p)} \\ \delta Y_k^{(p)} \end{bmatrix}$$

Using the equation defining  $\delta y_{k+p}$ , we obtain:

$$\delta y_k = \begin{bmatrix} C\kappa_u^{(p)} & C\kappa_y^{(p)} \end{bmatrix} \begin{bmatrix} \delta U_{k-p}^{(p)} \\ \delta Y_{k-p}^{(p)} \end{bmatrix} + \delta e_k$$

During the online identification, the values of the parameters  $C\kappa$  and  $D$  are estimated based on the measurements of  $y$  and  $u$ . These parameters define the behaviour of the wind turbine system, and are called the Markov parameters  $\Xi \in \mathbb{R}^{1 \times (r+1)p}$ :

$$\Xi = [C\kappa_u^{(p)} \quad C\kappa_y^{(p)}]$$

The Markov estimates are computed recursively at every time instant  $k$  as the unique solution of the equation:

$$\hat{\Xi}_k = \arg \min_{\hat{\Xi}_k} \sum_{i=-\infty}^k \left\| \delta y_i - \hat{\Xi}_k \begin{bmatrix} \delta U_{i-p}^{(p)} \\ \delta Y_{i-p}^{(p)} \end{bmatrix} \right\|$$

Given the definition of  $\Xi$ , it follows that this estimate  $\hat{\Xi}$  at time instant  $k$  contains:

$$\hat{\Xi}_k = [\widehat{C\tilde{A}^{p-1}B} \quad \widehat{C\tilde{A}^{(p-2)}B} \quad \dots \quad \widehat{CB} \quad \widehat{C\tilde{A}^{p-1}K} \quad \widehat{C\tilde{A}^{p-2}K} \quad \dots \quad \widehat{CK}]_k$$

It is important that the input of the system is persistently exciting of a sufficiently high order, in order to guarantee a unique solution of this least-squares problem, *Verhaegen and Verdult, 2007*. This problem is then solved using a QR recursive least-squares algorithm as presented in *Van der Veen e.a., 2013*. In this algorithm, a forgetting factor  $\lambda$  between 0 and 1 is introduced, in order to adapt to changes in the system dynamics. For this application, a large value ( $\lambda \approx 0.99$ ) is preferred to improve the robustness of the identification.

#### Repetitive Control

For repetitive control, the output needs to be predicted over one entire period  $P$ , with  $P \geq p$ , i.e., the output equation needs to be lifted over  $P$  to obtain  $\delta Y_{k+P}^{(P)}$ . To do this, the Toeplitz matrix  $\tilde{H}^{(P)} \in \mathbb{R}^{(n \cdot P) \times (n \cdot P)}$  and the extended observability matrix  $\tilde{\Gamma}^{(P)} \in \mathbb{R}^{(l \cdot P) \times P}$  are defined:

$$\tilde{H}^{(P)} = \begin{bmatrix} 0 & 0 & 0 & \dots & 0 \\ CB & 0 & 0 & \dots & 0 \\ C\tilde{A}B & CB & 0 & \dots & 0 \\ \vdots & \vdots & \ddots & \ddots & \vdots \\ C\tilde{A}^{p-1}B & C\tilde{A}^{p-2}B & C\tilde{A}^{p-3}B & \dots & 0 \\ 0 & C\tilde{A}^{p-1}B & C\tilde{A}^{p-2}B & \dots & 0 \\ \vdots & \vdots & \vdots & \ddots & \vdots \\ 0 & 0 & 0 & \dots & 0 \end{bmatrix}$$

$$\tilde{\Gamma}^{(P)} = \begin{bmatrix} C \\ C\tilde{A} \\ \vdots \\ C\tilde{A}^{p-1} \\ 0 \\ \vdots \\ 0 \end{bmatrix}$$

Similarly,  $H^{(P)}$  and  $\Gamma^{(P)}$  are defined similarly by replacing all  $\tilde{A}$  by  $A$  and  $\tilde{B}$  by  $B$ .  $\tilde{G}^{(P)}$  is defined by replacing  $\tilde{B}$  for  $\tilde{K}$  in  $\tilde{H}^{(P)}$ . Using these matrices, the lifted output equation can be defined:

$$\delta Y_{k+P}^{(P)} = \tilde{\Gamma}^{(P)} \delta x_{k+P} + [\tilde{H}^{(P)} \quad \tilde{G}^{(P)}] \begin{bmatrix} \delta U_{k+P}^{(P)} \\ \delta Y_{k+P}^{(P)} \end{bmatrix}$$

Substituting the approximation of  $\delta x_k$  as given above yields:

$$\delta Y_{k+P}^{(P)} = [\tilde{\Gamma}^{(P)} \kappa_u^{(P)} \quad \tilde{\Gamma}^{(P)} \kappa_y^{(P)}] \begin{bmatrix} \delta U_k^{(P)} \\ \delta Y_k^{(P)} \end{bmatrix} + [\tilde{H}^{(P)} \quad \tilde{G}^{(P)}] \begin{bmatrix} \delta U_{k+P}^{(P)} \\ \delta Y_{k+P}^{(P)} \end{bmatrix}$$

Note that, since  $A^j \approx 0 \forall j \geq p$ , the first  $P - p$  elements of  $\kappa_u^{(P)}$  and  $\kappa_y^{(P)}$  are also 0. Furthermore,  $\tilde{\Gamma}^{(P)} \kappa_u^{(P)}$ ,  $\tilde{\Gamma}^{(P)} \kappa_y^{(P)}$ ,  $\tilde{H}^{(P)}$  and  $\tilde{G}^{(P)}$  can be constructed from the Markov parameters  $\hat{\Xi}$ , since all its elements are also in  $\Xi$ . The predicted output  $Y_{k+p}^{(P)}$  can then be written as a function of the previous

outputs  $Y_k^{(P)}$ , increment outputs  $\delta Y_k^{(P)}$ , the increment inputs  $\delta U_k^{(P)}$  and  $\delta U_{k+P}^{(P)}$ , and the estimates obtained from the Markov parameters:

$$Y_{k+p}^{(P)} = \begin{bmatrix} \Gamma^{(P)} \widehat{\mathcal{K}}_u^{(P)} & \Gamma^{(P)} \widehat{\mathcal{K}}_y^{(P)} & I_{2P} \end{bmatrix} \begin{bmatrix} \delta U_k^{(P)} \\ \delta Y_k^{(P)} \\ Y_k^{(P)} \end{bmatrix} + \widehat{H}^{(P)} \delta U_{k+P}^{(P)}$$

This result is obtained by using the following equalities:

$$\begin{aligned} (I - \widetilde{G}^{(P)})^{-1} \widetilde{\Gamma}^{(P)} &= \Gamma^{(P)} \\ (I - \widetilde{G}^{(P)})^{-1} \widetilde{H}^{(P)} &= H^{(P)} \end{aligned}$$

This system is transformed into a state space representation:

$$\underbrace{\begin{bmatrix} Y_{k+p}^{(P)} \\ \delta U_{k+p}^{(P)} \\ \delta Y_{k+p}^{(P)} \end{bmatrix}}_{\mathcal{X}_{k+p}} = \underbrace{\begin{bmatrix} I_{2P} & \Gamma^{(P)} \widehat{\mathcal{K}}_u^{(P)} & \Gamma^{(P)} \widehat{\mathcal{K}}_y^{(P)} \\ 0_{2P} & 0_{2P} & 0_{2P} \\ 0_{2P} & \Gamma^{(P)} \widehat{\mathcal{K}}_u^{(P)} & \Gamma^{(P)} \widehat{\mathcal{K}}_y^{(P)} \end{bmatrix}}_{\mathcal{A}_k} \underbrace{\begin{bmatrix} Y_k^{(P)} \\ \delta U_k^{(P)} \\ \delta Y_k^{(P)} \end{bmatrix}}_{\mathcal{X}_k} + \underbrace{\begin{bmatrix} \widehat{H}^{(P)} \\ I_{2P} \\ \widehat{H}^{(P)} \end{bmatrix}}_{\mathcal{B}_k} \delta U_{k+P}^{(P)}$$

In the next section, this state-space representation will be used to synthesize a state feedback controller using the discrete algebraic Riccati equation (DARE).

#### Basis functions

In order to reduce the dimensionality of the optimization problem, the input vector  $U_k$  can be projected into a lower dimensional subspace by using the transformation matrix  $\phi$ :

$$U_k = \phi \theta_j$$

where the subscript  $j$  represents the iteration instance, which has a period  $P$ . This transformation matrix  $\phi$  consists of basis functions that are constructed such that the largest signals in the load signal lie in the direction of these basis vectors. Since the dominant load peaks are located at the frequency  $1P$  and its multiples, the basis functions should be sinusoidal signals of these frequencies. Considering that the bandwidth of the pitch motors limits the control authority to the  $1P$  and  $2P$  frequencies, only these frequencies will be present. This yields the following basis function:

$$\phi = \begin{bmatrix} \sin \frac{2\pi}{P} & \cos \frac{2\pi}{P} & \sin \frac{4\pi}{P} & \cos \frac{4\pi}{P} \\ \sin \frac{4\pi}{P} & \cos \frac{4\pi}{P} & \sin \frac{8\pi}{P} & \cos \frac{8\pi}{P} \\ \vdots & \vdots & \vdots & \vdots \\ \sin 2\pi & \cos 2\pi & \sin 4\pi & \cos 4\pi \end{bmatrix} \otimes I_2$$

where the symbol  $\otimes$  represents the Kronecker matrix product. This multiplication is necessary since  $u$  has size 2. As the pitch signal is now limited to be sinusoidal with frequencies  $1P$  and  $2P$ , and the system is assumed to be linear over one period  $P$ , the load signals  $Y_k$  will also be limited to these frequencies. As a result, we can also transform this signal using the same transformation:

$$Y_k = \phi \bar{Y}_j$$

Similarly, the lower dimensional signals  $\bar{Y}_j$  and  $\theta_j$  can be obtained from the original signals by using the Penrose-Moore pseudoinverse of  $\phi$ , represented by the superscript +:

$$\begin{aligned}\bar{Y}_j &= \phi^+ Y_k \\ \theta_j &= \phi^+ U_k\end{aligned}$$

Applying these transformations on the state-space system derived in the previous section, results in the following lower dimensional system:

$$\underbrace{\begin{bmatrix} \bar{Y}_j \\ \delta\theta_j \\ \delta\bar{Y}_j \end{bmatrix}}_{\bar{x}_{j+1}} = \underbrace{\begin{bmatrix} I_8 & \phi^+ \Gamma^{(P)} \kappa_u^{(P)} \phi & \phi^+ \Gamma^{(P)} \kappa_y^{(P)} \phi \\ 0_8 & 0_8 & 0_8 \\ 0_8 & \phi^+ \Gamma^{(P)} \kappa_u^{(P)} \phi & \phi^+ \Gamma^{(P)} \kappa_y^{(P)} \phi \end{bmatrix}}_{\bar{\mathcal{A}}_j} \underbrace{\begin{bmatrix} \bar{Y}_{j-1} \\ \delta\theta_{j-1} \\ \delta\bar{Y}_{j-1} \end{bmatrix}}_{\bar{x}_j} + \underbrace{\begin{bmatrix} \phi^+ H^{(P)} \phi \\ I_8 \\ \phi^+ H^{(P)} \phi \end{bmatrix}}_{\bar{B}_j} \delta\theta_j$$

Note that the matrix  $\bar{\mathcal{A}} \in \mathbb{R}^{24 \times 24}$ , while the original matrix  $\mathcal{A} \in \mathbb{R}^{6P \times 6P}$ . As usually  $P \gg 4$ , it is obvious that using basis functions significantly reduces the order of the optimization problem.

#### Synthesizing a state feedback controller

Similar to a LQR problem, the state feedback gain is now determined by finding the control input that minimizes a quadratic cost function:

$$J = \sum_{j=0}^{\infty} \left\| (\bar{x}_{j+1})^T Q \bar{x}_{j+1} + (\delta\theta_j)^T R \delta\theta_j \right\|_2^2$$

where  $Q$  and  $R$  are weighing matrices that can be tuned to influence the aggressiveness of the controller. As in LQR problems, the state feedback control gain can be found by solving the discrete algebraic Riccati equation (DARE) at iteration  $j$  using an initial estimate of  $P_R$ :

$$P_{R,j+1} = Q + \bar{\mathcal{A}}^T P_{R,j} \left( I_{24} - \bar{B} (\bar{B}^T P_{R,j} \bar{B} + R)^{-1} \bar{B}^T P_{R,j} \right) \bar{\mathcal{A}}$$

Subsequently, the optimal state feedback gain is defined as:

$$K_{f,j} = (R + \bar{B}^T P_{R,j} \bar{B})^{-1} \bar{B}^T P_{R,j} \bar{\mathcal{A}}$$

With the feedback gain determined, it is now possible to determine the control input vector  $\delta\theta_j$ , which, after a backwards transformation, can be implemented on the wind turbine. Using the state-feedback law, we obtain:

$$\delta\theta_j = -K_{f,j} \bar{x}_j$$

However, for implementation, we are not interested in the incremented input, but in the actual input:

$$\theta_j = \theta_{j-1} - K_{f,j} \begin{bmatrix} \bar{Y}_{j-1} \\ \delta\theta_{j-1} \\ \delta\bar{Y}_{j-1} \end{bmatrix}$$

This equation shows that the input at iteration  $j$  depend on the previous input and the state feedback. In order to give the possibility to manipulate the convergence characteristics of the algorithm, tuning parameters  $\alpha$  and  $\beta$  are added:

$$\theta_j = \alpha\theta_{j-1} - \beta K_{f,j} \begin{bmatrix} \bar{Y}_{j-1} \\ \delta\theta_{j-1} \\ \delta\bar{Y}_{j-1} \end{bmatrix}$$

Here, both  $\alpha$  and  $\beta$  should be between 0 and 1. If  $\alpha < \beta$ , the newer data will have a larger influence on the input and as a result, the algorithm will have a faster convergence. If  $\beta < \alpha$ , the opposite is true, but the algorithm will also be less sensitive to disturbances or modelling errors. In general,  $\alpha \ll \beta$  is chosen to guarantee sufficiently fast convergence. The wind turbine input can now be determined by using the inverse basis function transformation:

$$U_k = \phi^+ \theta_j$$

However, we are only interested in the first instance of this lifted vector, *i.e.*, the input  $u_k$  at a given time instant  $k$ :

$$u_k = \left( \left[ \sin \frac{2\pi k}{P} \quad \cos \frac{2\pi k}{P} \quad \sin \frac{4\pi k}{P} \quad \cos \frac{4\pi k}{P} \right] \otimes I_2 \right) \theta_j$$

Finally, the angle  $\frac{2\pi k}{P}$  is equal to the rotor azimuth  $\psi$ , which is being measured. As a result, the azimuth at time instant  $k$  can be used to determine the input:

$$u_k = ([\sin \psi_k \quad \cos \psi_k \quad \sin 2\psi_k \quad \cos 2\psi_k] \otimes I_2) \theta_j$$

By implementing the azimuth, the algorithm is not susceptible to small variations in rotor speed. Using this equation, the control input can be updated at each time instant  $k$ . The value of  $\theta_j$  is updated once every period  $P$ . The control scheme for 1P loads is represented in the figure below, where  $P$  represents the wind turbine plant. The implementation of 2P load reduction is done in a similar way, but left out here for visibility reasons.

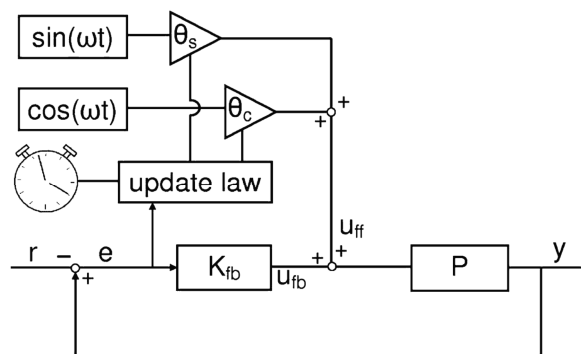


Figure 17, Scheme for the receding horizon implementation of the SPRC update law

#### 5.4 2P Individual Flap Control

Besides Individual Pitch Control, it is also possible to actuate the Free Floating Flaps (FFF) that were mentioned in Chapter 3. Using piezo-actuators, the shape of these flaps can be influenced. The control authority of these flaps is significantly smaller than the control authority of the pitch angles, but the bandwidth is much higher. As a result, Individual Flap Control (IFC) can be used to alleviate the higher frequency harmonics of the blade loads.

In these experiments, IFC will be used to regulate the 2P loads of the blades. The method is essentially the same as for LIPC: first, the loads undergo a coordinate transformation to obtain the 1P and 2P equivalent loads. Then, a similar notch filter is applied:

$$H_{notch} = \frac{2\beta\omega s}{s^2 + 2\beta\omega s + \omega^2}$$

Where in LIPC this notch was applied on the 1P signal, it will be applied on the 2P load signal in LIFC. Subsequently, the parameter  $\omega$  will not be, as it was with LIPC, the rotor speed, but rather twice the rotor speed.

As discussed, the control authority of LIFC is limited compared to the IPC methods. As a result, flap control will only be applied combined with LIPC. The results of this combination of pitch and flap control, as well as other results, will be shown

## 5.5 Results

In this section, the results of the SPRC algorithm deliberated in Section 5.3 will be discussed. The SPRC algorithm, as well as the CIPC and LIPC algorithms, have been implemented on a model wind turbine (see Chapter 3) in the wind tunnel with active grid discussed in Chapter 4. Using the pitch actuators, SPRC will be used to reduce the periodic loads on the blades as measured by strain gauges.

The control algorithms will be tested for varying wind conditions: the wind speed will be varied between 4 and 5 m/s, and different active grid protocols will be used to influence the turbulence intensity as discussed in Section 5.2. The turbine generator is connected in series to a dump load. As a result, both the dump load, acting as the generator torque, and the pitch angle can be used to influence the rotor speed. However, since the influence of the dump load on the rotor speed is found to be limited, it is only turned on (when braking torque is desired) or off (when it is not).

First, the performance of the CIPC and LIPC algorithms will be shown. These controllers will then be used to evaluate the performance of the SPRC algorithm in the different wind conditions mentioned above. Finally, the performance of SPRC will be evaluated for changing conditions, showing that the algorithm is in fact able to adapt to these changes.

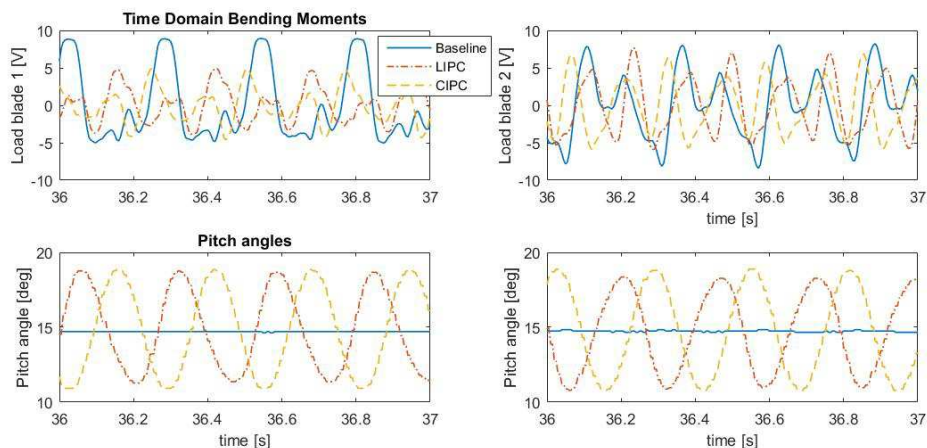
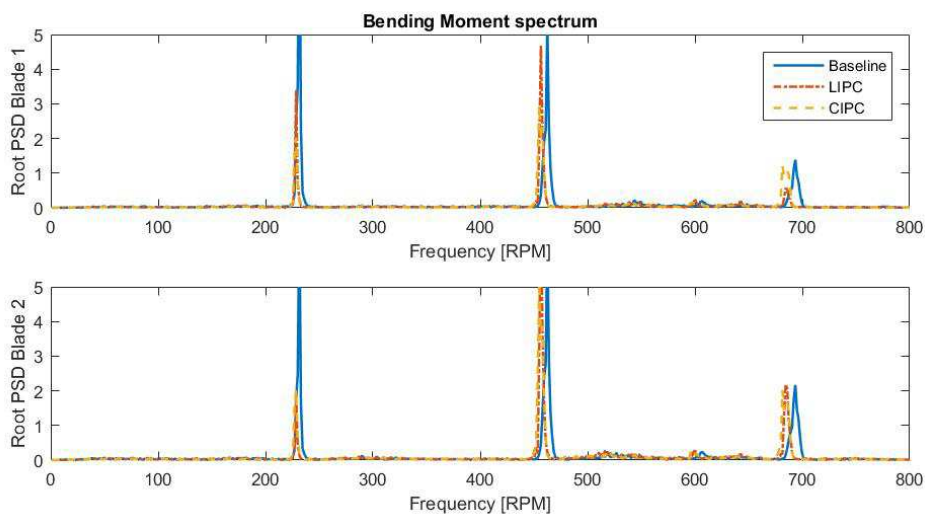


Figure 18, Blade loads and pitch action for LIPC and CIPC for a static 0 degrees grid with  $v = 5m/s$ .

*LIPC and CIPC: baseline controllers*

The LIPC and CIPC algorithms are tested under different wind conditions. Note that these controllers are only used to mitigate the 1P loads. Figure 18 shows the blade loads and pitch action of the turbine in low turbulent conditions, *i.e.*, with a static open grid. For this experiment, the wind inflow velocity was 5 m/s with a pitch angle of 15 degrees, resulting in a rotational velocity of 230 rpm. As we can see in Figure 18, both blade moments are slightly reduced, albeit blade 1 significantly more than blade 2. The blade load variance reductions are 71.5% and 79.8% for blade 1 and 22.2% and 39.9% for blade 2, for LIPC and CIPC respectively. We can see from Figure 18 that both controllers perform similarly, but CIPC seems to perform slightly better than LIPC.



**Figure 19, Blade root loads in the frequency domain for LIPC and CIPC compared to no control.**

Figure 19 shows the root Power Spectral Density (PSD) of the blade loads for the controllers compared to the baseline case of no control action. The three peaks in this figure represent the 1P, 2P and 3P loads. As expected, the 2P and 3P loads remain similar, whereas the 1P loads are significantly reduced by both controllers.

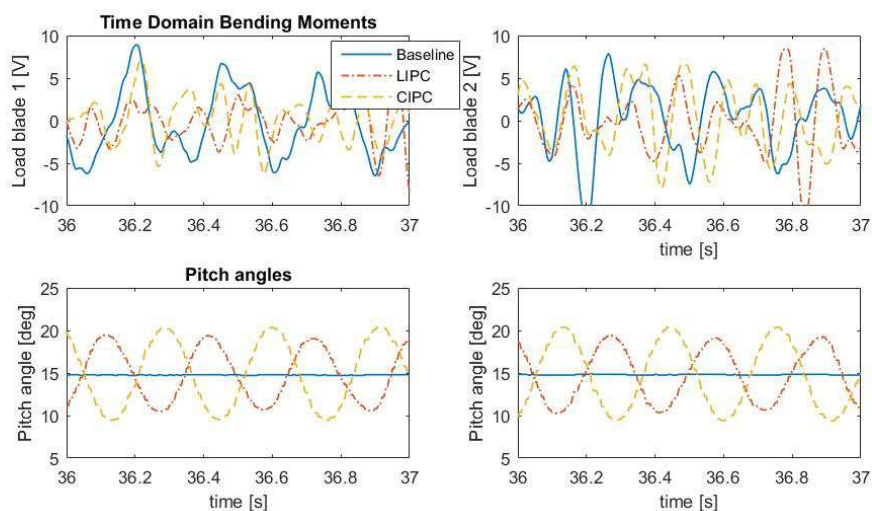


**Figure 20, Blade loads and pitch action for the Lidar protocol, with an inflow velocity of 5 m/s.**

Similar results are obtained when the Lidar protocol is turned on. In general, this increases the turbulence intensity whilst slightly reducing the wind speed. As a result, the rotor speed drops to 210 RPM for an inflow velocity of 5 m/s, and the blade loads increase. We can see from Figure 20 that the LIPC and CIPC algorithms still reduce the loadings, although less than in the low TI case. The blade load variance reductions now are 68.1% and 75.8% for blade 1 and 17.7% and 34.5% for blade 2, for LIPC and CIPC respectively.

If we look at Figure 21, we can see that the peaks associated with the rotor speed are now in general lower but wider than for the low-TI case. Due to the turbulence, the rotor speed varies more over time, resulting in a wider peak in the frequency domain.

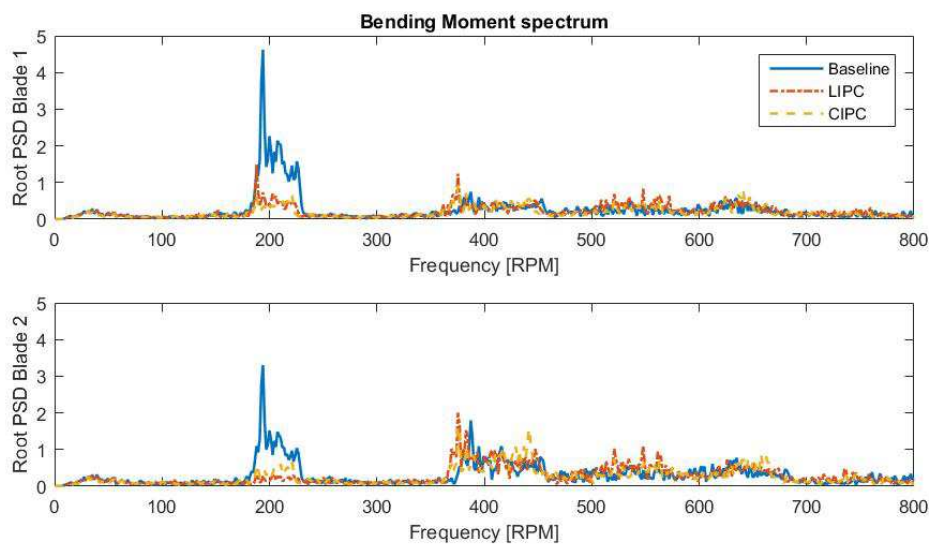


**Figure 21, Blade root loads in the frequency domain for LIPC and CIPC compared to no control with the Lidar grid protocol.**

Figure 21 shows that the LIPC and CIPC algorithms still manage to significantly reduce the 1P loads, with very little difference in performance between the two. Other wind conditions show a similar trend and are therefore omitted here.

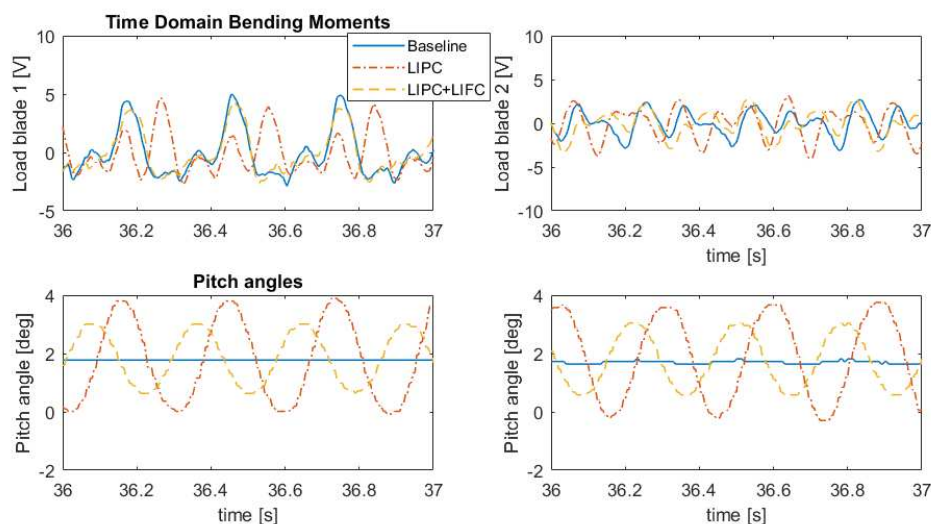
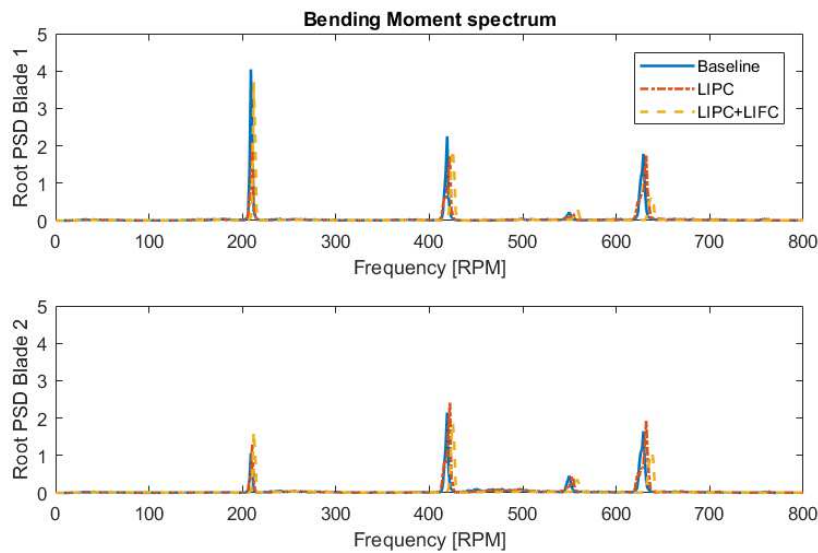


**Figure 22, Blade loads and pitch action for LIPC with and without LIFC for a static 0 degrees grid with  $v = 4\text{m/s}$ .**

*LIPC combined with flap control*

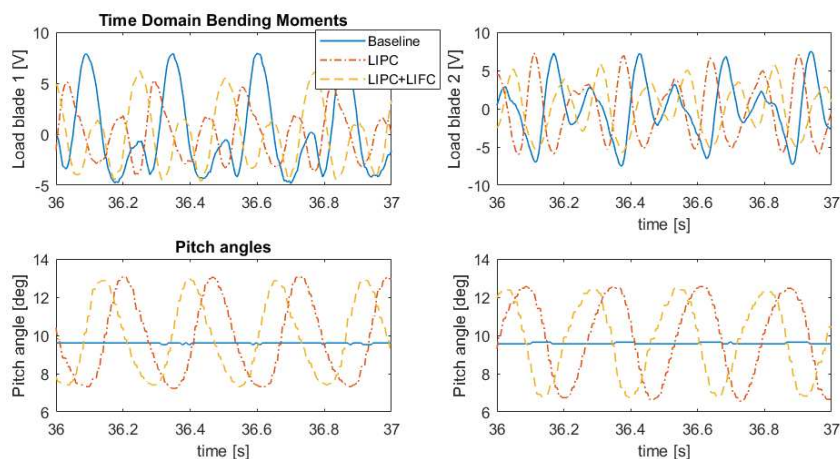
As mentioned in Section 5.3, it is also possible to combine IPC with Individual Flap Control (IFC). The results of LIPC combined with linear IFC will be shown here, and will be compared to the case where only LIPC is applied.

In Figure 22, the blade loads and pitch actions are shown for LIPC with and without LIFC for an open grid (TI: 2.5%) and a wind speed of 4 m/s (200 RPM). This figure shows that the loads are slightly reduced by adding 2P LIFC control. Furthermore, the pitch action to achieve this is somewhat reduced due to the flap control action. With LIFC, the blade load variance is reduced with 22.0% for blade 1 and 1.0% for blade 2, whereas without LIFC, this controller increased the loads on blade 2 significantly.



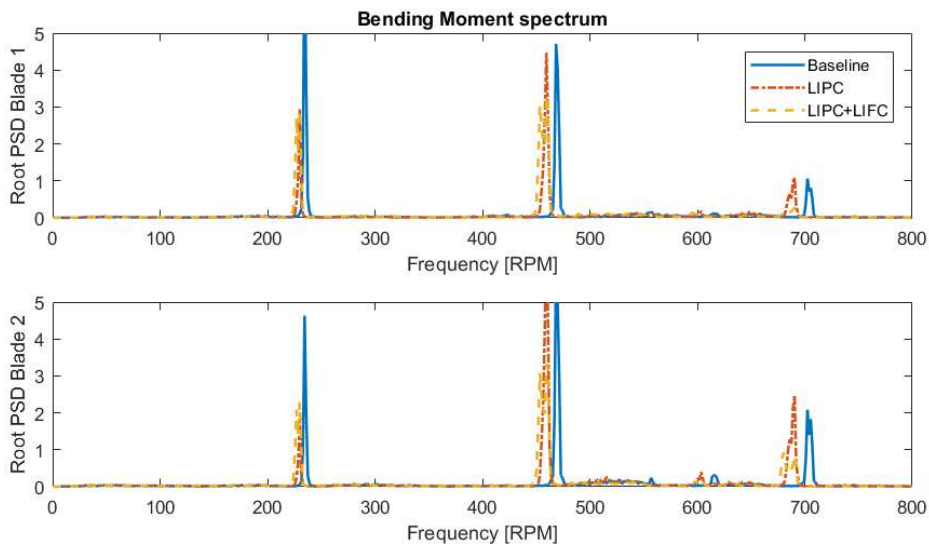
**Figure 23, Blade root loads in the frequency domain for LIPC with and without LIFC for a static 0 degrees grid and  $v = 4m/s$ .**

Figure 23 shows the power spectral density plot of the same experiment. Here we see that the 1P loads increase slightly with LIFC. This can be explained by the smaller pitch action that is used. However, the 2P loads have a small reduction, and also the 3P loads seem to have been reduced, even though there is no specific control on these harmonics.



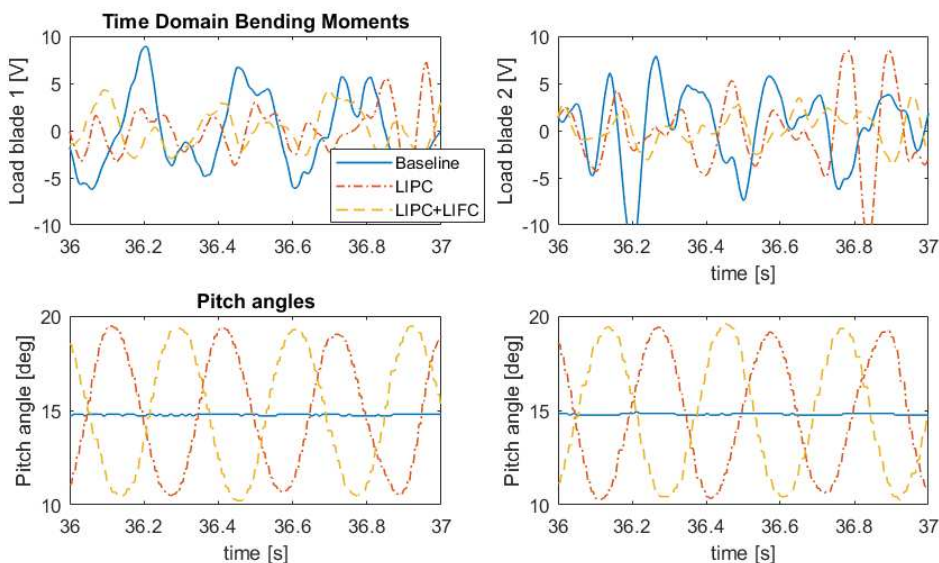
**Figure 24, Blade loads and pitch action for LIPC with and without LIFC for  $v = 4.5\text{ m/s}$ .**

These results become even more clear at higher wind speeds. For a wind speed of 4.5 m/s, which results in a rotor speed of 230 RPM, the solo LIPC algorithm struggles to reduce the load of both blades. In this experiment, the blade load variance is reduced by 60.2% for blade 1, but increases with 4.5% for blade 2. However, if we add flap control, the blade loads are reduced more uniformly. Combining LIPC with LIFC results in a load variance reduction of 42.1% (blade 1) and 36.0% (blade 2). This is shown in Figure 24.



**Figure 25, Blade root loads in the frequency domain for LIPC with and without LIFC for a static 0 degrees grid and  $v = 4.5\text{ m/s}$ .**

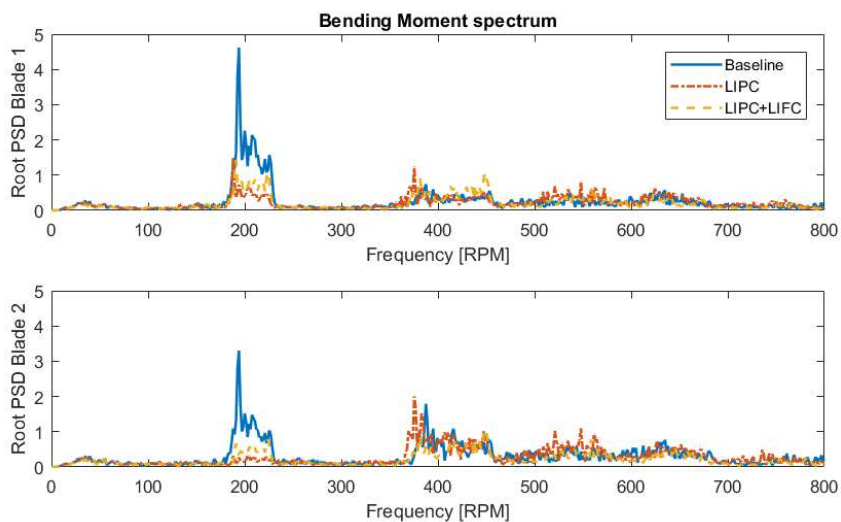
Figure 25 shows the frequency domain plot of the same experiment. Here we see, more clearly now than in the 4 m/s case, that the 2P loads are significantly reduced by the LIFC action. Again, we notice that also the 3P load is reduced somewhat. In this experiment, the 1P load is almost identical for LIPC with and without LIFC, which can be explained by the pitch action, which was also very similar for both cases.



**Figure 26, Blade loads and pitch action for LIPC with and without LIFC for the Lidar grid with  $v = 5m/s$ .**

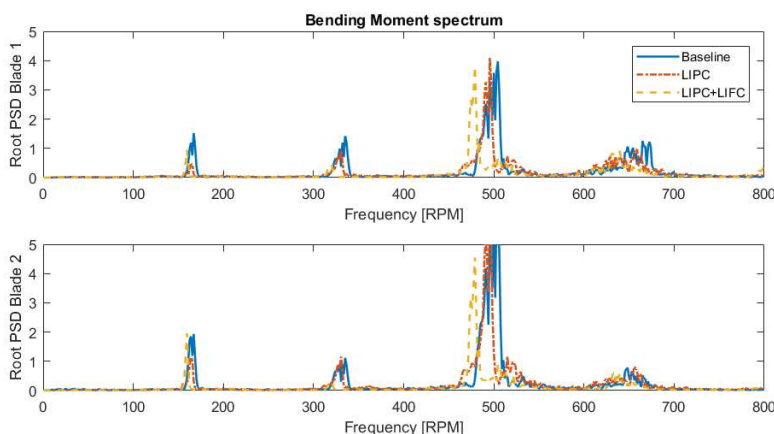
For higher turbulent cases, the effect of adding flap control becomes even bigger. Figure 26 shows the time domain response of LIPC with and without flap control for the Lidar protocol (TI: 8.8%) at a wind speed of 5 m/s. The blade load variance was reduced with 68.1% and 17.7% for blades 1 and 2 respectively without LIFC. With flap control added, this is now 62.2% and 58.4% respectively. So overall, the LIPC+LIFC combination performs slightly better than without LIFC.

Figure 27 shows the power spectral density of the root blade loads. Notice again that the 1P and 2P peaks are much broader here than in the low-TI case. We see again that the 1P loads are slightly higher when LIFC is added, but the 2P loads, especially for blade 2, are reduced significantly.



**Figure 27, Blade root loads in the frequency domain for LIPC with and without LIFC for the Lidar grid and  $v = 5m/s$ .**

In particular situations, the performance of flap control is more evident. One of these situations is when a wind turbine experiences a high level of shear, *i.e.*, big differences in wind speed in the rotor plane. This situation can be created with the active grid, by varying the angle of the rods in the grid from left to right, from 90° (completely closed) on the far left to 0° (completely open) to the right of the middle.



**Figure 28, Blade root loads in the frequency domain for LIPC with and without LIFC for the Shear grid and  $v = 4m/s$ .**

For this situation, the 1P and 2P loads are no longer the dominant harmonics, as can be seen in Figure 28, which shows the PSD of the root blade loads. Here we see that the 3P load is now the dominant factor in the loads. As mentioned earlier, the flap control reduces this 3P load slightly, thus reducing the overall loads. Notice also that the 2P loads have almost completely disappeared thanks to LIFC.

From the time domain plots (Figure 29), we can indeed see that loads vary much faster than in earlier examples with a similar rotor speed ( $\approx 180$  RPM). It is also evident that the LIPC+LIFC algorithm achieves a major load reduction. This is also apparent from the blade load variances: these are reduced with 45.6% and 65.9% for blades 1 and 2 respectively. For comparison: by only applying LIPC, this is 43.9% and 45.4% with respect to the baseline case of no control.

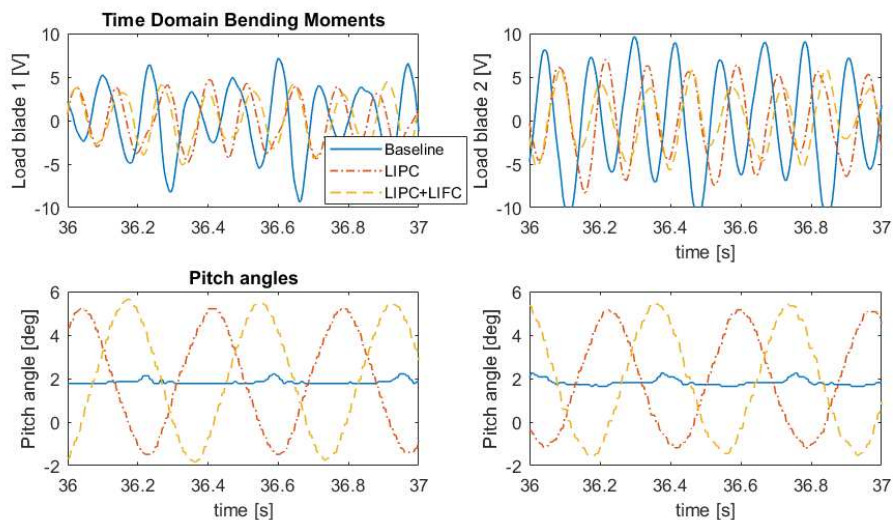


**Figure 29, Blade loads and pitch action for LIPC with and without LIFC for the Shear grid with  $v = 4m/s$ .**

From these results, it becomes clear that as higher frequency harmonics (3P and up) start playing a larger role in the loads, flap control becomes a viable control option compared to pitch control. The control authority is still limited, but the higher bandwidth makes it possible to reduce loads that the limited bandwidth of the pitch motors cannot reach.

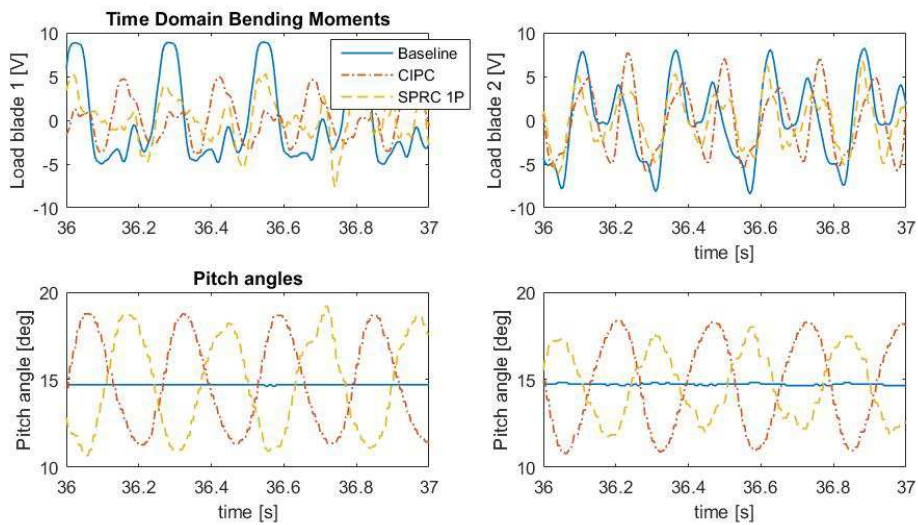


Figure 30, Blade loads and pitch action for CIPC and 1P SPRC for a static 0 degrees grid with  $v = 5m/s$ .

*SPRC for constant wind conditions*

In this section, the performance of the SPRC algorithm will be compared to CIPC. Note that, unlike CIPC and LIPC, SPRC was used to mitigate both the 1P and 2P loads. Although this is generally undesirable, it is possible to only use the 1P load control. This is shown in Figure 30, where 1P SPRC is compared to CIPC for the same low-TI conditions as shown above.

Figure 30 shows that the performance of SPRC is similar to that of CIPC. If we look at the blade load variance, we see that 1P SPRC performs slightly better. The load SD is reduced with 73.1% and 48.1% for blades 1 and 2 respectively, compared to 71.5% and 22.2% with CIPC. This can also be observed in Figure 31, where the root PSD is plotted once more. Here we see that the 1P load reductions of blade 1 are similar, whereas for blade 2, SPRC performs better than CIPC.

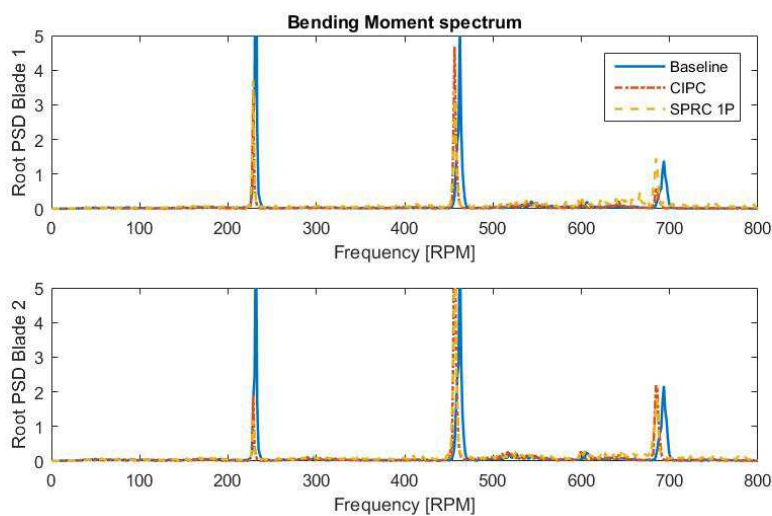
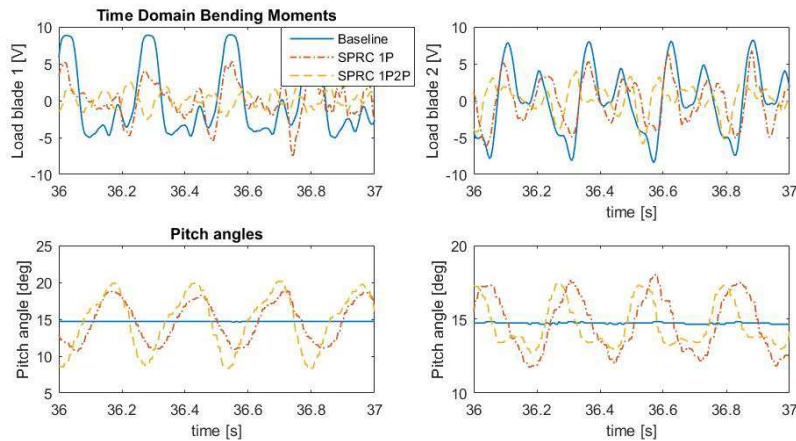


Figure 31, Blade root loads in the frequency domain for CIPC and SPRC compared to no control.

The full potential of SPRC becomes visible when both 1P and 2P load control is enabled. Figure 32 shows the blade loads and pitch action of this controller compared to 1P SPRC. With 1P2P SPRC, the blade load SD is reduced by 94.8% and 77.3% for blades 1 and 2 respectively, with more or

less the same pitch action. The pitch motors also seem to have sufficient bandwidth to regulate the 2P frequency.



**Figure 32, Blade loads and pitch action for CIPC and 1P2P SPRC for a static 0 degrees grid with  $v = 5m/s$ .**

Figure 33 shows the root PSD plot of the measurement shown above. We can see that both the 1P and 2P blade loads are significantly reduced by the controller, especially on the first blade: the 1P peak in the frequency domain plot has nearly disappeared here. Also the 2P loads are considerably lower than in the baseline case, as well as the 1P SPRC case.

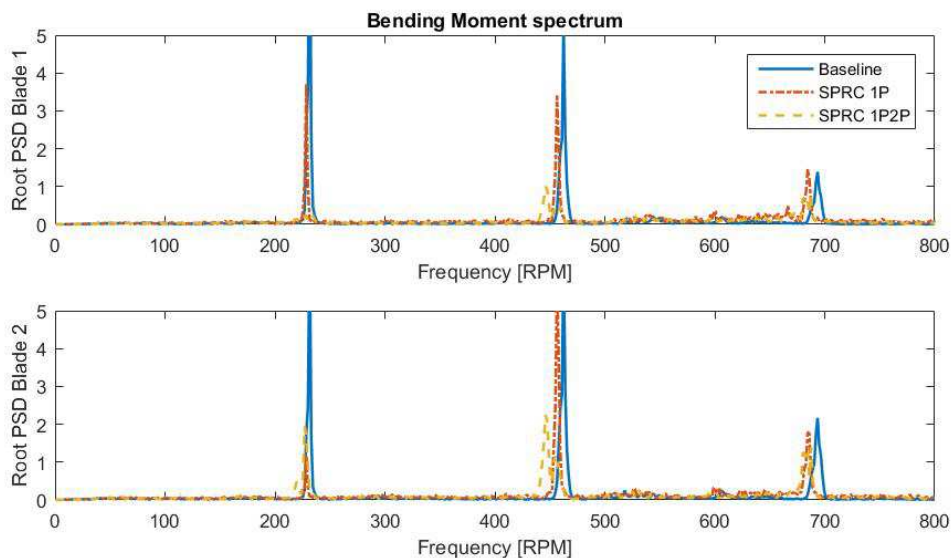


**Figure 33, Blade root loads in the frequency domain for 1P SPRC and 1P2P SPRC compared to no control.**

For the higher turbulence cases, the SPRC algorithm performs less superior compared to conventional IPC, as can be seen in Figure 34. SPRC still reduces the blade load variance more than CIPC, but the difference is now much smaller: 78.2% and 47.1% for 1P2P SPRC compared to 75.9% and 31.1% for CIPC. This can be easily explained. The SPRC algorithm uses random pitch signals to identify the system. As the turbulence intensity increases, it becomes more and more difficult for the algorithm to distinguish between load effects caused by the pitch change and that caused by the – unknown – turbulence. Hence, the identified model on which the control is based will likely become less accurate as the TI increases.

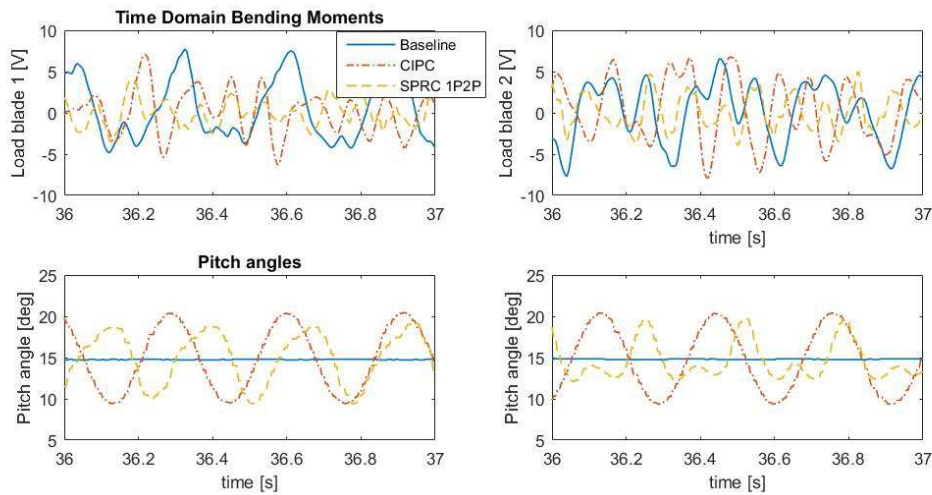


Figure 34, Blade loads and pitch action for CIPC and 1P2P SPRC for the Lidar grid protocol with  $v = 5\text{m/s}$ .

If we look at the frequency domain, we notice that indeed the 1P load reduction, although still significant, is smaller for SPRC than for CIPC. It is due to the 2P load reduction that the SPRC algorithm still performs better than CIPC.

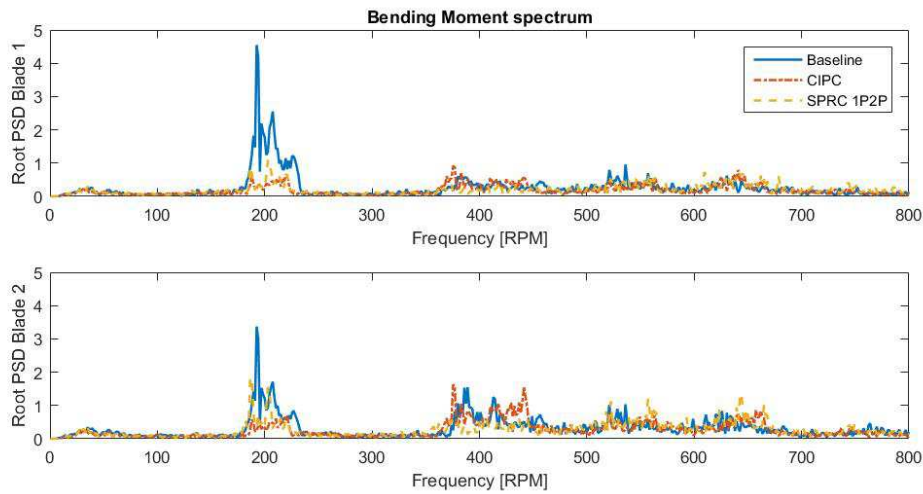
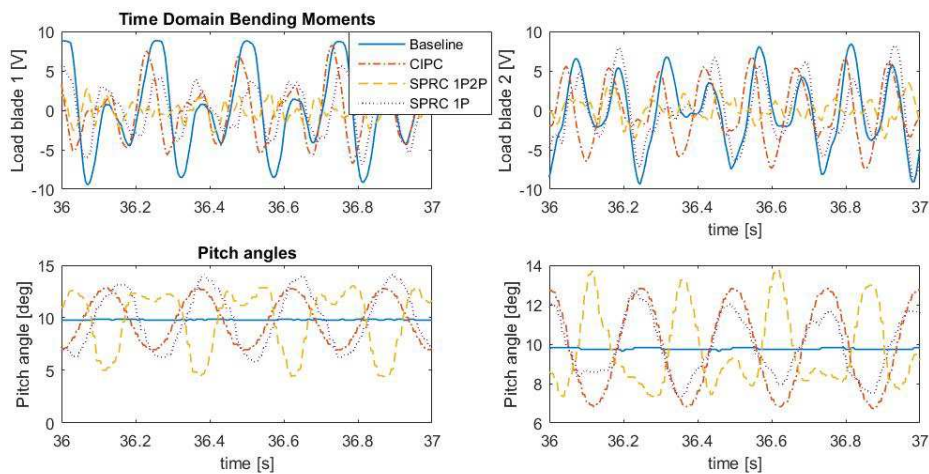


Figure 35, Blade root loads in the frequency domain for CIPC and 1P2P SPRC compared to no control.

Note that, with a centreline TI of 8.8%, the turbulence is substantial in this experiment. As expected, the SPRC algorithm performs better under lower TI conditions. Figure 36 shows the time domain response of both 1P and 1P2P SPRC in the static 45 degrees grid protocol. This protocol has a centreline TI of 3.7%, while the inflow wind velocity is set to 5 m/s. For these wind conditions, the SPRC algorithm performs significantly better than CIPC.



**Figure 36, Blade loads and pitch action for CIPC and 1P2P SPRC for the static 45 degrees grid protocol with  $v = 5\text{m/s}$ .**

When we look at the power spectral density plot of the root blade loads, Figure 37, the performance of 1P2P SPRC becomes even clearer: where CIPC already reduces the 1P peak significantly, both the 1P and 2P peaks disappear almost completely. The performance of SPRC can also be observed when the reduction in blade load variance is calculated: for CIPC, this reduction is 51.8% and 15.7% for blades 1 and 2 respectively, while for 1P SPRC it is 61.3% and 26.5%. For the 1P2P SPRC algorithm, it goes up to no less than 94.0% and 91.6% for blades 1 and 2 respectively. Evidently, a substantial reduction of the blade loads is achieved by SPRC.

It must be noted that this reduction was not observed for all wind velocities using this grid protocol. With an inflow velocity of 4 m/s, the SPRC identification diverged, resulting in an increase of loads on the blades for the 1P2P SPRC algorithm. Although the loads are reduced for the  $v = 4.5\text{m/s}$  case, SPRC still performed slightly worse than CIPC for these conditions. Clearly, if the algorithm fails to sufficiently identify the system, the SPRC algorithm will not always result in an optimal controller.

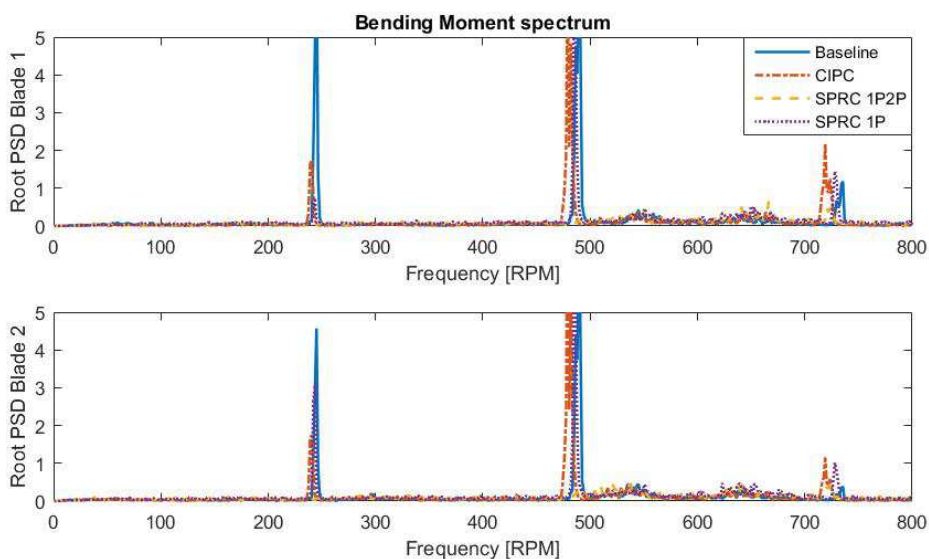


**Figure 37, Blade root loads in the frequency domain for CIPC and 1P and 1P2P SPRC compared to no control.**

Finally, the results of SPRC with the Gusts protocol, which had an average centreline TI of 4.2%, will be discussed. Although the centreline TI of this protocol is similar to the previously discussed 45 degrees static protocol, the TI at the shifted position is considerably larger (7.2% instead of 5.1%). As a result, the performance of the controllers is expected to be slightly less than in the previous experiment.

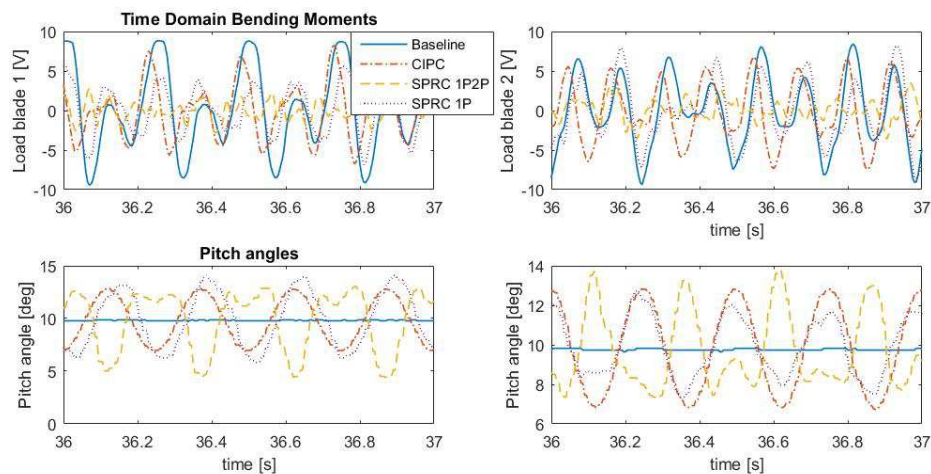


Figure 38, Blade loads and pitch action for CIPC and 1P2P SPRC for the Gusts protocol with  $v = 4.5 \text{ m/s}$ .

As can be seen in Figure 38, all controllers achieve a load reduction for this protocol. The 1P2P SPRC algorithm again has the largest load reduction, 86.0% and 74.6% for blades 1 and 2 respectively. 1P SPRC achieves a reduction of 76.2% and 30.3%, still slightly better than CIPC (74.9% and 22.0%). Figure 39 shows the root PSD, which looks very similar to the low-TI experiment shown in Figure 33. It can therefore be concluded that a small rise of TI does not significantly influence the performance of the SPRC algorithm.

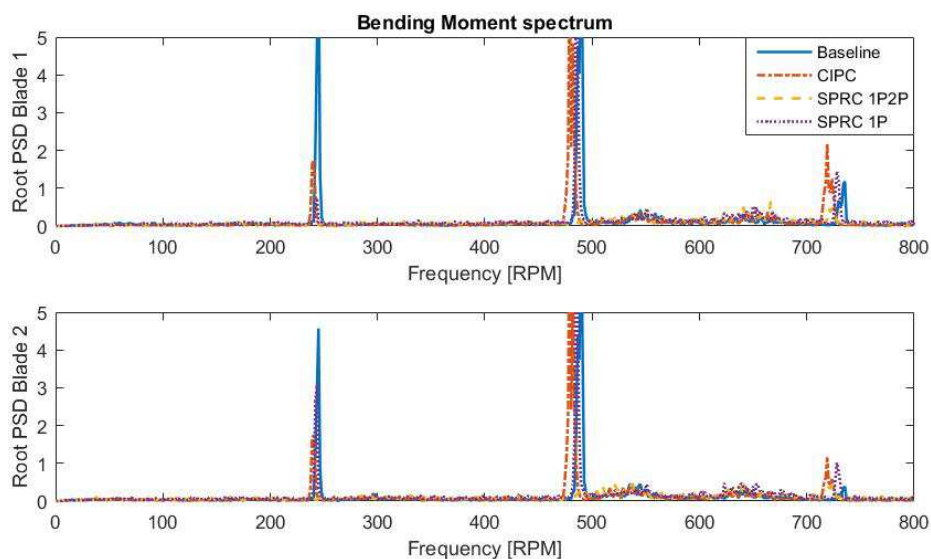


Figure 39, Blade root loads in the frequency domain for CIPC and 1P and 1P2P SPRC compared to no control.

All the results of the different controllers are summarized in Table 14, which shows the load variance of the blades with the different controllers compared to the baseline case of no IPC. Notice that all controllers have had certain conditions in which the variance of the load was

actually increased. Overall, all controllers reduce the blade load variance nevertheless. In almost all cases, the 1P2P SPRC performs superior compared to the baseline LIPC and CIPC control algorithms.

**Table 14: Blade load variance compared to baseline for all controllers in different wind conditions. The best controller for each case and blade is put in *italic*, cases where the loads are increased in red.**

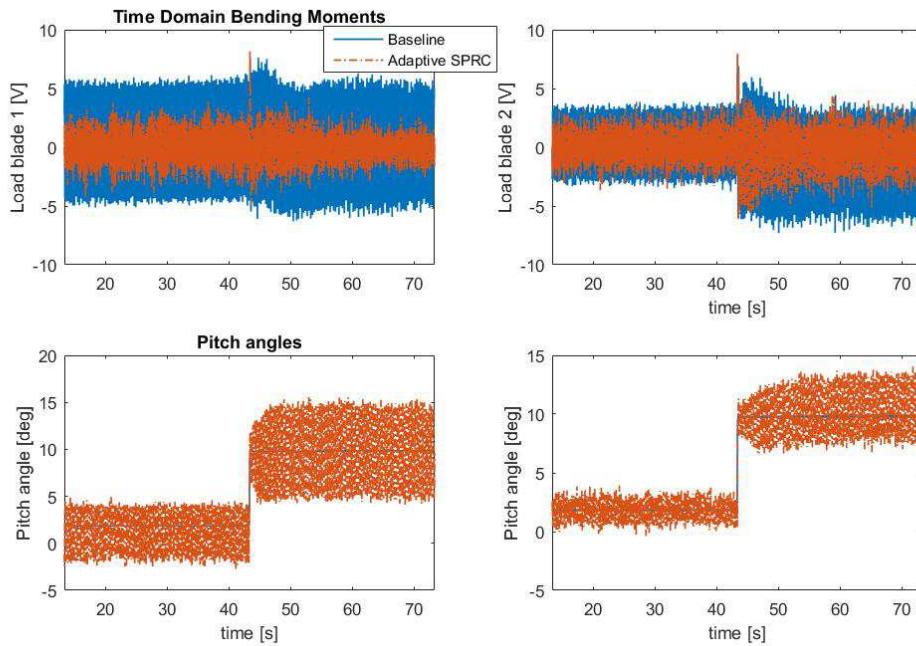
	LIPC		CIPC		LIPC + LIFC		1P SPRC		1P2P SPRC	
<b>Static 0°</b>	<i>Blade1</i>	<i>Blade2</i>								
4 m/s	-49.4%	44.7%	-67.6%	27.1%	-22.0%	-1.0%	-76.3%	-14.0%	-79.3%	-59.1%
4.5 m/s	-60.2%	4.5%	-79.6%	-30.1%	-42.1%	-36.0%	-71.3%	-31.6%	-84.7%	-80.8%
5 m/s	-71.5%	-22.2%	-79.8%	-39.9%	-47.9%	-41.5%	-73.0%	-48.1%	-94.8%	-77.3%
<b>Static 45°</b>										
4 m/s	-60.0%	-55.2%	-61.4%	-41.9%	-55.7%	-61.5%	-17.1%	39.6%	2.4%	65.3%
4.5 m/s	-80.3%	-29.6%	-86.1%	-57.7%	-66.8%	-55.7%	-67.1%	-11.5%	-83.8%	-32.4%
5 m/s	-29.2%	-3.9%	-51.8%	-15.7%	-27.7%	-8.9%	-61.3%	-26.5%	-94.0%	-91.6%
<b>Lidar</b>										
4 m/s	-36.2%	12.8%	-36.0%	6.7%	-30.1%	-18.5%	-43.5%	16.7%	-43.0%	-8.0%
4.5 m/s	-67.4%	-35.3%	-68.3%	-30.5%	-53.4%	-45.6%	-59.0%	-28.0%	-64.3%	-38.9%
5 m/s	-68.1%	-17.7%	-75.8%	-34.5%	-62.2%	-58.4%	-50.1%	8.3%	-78.1%	-49.7%
<b>Gusts</b>										
4 m/s	-54.3%	24.3%	-68.7%	14.8%	-33.2%	-0.9%	-47.0%	18.6%	-69.2%	-42.6%
4.5 m/s	-65.8%	1.2%	-74.9%	-22.0%	-38.6%	-14.7%	-76.2%	-30.3%	-86.0%	-74.6%
5 m/s	-63.0%	-26.1%	-63.4%	-25.4%	-58.1%	-57.8%	-72.1%	-37.3%	-75.5%	-66.9%

#### Adaptive control using SPRC

In the previous section, the operating conditions were assumed to be constant over time. However, an operating wind turbine will be subject to changes in wind conditions. When the wind conditions change, the system parameters also change. To accommodate this effect, SPRC can update the Markov parameters during operation: this way, the system gets updated when the operating conditions change.

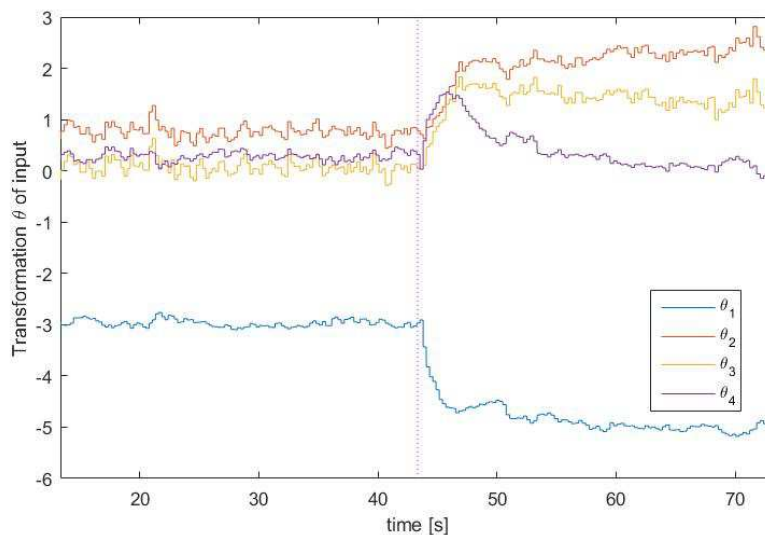
As mentioned in Chapter 5.3, the rotor speed depends on both the pitch angles and the wind inflow velocity. The effect of varying the pitch angle set-points, as well as changing wind conditions, will be evaluated in this section. We will show that SPRC is able to adapt to small changes in operating conditions, and still provide a controller that reduces the 1P and 2P blade loadings.

Figure 40 shows the blade loads and pitch action with a static 0° protocol and an inflow velocity of 4 m/s. At approximately 42 seconds, the pitch reference angle is set from 2 to 10 degrees, which approximately reduces the rotor speed from 230 to 210 rpm. It can be seen that initially the loads increase slightly, but after approximately 10 seconds, the SPRC algorithm has adapted and the loads are reduced again. Before the change, the loads are reduced with 74.6% and 59.7% for blades 1 and 2 respectively. Afterwards, this becomes 88.8% and 60.3% for blades 1 and 2 respectively. So for this particular situation, SPRC is able to improve its performance when the operating conditions are changed.



**Figure 40, Blade loads and pitch action when the reference pitch angle is changed from 2 to 10 degrees, with a static  $0^\circ$  protocol and  $v = 4\text{m/s}$ .**

Figure 41 shows the evolution of the parameters  $\theta$ , which are the inputs  $u$  before the inverse basis function transformation is applied. Before the pitch angles are changed, the values of  $\theta$  only undergo small changes, indicating that the identification has been successful and the system parameters have converged. Immediately after the pitch angle is changed (indicated by the vertical line), all parameters change significantly. Within a few seconds, the parameters converge to a new point, indicating that the identification algorithm has found a new optimum.



**Figure 41, Evolution of 4 of the  $\theta$ -variables over time. The vertical line represents the moment the reference of the pitch angles changes.**

Similarly, the wind velocity can also be changed to vary the system parameters. In the following experiment, a small change of the wind speed will occur, to which the SPRC algorithm will need to adapt. If the wind speed is changed from 4 to 4.5 m/s for a reference pitch angle of  $10^\circ$ , the rotor

speeds varies approximately from 180 to 210 rpm, as can be seen in Figure 42. Please note that the wind speed is changed manually, and subsequently the change is not identical in different experiments. In Figure 42 and subsequent similar figures, the plots are aligned such that the behaviour of SPRC can be compared with the baseline case.

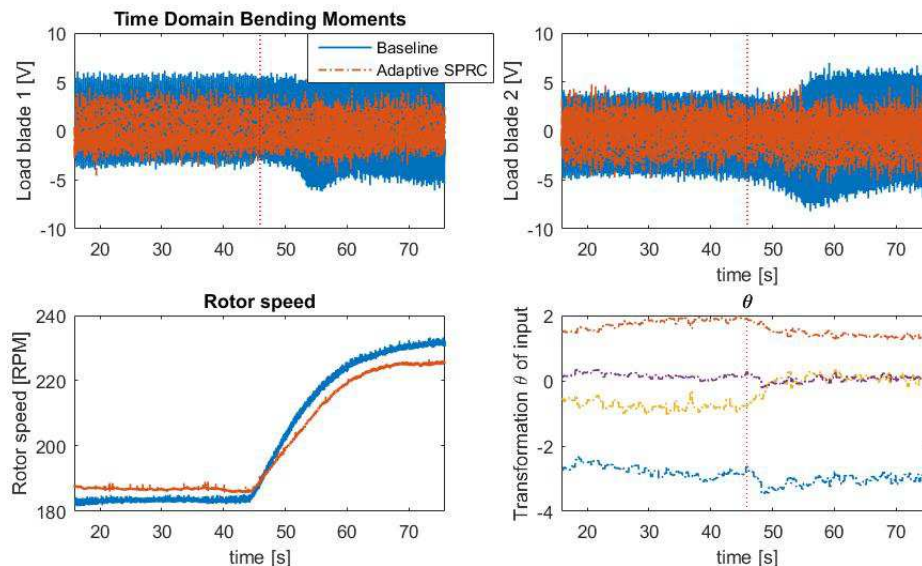


Figure 42, The time domain response for wind speed varying from 4 to 4.5 m/s, with a static 0° grid.

In Figure 42, we can see the blade loads, the rotor speed and  $\theta$  as the wind speed is increased. From the bottom right figure, we deduce that the identification process quickly converges again, but that the effect on the system is much smaller than when the pitch set-points were changed. At 4 m/s, SPRC reduces the blade load variance with 57.0% and 59.0% for blades 1 and 2 respectively. Due to the quick convergence, this is increased to 81.9% and 71.0% when the wind speed increases to 4.5 m/s.

Also in higher turbulent cases, SPRC is able to handle variations in operating conditions. An example is given below: here, the pitch set-points are changed once again from 2 to 10 degrees, this time for a wind speed of 4.2 m/s. The active grid is running the Gusts protocol, with an average centreline TI of 4.2%. Figure 43 shows the time domain response of this experiment.

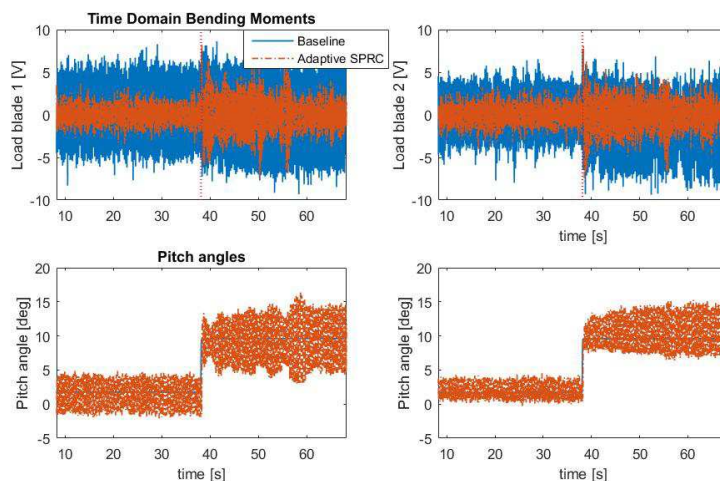
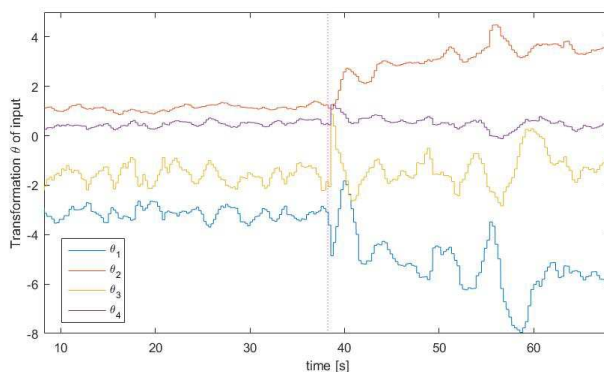


Figure 43, The time domain response for the pitch set-points varying from 2 to 10°, with the Gusts protocol.

Like in the low-TI experiment, we notice that the loads initially peak after a change is applied. Afterwards, the algorithm is again able to adapt to the new conditions, and the loads are once again reduced. With the pitch set-points at  $2^\circ$ , the load variance is reduced by 87.8% and 82.4% for blades 1 and 2 respectively. After the modification of pitch set-points, the performance is slightly less. However, with a load variance reduction of 75.8% (blade 1) and 68.5% (blade 2), it is still a considerable load reduction. From Figure 44, we see that it takes slightly longer for the parameters to converge in this higher-TI case, but in the end, the parameters converge nonetheless.



**Figure 44, Evolution of 4 of the  $\theta$ -variables over time. The vertical line represents the moment the reference of the pitch angles changes.**

Similar results are obtained for changing wind conditions under higher-TI circumstances. This is demonstrated with the static  $45^\circ$  protocol (TI: 3.7%). The wind velocity is changed from 4.5 m/s to 5 m/s, resulting in a change of rotor speed from approximately 210 rpm to 240 rpm. Like in the low-TI case, the system parameters change considerably less than when the pitch angle changes, as can be seen in the bottom right plot of Figure 45. Notice that as the loads increase due to the higher wind speed in the baseline case, this is barely the case with SPRC. As a result, the variance in blade loads is reduced even further after the wind speed increases: from 93.7% (blade 1) and 75.2% (blade 2) at 4.5 m/s to 92.7% and 86.1% at 5 m/s. Consequently, we can conclude that SPRC is able to adapt very well to changing operating conditions.

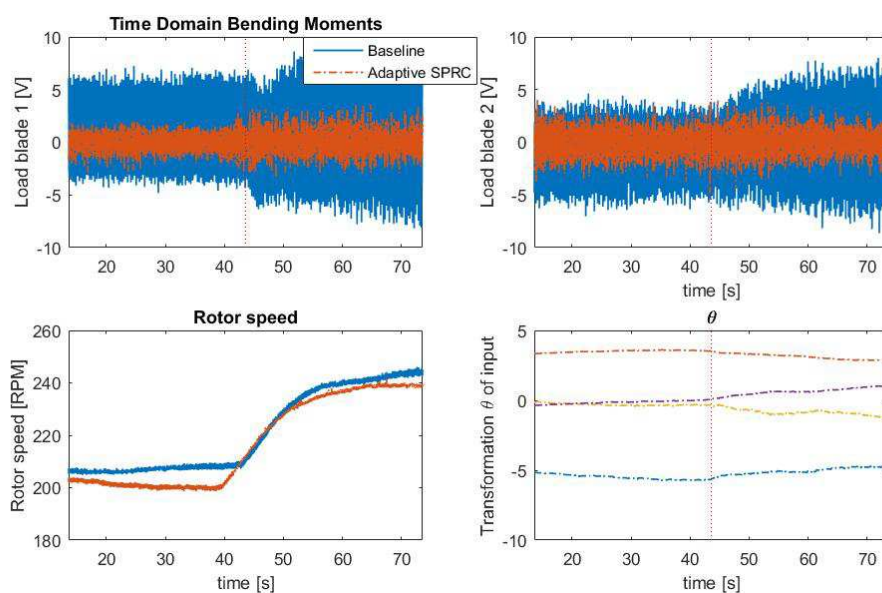


**Figure 45, The time domain response for wind speed changing from  $v = 4.5\text{ m/s}$  to  $v = 5\text{ m/s}$ , with the static  $45^\circ$  protocol.**

## 5.6 Conclusions

In this chapter, Subspace Predictive Repetitive Control (SPRC) has been tested under different wind conditions, and has been compared to the more traditional CIPC and LIPC strategies. Different wind velocities – between 4 and 5 m/s – resulting in rotor speeds varying approximately between 180 and 250 rpm have been evaluated, as well as different Turbulence Intensities (TI's). By means of the active grid in the open wind tunnel in Oldenburg, different reproducible scenario's with TI's ranging from 2.5% to 8.8% can be obtained. Both constant and varying operating conditions have been studied.

First, the influence of applying Individual Flap Control (IFC) on the 2P blade loads was investigated. The results have shown that with 2P Linear IFC in addition to 1P LIPC, it is possible to obtain slightly smaller blade load variances. An added advantage is that, in some cases, the pitch action can be reduced without affecting the performance of the controller. However, the control authority of the flaps is limited, and as a stand-alone controller has very little influence on the blade loads.

The biggest advantage of flap control is the bandwidth of the piezo-actuators, which is much higher than the bandwidth of the pitch motors. Therefore, IFC could be applied on higher frequency harmonics (3P and up), where pitch actuation would be useless. This was also shown with the Shear protocol, where the 3P loads were dominant: here, LIFC added significant load reductions to the pitch control.

For the low-TI case of a static  $0^\circ$  grid (centreline TI: 2.5%), SPRC exhibits superior behaviour compared to the traditional CIPC and LIPC algorithms. For all tested wind speeds, 1P SPRC performs similar to CIPC and better than LIPC, and guarantees significant load reductions compared to the baseline case of no control. SPRC for both the 1P and 2P loads performs even better, showing a reduction of load variance from 59% up to 95%. Root power spectral density plots also show that the 1P and 2P loads are substantially reduced by the SPRC algorithm, and in some cases completely removed. We can therefore conclude that SPRC is capable of reducing the blade loads in low-TI wind conditions.

At higher TI's, the performance of all the controllers declines slightly. In some cases, the load of one of the blades actually increases due to the control. This is a problem that occurs for both the traditional IPC methods and for the SPRC algorithm. However, in general, the variance of the loads is still reduced significantly by all the controllers, including SPRC. This shows especially at the highest wind speed that has been tested, 5 m/s, when the loads are the highest. Here, SPRC performs notably better than CIPC and LIPC, and is able to reduce the variance of loads with up to 94%. Like in the low-TI cases, frequency domain analysis again shows that the 1P and 2P peaks are considerably reduced, also in comparison with CIPC and LIPC.

A difficulty that does arise at higher TI's, is that the identification process sometimes takes longer to converge. Due to the turbulent wind conditions, it becomes harder to recognize whether load variations are caused by the inputs or by the wind. For the conditions tested here, the identification eventually converged and consequently, positive results were obtained for almost all cases. Hence, the conclusion can be drawn that for TI's up to 8.8%, SPRC is a viable control option to significantly reduce blade loadings.

Finally, the performance of SPRC in varying operating conditions has been evaluated. We have seen that for both a variation in pitch set-points and a change in wind velocity, the algorithm quickly converged to a new control input, whilst still reducing the blade loads. The effect of changing the pitch angles was observed to be larger than the change in wind speed, even though the differences in rotor speed were comparable in both cases. Also in higher TI cases, the performance of SPRC under varying conditions was retained. This is a very useful observation,

since this is a more realistic representation of the operating conditions of a full-scale wind turbine in the field. We consequently conclude that SPRC appears to be a viable option to be implemented on such turbines.

To summarize, the experiments that have been executed here have shown that with Subspace Predictive Repetitive Control it is possible to significantly reduce the 1P and 2P blade loads of a turbine by using individual pitch control action. SPRC shows promising results in both low and high TI conditions at different wind speeds varying from 4 to 5 m/s. It is furthermore able to adapt to changing operating conditions and consistently outperforms traditional IPC methods.

## 5.7 References

Chiuso, Alessandro. "The role of vector autoregressive modeling in predictor-based subspace identification." *Automatica* 43.6 (2007): 1034-1048.

Houtzager, I., J. W. van Wingerden, and M. Verhaegen. "Wind turbine load reduction by rejecting the periodic load disturbances." *Wind Energy* 16.2 (2013): 235-256.

Navalkar, S. T., J.W. van Wingerden, E. van Solingen, T. Oomen, E. Pasterkamp and G.A.M. van Kuik. "Subspace predictive repetitive control to mitigate periodic loads on large scale wind turbines." *Mechatronics* 24.8 (2014): 916-925.

Navalkar, Sachin Tejwant, Edwin van Solingen, and Jan-Willem van Wingerden. "Wind tunnel testing of subspace predictive repetitive control for variable pitch wind turbines." *IEEE Transactions on Control Systems Technology* 23.6 (2015): 2101-2116.

van der Veen, Gijs, Jan-Willem van Wingerden, and Michel Verhaegen. "Global identification of wind turbines using a Hammerstein identification method." *IEEE transactions on control systems technology* 21.4 (2013): 1471-1478.

Verhaegen, Michel, and Vincent Verdult. "Filtering and system identification: a least squares approach". Cambridge university press, 2007.

## PART 2

## 6 DESIGN OF A MORPHING WING [BRISTOL]

### 6.1 Introduction

The motivation of the research outlined in this chapter is to investigate the feasibility of using novel shape-adaptive structures on wind turbine blades for flow control purposes. Described in this chapter are the background, concept down-selection, design and testing activities carried out in the Bristol University. Subsequent tests are planned and to be conducted by the Denmark Technological University and summarised in the chapter 7.

### 6.2 Background

Shape-adaptive light-weight structures are promising candidates for the next-generation of high-lift devices for wind turbine blades [1-3]. These types of intelligently responsive structures, which remain conformal to the flow, are increasingly known as morphing structures. Containing a continuous structural surface and smooth geometric changes, morphing structures have significant potential to contribute to the drag reduction and noise decrease of wind turbine blades [4].

It is of utter importance in the synthesis of a realistic morphing concept to simultaneously satisfy the conflicting stiffness requirements of the light-weight, shape-adaptivity and load-carrying capability (see Fig. 1). For instance, a reliable and practical morphing trailing edge design for a wind turbine blade should be stiff enough to carry and transfer the aerodynamic loads while maintaining its structural integrity; the essential functionality of the control surface requires a low stiffness to enable the target geometric changes and more viable actuation methods. Numerous research activities have been carried out that are concerned with topics including concept development, material selection and characterisation, actuation method development and mechanical testing [5-9].

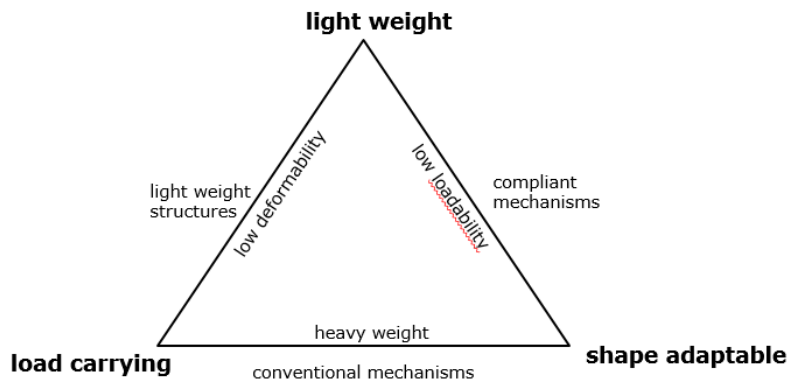


**Figure 1. Stiffness requirement triangle of a light-weight morphing structure [10]**

Though promising progress has been made in the application of morphing structures, there are still significant challenges left to increase the associated technology readiness level. This study of design, building and testing of a morphing trailing edge device for a wind turbine blade in the INN WIND project is considered as a forward step towards the aim of using morphing structures in future wind turbine blades of improved performance. The morphing trailing edge concept selected has been under continuous research development in the past eight years [11-15] including material selection, demonstrator building and testing of prototypes in wind tunnel.

Extending the previous morphing flap design, a novel concept based on a new turbine blade aerofoil, ECN-G7-18-60, was designed, built and mechanically tested at the University of Bristol. Section 6.3 describes the concept and detailed design of the morphing flap device. The

demonstrator manufacture and mechanical testing process are introduced in Section 6.4. The chapter finishes with conclusions and discussions of future work regarding the morphing flap design.

### 6.3 Morphing flap design

The wind turbine blade profile used in the morphing flap design was an aerofoil, ECN-G30-18-60, provided by the Denmark Technological University after a series of optimization design studies. As shown in Fig. 2, the new aerofoil has a relatively large thickness at the first 50% chord length and is asymmetric. The design specifications for the morphing trailing edge are: the morphing flap should extend to a 2m long turbine blade and account for 20% of the chord length for the 1 m long aerofoil, namely 200 mm in chord. Considering the actuation requirements, eight uniform morphing trailing edges that have a span of 249mm are selected and are actuated separated using linear motion servo-motors. The morphing flaps are installed on the rotating test rig for wind turbine blades [16], as shown in Fig. 3.

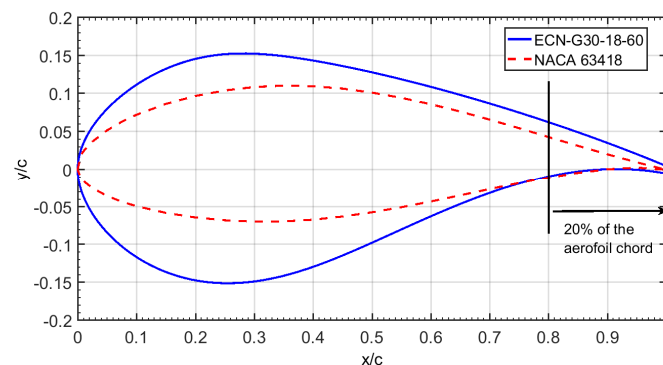


Figure 2. Aerofoil geometry of the ECN-G30-18-60



Figure 3. View of the turbine blade section with a morphing flap (Skins are removed for clarity purpose, Courtesy of DTU.)

#### The morphing flap concept

The morphing flap concept extends from previous research work by Daynes and Weaver [11,12], Lachenal and Weaver [13] and Ai and Weaver [14-15]. The morphing flap device consists of four components (See Fig. 4): 1) a carbon fibre reinforced plastic (CFRP) laminate upper skin on the suction side of the aerofoil; 2) a 3D printed honeycomb core of zero Poisson's ratio along the aerofoil chord providing the through-thickness support to the structure; 3) a silicon lower skin on the pressure side to provide a smooth aerodynamic surface and 4) a carbon fibre rod with a diameter of 2 mm as an actuation rod. The upper laminate skin is 0.4 mm thick and has a layup of [90/0/90] with 0° aligning with the aerofoil chord. The carbon fibre prepreg is Hexcel IM7/8550 and its properties are provided by the supplier [17]. Honeycomb cores have been widely used in many morphing structures for their highly anisotropic mechanical properties [9,18,19]. However,

in many one-dimensional morphing behaviours, zero Poisson's ratio honeycomb core receives growing interest due to its ability to provide large deformation in one direction without causing geometric changes in the perpendicular direction [20-22]. In the morphing trailing edge designed, built and discussed in this report, a zero Poisson's ration honeycomb core was selected and manufactured using Lase-Sintering technology by i.Materialise using polyamide material [23].

One carbon fibre reinforced plastic push/pull rod was selected as an actuation method for the morphing flap designed. The rod is attached to the honeycomb core through constraint holes on the core's cell walls and glued to the trailing edge using epoxy at one end. These constraints allow the rod to move in/out along the bottom surface of the honeycomb core without any movement along the through-thickness direction. The rod is sufficiently stiff to carry and transfer the actuation load to the core and has the flexibility to bend along with the core's bottom surface. After parametric studies, a diameter of 2 mm carbon rod with a longitudinal Young's modulus of 150 GPa and lateral Young's modulus of 10 GPa was chosen.

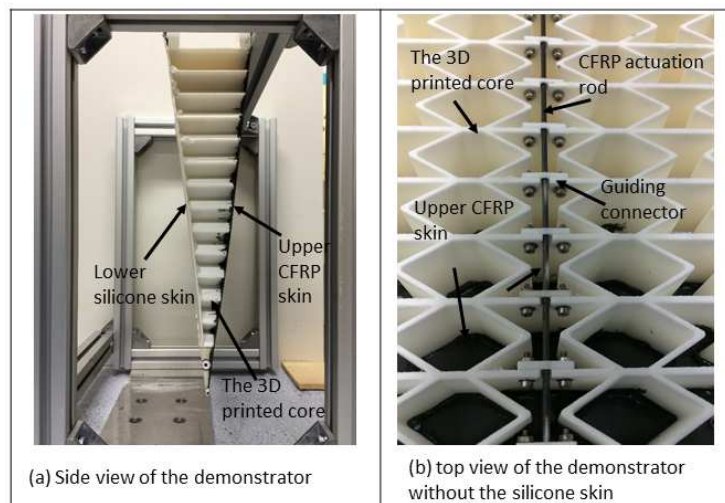


**Figure 4. The morphing flap device using 3D printed honeycomb core [13,14]**

### Finite element analysis

The finite element method (FEM) was used in the detail design phase to quantify the structural responses of the morphing flap designed under actuation forces and aerodynamic pressure loads. The main objective was to obtain the trailing edge displacement-actuation load curve for the actuator selection purposes. The FEM model was prepared using commercial software, ABAQUS.

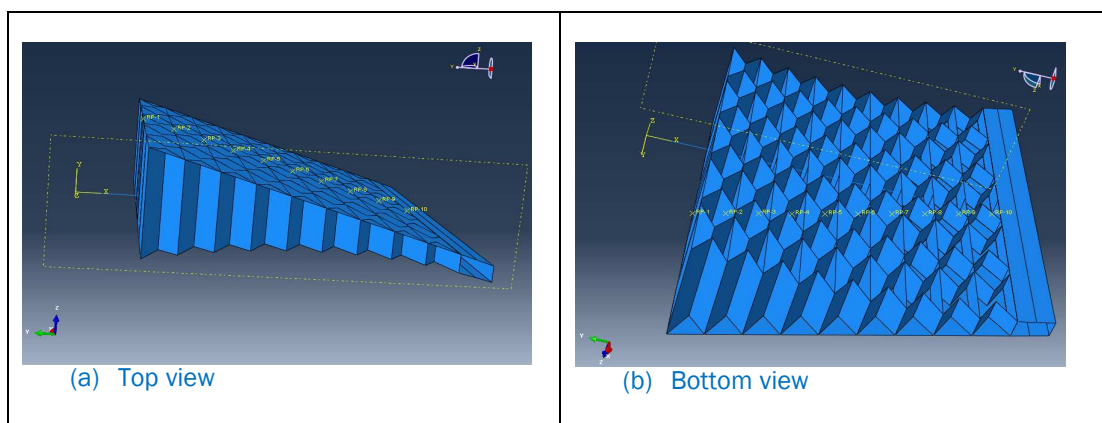


**Figure 5. FEM model of the morphing flap design (bottom skin removed for clarity purposes)**

The morphing flap model shown in Fig. 5 has a chord of 200 mm and a span of 249 mm. Skins and honeycomb core are modelled using S4R shell elements and the CFRP actuation rod is modelled using B31 beam elements. The CFRP actuation rod is constrained to the bottom surface at the mid-span using coupling which prevents the rod from moving through the core thickness direction without affecting its freedom to move in/out of the core. Clamped boundary conditions are applied to the rear spar of the morphing flap. Displacement boundary conditions are applied at the free end of the CFRP actuation rod while the other end of the rod is tied to the flap trailing edge. Reaction forces at the free end of the rod are measured as the required actuation forces for the given flap trailing edge deflection.

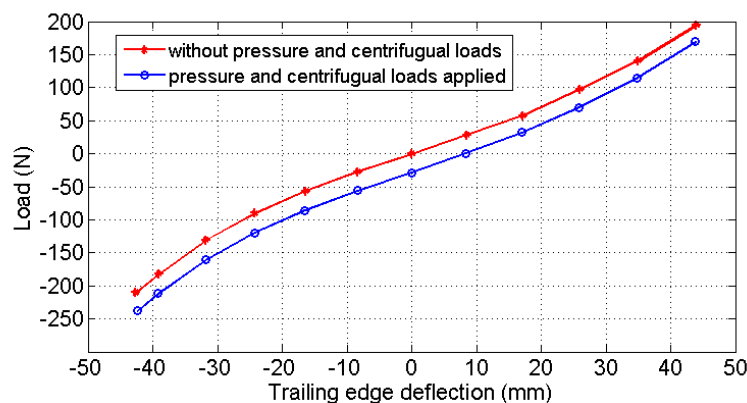


**Figure 6 The actuation force requirements of the morphing flap**

In order to account for the testing environment of the rotating rig [16], the centrifugal forces and aerodynamic pressure loads on the flap are considered in the current FEM model. However, due to the morphing flap's nature of being light-weight, the centrifugal forces were found to affect the actuation force requirements to an insignificant level. At the same time, it is worth noting in Fig. 6 that the pressure loads on the morphing flap can significantly change the actuation force (up to 15%) depending on whether the flap morphs towards the suction side or pressure side. With the preliminary FEM analyses of the proposed flap design, it is found that for a flap with selected size and materials, an actuation force range of -250 N to 200 N is necessary, which is on a comparable level with the findings in Refs [11-15].

#### 6.4 Building and testing of the demonstrator

Following the preliminary FEM analysis, a prototype was substantiated in the structural lab of ACCIS for mechanical testing purposes. Fig. 7 presents the production process of the demonstrator, which is then adopted for the manufacturing of all ten morphing flaps supplied to the DTU testing team. A 3D printed honeycomb core using laser sintering technique was supplied by I.materialise. Ltd. Joining methods/parts of the morphing flap to the turbine wing structure are as proposed by DTU and manufactured as an integrated rear spar on the 3D printed honeycomb core. Hexcel IM7/8552 carbon/epoxy prepreg was used in the suction side laminate skin with a layup of [90/0/90] with 0 deg aligning with the aerofoil chord-direction. The laminate skin thickness is 0.4 mm. The pressure side has a pre-tensioned silicone skin which has a thickness of 1.5 mm. Pre-stressing technique was used here to mitigate the buckling phenomenon in the lower skin when the flap has a large deformation towards the pressure side.

It is worth noting that in the design phases, two different ways of installing the CFRP actuation rod were proposed and tested. In the first method, the honeycomb core used in the morphing flap is split into two components: the rigid tip and the flexible core section. The tip and the core section can be joined mechanically for an easy and quick replacement. The actuation rod is connected to the flap tip (3D printed plastic part or CNC machined Aluminium part) using mechanical linkages

including a threaded rod head and an inserted coil in the tip. However, in the trial case carried out at the University of Bristol, a rigid tip section was produced using ABS plastic with a Stratasys rapid prototyping machine. A helical coil was then inserted into the tip and the CFRP actuation rod was then installed with a corresponding threaded head. Such a design allows for rapid interchange and replacement of broken components, which is economically advantageous. However, due to the brittle nature of the ABS plastics used for the tip section, the helical coil slipped out of the tip section during a fatigue test. It is envisaged that changing the ABS plastics to aluminium would improve the quality and reliability of the proposed design. The second method was then proposed and tested due to time and budgetary considerations. In the chosen design (see Fig. 7), an integrated honeycomb core was selected and the CFRP rod was then connected to the tip section using epoxy glue before skins were added. This joining method provided a robust and reliable performance for the demonstrators, but limits the possibility of replacement of broken components. However, at the early stage of the testing plan, it serves as a better option compared to the first method.

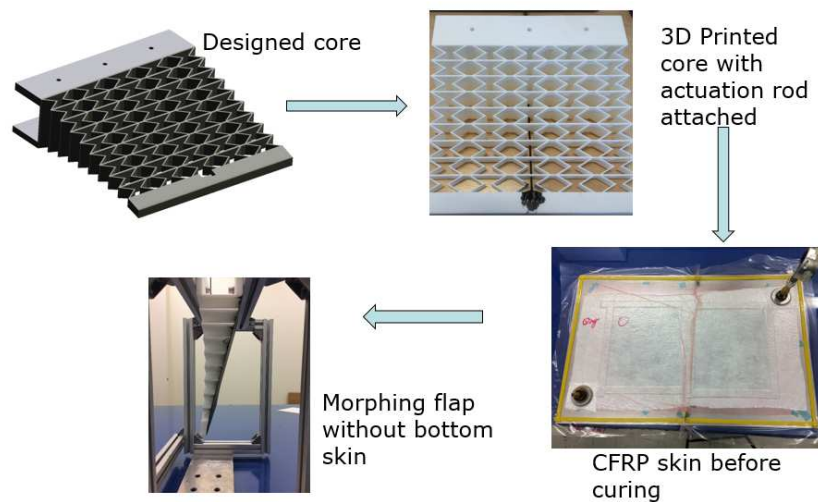


**Figure 7** Manufacturing process of the morphing flap

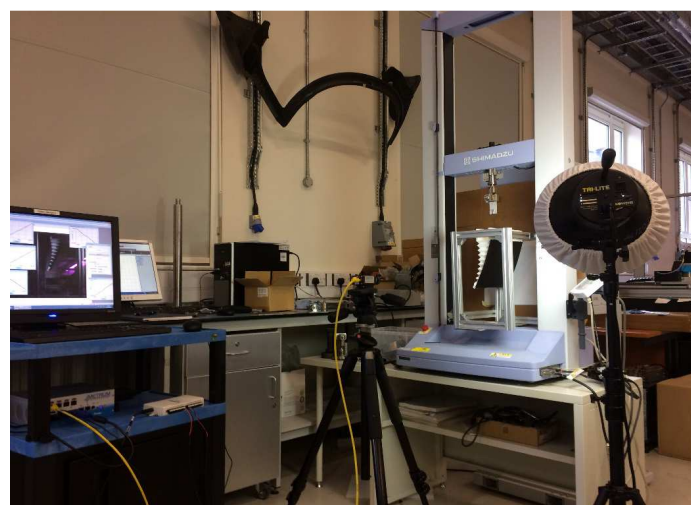


**Figure 8.** Mechanical testing set-up of the morphing flap demonstrator

The morphing trailing edge demonstrator is subsequently tested for actuation requirements and particularly for the morphing shape. The static mechanical test set-up is shown in Fig. 8 and a test

rig was prepared to support the demonstrator and the morphing trailing edge was fixed to the top spars of the rig for the clamped boundary condition. The CFRP actuation rod was connected to the 1 kN load cell of a Schimadzu universal/tensile testing machine. In the tests, stroke control is used which applies displacements to the actuation rod and the corresponding reaction load is monitored. An Imetrum video gauge system (see Fig. 8) is used to monitor the real-time deformed shape of the morphing trailing edge simultaneously with the load/stroke control system. Sixteen targets were selected along the edge of the top skin from the root to the trailing edge. The video was recorded together with the static mechanical tests and processed to calculate the transverse displacement of the selected monitoring targets. After a comprehensive parametric study with testing under different load types, *i.e.* single, cyclic and increasing test speeds, the morphing trailing edge deformation found to be linearly correlated to the stroke applied. This phenomenon was also observed in previous studies [11,12]. Different test speeds have been selected and converted into deformation angle speeds. Fig. 9 presents measured actuation force requirements of the morphing flap demonstrator at various stroke speeds. Results show that the FEM model provides accurate prediction of the actuation force relative to the experimental measurements. Testing speed was not found to significantly affect the actuation force at this static testing bench.

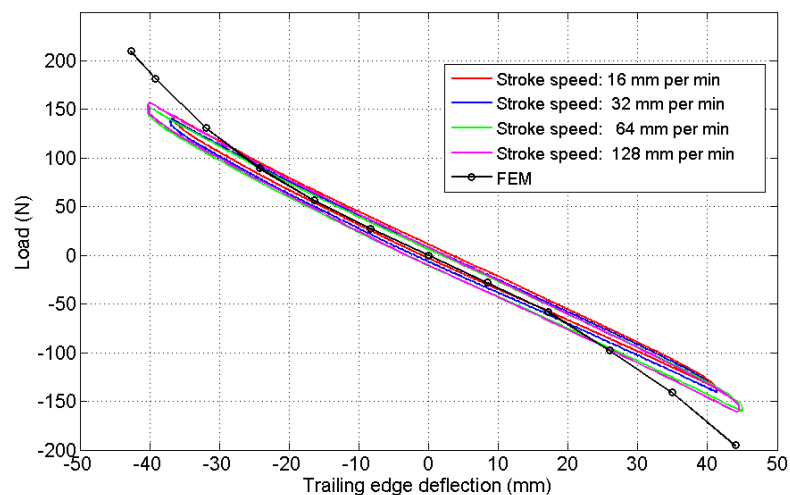


**Figure 9. The measured actuation force requirements of the designed morphing flap**

## 6.5 Conclusion

A novel morphing flap device has been successfully designed, prototyped and tested at the initial phase of the efforts to install such control surfaces on a rotating test rig. By extending previous research work, the morphing flap designed can provide large trailing edge deflections to achieve flow control whilst requiring reasonably low actuation force requirements. Finite element models were conducted with commercial package, ABAQUS, to provide a robust, reliable and detailed design. A demonstrator was built and tested before manufacturing all ten flaps requested by the project partner. Static mechanical testing was carried out to measure the actuation forces and monitor the structural responses of the morphing flap. Good agreement was observed between the FEM predictions and the experimental measurements.

Based on the promising results obtained in the design and analysis phases, all morphing flaps were manufactured and sent to the DTU team for further testing activities, which is described in Chapter 7 of this report.

## 6.6 References

1. Barlas, T. K., van Kuik, G. A. M., *Review of state of the art in smart rotor control research for wind turbines*. Progress in Aerospace Sciences, 2010. **46**(1): p. 1-27.
2. Johnson, S.J., Baker, J.P., van Dam, C.P., Berg, D. *An overview of active load control techniques for wind turbines with an emphasis on microtabs*. Wind Energy, 2009. **13**:239-253. DOI: 10.1002/we.356.
3. Lachenal, X., Daynes, S., Weaver, P. *Review of morphing concepts and materials for wind turbine blade applications*. Wind Energy, 2013. **16**:283-307. DOI: 10.1002/we.531.
4. Dobrzynski, W. *Almost 40 years of airframe noise research: what did we achieve?*. Journal of Aircraft, 2010. **47**(2):353-367. DOI: 10.2514/1.44457.
5. Chopra, I. *Review of state of art of smart structures and integrated systems*. AIAA Journal, 2002. **40**:2145-2187. DOI: 10.2514/2.1561.
6. Daynes, S., Nall, S. J., Weaver, P. M., Potter, K. D., Margaris, P., Mellor, P. H., *Bistable composite flap for an airfoil*. Journal of Aircraft, 2010. **47**(1): p. 334-338.
7. Daynes, S., Weaver, P. M., *A wind turbine blade having a flap*. Danish Patent Office, 2011. 70059.
8. Gandhi, F., Anusonti-Inthra, P., *Skin design studies for variable camber morphing airfoils*. Smart Materials and Structures, 2008. **17**(1): p. 015025.
9. Thill, C., Etches, J., Bond, I., Potter, K., Weaver, P., *Morphing skins*. The Aeronautical Journal, 2008. **112**(1129): p. 117-139.
10. Campanile, L. F., *Adaptive structures: engineering applications*. 2007, Chichester, UK: John Wiley & Sons Ltd. Chapter 4; Lightweight shape-adaptable airfoils: a new challenge for an old dream, p. 97.
11. Daynes, S., Weaver, P.M. *A morphing trailing edge device for a wind turbine*. Journal of Intelligent Material Systems and Structures, 2012. **23**(6):691-701. DOI: 10.1177/1045389X12438622.
12. Daynes, S., Weaver, P.M. *Design and testing of a deformable wind turbine blade control surface*. Smart Materials and Structures, 2012. **21**:105019(10p). DOI:10.1088/0964-1726/21/10/105019.
13. Lachenal, X., Weaver, P. *New morphing blade section designs and structural solutions for smart blades*. INN WIND.EU report, Deliverables 2.23, Chapter 3, pp: 79-96.
14. Ai, Q., Azarpeyvand, M., Lachenal, X., Weaver, P.M. *Aerodynamic and aeroacoustic performance of airfoils with morphing structures*. Wind Energy, 2015. **19**(7):1325-1339. DOI: 10.1002/we.1900.
15. Ai, Q., Weaver, P.M., Azarpeyvand, M. *Design and mechanical testing of a variable stiffness morphing trailing edge flap*. Journal of Intelligent Material Systems and Structures. Accepted on June 2017.
16. Barlas, T.K., Madsen, H.A., Andersen, T.L. *Design and simulation of the rotating test rig in the INDUFLAP project*. 2014. Department of Wind Energy, Denmark Technological University, E Report 2015.
17. Hexcel, Hexcel Corporation, Stamford, CT, *HexPly® 8552 180 °C Curing Epoxy Matrix Product Data*. 2008. Publication FTA 072c: p. 1-6.
18. Bartley-Cho, J. D., Wang, D. P., Martin, C. A., Kudva, J. N., West, M. N., *Development of high-rate, adaptive trailing edge control surface for the smart wing phase 2 wind tunnel model*. Journal of Intelligent Material Systems and Structures, 2004. **15**(4): p. 279-291.
19. Kudva, J. N., *Overview of the DARPA smart wing project*. Journal of Intelligent Material Systems and Structures, 2004. **15**(4): p. 261-267.
20. Olympio, KR., Gandhi, F. *Zero Poisson's ratio cellular honeycombs for flex skins undergoing one-dimensional morphing*. Journal of Intelligent Material Systems and Structures, 2010. **21**:1737-1753. DOI: 10.1177/1045389X09355664.

21. Bubert, EA., Woods. B KS., Lee, K., Kothera, CS., Wereley, NM. *Design and fabrication of a passive 1D morphing aircraft skin*. Journal of Intelligent Material Systems and Structures, 2010. **20**:1699-1717. DOI:10.1177/1045389X10378777.
22. Olympio, K. R., Gandhi, F., *Zero-v cellular honeycomb flexible skins for one-dimensional wing morphing*. 48th AIAA/ASME/ASCE/AHS/ASC Structures, Structural Dynamics and Materials Conference. 2007. Waikiki, HI.  
<https://i.materialise.com/>. [Last access on 03/07/2017]

## 7 ROTATING RIG EXPERIMENTS AND ANALYSIS [DTU+NTUA]

### 7.1 Introduction

Testing the performance and robustness of the smart blade technology has been an important part of the INNWIND project. Wind tunnel testing of present flap systems has been already performed in a variety of campaigns and has verified the actuation concepts and aerodynamic performance in a wind tunnel environment. However, there is big step from wind tunnel testing on a stationary blade section to full scale turbine application and therefore a so-called rotating test rig has been developed at DTU and has been already utilized in testing active flap systems[1][2][3][4][5].

The main objective is to conduct tests of the developed morphing trailing edge flap system under realistic inflow conditions in the rotating test rig and in addition benchmark the capability of ranging fidelity simulation tool in accurately simulating the testing setup.

### 7.2 Description of the rotating rig

In order to fill in the gap between full-scale MW experiments and wind tunnel tests the rotating rig situated at the test field at Risø campus of DTU, plays an important role as a test bed for aerodynamic and aeroservoelastic experiments. The rotor on the former 100 KW Tellus turbine is replaced by an elastic beam. On the outer part of the beam different elements to be tested can be mounted for characterization of aerofoil characteristics based on pressure measurements and testing of pitch and flap control systems. Besides the main boom, a counter weight is mounted to balance the beam and the aerofoil section. During the measurements the turbine is driven by a motor with a frequency converter in order to control the rotational speed. The idea behind the test rig is that the testing should be as close as possible to the rotating test environment on the real turbine and have the same unsteady inflow conditions and a size of the flap close to a full scale application. This has been obtained by manufacturing a blade section with a 1m chord and 2m span and mounting it on a 10m long boom on the rotating rig (Figure 46, Figure 47). A comprehensive instrumentation of the test rig has been carried out and includes sensors for the blade surface pressure distribution on the mid span position, which enable a continuous monitoring of the instantaneous sectional aerodynamic loading on blade, and thus also allow measuring the exact response of flap actuation. Another part of the instrumentation comprises two five-hole pitot tubes of the leading edge of the blade section for measuring the inflow to the blade. Finally, metrological data such as wind speed and wind direction is measured in three heights in a nearby met mast.



**Figure 46** The rotating rig with the mounted morphing wing.

Main advantages of the setup include:

- easy access to the test rig for researchers and a size where installation of equipment does not require a large crane
- very suitable to perform aeroelastic experiments and test prototypes of inflow sensors, flaps, aerodynamic devices
- the measurement of aerodynamic characteristics in free wind could be an important supplement to wind tunnel measurements on aerofoil sections
- proof of concept of the flap system in atmospheric conditions and in a realistic scale
- scale of flap system and blade section close to real scale

In this measurement campaign, signals from various sensors on the rotating rig and the met mast are recorded. Data channels involve sensor signals related to:

- operation of rotating rig (rotor speed, rotor azimuth, yaw angle)
- inflow (wind speed, wind direction)
- flap operation (flap angle)
- blade section aerodynamics (pressure distribution from 57 chordwise and 16 spanwise pressure taps, 2 Pitot tubes inflow angle and velocity)
- boom and blade section structural response (flapwise and edgewise strains at the root and at the wing, flapwise and edgewise acceleration at the wing)

In total, 130 data channels are recorded. The sensor signals in use have been converted from a raw (voltage) signal into a physical quantity already within the acquisition software processing.



Figure 47 The morphing wing mounted on the rotating rig boom before installation.

### 7.3 Development of the blade section

For testing of the Bristol University morphing flap design, described earlier, a wind turbine blade profile, ECN-G30-18-60 designed by ECN in the INN WIND project, was realized.

Overall concept consists of a spanwise 2.0 meter long section, with a constant cross section, having a chord of 1.0 meter covered with composite side pods in each end giving a total length of 3.25 meter. The section has an inner aluminum skeleton covered with shells of composite material and hatches for easy access to the instrumentation inside blade. The section was dimensioned for test up to 30rpm.

The actuation of the morphing flap and the adapter for mounting of the flap was designed in cooperation with Bristol University. The cross section of the flap mounted by adapter to the blade section is shown in Figure 48.

Composite parts were manufactured by vacuum infusion (Figure 49), trimmed and mounted on inner aluminum skeleton with glue.

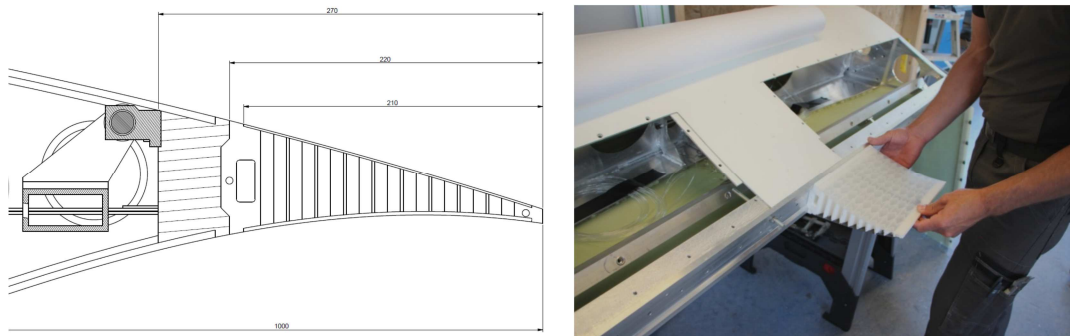


Figure 48 Cross section of morphing flap mounted on blade section and blade section with open hatches.

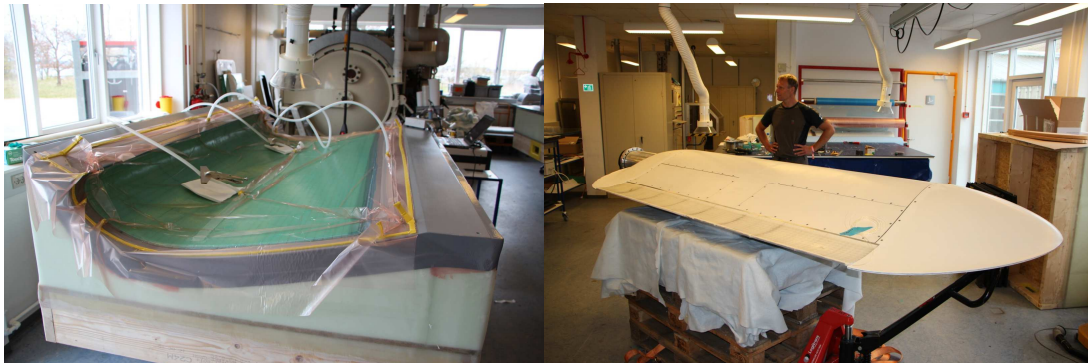


Figure 49 Vacuum infusion of composite shell and blade section with mounted morphing flap parts.

The aerofoil section of the morphing wing is the ECN-G7-30 designed by ECN in the INNWIND project. The blade section is instrumented with 57 pressure taps distributed in the chord-wise direction in the mid-section of the wing (Figure 50). Two of the taps are installed inside the trailing edge of the flap. Furthermore, 16 pressure taps are distributed in the span of the wing at the 27% of the chord length from the leading edge. Considering the actuation requirements, the eight uniform morphing trailing edges developed at the University of Bristol, which have a span of 249mm each, are actuated in a connected motion using a linear motion servo-motor.

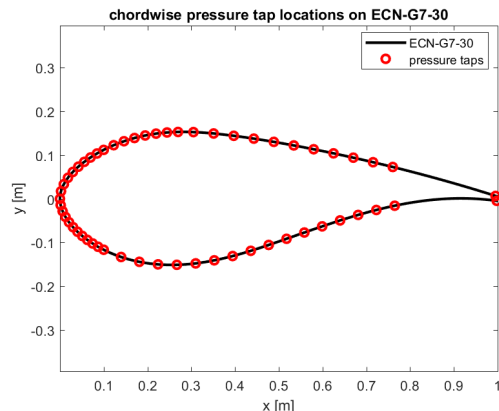


Figure 50 Mounting of pressure taps in morphing flap and pressure tap locations on the blade section (chord-wise).

## 7.4 Test cases

It is important to observe the performance of the blade section and active flap at a range of angles of attack and Reynolds numbers representative of the scenarios in which the active flap could eventually operate on a MW-scale turbine. The angle of attack range is roughly +/-15 degrees under a normal production scenario. The angle of attack is determined by wind speed, rotor speed, and boom pitch. The Reynolds number is determined by wind speed and rotor speed and should be at least 1 million, and preferably 3 - 10 million. Due to vibration restrictions, the rig can only operate up to roughly 20rpm, while the boom pitch is limited to +15/-15 degrees about zero. Although the flap is capable of a maximum range of  $\pm 10$ deg, the flap angle range in all tests has been limited to  $\pm 5$ deg in order to limit any risk of placing extreme stress on the actuator. In all cases, unless specified otherwise, the rotor is placed at the mean wind direction. The test matrix is defined based on the capabilities of the rig, with resulting angles of attack and Reynolds numbers suitable enough to produce useful results, with the target to test the average aerodynamic

performance of the morphing wing, its transient response, and its load control capability. The following cases are tested in this campaign:

- Flap steps  
Steps of the flap angle to its maximum angle range around the neutral position, in order to derive average aerodynamic polars in atmospheric conditions, and estimate the flap effectiveness.
- Periodic feed-forward flap control  
Azimuth-based flap angle variation to counteract periodic loading due to yaw misalignment and downwind operation.
- Inflow feed-forward flap control  
Proportional flap command based on filtered Pitot tube inflow angle.

The full test matrix is shown in Table 15.

Test cases					
case	rotor speed [rpm]	pitch angle [deg]	flap	runs	duration [min]
1	20	0	no	2	5
2	20	0	steps	2	5
3	20	5	no	2	5
4	20	5	steps	2	5
5	20	10	no	2	5
6	20	10	steps	2	5
7	20	15	no	2	5
8	20	15	steps	2	5
9	20	-1	no	2	5
10	20	-15	steps	2	5
11	20	-10	no	2	5
12	20	-10	steps	2	5
13	20	-5	no	2	5
14	20	-5	steps	2	5
15	20	-5	azimuth control - yaw	8	5
16	20	-5	azimuth control - downwind	4	5
17	20	-5	inflow control	2	5

**Table 15 Test cases in the rotating rig experiments.**

In the first type of cases (1-14), 5min tests are conducted with the flap angle fixed at zero, as well as with step changes in flap angle every 10 seconds for a range of pitch settings. This is sufficient to measure both the transient and steady state response of the aerodynamics to the changing flap angles. For the case of square flap input signals, the derived aerodynamic data is averaged over smaller periods during the flap activation cycle. In all cases a square input of 0.025 Hz is used, so the flap activation cycle is divided into 4 sections of 10s each. The positive flap region is defined as the 1<sup>st</sup> section, the neutral flap region as the 2<sup>nd</sup> section, and the negative flap region is defined as the 3<sup>rd</sup> section. This is shown in Figure 51, where the positive, neutral and negative flap regions are shown in red, black and green, respectively.

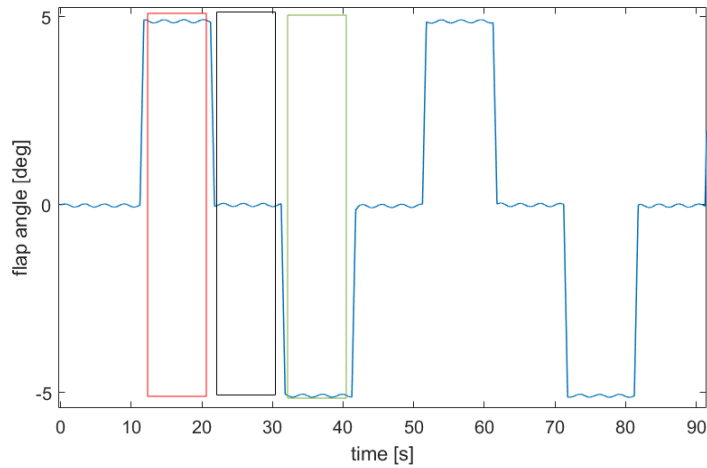


**Figure 51** Flap step signal indicating time periods of flap states for data binning.

The second type of cases (15-16) concerns prescribed azimuth-based flap control, which comprise 5min time series with the flap activated once per revolution towards its maximum positive or negative angles in order to counteract 1P periodic loading fluctuations. The flap signal is a 0.33Hz harmonic signal (1/rev) with a tuned phase, which comprises an approximate half-sinusoidal signal from zero flap angle to either maximum positive or negative flap deflection (Figure 53). All normal upwind configuration cases are conducted at a pitch setpoint of -5 deg., which corresponds, to an average angle of attack close to the design point. The flap is scheduled to be active for two revolutions, followed by two revolution of no flap activation. In order to test this periodic controller, cases where the rotor is placed at an average of 30deg yaw misalignment, and at a downwind configuration are measured. A photo of the flap activation seen from the connection of the wing to the boom during the tests is shown in Figure 122.



**Figure 122** Photo of wing with deflected flap during operation.

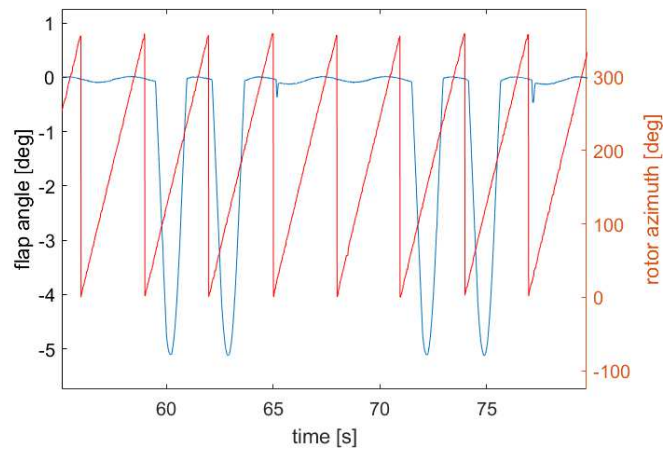


**Figure 53 Flap signal as a function of the rotor azimuth (activation at blade top position in this case).**

The third type of cases (17) concerns inflow-based feed-forward flap control, which comprise 5min with the flap activated with a proportional gain on the band-pass filtered inflow angle from the outboard Pitot tube. The inflow angle signal is filtered between 0.04Hz-1Hz, in order to remove the static gain and react to frequencies up to 3P. The proportional gain is tuned in order to achieve maximum flap angle range for the maximum variation of the inflow.

## 7.5 Test results

The integrated aerodynamic forces at the wing section are calculated from the pressure tap measurements on the aerofoil, also utilizing the Pitot tube pressure measurements. In one part of the post-processing the local flow angle and local flow velocity are derived from the Pitot tube pressure differences. In the other part of the post-processing, the chordwise pressure tap data is utilized and corrected in order to derive the integrated aerodynamic forces and coefficients.

For the first type of cases (flap steps), the pressure data is post-processed and  $C_L$  values are sorted based on the angle of attack and flap angle average values. The binned data is shown and compared to Ellipsys 2D CFD data in Figure 124. It is seen that the overall aerodynamic impact of the flap is captured well, with an average estimated variations in the linear region of  $\Delta C_L = +0.2$  and  $\Delta C_L = -0.25$  for the +5deg and -5deg flap angle respectively. The CFD data provide an estimated average variation of  $\Delta C_L = +0.25$  and  $\Delta C_L = -0.3$ . It should be noted that the calculated angle of attack and dynamic pressure from the Pitot tube signals does not account for 3D effects, and includes some measurement uncertainty related to the Pitot tube signals, thus the absolute values of the polars are seen to have an angle of attack offset and reduced slope compared to 2D simulations. Further analysis is needed to establish an accurate translation of aerodynamic measurements on the rotating rig to 2D aerodynamic polars from wind tunnel tests and CFD simulations.

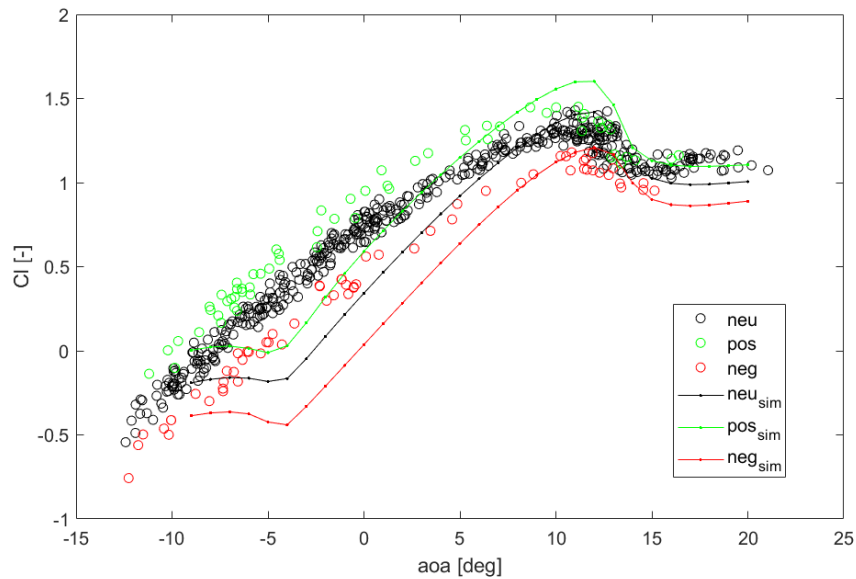


**Figure 124** Binned measured  $C_L$  data for samples without flap (neu), +5deg flap (pos) and -5deg flap (neg) as a function of inflow angle. Comparison with 2D CFD data.

The pressure coefficient data ( $C_p$ ) is also binned around the design angle of attack of 8deg for the baseline and flap angle range samples. The binned data is shown and compared to Ellipsys 2D CFD data in Figure 125. It is seen that the overall  $C_p$  curve shape is captured well, along with the effect of the flap deflections. Again, it should be noted that the uncertainty of the inflow angle and lack of 3D corrections is included in the results.

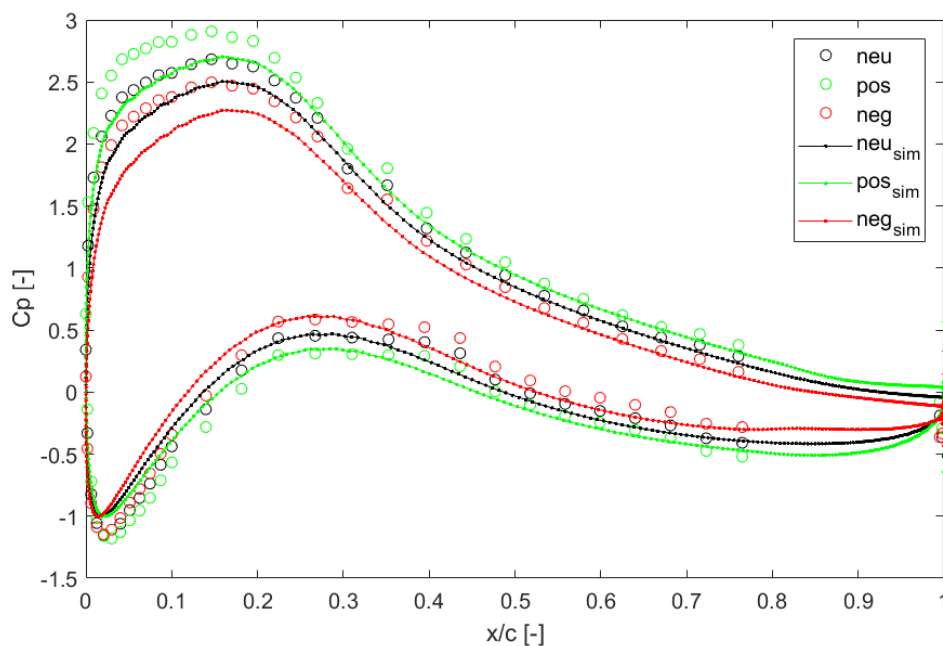


**Figure 125** Binned measured  $C_p$  data at 8deg inflow angle for samples without flap (neu), +5deg flap (pos) and -5deg flap (neg) as a function of inflow angle. Comparison with 2D CFD data.

For the second type of cases (azimuth flap control), the data from the flapwise strain sensor is post-processed and sorted for every sample consisting of two revolutions without control and two revolutions with the flap controller active. The statistics of every consecutive samples are then compared. Firstly, the rotor is placed at a yaw misalignment angle of 30deg and the pitch angle is set to -5deg, corresponding to an average inflow angle close to the design angle of attack. The time series of the flapwise moment at the connection of the wing to the boom is shown in Figure 126, together with the flap angle which is activated for two revolutions followed by two revolutions without activation. The flap angle is driven to the maximum negative angle of -5deg when the blade is at its top position, targeting the alleviation of peak loading. The comparison of the standard deviation of the flapwise moment for every consecutive sample of no activation and azimuth-based flap activation is shown in Figure 127. Although, as expected, the prescribed azimuth-based flap activation is not robust, it results in an average reduction of the standard deviation of the flapwise moment of 12%.

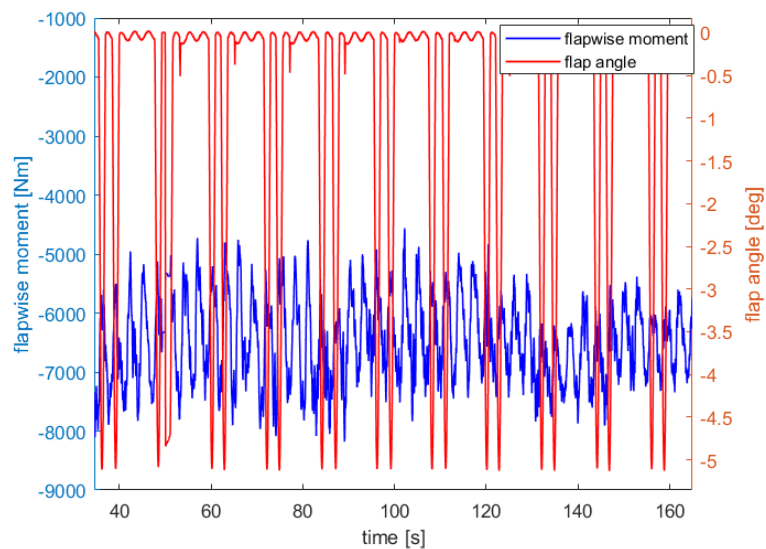


Figure 126 Time series of flapwise moment and azimuth-based flap activation (yaw misalignment case).

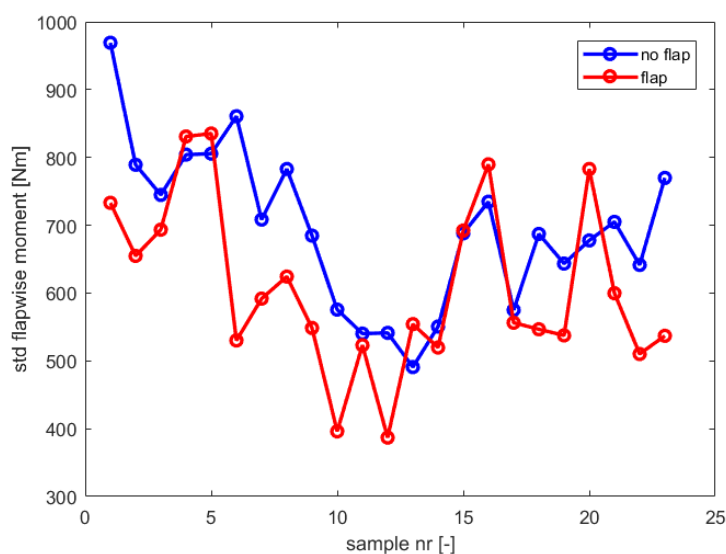


Figure 127 Comparison of standard deviation of flapwise moment with azimuth-based flap activation (yaw misalignment case).

In the following case variation, the rotor is placed at a downwind configuration in order to introduce increased tower shadow effects and the pitch angle is set to +5deg, corresponding to an average inflow angle close to the design angle of attack. The time series of the flapwise moment at the connection of the wing to the boom is shown in Figure 128, together with the flap angle which is activated for two revolutions followed by two revolutions without activation. The flap angle is driven to the maximum positive angle of +5deg when the blade is at its lowest position during the tower passage, targeting the alleviation of negative peak loading. The comparison of the standard deviation of the flapwise moment for every consecutive sample of no activation and azimuth-based flap activation is shown in Figure 129. Although, as expected, the prescribed azimuth-based flap activation is not robust, it results in an average reduction of the standard deviation of the flapwise moment of 5%.

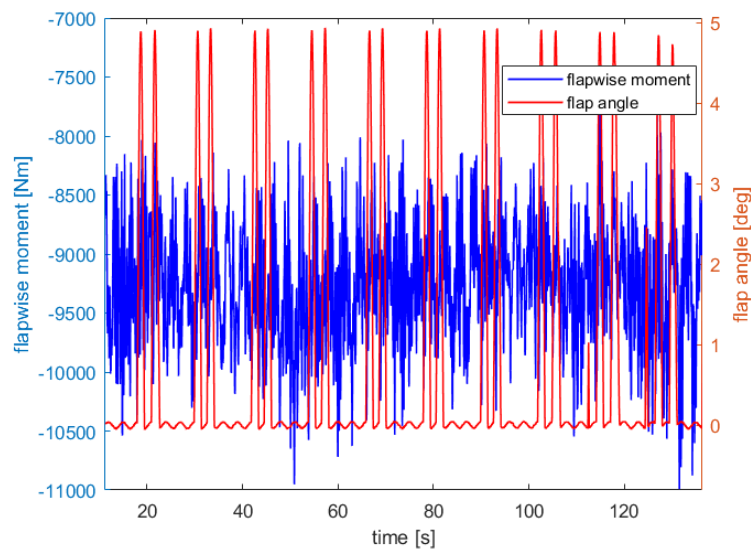


Figure 128 Time series of flapwise moment and azimuth-based flap activation (downwind case).

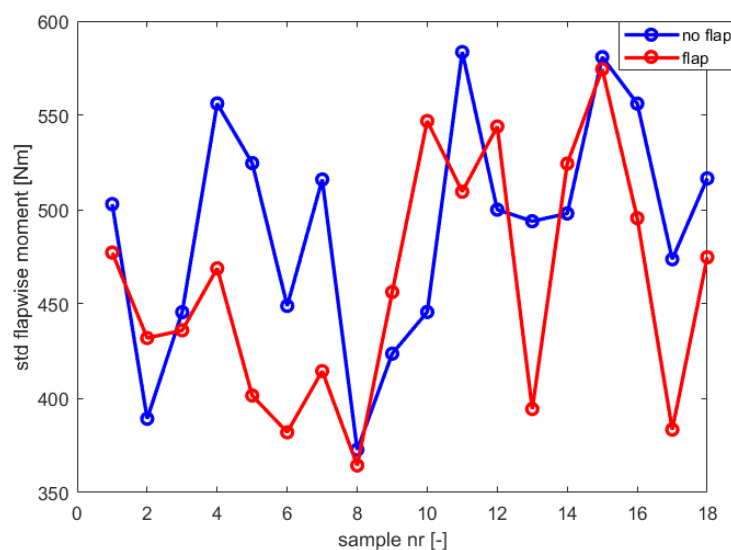


Figure 129 Comparison of standard deviation of flapwise moment with azimuth-based flap activation (downwind case).

For the third type of cases (inflow flap control), the data from the flapwise strain sensor is post-processed and sorted for every sample consisting of 10s without control and 10s with the feed-forward inflow-based flap controller active. The statistics of every consecutive samples are then compared. The time series of the flapwise moment at the connection of the wing to the boom is shown in Figure 130, together with the flap angle which is activated for 10s followed by 10s without activation. The flap angle in this case reacts to fluctuations of the inflow angle within the band-pass filtered range of frequencies up to 3P. The comparison of the standard deviation of the flapwise moment for every consecutive sample of no activation and azimuth-based flap activation is shown in Figure 131. The flap controller results in an average reduction of the standard deviation of the flapwise moment of 11%.

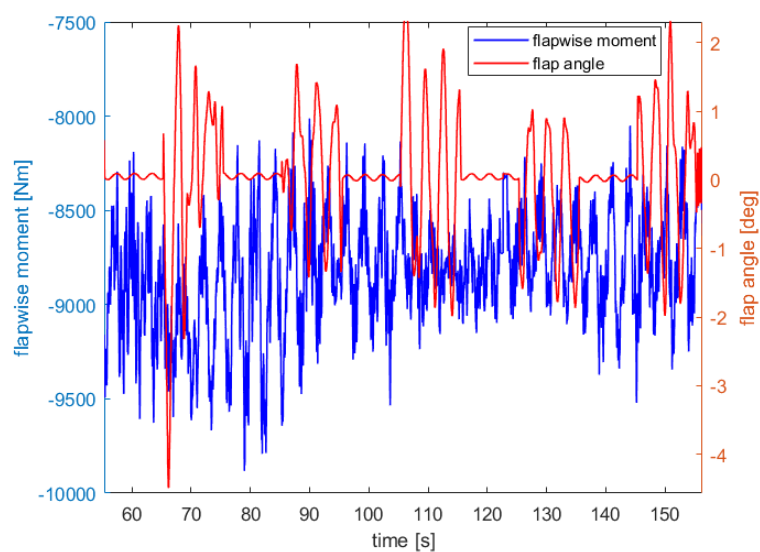


Figure 130 Time series of flapwise moment and inflow-based flap activation.

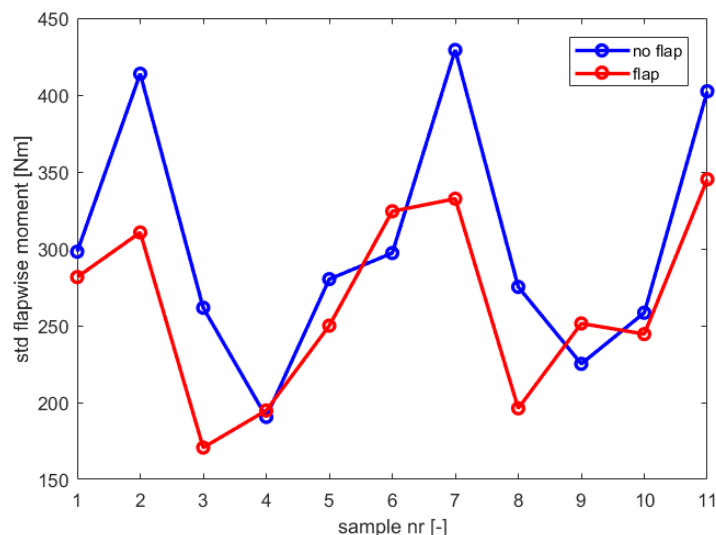


Figure 131 Comparison of standard deviation of flapwise moment with inflow-based flap activation.

## 7.6 Rotating rig simulations cases

In order to benchmark the capability of ranging fidelity simulation tools in accurately simulating the rotating rig testing setup, the flap step cases have been simulated by DTU and NTUA. The simulations focus on a stiff structure configuration, in order to evaluate the detailed predictions of time-varying aerodynamic loading. The rotating rig with the morphing wing is modeled and simulated for constant uniform inflow of 5 m/s with the flap step cases which have been tested (Table 15). The BEM-based aeroelastic codes Hawc2 [6] and hGAST [7] are utilized, where the near wake induction model [8] is also enabled in Hawc2. Both tools use the same aerofoil static aerodynamic input data, which is generated using NTUA's FOIL2W [9] (Figure 132). The flap steps have been prescribed as in the test cases (Figure 51), including a 1<sup>st</sup> order system response with a time constant of 100ms, simulating the actuator dynamics.

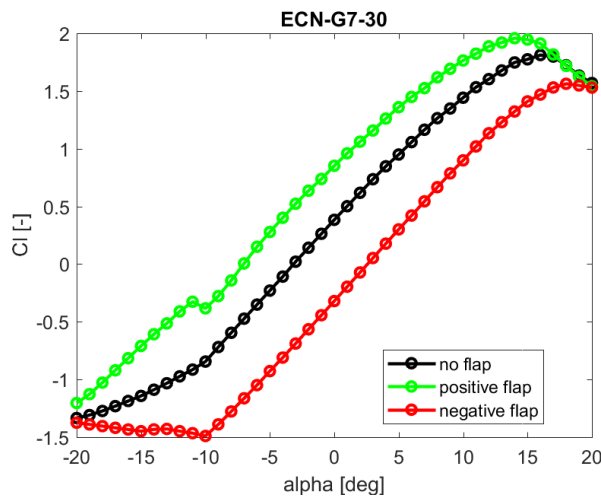


Figure 132  $C_l$  polar for the aerofoil with maximum flap deflections (+/-10deg).

## 7.7 Simulation results

For all the flaps step cases at the different pitch settings, the time series of the normal and tangential forces at the mid-flap location are compared, along with radial distribution of the normal and tangential forces. For one operating case at 0 deg pitch, in Figure 133 and Figure 134, the predictions of the normal and tangential force at the mid-flap location are compared between hGAST, Hawc2 and Hawc2 with the near wake induction model. In Figure 135, Figure 136, and Figure 137, the radial distribution of the normal force is compared for the case of no flap deflection, +10deg flap deflection and -10deg flap deflection respectively. In Figure 138, Figure 139, and Figure 140, the radial distribution of the tangential force is compared for the case of no flap deflection, +10deg flap deflection and -10deg flap deflection respectively.

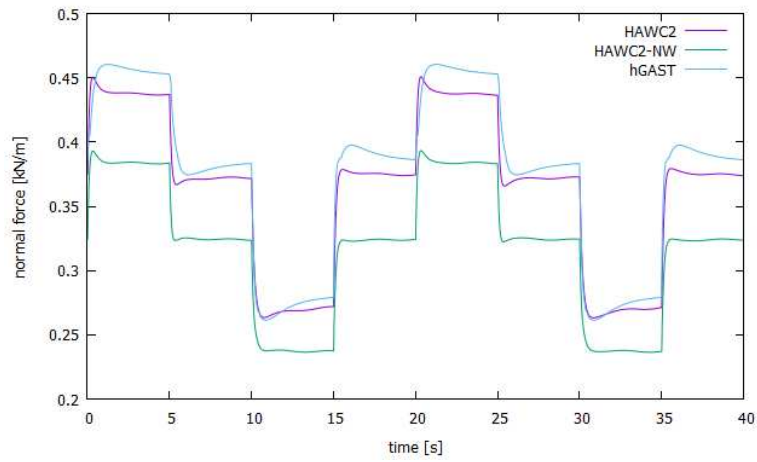


Figure 133 Comparison of normal force time series at mid-flap position (20rpm, 0deg pitch).

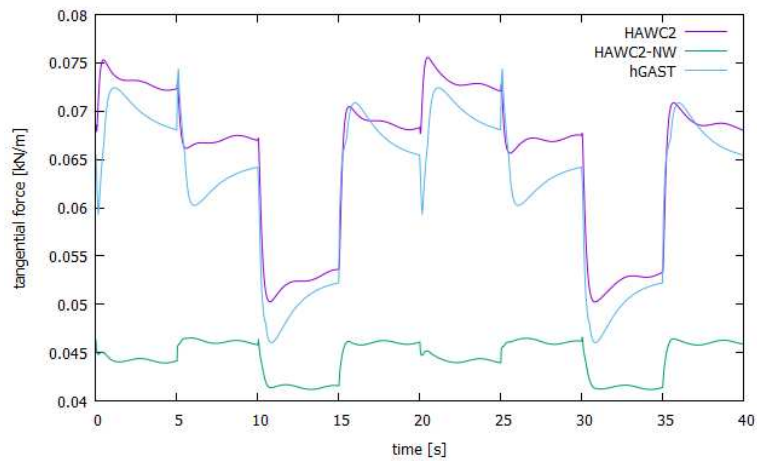


Figure 134 Comparison of tangential force time series at mid-flap position (20rpm, 0deg pitch).

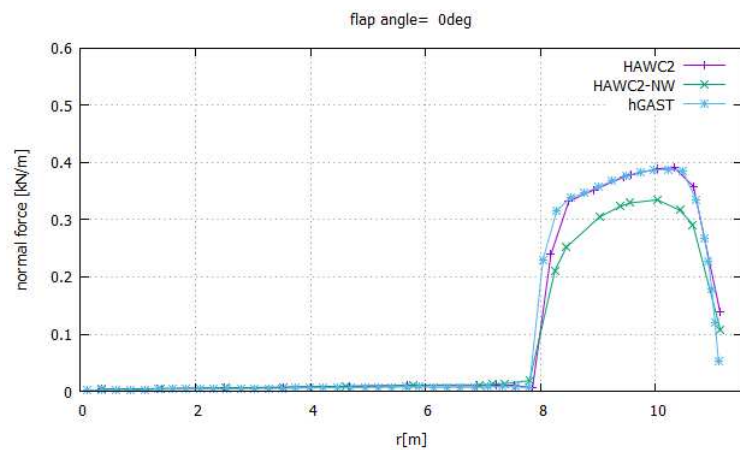


Figure 135 Comparison of normal force radial distribution at 0 deg flap angle (20rpm, 0deg pitch).

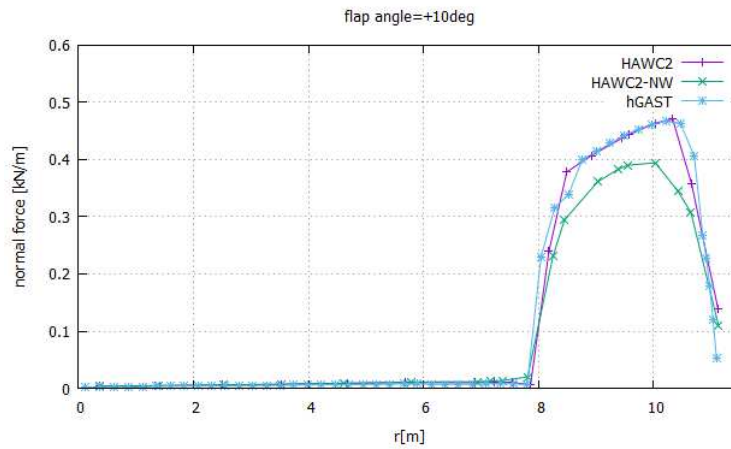


Figure 136 Comparison of normal force radial distribution at +10 deg flap angle (20rpm, 0deg pitch).

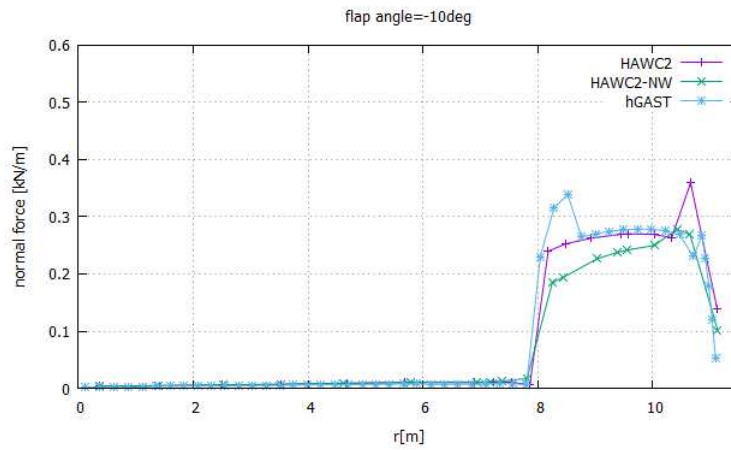


Figure 137 Comparison of normal force radial distribution at -10 deg flap angle (20rpm, 0deg pitch).

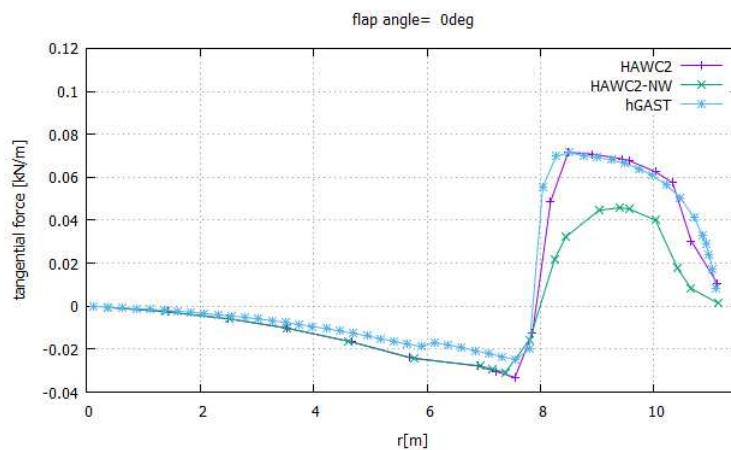


Figure 138 Comparison of tangential force radial distribution at 0 deg flap angle (20rpm, 0deg pitch).

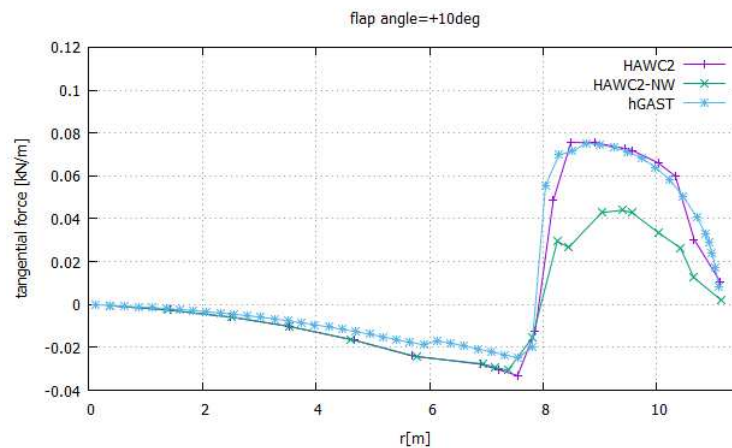


Figure 139 Comparison of tangential force radial distribution at +10 deg flap angle (20rpm, 0deg pitch).

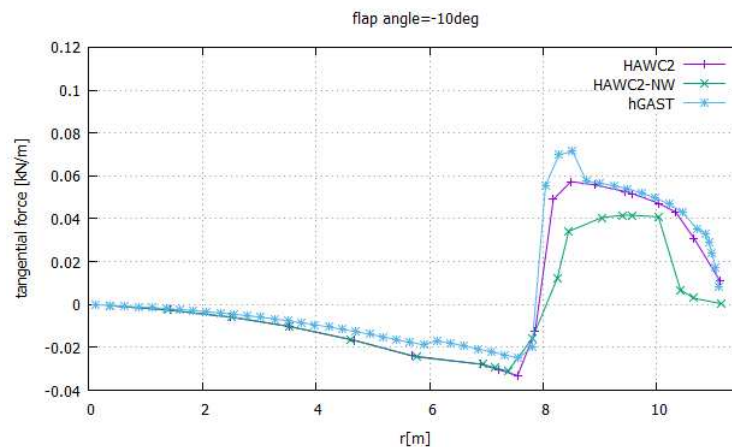


Figure 140 Comparison of tangential force radial distribution at -10 deg flap angle (20rpm, 0deg pitch).

It is seen that the prediction of the unsteady force response with the flap steps between the two BEM-based codes is fairly good, capturing the peak values and dynamics of the response. The prediction of the tangential force shows more differences, especially at the point of stepping to and from the positive flap angle. The radial distribution of forces agrees very well at the mid-aerofoil sections, and as expected, the near wake model shows a lower force amplitude with smooth distribution, accounting for the effect of the trailing vorticity at the edges of the morphing wing.

## 7.8 Conclusions

In the testing campaign utilizing DTU's rotating rig, the morphing flap technology developed in collaboration with the University of Bristol has been evaluated and successfully demonstrated. It is shown that the morphing wing achieves good performance in terms of aerodynamic load response, close to numerical estimations. Moreover, simple controller implementations show promising results in terms of dynamic load alleviation. In addition, the aerodynamic performance of ECN's new aerofoil has been evaluated in atmospheric conditions. Furthermore, the BEM-based codes from DTU and NTUA show good performance in the prediction of the unsteady force response with the flap activation.

## 7.9 References

- [1] Barlas, TK, Aagaard Madsen, H & Løgstrup Andersen, T 2014, Design and simulation of the rotating test rig in the INDUFLAP project. DTU Wind Energy. DTU Wind Energy E, no. 0063(EN).
- [2] Barlas, A, Aagaard Madsen, H, Enevoldsen, K & Klemmensen, K 2014, Flap testing on the rotating test rig in the INDUFLAP project. DTU Wind Energy. DTU Wind Energy E, no. 0064(EN).
- [3] Aagaard Madsen, H, Barlas, A & Løgstrup Andersen, T 2015, Testing of a new morphing trailing edge flap system on a novel outdoor rotating test rig. in Scientific Proceedings. EWEA Annual Conference and Exhibition 2015 . European Wind Energy Association (EWEA), pp. 26-30.
- [4] Barlas, A & Aagaard Madsen, H 2015, Atmospheric Full Scale Testing of a Morphing Trailing Edge Flap System for Wind Turbine Blades. in Proceedings. 26th International Conference on Adaptive Structures and Technologies.
- [5] Aagaard Madsen, H, Barlas, A & Løgstrup Andersen, T 2015, A morphing trailing edge flap system for wind turbine blades. in AL Araújo & CA Mota Soares (eds), Proceedings of the 7th ECCOMAS Thematic Conference on Smart Structures and Materials (SMART 2015). IDMEC.
- [6] Larsen, TJ & Hansen, AM 2007, How 2 HAWC2, the user's manual. Risø National Laboratory. Denmark. Forskningscenter Risoe. Risoe-R, no. 1597(ver. 3-1)(EN).
- [7] Pirrung, G, Hansen, MH & Aagaard Madsen, H 2014, 'Improvement of a near wake model for trailing vorticity' Journal of Physics: Conference Series (Online), vol 555, 012083. DOI: 10.1088/1742-6596/555/1/012083.
- [8] Manolas, DI, Riziotis VA, and Voutsinas, SG, 2015, 'Assessing the importance of geometric non-linear effects in the prediction of wind turbine blade loads' Computational and Nonlinear Dynamics Journal 10 041008 2015.
- [9] Riziotis VA, and Voutsinas, SG, 2008, 'Dynamic stall modelling on airfoils based on strong viscous-inviscid interaction coupling' International Journal for Numerical Methods in Fluids 56: 2 185-208, 2008.

## PART 3: High-Fidelity Simulations

## 8 TRAILING EDGE FLAPS ON THE 20MW TURBINE [NTUA]

### 8.1 Introduction

The possibility of alleviating wind turbine blade loads by means of camber line morphing techniques is investigated in the present section. Loads alleviation is realized through active control of the camber line shape in the TE region. Analysis is performed on the up-scaled Innwind.EU 20MW Reference Wind Turbine while assessment and comparison of the obtained load reduction levels against those of the 10MW RWT is performed.

The development of blade sections capable of undergoing significant geometry adaptations to optimally and timely respond to wind fluctuations is the key objective for successful control of loads. Ongoing research conducted by the University of Patras (UP) and the National Technical University of Athens (NTUA) is focused on designing Shape Memory Alloy (SMA) actuators as a mean for active load control. It has been shown in [1] and [2] that SMA actuators can constitute the basis for effectively controlling the shape of the blade camber line when implemented along with an appropriate morphing mechanism. The present study is mainly focusing on the definition of the appropriate morphing shape so that satisfactory fatigue load reduction is achieved with control actuation speeds attainable by SMA type actuators.

Aeroelastic control of the blade fatigue loads is realized through the use of a standard individual flap controller (IFC). The controller is based on the decomposition of the blade root out-of-plane moments of the three blades (measured in the rotating reference frame) into yaw and tilt moments in the hub fixed system (expressed in the non-rotating frame) through application of Coleman's transformation. The hub fixed moments represent the control input variables through which two output cyclic flap angles are defined. Re-modulation of the output cyclic flap angles by means of the inverse Coleman transformation provides the individual flap angles of the three blades [3]. Furthermore, flap control is combined with individual pitch control (IPC) based on the same working principle. In the combined IFC&IPC controller, individual flap control is supported by simultaneous individual control of the pitch angle of the three blades.

The smooth output of IFC and IFC&IPC controllers that follows a  $1p$  variation, seems to be well suited for the relatively slow SMA actuators (as compared to conventional ones), especially for slowly rotating large rotors. In this work, Shape Memory Alloy in 1D form (wires) are considered, in order to provide the actuation forces required to morph the flap to the desired configuration. Due to their intrinsic high actuation energy density they are adequate for lightweight morphing concepts and large movements. Preliminary studies presented in [1], [2] have proven that SMA's can perform satisfactorily at  $1p$  actuation frequencies. Therefore, they are adopted as actuators in this study, instead of conventional actuators, such as servomotors or pneumatic actuators, due to their simplicity, compactness and performance. An articulated finger like mechanism has been designed as baseline actuator. This morphing mechanism is activated by pairs of SMA wire actuators in an antagonistic configuration scheme.

Higher load reduction requirements on larger rotor can be met by extending the length of the TE flap in the chordwise direction. As discussed next, the requirement for longer flaps that undergo large curvature variations can be satisfied through the use of multi-element sections in which multiple SMA wires can be easily accommodated, as shown in [1], [2]. In the present work the effect of different morphing shapes of the TE region on the lift characteristics of the blade section is assessed. Once the appropriate trailing edge shape is fixed, load reduction capabilities are assessed for different chordwise and spanwise lengths of the control surface.

### 8.2 Camber line morphing

Camber line morphing is performed on the outer part of the blade of the Innwind.EU 10 MW and 20 MW RWT. The blade of the reference turbine comprises FFA-w3 series airfoils. The relative

thickness of the outer 35% of the blade is constant and equal to  $t/c=0.24$  while further inboards the relative thickness increases to  $t/c=0.30$  at  $r/R=0.4$ .

Different morphing shapes of the TE region have been tested. All deformation shapes extend to 30% of the chord length. Longer flaps can be more easily realized by a modular section type. In this case, it is possible to extend the deformable part of the flap to a larger chordwise length and at the same time build the deformation of the camber line more gradually as shown in Figure 141. The articulated shape of the mechanism and the way that the moving parts are arranged, provides greater flexibility than other types of actuators. The morphing mechanism structure consists of pinned moving parts that are designed in a way that can be adjusted and arranged so as the target shape is best followed. Moreover, each part can be activated independently. Thus it is possible to achieve different complex target shapes. Details on the functional characteristics and operation of the actuator can be found in [4]. In the same report a FEM model for the actuator dynamics is presented. Simulation results of the response of the controller, in prescribed flap motion, determined through IFC feedback control are shown. It is proven that SMA actuators is capable of closely following the flap angle demand set by the feedback loop.

Different morphing shapes (see Figure 142) based on spline curves are assessed in terms of the achieved change in  $C_L$  ( $\Delta C_L$  in Figure 143) for different flap deployment angles. As Aerodynamic polars have been computed with FOIL2W code. Among the various shapes those exhibiting a monotonic behavior (no change of curvature) are qualified and finally the one that provides the maximum  $\Delta C_L$  (slope  $3^\circ$ ) is down selected as baseline configuration for the present analysis.

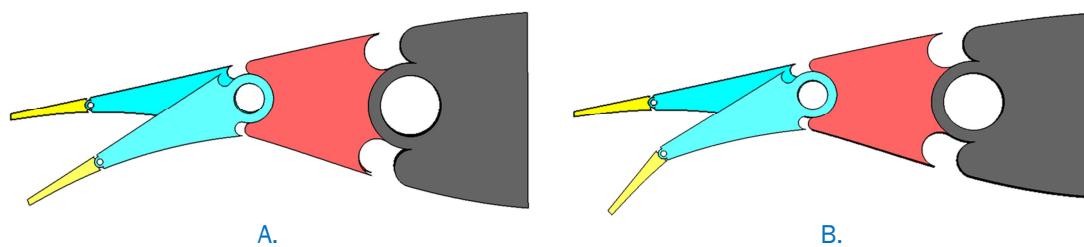


**Figure 141. Morphing capabilities by applying a modular flap controlled by SMAs. Morphing Cases for the 20MW WT Section. A. Independent Movement of 30% Flap and B. Combined Movement of 10% and 30% Modular Flaps [4].**

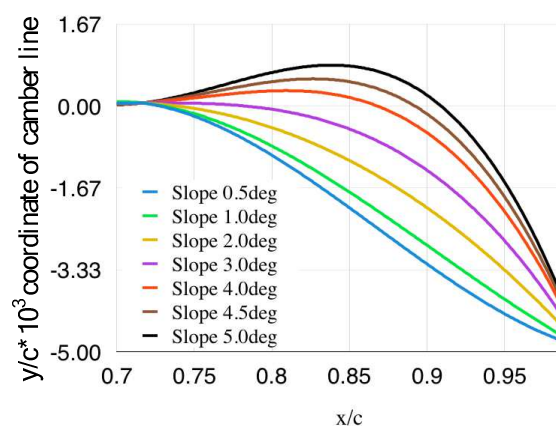


**Figure 142. The various Trailing Edge camber line geometries studied.**

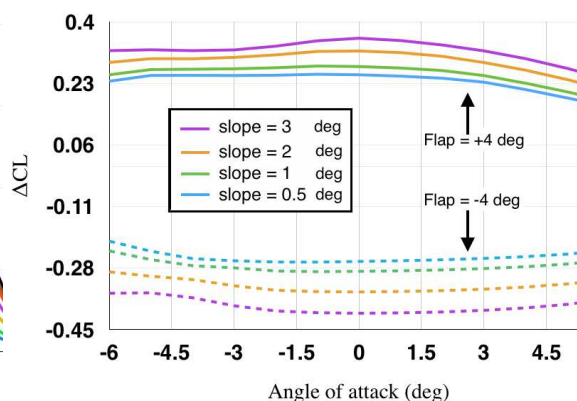


**Figure 143.  $\Delta C_L$  vs. angle of attack for different camber line geometries. Flap angle  $\pm 4$  deg.**

### 8.3 Controller description

Individual trailing edge (TE) flap control has been superimposed on the standard power speed controller of the Innwind.EU 10MW and 20MW turbines. A standard individual flap controller (IFC) has been employed [5],[6]. The blade root out-of-plane bending moment signals are transformed into yaw and tilt moments  $M_{yaw}$  and  $M_{tilt}$  by applying the Coleman transformation. 3p and 6p band-stop filters are applied to  $M_{yaw}$  and  $M_{tilt}$ . The filtered moments are then passed through an integral control element (I) and the cyclic  $\beta_{yaw}$  and  $\beta_{tilt}$  angles are obtained. These angles are then back transformed into flap angles  $\beta_f$  of the individual blades via an inverse Coleman transformation. The block diagram of the IFC is illustrated in Block diagram of IFC controller. Figure 144. In the present work IFC is combined with individual pitch control (IFC&IPC) which based on the same working principle [6]. In the IFC&IPC controller, flap control is supported by simultaneous individual control of the pitch angle of the three blades.

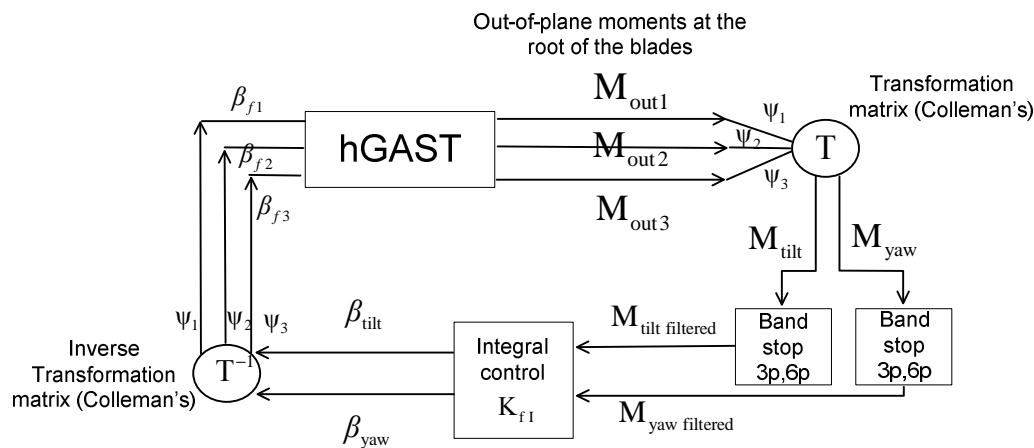


Figure 144. Block diagram of IFC controller.

Trailing edge (TE) camber line morphing is performed on the outer part of the blade of the RWT (10MW and 20MW). The blade of the reference turbine comprises FFA series airfoils. The relative thickness of the outer 35% of the blade is constant and equal to  $t/c=0.24$ . The camber line shape presented in section 8.2, extending to 30% of the section chord length was employed. The spanwise extent of the flap was 22.5% of the blade radius (see details in Table 16).

Table 16: TE flap layout.

	Flap configuration	
	10MW RWT	20MW RWT
Chordwise extent	30%	30%
Deflection angle limits	$\pm 10^\circ$	$\pm 10^\circ$
Deflection speed limit	20°/s	20°/s
Spanwise length	20 m (~22.5% of blade length)	28.28 m (~22.5% of blade length)
Spanwise location	60 m-80 m (from rotor centre)	84.85 m-113.14 m (from rotor centre)
Airfoil	FFA-W3-241	FFA-W3-241

In the present analysis constant controller gains have been used both for individual flap control. They have been decided on the basis of a sensitivity analysis performed over the wind speeds range of 11-25 m/s. Controller gains used in the different control loops and turbine sizes are summarized in . Flap motion is bounded in the range  $[-10^0, +10^0]$ . In addition, saturation limits have been imposed on the velocity of the flap motion to  $20^0/s$ . In all configurations a delay of 0.1 s has been imposed on the flap motion in order to account for the dynamics of the flap actuator (through a first order filter in flap response).

**Table 17: Controller gains for the different loops and turbine sizes.**

	10MW	20MW
IPC	$K_{pl} = 1 \times 10^{-9} \text{ deg/ s / Nm}$	$K_{pl} = 0.5 \times 10^{-9} \text{ deg/ s / Nm}$
IPC+IFC	$K_{pl} = 0.6 \times 10^{-9} \text{ deg/ s / Nm}$ $K_{fl} = 7 \times 10^{-9} \text{ deg/ s / Nm}$	$K_{pl} = 0.2 \times 10^{-9} \text{ deg/ s / Nm}$ $K_{fl} = 2 \times 10^{-9} \text{ deg/ s / Nm}$

#### 8.4 Results and discussion

Assessment of load reduction capabilities of the different control methods is performed both on fatigue and ultimate loads. Fatigue loads are assessed on the basis of IEC DLC 1.2 (normal operation with normal turbulence conditions NTM) while ultimate loads are estimated through DLC 1.3 (normal operation with extreme turbulence conditions ETM). Simulated conditions and wind speeds are summarized in Table 18. For all turbulent wind simulations (i.e. NTM, ETM) three seeds are simulated.

In Table 19 the list of 10MW and 20MW configurations compared in the present study is provided. For the IA 10MW RWT and the IC 20MW RWT, simulations are performed (a) for the baseline turbine without IPC or/and IFC (thereafter called “no control”), (b) for the turbine with IPC only and (c) for the turbine with combined IPC&IFC. The aim of the analysis is i) to assess load reduction capabilities of the combined pitch/flap control loop against pure IPC and ii) to assess pitch actuator duty cycle reduction for IPC as a result of the operation of the flaps. Lifetime fatigue loads are calculated assuming the following Weibull parameters:  $C=11 \text{ m/s}$  and  $k=2$  for both turbines. IPC and IFC is usually not recommended in the partial load region since the interaction of the pitch/flap controller with the basic power-speed controller could compromise power production. However, in order to assess load reduction capabilities at lower wind speeds in the present work IPC and IFC operation has been also extended to wind speeds below rated.

**Table 18: Definition of simulated DLCs**

DLC	Wind	BINS [m/s]	Yaw [deg]	s.f.
1.2	NTM	5-25, step 2	0.0	-
1.3	ETM	11-25, step 2	0.0	1.35

**Table 19: List of configurations tested.**

10MW [class - IA]	20MW [class -IC]
10MW RWT - no control	20MW RWT - no control
10MW RWT - IPC	20MW RWT - IPC
10MW RWT - IPC&IFC	20MW RWT - IPC&IFC

## 10 MW

### Fatigue loads (Figure 145-Figure 146 and Table 20)

- Flapwise bending moment DEL significantly decreases both with IPC and IPC&IFC. Slightly higher flapwise bending moment DEL reduction is achieved through IPC&IFC (27.6% against 25.5% for pure IPC). Higher load reduction is obtained in the full load region. DELs decrease by 25%-30% for wind speeds higher than 15m/s. In the partial load region flapwise moment reduction is of the order of 12-14%.
- Edgewise bending moment DEL also slightly decreases. A DEL reduction of about 2.5% is achieved by both control methods. Edgewise moment reduction is higher in the vicinity of the rated speed.
- Torsion moment decreases with pure IPC (11.6%) while considerably increases (by more than 50%) when combined IPC&IFC is performed. TE flap morphing locally increases the twisting moment of the blade sections equipped with flaps. Torsion moment increase is higher in the full load region.
- Tower bending moments increase both with IPC and IPC&IFC. A slightly higher fatigue load increase is obtained by combined IPC&IFC. Both IPC and IFC have been designed to reduce blade loads. So, no control logic exists in the design of the control loop that could effectively be used for the mitigation of the tower loads. However, the increase in the DEL of the fore-aft bending moment is rather marginal for IPC&IFC (equal to 2.4%). The increase in the lateral moment is somewhat higher (6.6% for IPC&IFC) however the fore-aft component is the one that dominates combined tower moment (fore-aft DEL is two times higher than side-side).
- Tower yaw moment slightly decreases both with IPC and IPC&IFC. Higher yaw moment decrease is obtained in the vicinity of the rated wind speed.

### Ultimate loads (Table 21)

- Extreme flapwise bending moment load decreases both with IPC and IPC&IFC. Slightly higher flapwise bending moment reduction is achieved through combined IPC&IFC. A 7.4% maximum flapwise moment reduction is obtained with IPC&IFC while for IPC the maximum flapwise moment reduction is 4.5%.
- Maximum edgewise moment decreases both with IPC (8.8%) and IPC&IFC (9.1%). On the other hand minimum edgewise moment increases with IPC (5.7%) while decreases with combined IPC&IFC (2.3%).
- Torsion moment considerably increases with IPC&IFC,
- Combined blade moment decreases by 4.3% with IPC and 5.5% with the combined IPC&IFC.
- Maximum tower fore-aft moment considerably increases (by 8.2%) when combined IPC&IFC is applied. Pure IPC gives rise to a marginal reduction of 0.3% in the maximum fore-aft moment. Minimum (negative moment) increases (in absolute value) with both control methods however it is noted that minimum moment is three times smaller (again in absolute value) than maximum. Therefore, maximum moment is expected to be the one that drives the design.
- A slight reduction is obtained, by both control methods, in the maximum side-side moment. Again maximum load is the design driving load.
- A significant reduction is obtained in the minimum (negative) extreme yaw moment (~19%) by both control methods. It is noted that minimum yaw moment is higher in absolute value than the maximum.
- Finally combined tower extreme moment slightly decreases with IPC while considerably increases (by 8.1%) with IPC&IFC. The increase in the combined load is almost equal to the increase in the fore-aft maximum moment. Thereby, it is concluded that maximum fore-aft bending moment drives ultimate design load of the tower.

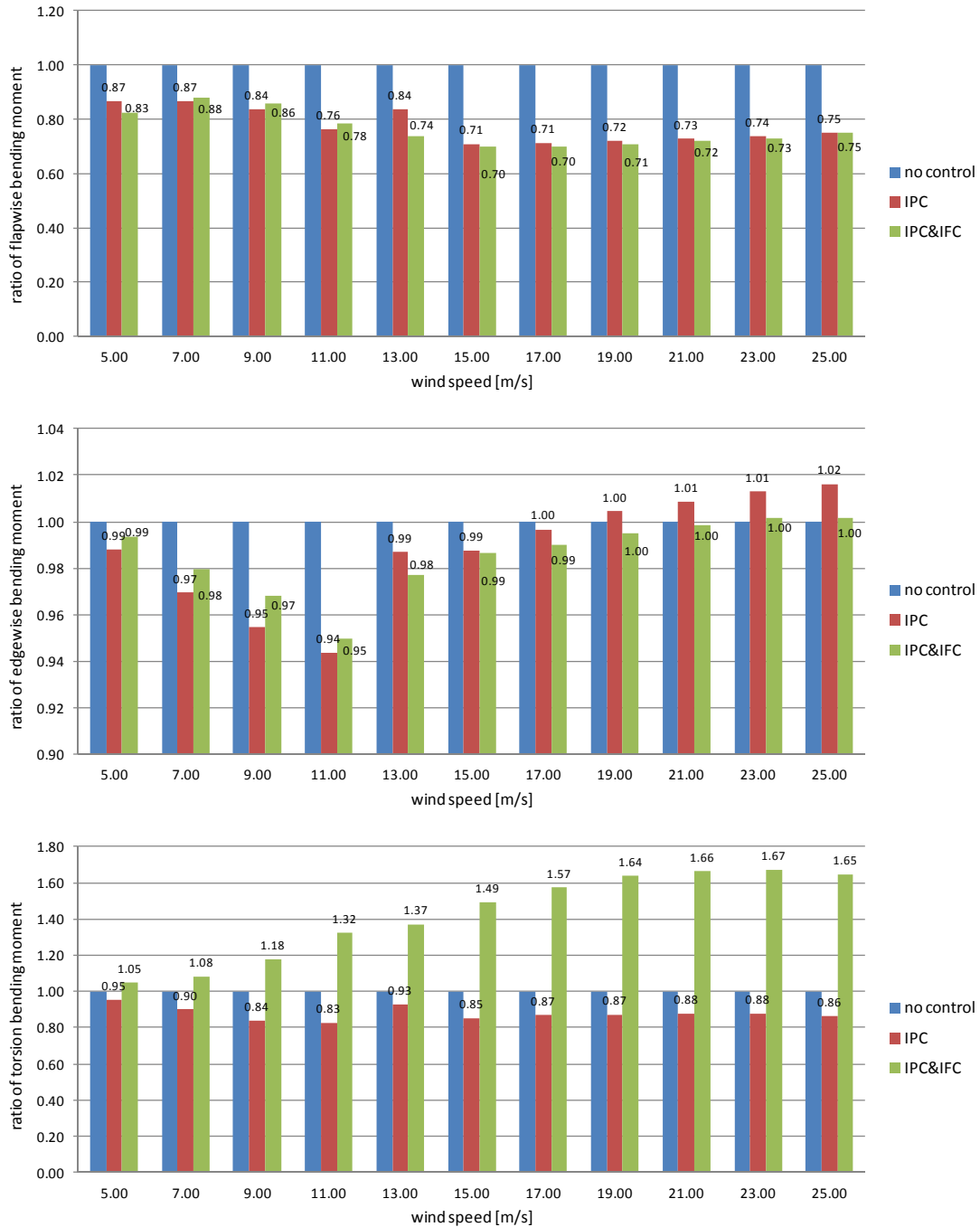


Figure 145. 10MW RWT. Blade fatigue load reduction (DEL, 1hz, m=10) ratio for IPC and combined IPC&IFC.

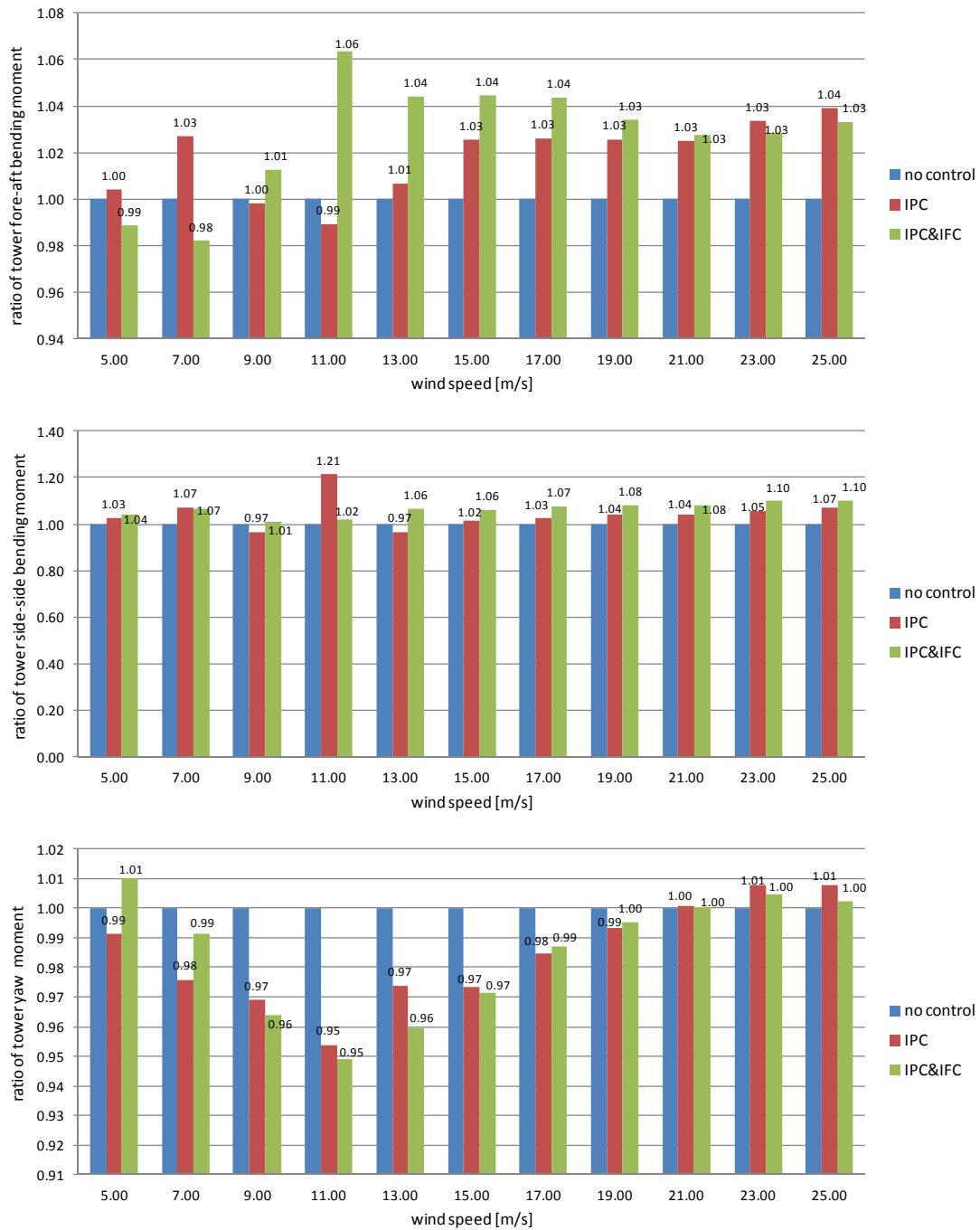


Figure 146. 10MW RWT.Tower fatigue load reduction (DEL, 1hz, m=10) ratio for IPC and combined IPC&IFC.

Table 20: 10MW RWT. Lifetime DELs calculated for C=11 m/s and k=2.

design	ROOT BLADE			TOWER BASE		
	edge	flap	torsion	side	fore	yaw
10MW RWT - no control (kNm)	24219	31051	382	49299	84986	20218
10MW RWT - IPC	-2.6%	-25.5%	-11.6%	5.4%	1.8%	-1.5%
10MW RWT - IPC&IFC	-2.5%	-27.6%	52.7%	6.6%	2.4%	-1.7%

Table 21: 10MW RWT. Ultimate loads calculated on the basis of IEC DLC 1.3.

design	ROOT BLADE							TOWER BASE						
	edge		flap		torsion		combined	side		fore		yaw		combined
	max	min	max	min	max	min	max	max	min	max	min	max	min	max
DLC 1.3 10MW RWT - no control	29537	-24930	65708	-38592	616	-652	67919	130961	-79982	341248	-99608	44929	-66528	342157
10MW RWT - IPC	-8.8%	5.7%	-4.5%	-29.2%	-12.2%	-0.6%	-4.3%	-0.6%	5.8%	-0.3%	24.6%	-1.1%	-19.1%	-0.4%
10MW RWT - IPC&IFC	-9.1%	-2.3%	-7.4%	-23.6%	25.4%	38.8%	-5.5%	-1.8%	9.7%	8.2%	15.7%	-2.9%	-18.8%	8.1%

## 20 MW

### Fatigue loads (Figure 147-Figure 148 and Table 22)

- Flapwise bending moment DEL significantly decreases both with IPC and IPC&IFC. Slightly higher flapwise bending moment DEL reduction is achieved through IPC (27% increase against to 25.3% for the combined IPC&IFC case). For the IC 20MW turbine, flapwise moment DEL reduction is almost constant over the whole range of operational wind velocities. The levels of flapwise moment reduction are comparable to those of the 10MW turbine.
- Edgewise bending moment DEL also slightly decreases. A DEL reduction of 1.6% is achieved with IPC while 1.1% reduction is obtained with IPC&IFC. Edgewise moment reduction is higher in the vicinity of the rated speed as in the case of the 10MW turbine.
- Torsion moment decreases with pure IPC (by 9.5%) while considerably increases (by 31.9%) when combined IPC&IFC is performed.
- Tower bending moments increase both for IPC and IPC&IFC. A slightly higher DEL increase is obtained on the 20MW turbine as compared to the 10MW turbine. For IPC&IFC, the increase in the fore-aft moment is 4.7% while for the side-side moment is 12.2%.
- Contrary to the 10MW case tower yaw moment slightly increases both for IPC and IPC&IFC. Yaw moment DELs increase at high wind speeds in the full load region.

### Ultimate loads (Table 23)

- Flapwise bending moment extreme load decreases both with IPC and IPC&IFC. Slightly higher flapwise bending moment reduction is achieved through combined IPC&IFC. A 6.2% maximum flapwise moment reduction is obtained with IPC&IFC while for IPC the maximum flapwise moment reduction is 4.9%.
- Maximum edgewise moment decreases with IPC (by 1.7%) while increases with IPC&IFC (2.1%). On the other hand, minimum edgewise moment slightly decreases both with IPC (0.7%) and IPC&IFC (0.8%).
- Torsion moment considerably increases with IPC&IFC,
- Combined blade moment decreases by 3.7% with IPC and 4.7% with the combined IPC&IFC.
- As opposed to the 10MW turbine case, maximum tower fore-aft moment presents a marginal decrease of 0.3% when combined IPC&IFC is applied. Pure IPC gives rise to a marginal as well reduction of 1.6% in the maximum fore-aft moment. Minimum (negative moment) increases (in absolute value) with both control methods however it is seen that minimum moment is more than three times smaller (again in absolute value) than the maximum. Therefore, maximum moment is expected to be the one that drives the design.
- Similar to the 10MW case, a slight reduction is obtained, by both control methods, in the maximum side-side moment. Again maximum load is the design driving load.
- A reduction is obtained in the minimum (negative) extreme yaw moment by both control methods. It is noted that minimum yaw moment is higher in absolute value than the maximum.
- Finally combined tower extreme moment slightly decreases with both control methods. The variation in the combined load is almost equal to the variation in the fore-aft maximum moment. Thereby, it is concluded that maximum fore-aft bending moment drives ultimate design load of the tower.

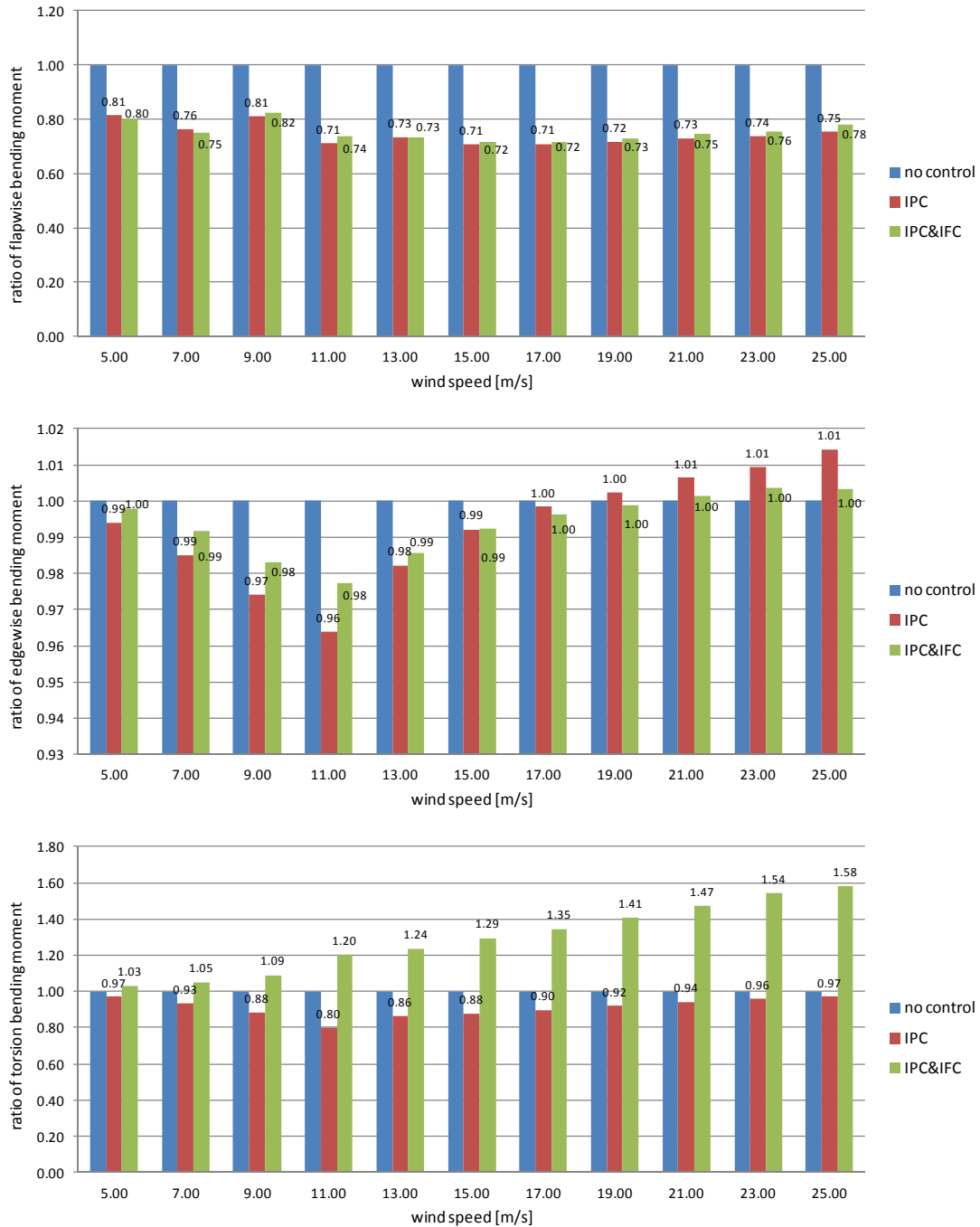


Figure 147. 20MW RWT. Blade fatigue load reduction (DEL, 1hz, m=10) ratio for IPC and combined IPC&IFC.

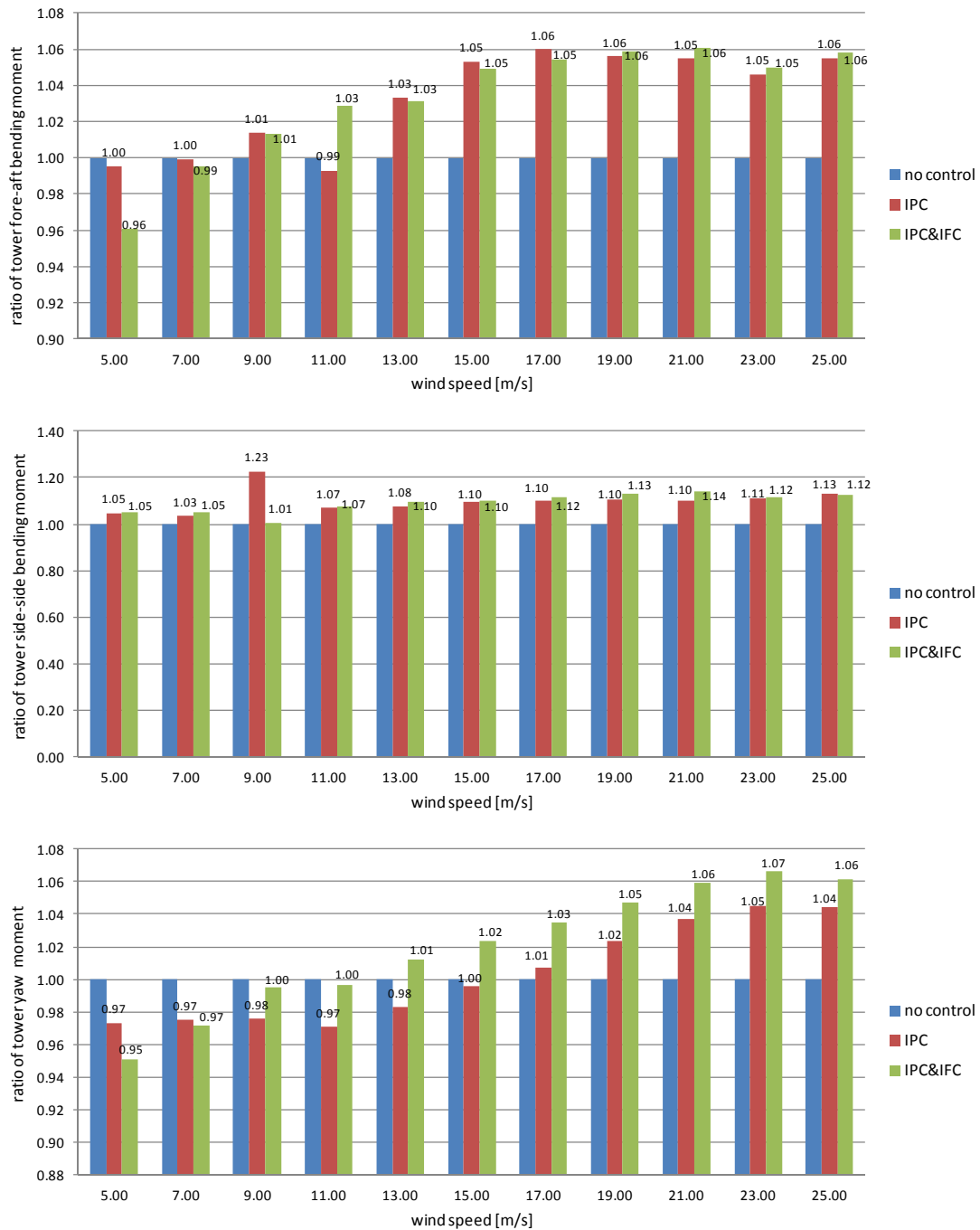


Figure 148. 20MW RWT.Tower fatigue load reduction (DEL, 1hz, m=10) ratio for IPC and combined IPC&IFC.

Table 22: 20MW RWT. Lifetime DELs calculated for C=11 m/s and k=2.

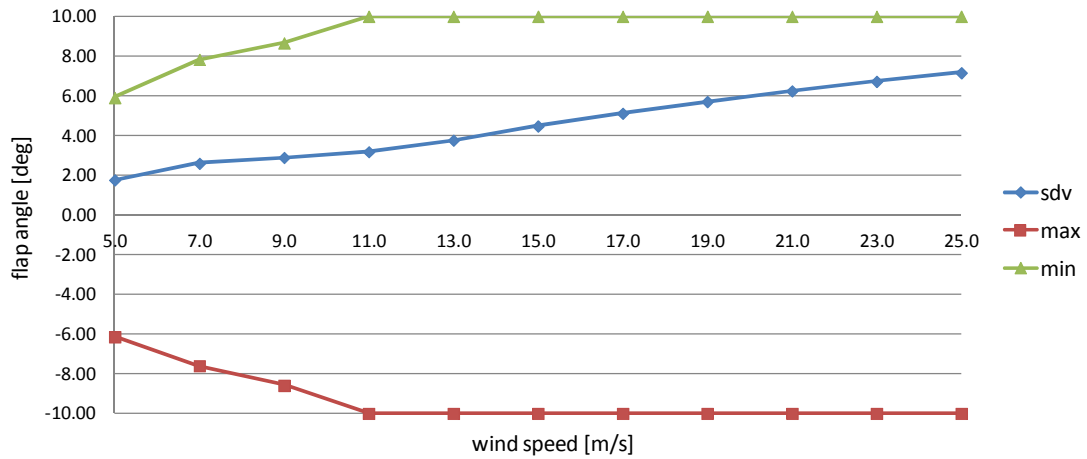
design	ROOT BLADE			TOWER BASE		
	edge	flap	torsion	side	fore	yaw
20MW RWT - no control (kNm)	91019	72693	1160	76684	155124	42124
20MW RWT - IPC	-1.6%	-27.0%	-9.5%	10.8%	4.6%	1.1%
20MW RWT - IPC&IFC	-1.1%	-25.3%	31.9%	12.2%	4.7%	3.6%

Table 23: 20MW RWT. Ultimate loads calculated on the basis of IEC DLC 1.3.

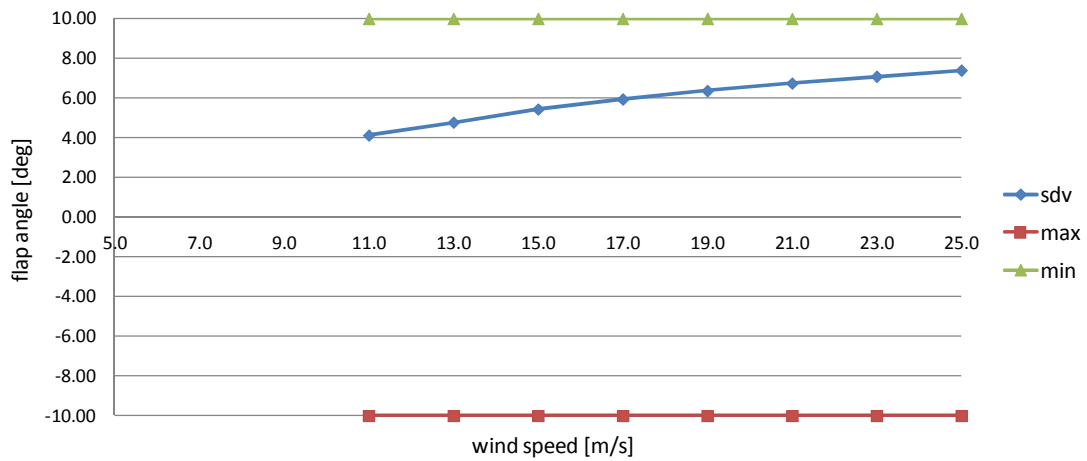
design	ROOT BLADE							TOWER BASE						
	edge		flap		torsion		combined	side		fore		yaw		combined
	max	min	max	min	max	min	max	max	min	max	min	max	min	max
<b>DLC 1.3</b> 20MW RWT - no control	81497	-80315	174990	-103674	1395	-1840	184552	330312	-159556	894921	-242860	99895	-133331	896241
20MW RWT - IPC	-1.7%	-0.7%	-4.9%	-41.7%	-7.4%	-3.9%	-3.7%	-6.2%	42.8%	-1.6%	23.6%	-4.5%	-8.6%	-1.6%
20MW RWT - IPC&IFC	2.1%	-0.8%	-6.2%	-39.7%	46.1%	33.8%	-4.7%	-5.5%	38.1%	-0.3%	20.2%	-0.1%	-4.4%	-0.3%

In Figure 149-Figure 152 the flap and pitch motion characteristics of the two turbine sizes are presented both for NTM and ETM conditions. For the 10MW turbine it is seen that the flap angle reaches the saturation limits of +/-10deg at wind speeds higher than the rated speed (see Figure 149). The difference in the sdv between the NTM and the ETM case is relatively small. This indicates that independent of the turbulence of the wind the flap angle continuously varies between the upper and lower bounds for wind speeds within the full load region. For the 20MW turbine, as a result of the lower design turbulence (IEC IC conditions) the bounds of the flap angle are reached with some delay (as seen in Figure 151) at the wind speed of 13m/s (for NTM conditions). Again the sdv of the flap angle for the ETM case appears to be slightly higher than that of the NTM case.

In Figure 150 the sdv of the pitch motion is presented for the 10MW turbine. It is seen that the sdv of the pitch motion increases by up to 50% (and even more) with pure IPC. When IFC is applied simultaneously with IPC the sdv of the pitch motion only slightly increases as compared to the “no control” case. A maximum increase of the pitch sdv of 14% is recorded at very high wind speeds close to the cut out speed. The average increase in the sdv of the pitch motion over the whole range of wind speeds is 5-6% for the combined IPC&IFC. In Figure 152 the sdv of the pitch angle motion of the 20MW turbine is shown. On the 20MW turbine the sdv of the pitch motion in pure IPC increases by up to 120%. So, it is more than double than that of the 10MW turbine. When IFC is applied simultaneously, the increase in the pitch sdv does not exceed 25%, while the average increase over the whole range of wind speeds is of the order of 10%. So, a significant saving of the duty cycle of the pitch actuator is obtained which increases with the size of the turbine.

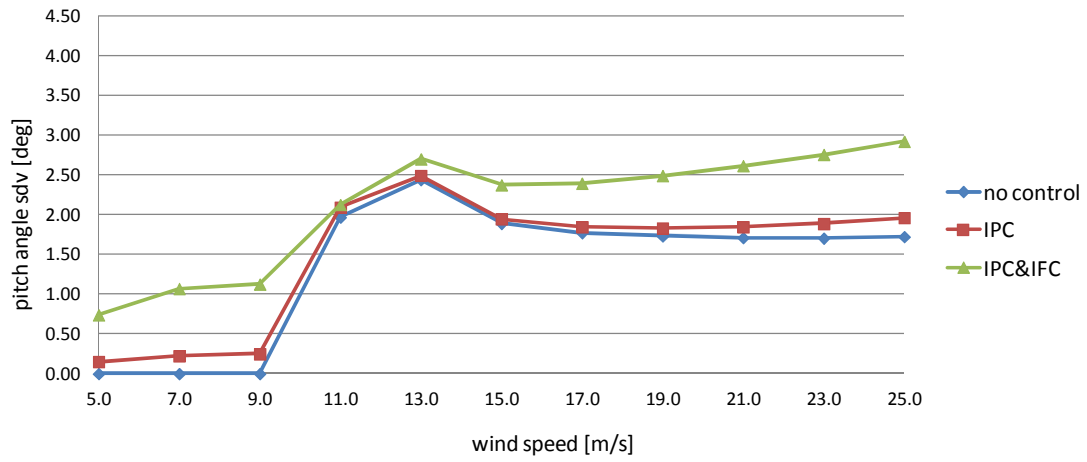


NTM

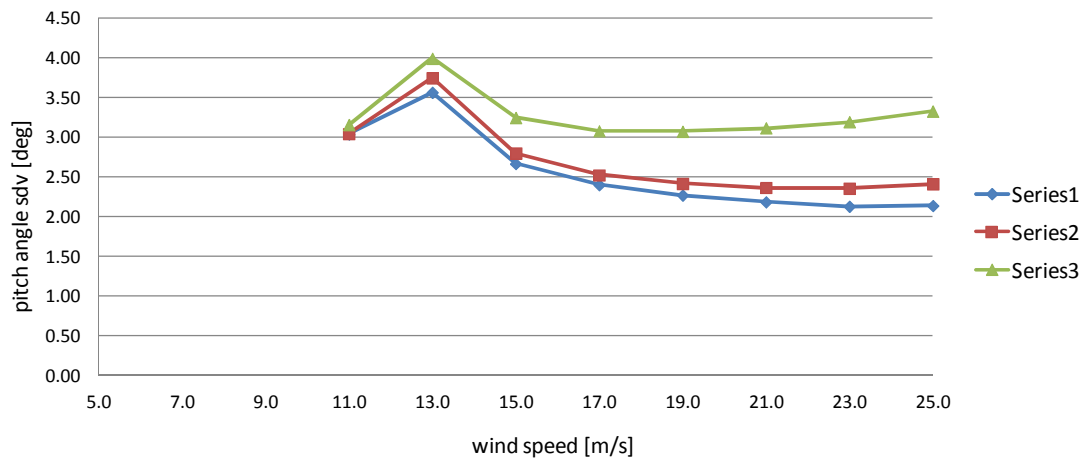


ETM

Figure 149. 10MW RWT. Flap angle variation.

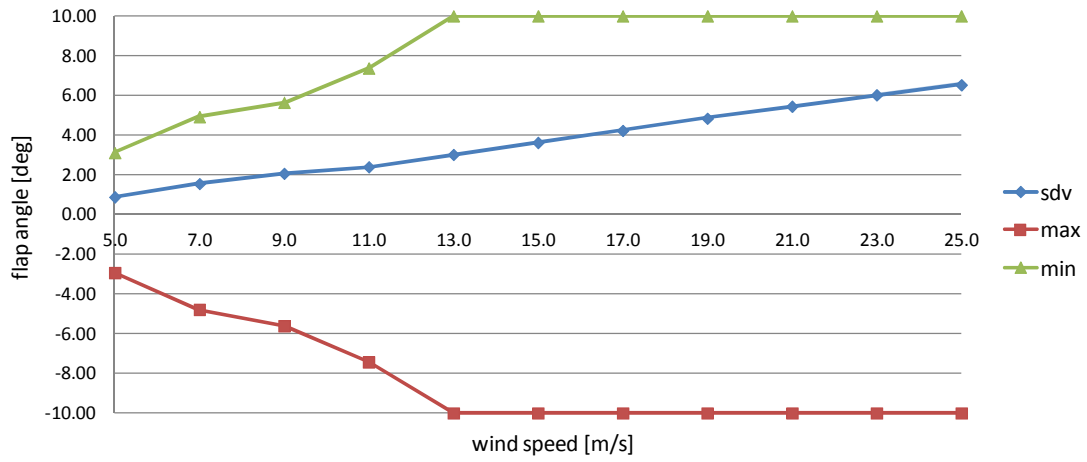


NTM

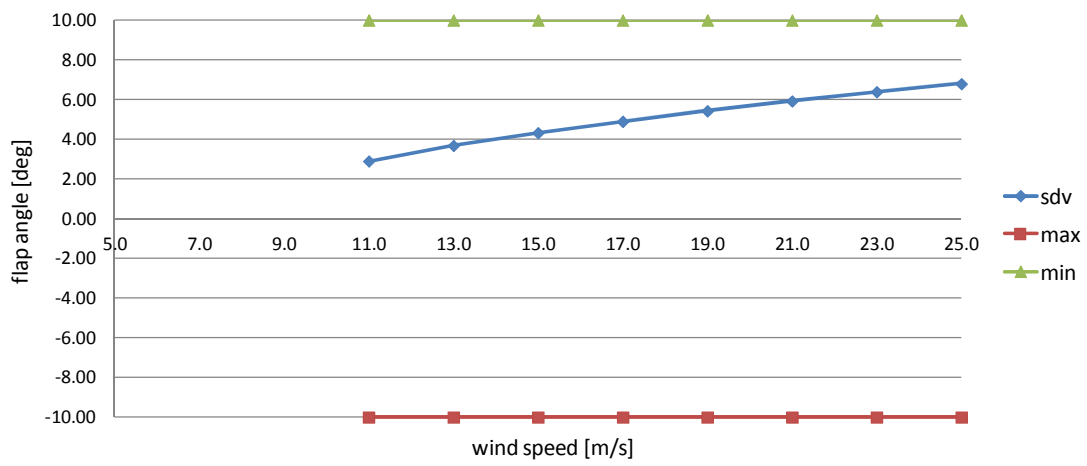


ETM

Figure 150. 10MW RWT. Pitch angle variation.

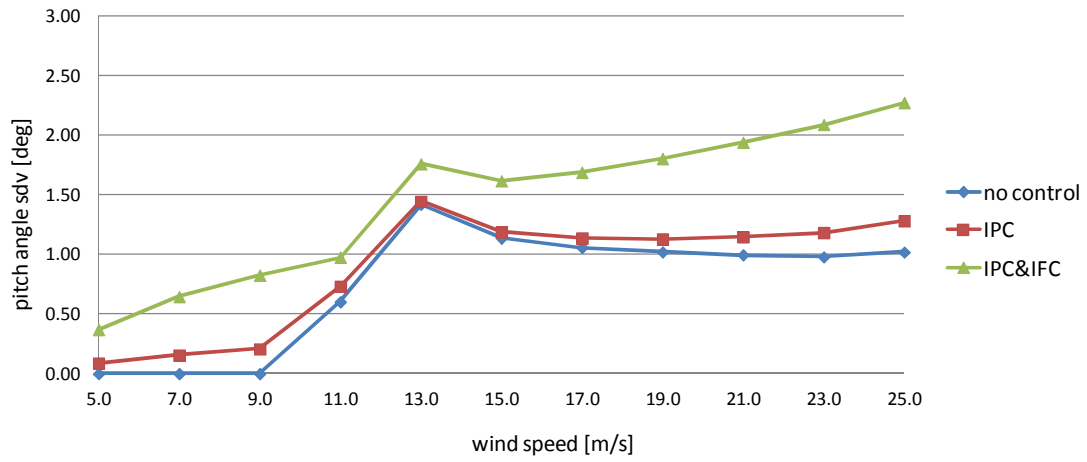


NTM

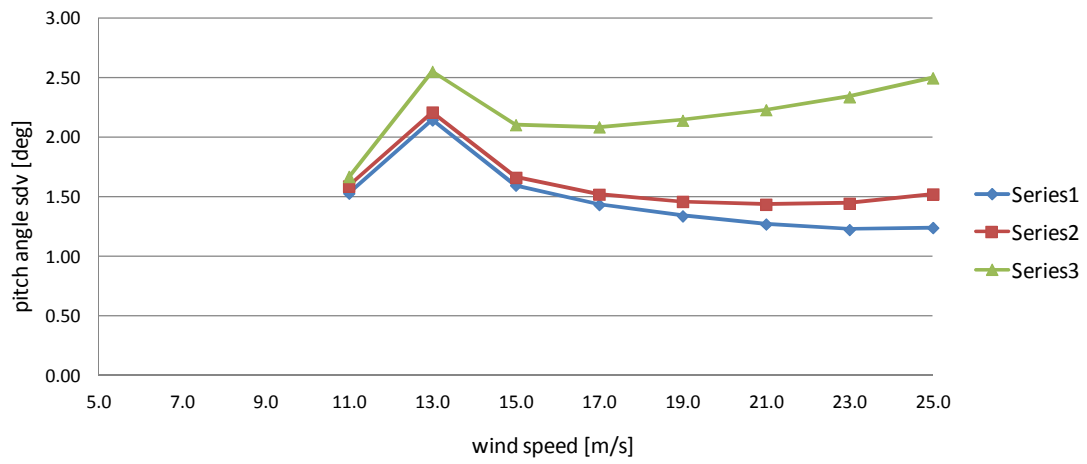


ETM

Figure 151. 20MW RWT. Flap angle variation.



NTM



ETM

Figure 152. 20MW RWT. Pitch angle variation.

## 8.5 Conclusions

Fatigue and extreme load reduction capabilities of IPC and IPC&IFC are assessed on the 10 MW and 20 MW Innwind.EU RWT. Blade flapwise fatigue load reduction of about 25% is attained with both control strategies tested in the present study (ie. IPC and combined IPC&IFC), independent of the turbine size. Overall, tower fatigue loads slightly increase for both turbine sizes and both control strategies. A slightly higher increase is noted on the fatigue loads of the up-scaled 20 MW turbine. This is because the proposed control loops have been only designed for the alleviation of the blade loads while they are not aiming at tower loads. Minor is the effect on ultimate loads by both control concepts. As a result of the combined application of IPC and IFC a 6% reduction of the blade extreme flapwise load is obtained on the 20MW turbine. The combined application of IPC&IFC while it results in the same blade load reduction as IPC it considerably reduces pitch mechanism duty cycle. For the 20MW turbine the increase in the sdv of the pitch motion exceeds 100% while it is reduced to about 10% when IFC is activated.

## 8.6 References

- [1] Karakalas, A., Machairas, T., Solomou, A., Riziotis, V., Saravanos, D. 2014, Design and Simulation of Morphing Airfoil Sections with SMA Actuators for Wind Turbine Rotors. ICAST2014: 25nd International Conference on Adaptive Structures and Technologies, October 6-8th, The Hague, The Netherlands, ICAST2014 082.
- [2] Karakalas, A., Machairas, T., Solomou, A., Riziotis, V., Saravanos, D., 2015, Morphing Airfoil with Shape Memory Alloy Wire Actuators for Active Aerodynamic Load Control in Large Wind-Turbine Blades, *EWEA annual event*, 17-20 November, Paris.
- [3] Bossanyi, E.A., 2003, Wind Turbine Control for Load Reduction, *Wind Energy*, 2003, 6, 229-244.
- [4] Madsen, H.A, "New aero-structure rotor concepts and evaluation for 20 MW turbines," Innwind.EU deliverable report 2.1.4, 2017
- [5] Bæk P., Unsteady Flow Modeling and Experimental Verification of Active Flow Control Concepts for Wind Turbine Blades, DTU RISOE, 2011. PhD Thesis.
- [6] Tsiantas, T., Manolas, D.I., Machairas, T., Karakalas, A., Riziotis, V.A., Saravanos, D., Voutsinas, S.G., "Assessment of fatigue load alleviation potential through blade trailing edge morphing," Proceedings of the Science of Making Torque from Wind Conference, TORQUE 2016, Munich, Germany, 5-7 October.

## 9 ADAPTIVE TRAILING EDGE FLAPS (ATEF) ON A 2.1 MW COMMERCIAL TURBINE [SE BLADES]

### 9.1 Executive Summary

The contribution of Suzlon to the INNWind project Work Package on Smart Rotors consists in carrying out an aero-servo-elastic analysis of the application of Adaptive Trailing Edge Flaps (ATEF) on Suzlon's 2.1 MW wind turbine model S111.

The aim is to evaluate through aeroelastic simulations the impact of controlled ATEF on the wind turbine and obtain a preliminary quantification of the effects in terms of fatigue and ultimate load alleviation, as well as the potential for AEP increase.

The aeroelastic analysis is performed with the code HAWC2 [8], the aerodynamic model accounts for the flaps unsteady aerodynamics [3, 5], and the turbine is controlled through a .dll adaptation of the standard Suzlon's controller. The same flap control as developed at DTU by Barlas et al. [1,2,9] is considered in the analysis. The controller has three operational modes:

1. Operational Load Alleviation. As described by Barlas et al. [1] and Pettas et al. [9] the flap angle is determined on each blade separately based on high-pass filtered measurements of the blade root flapwise bending moment. Each blade is an independent SISO system with a PD controller on the filtered blade root moment. The controller is tuned using a Ziegler-Nichols method based on an high-fidelity Linear Time Invariant (LTI) of the wind turbine aero-servo-elastic response [4]. The LTI model is obtained with the HAWCStab2 code [6].
2. Reaction to Extreme Loads threshold [2]. The flaps react collectively by switching to a predetermined deflection angle that lowers the blade lift in case a specified flapwise bending moment threshold is exceeded, or a brake program signal is given based on the status returned by the main turbine controller.
3. Power Output Increase [9]. Below rated power the flaps are set collectively to a deflection angle specified as function of a low-pass filtered wind speed with the aim of increasing the aerodynamic power output of the rotor.

The flap reference signal from the controller is passed through a first order low-pass filter that simulates the delay of a flap servo mechanism. The time constant of the flap servo low pass filter is here set to 0.1 s as in [1].

Aeroelastic simulations of the turbine with and without Adaptive Trailing Edge Flaps (ATEF), and considering different flap control modes are performed reproducing the IEC operational Design Load Cases (DLC 1.1 to DLC 1.5) and the idling rotor case (DLC 1.6). The effects of the ATEF control are quantified in terms of fatigue and ultimate load variations, as well as increase in the AEP:

- The increase of turbine power below rated wind speed obtained with the flaps yields to an AEP increase of 1.7 % (Rayleigh distribution with 7.5 m/s average).
- The increase in power output yields also to a significant increase of thrust loads, causing higher fatigue and ultimate loads. The collective flap deflection for power increase brings the rotor induction level closer to the optimal one, and thus also increases the thrust coefficient, counteracting the thrust peak shaving efforts from the turbine standard controller.
- As a Class III A turbine is considered, the increase of fatigue loads below rated power caused by the power increase flap control mode has a relatively large impact on the overall lifetime fatigue DEL: the blade fatigue DEL are brought back to baseline level, and the fatigue loads on the tower fore-aft moment is significantly increased (+40 %).
- Excluding the power control mode, the flap control allows for a reduction of the blade flapwise fatigue lifetime DEL of 9 %. The tower fore-aft DEL is also reduced by 4 %, whereas the fatigue loads on the shaft are increased by about 14 %.

- The increase of pitch activity indicates a negative interaction between the turbine standard controller and the flap controller. A more careful tuning of either flap or standard control parameters and filter frequencies could probably limit such interaction.
- The ultimate loads observed among the simulated cases are generally increased by the flap control, especially so as the power increase flap control mode is active, imposing higher thrust levels on the rotor. The tower fore-aft and main-bearing tilt ultimate bending moments are slightly decreased by the flap load alleviation control mode.
- No significant changes in either fatigue or ultimate loads are observed by enabling or disabling the control mode with the flaps reacting to an extreme load threshold. Maybe a more careful tuning and selection of the parameters for this control mode might allow for further reduction on the simulated ultimate loads.
- In spite of the slight increase of ultimate blade flapwise moment, the flap load control leads to an increase of the minimum tower-blade tip clearance of about 25 % for the simulated DLB. The clearance increase is significant, but should be verified in a full design load bases, considering also cases of faults on the controlled flaps.

Overall the flap control achieves its main objective of alleviating the blade root flapwise fatigue loads, whereas the power increase control mode yields to an increase of both fatigue and ultimate loads, which the observed increase in AEP is probably not sufficient to justify.

A more carefully tuned control system, or maybe a more sophisticated control algorithm would probably allow to achieve higher load reduction with the ATEF, especially considering the ultimate loads.

Whether the load alleviations achieved with the flaps in the simulated cases would ultimately be sufficient to justify the increase in complexity for a class III A turbine remains an open question. The answer would require a redesign of the rotor considering the modification to the loads constraints given by the active flaps, and an estimation of the costs of rotor, other turbine components, and also of the flap system.

## 9.2 Introduction

The chapter reports the results of the aero-servo-elastic analysis of the application of Adaptive Trailing Edge Flaps on a Suzlon's commercial wind turbine model: the Suzlon S111.

The aim is to evaluate through aeroelastic simulations the impact of controlled ATEF on an existing wind turbine model and thus obtain a preliminary quantification of the effects in terms of fatigue and ultimate load alleviation, and AEP increase.

The Suzlon S111 has a rated power of 2.1 MW [10], a rotor diameter of 111.8 m, and is placed on a 90 m tubular steel tower. The turbine is certified as a class IIIA turbine, and corresponding wind and turbulence definitions [7] are used in the analysis.

The aeroelastic analysis is performed with the code HAWC2 [8], the aerodynamic model accounts for the flaps unsteady aerodynamics [3, 5], and the turbine is controlled through a .dll adaptation of the standard Suzlon's controller that regulates power output and rotor speed by acting on the generator torque and collective blade pitch angle. The original controller is maintained unchanged both in the references case without flaps, as well as when the flaps are active.

The same flap control as developed by Barlas et al. [1,2,9] is considered in the analysis, Figure 153 . When active, the controller works according to one of the following operational modes:

4. Operational Load Alleviation. As described by Barlas et al. [1] and Pettas et al. [9] the flap angle is determined on each blade separately based on high-pass filtered measurements of the blade root flapwise bending moment. Each blade is an independent SISO system with a PD controller on the filtered blade root moment.
5. Reaction to Extreme Loads threshold [2]. The flaps react collectively by switching to a predetermined deflection angle that lowers the blade lift in case a specified flapwise bending moment threshold is exceeded, or a brake program signal is given based on the status returned by the main turbine controller.

6. Power Output Increase [9]. Below rated power the flaps are set collectively to a deflection angle specified as function of a low-pass filtered wind speed with the aim of increasing the aerodynamic power output of the rotor.

The flap reference signal from the controller is passed through a first order low-pass filter that simulates the delay of a flap servo mechanism. The time constant of the flap servo low pass filter is here set to 0.1 s as in [1].

The proportional and derivative gains of the flap controller in operational conditions are tuned based on a high-fidelity Linear Time Invariant model of the turbine aeroelastic response. The aero-servo-elastic LTI model of the turbine with flaps is obtained with the HAWCStab2 code [6,4] for the operational conditions above rated power. The control on the flaps is introduced by closing the loop between the collective blade root flapwise bending moment and the collective flap deflection angle with a Proportional-Differential controller. The controller gains are determined at each operational wind speed above rated power simply with a Zielger-Nichols tuning method [4]. A linear gain scheduling as function of low-pass filtered wind speed is then apply to account for the gain variation with the mean wind speed.

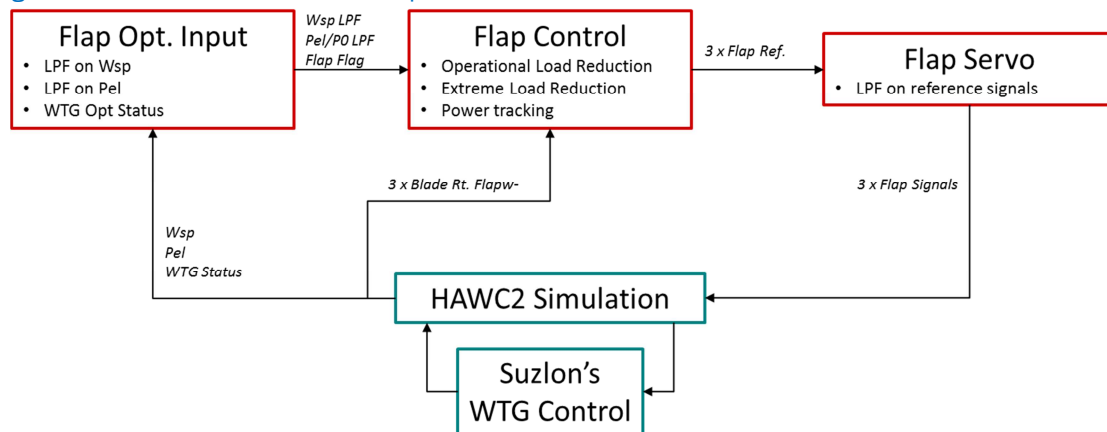


**Figure 153 Sketch on Flap Control Setup in relation with the standard aero-servo-elastic simulation setup**

The effects of the flap control are evaluated by performing aeroelastic simulations of the following Design Load Cases, as defined in the IEC standard [7]:

- DLC 1.1 and DLC 1.2. Wind turbine in normal operation. Mean wind speed from 4 to 20, and yaw misalignments of 0, +7 and -7. Turbulence intensity according to the standards for class A. 6 turbulence seeds per wind speed and wind direction are considered.
- DLC 1.3. Extreme turbulence model. Same set-up in terms of yaw misalignment (3x), wind speeds (9x) and turbulence seeds (6x). For a total of 162 simulations of 10 minutes series.
- DLC 1.4. Extreme coherent gust with direction change at 3 wind speeds around rated.
- DLC 1.5. Extreme wind shear. 9x wind speed for 4x gust phases.
- DLC 6.1. Turbine parked in idling conditions. 6x seeds at 2x yaw positions at  $V_{ref}$  wind speed.

A total of 375 series are simulated, corresponding to approximately 54 hours of simulated response time. The simulation sets are repeated for four configurations of the flap control system:

- Flaps not active (baseline case)
- Flaps active on all operational modes: load alleviation, power output increase, deflection for extreme load threshold.
- Flaps not reacting to extreme load threshold (still controlled for load alleviation and power output increase).
- Flaps mainly targeting operational load alleviation, power output increase not active, nor reaction to loads threshold.

The effects of the flap control are then quantified in terms of:

- Fatigue load alleviation (from DLC 1.1)
- Extreme load variation (from the maximum loads among the cases including safety factors as specified in IEC standards)
- Variation of power output below rated conditions.

In the following sections the setup of the wind turbine with flaps is specified, as well as the method used to tune the flap controller. The results from the aeroelastic simulations are then presented comparing the set of simulations with flap against the baseline aeroelastic simulation set.

### 9.3 Flap Setup

#### 9.3.1 Flap characteristics

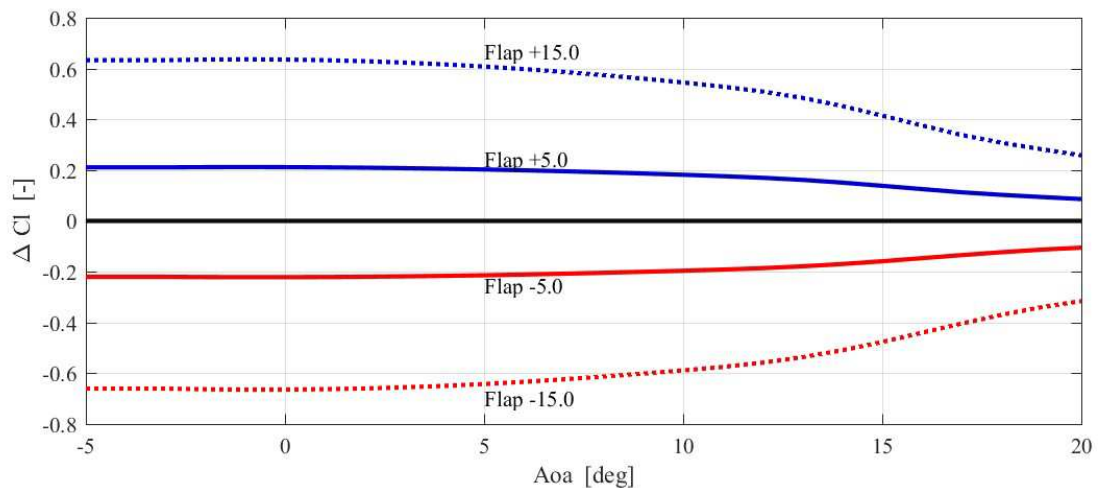
A similar setup as previously considered in DTU [1,2,3,9] is used:

- Adaptive Trailing Edge Flap (ATEF) extend 10 % chord length with a deflection range of  $\pm 15$  degrees.
- Flap spanwise extension: 30 % of blade length (16.44 m)

The flap aerodynamic characteristics are assumed the same as defined by DTU by means of RANS simulations of the steady response of a 10% chord flap [3]. They are represented in terms of variation of steady lift, drag and moment coefficients as functions of flap deflection, ad angle of attack.

Specifically, the flap can generate:

- Maximum lift coefficient variations:  $+0.636$  for  $+15$  degrees deflection (positive flap points downwards),  $-0.664$  for  $-15$  degrees.
- Maximum aerodynamic moment coefficient variations:  $-0.131$  @  $+15$  deg and  $+0.137$  @  $-15$ deg
- The drag coefficient variation is relatively small for angles of attack below 10 degrees.



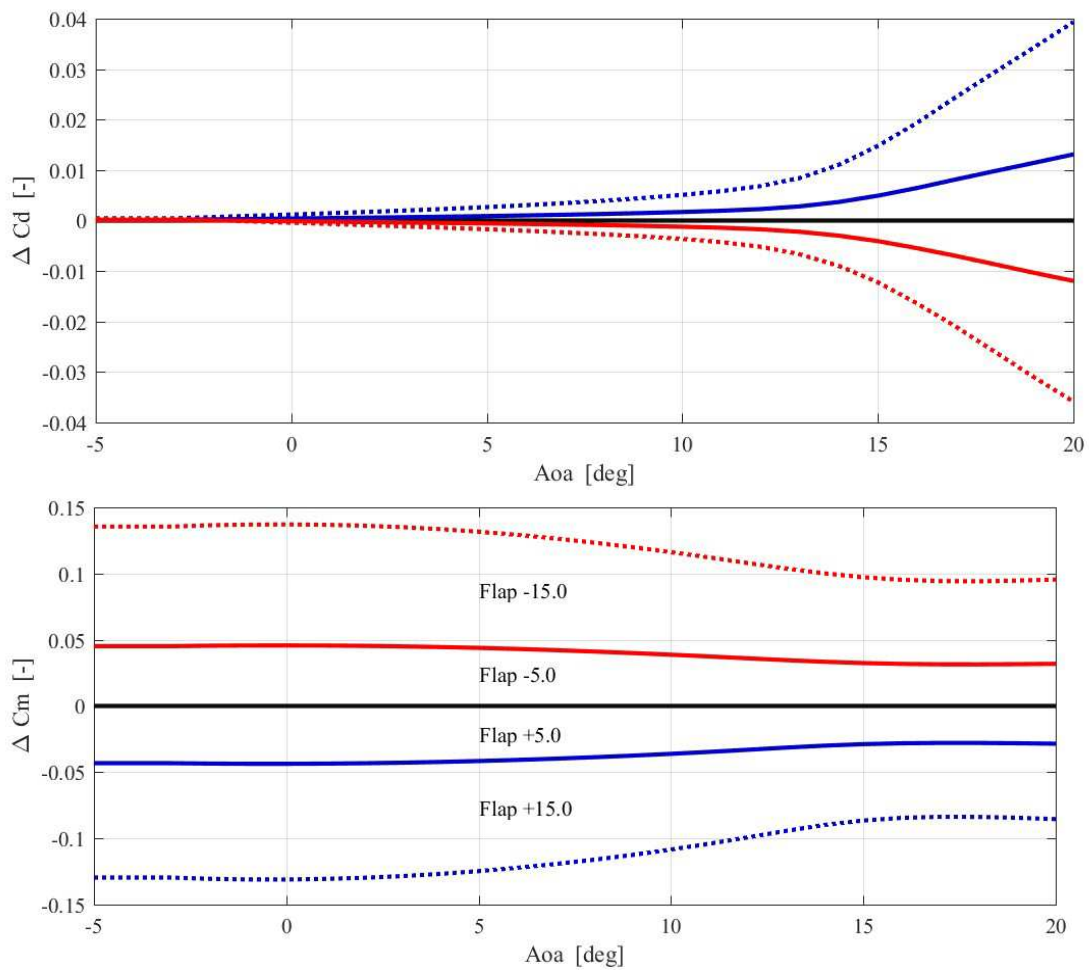
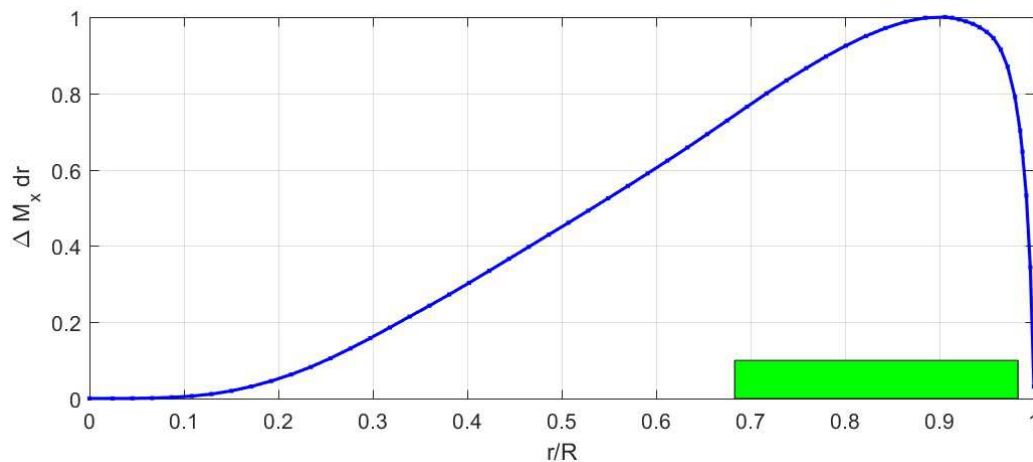


Figure 154 Flap steady aerodynamic variation

### 9.3.2 Flap location along the blade span

The 16.44 m spanwise section with flaps is located along the blade span so to maximize the steady root flapwise bending moment variation achieved by the flaps. The variation of the bending moment from aerodynamic forces (on a stiff blade) is proportional to the cube of the radius time the section chord [3]. Following this approximation, in order to obtain the maximum flapwise root bending moment variation the flap are located from 67 % to 97 % of the blade span.



**Figure 155 Analytical equation for the variation of the blade root bending moment for flap located at different positions along the blade span.**

The continuous flap section is separated in three blocks and aerodynamic calculation points are added just before and after each flap section, to be sure to correctly model the variation of aerodynamic forces.

The steady aerodynamic input for the flap model is made by adding the steady coefficient variations caused by the flap to the steady aerodynamic coefficients of the corresponding airfoils.

### 9.3.3 Response to Flap Step

As a simple check, a simulation is performed to get the response of the collective blade root flapwise bending moment to a collective flap deflection of +10 degrees.

The normalized time series of the flapwise bending moment of blade number 1 shows a non-minimum phase response at the beginning of the time series, and then a decrease of the flapwise bending moment, corresponding to the blade bending forward toward the pressure side (negative bending moment in the chosen reference system).



**Figure 156 Blade Root Flapwise Bending Moment response to a flap deflection of +10 degrees**

## 9.4 Flap Control Tuning

As mentioned in the introduction, the flap control consists of three independent, and mutually exclusive, control modes:

- Power output increase: aims at improving the turbine power output below rated conditions by setting the flaps to a collective deflection angle.
- Operational Load Alleviation: reduction of loads during normal operation of the wind turbine. The controller considers each blade as an independent SISO system, and prescribes a flap deflection for each blade with a PD control of high-pass filtered blade root flapwise bending moment measurements.
- Reaction to extreme loads: whenever the root flapwise bending moment on any of the blade exceeds a given threshold all the flaps deflect to a prescribed deflection angle (-15 degrees), so to rapidly decrease the lift force on the blade. The same behavior is prescribed whenever the main turbine controller returns a status signal corresponding to a parked turbine, or to a brake program.

### 9.4.1 Settings for Power Output increase

The angles at which to set the flaps to track the maximum power output below rated are determined by simulating the response of the wind turbine to a steady wind field for different wind speed below rated power, and for different flap deflection angles.

The flap angles are determined simply by choosing the angles that return the maximum power output, thus neglecting any consideration on increase of the loading to the rotors below rated conditions.

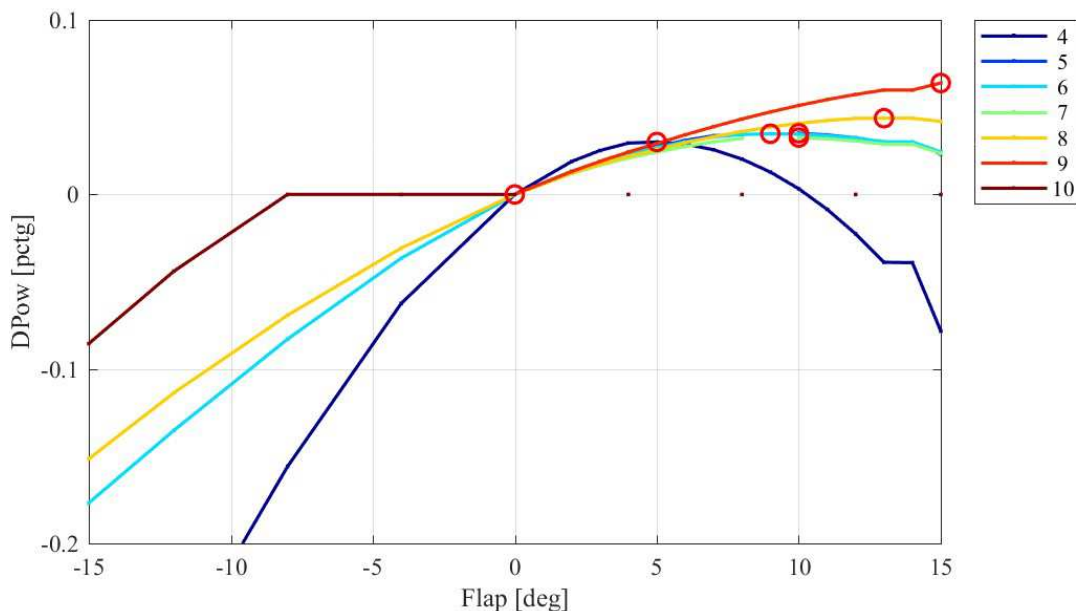


**Figure 157 Power output increase as function of the collective flap deflection angle. Each line represent a different steady wind speed, and the red circles indicates the flap position corresponding to the maximum power output increase.**

The tendency is to set the flap to low deflection angles at low wind speeds, slightly larger angles in the variable speed range to increase the loading on the rotor, and even higher deflection angle are set at higher velocities. Note that this behavior, aiming at increasing the rotor power coefficient ( $C_p$ ), will also increase the rotor thrust coefficient ( $C_t$ ), thus partly counter-acting the thrust peak shaving settings of the original controller.

### 9.4.2 Operational Load Alleviation Control

The flap control for the turbine in normal operation consists of three independent SISO systems, one per blade. Measurements of the blade root flapwise bending moment are first high pass filtered, to limit the interaction between the flap control and the collective pitch power control [1,9]. The high pass filtered signal is then fed to a PD controller that returns the reference flap

signal that will be passed to the flap servo model (a first order low pass filter with time constant of 0.1 s [1]). The first order high pass high filter is here set to a corner frequency of approximately 0.06 Hz.

The proportional and derivative gains of the flap controller in operational conditions are tuned based on a high-fidelity Linear Time Invariant model of the turbine aeroelastic response [6,4]. The aero-servo-elastic LTI model of the turbine with flaps is obtained with the HAWCStab2 code for the operational conditions above rated power. The control on the flaps is introduced by closing the loop between the collective blade root flapwise bending moment and the collective flap deflection angle with a Proportional-Differential controller. The controller gains are determined at each operational wind speed above rated power simply with a Ziegler-Nichols tuning method [4]. The poles of the closed loop LTI system are tracked for increasing proportional gains of the collective flap control. The gain at which a pole first become unstable (negative damping ratio in the figure) is the critical gain, and, following Ziegler-Nichols formulation [4], the derivative gain is proportional to the frequency of the mode becoming unstable.

The tuning method is rather primitive and does not account for the deflection limitations of the flaps, nevertheless it provides a systematic and automated algorithm for the control tuning. As the tuning method does not account for the flap deflection limits, it is found that the proportional gain found with the Ziegler-Nichols tuning should be further reduced to avoid the flap reference signal to saturate too often above the deflection limits. The proportional gain is reduced by a factor of 0.6, whereas the derivative gain is still retrieved as one eighth of the ratio between the scaled down proportional gain and the critical pole frequency.

The gain tuning is repeated for LTI system descriptions obtained at wind speeds above rated between 10 and 20 m/s. The gain scheduling for the flap gains as function of the low pass filtered wind speed is then retrieved from linear fitting of the resulting proportional and differential gains. Both the proportional and the differential gain decrease for increasing wind speeds.

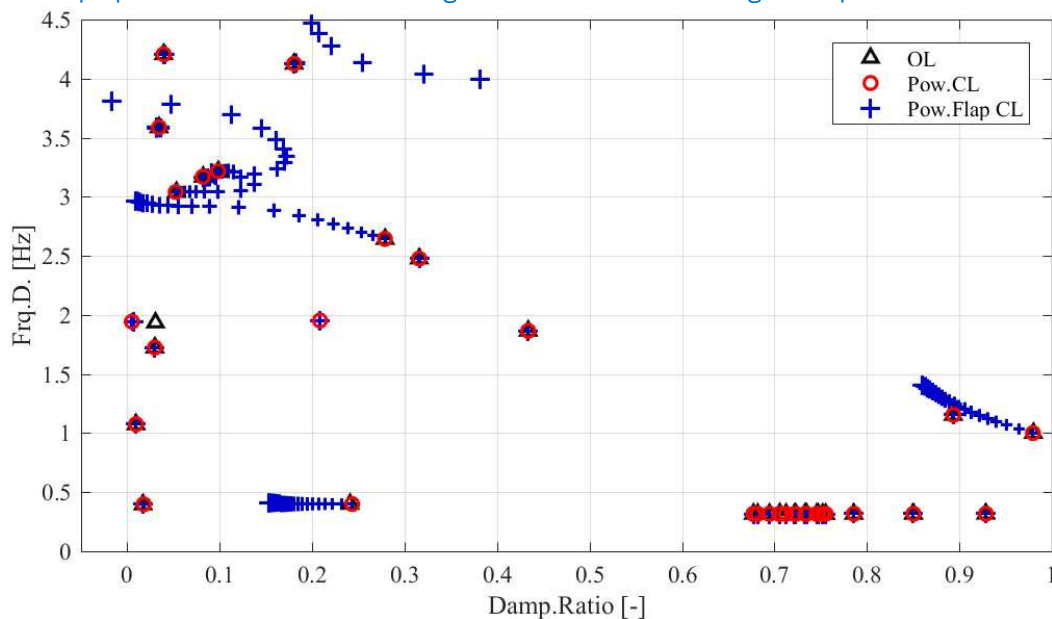


**Figure 158** Normalized pole plot for the LTI system representing the wind turbine with flaps. Both frequency and damping are normalized by frequency and damping values of a pole of choice.

### 9.4.3 Reaction to Extreme Loads

The threshold for the flap to react to an extreme loads is set so that the flap will collectively deflect to -12 degrees whenever:

- Blade root bending moments 20 percent higher than what expected in normal operation are encountered on any of the blades. For blade root loads between 15 and 20 percent higher than what expected in normal operation, the flaps are set to 0.0.

- Or the low pass filtered wind speed exceeds a threshold of 35 m/s.

The flaps are instead set at -8 degrees when the turbine is in parked condition, to maintain the rotor idling.

## 9.5 Aeroelastic Simulations

Aeroelastic simulations for the wind turbine equipped with Adaptive Trailing Edge Flaps are compared against the baseline case of the turbine without flaps.

Similar to other tasks in the INNWind projects, an indicative reduced set of Design Load Cases is considered in the simulations. The following Design Load Cases (DLC), as defined in the IEC standard [7] are simulated:

- DLC 1.1 and DLC 1.2. Wind turbine in normal operation. Mean wind speed from 4 to 20, and yaw misalignments of 0, +7 and -7. Turbulence intensity according to the standards for class A. 6 turbulence seeds per wind speed and wind direction are considered.
- DLC 1.3. Extreme turbulence model. Same set-up in terms of yaw misalignment (3x), wind speeds (9x) and turbulence seeds (6x). For a total of 162 simulations of 10 minutes series.
- DLC 1.4. Extreme coherent gust with direction change at 3 wind speeds around rated.
- DLC 1.5. Extreme wind shear. 9x wind speed for 4x gust phases.
- DLC 6.1. Turbine parked in idling conditions. 6x seeds at 2x yaw positions at  $V_{ref}$  wind speed.

In addition, an additional non-standard design load case is simulated to better evaluate the effects of the flap on the power output. The case consider the turbine in normal operation in sheared and turbulent wind flow (as in DLC 1.1), with no yaw misalignment and normal operation control. Average wind speeds with 1 m/s resolution are considered between 4 and 10 m/s, 4 turbulence seeds for each wind speed.

Each DLC set is repeated with the following flap controller settings (the standard turbine controller is left un-modified in all cases):

- **Baseline.** The flap is kept at 0.0 degrees. The case represent the actual Suzlon S111 turbine in its standard configuration, without Adaptive Trailing Edge Flaps.
- **Flap All.** The ATEF are active in all their operational modes: power output increase, operational load alleviation, collective deflection reaction to extreme loads.
- **Flaps no Extreme Loads (FI.No ExtL).** The ATEF are not reacting to the Extreme Loads exceeding the given threshold. The operational load alleviation (or power tracking) flap control modes are maintained until a turbine break program is triggered (the flaps are then collectively deflected to -12 degrees).
- **Flap no Power Increase (FI. No PowI).** Only the operational load alleviation control mode of the flaps is active. Below rated power the flaps are only active whenever the low pass filtered electric power output is above 80 % of the rated power.

### 9.5.1 Fatigue Loads

The effects of the ATEF control on the fatigue loads is quantified in terms of variations of Damage Equivalent Loads, which are determined through rain flow counting of the simulated time series. Only DLC 1.2 is here considered for the fatigue loads.

The active control of the ATEF would reduce the lifetime fatigue load on the blade root flapwise bending moment by nearly 9 % (FI.No PowI), Figure 159 Damage Equivalent Loads (DEL) at the blade root: Flapwise ( $M_{xBR}$ ), Edgewise ( $M_{yBR}$ ), and Torsion ( $M_{zBR}$ ). Variation of the DEL compared to the Baseline case without flaps. Figure 159. On the other end, enabling the power output increase control mode of the flap causes an increase of the flapwise DEL below rated, which brings back the lifetime DEL to the baseline level, in spite of the load alleviation achieved at wind speeds above rated power. The edgewise fatigue DEL, and especially the blade torsion DEL

are increased by the flap control. No significant variations of the lifetime DEL are caused by the control mode reacting to extreme loads.

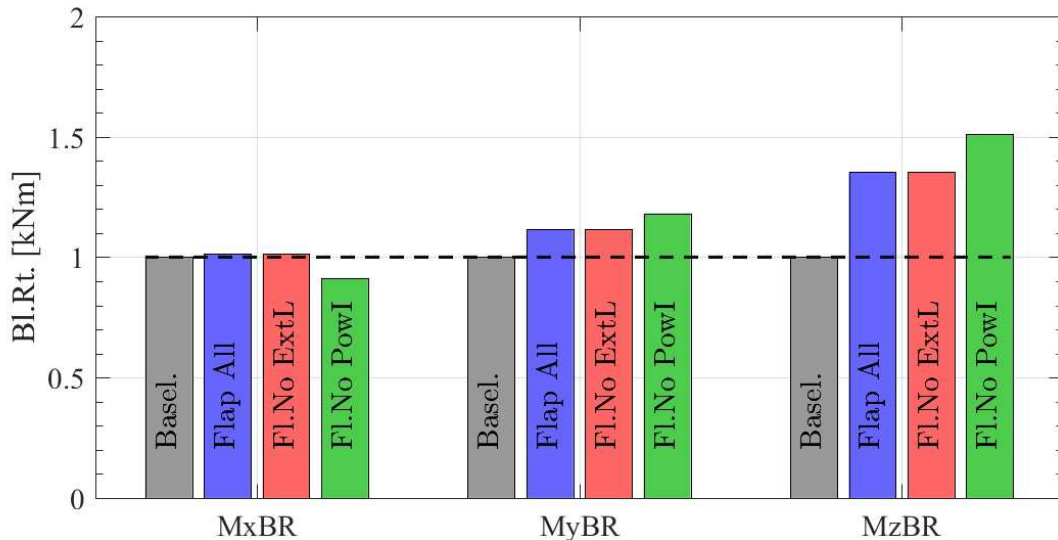


**Figure 159** Damage Equivalent Loads (DEL) at the blade root: Flapwise (MxBR), Edgewise (MyBR), and Torsion (MzBR). Variation of the DEL compared to the Baseline case without flaps.

A similar trend is observed on the tower bottom flange fatigue DEL, Figure 160. The operational load alleviation flap control mode brings a 4 % decrease of the tower Fore-Aft fatigue load, even though they are not directly targeted by the controller. On the other hand, the increased power output control of the flap produces a significant increase of the tower fore-aft lifetime DEL (up to 40 %). The variations on the tower Side-to-Side DEL are smaller, whereas the tower torsion DEL, of a much smaller order of magnitude, is increased in all cases with ATEF.

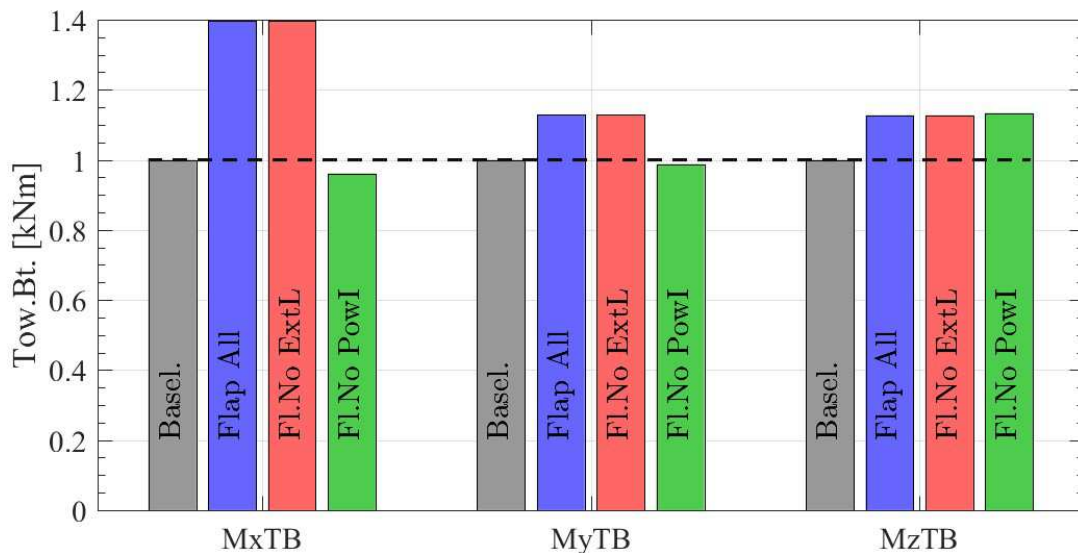


**Figure 160** Tower bottom fatigue DEL: Fore-Aft (MxTB), Side-to-Side (MyTB), tower torsion (MzTB). DEL variation compared to the baseline case

The fatigue loads at the main bearing and on the shaft show an increase of DEL for all cases when the ATEF control is on, Figure 161 .

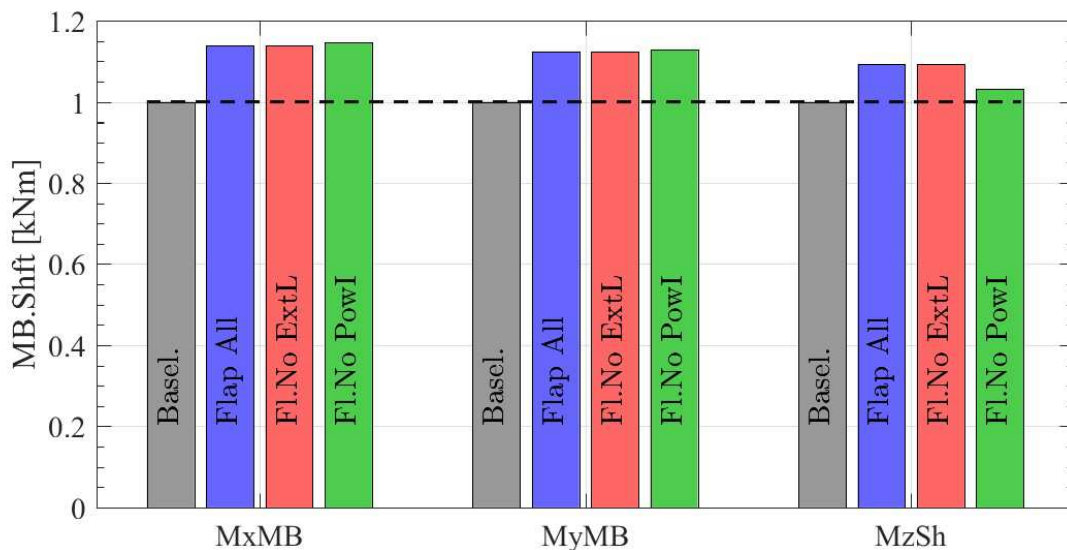


**Figure 161 Main Bearing and Shaft Damage Equivalent Loads: Tilting Moment (MxMB), yawing moment (MyMB), and shaft torsion (MzSh).**

By monitoring the pitch activity, Figure 162, an increase of activity (between 8 to 16 %) is observed, thus indicating an interaction between the flap controller and the standard turbine controller. The lifetime pitch bearing damage is evaluated here as the integral over lifetime of the pitch angle variation times the flapwise bending moment at the same instant. When excluding the Power Output increase control mode, in spite of an increase of lifetime pitch activity close to 8 %, the increase of the lifetime pitch bearing damage is smaller (app. 3 %). A significant increase of both activity and bearing damage is observed as the power increase mode is activated.

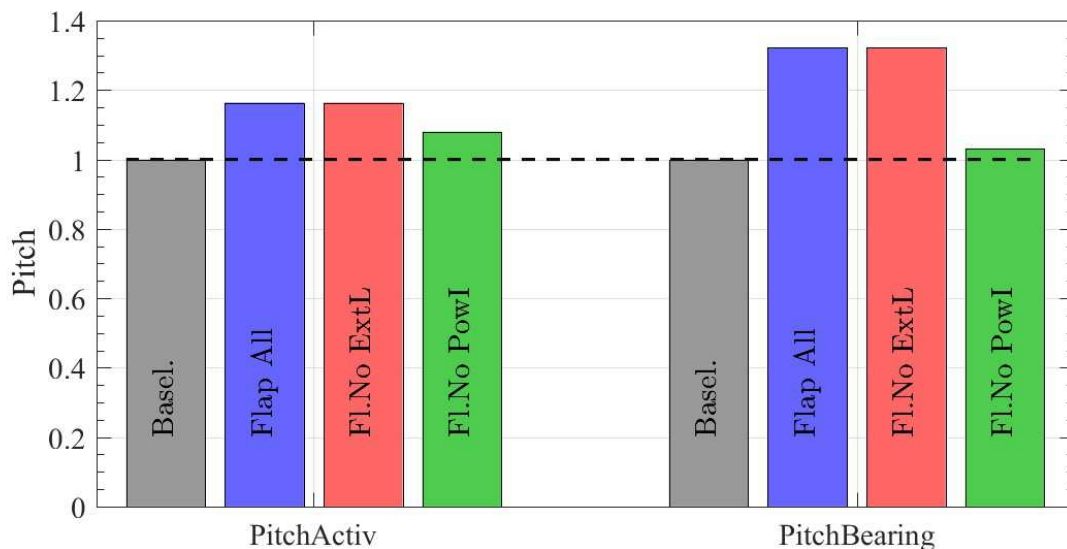


**Figure 162 Variation of the pitch activity and pitch bearing damage over the turbine lifetime.**

### 9.5.2 Ultimate Loads

The impact on the ultimate loads is assessed by considering as ultimate loads for each simulation set the maximum, in absolute term, observed among all the time series of the simulated cases, including partial safety factors as specified by the IEC standard. Since no averaging in between turbulence seeds is applied, the numerical value of the maximum loads might be dependent on the seed choice. Nevertheless as the same turbulence boxes are applied for the four simulation sets, the seed dependence is expected to be lower for the ultimate loads normalized by the baseline loads.

Although a reduced number of design load cases is considered, compared to a full IEC standard design load bases, the ultimate loads encountered are considered indicative of the variations of the overall design giving loads.

The ultimate loads at the blade root in the flapwise direction among the simulated cases are increased by approximately 4 % by the flap operational controller, and up to 13 % whenever the power increase mode is activated, thus confirming that the increase in power output below rated also implies an increase of the thrust over the rotor. Nearly no changes are observed by enabling the flap reaction to the extreme load threshold. In all cases the DLC returning the ultimate loads is DLC 1.3 (operation in extreme turbulence). For the flap controlled case the highest flapwise bending moment is given by the time series with positive yaw misalignment and average wind speed of 8 m/s, where the flaps control switches continuously between being active and not (due to the rated power threshold). A more accurate tuning of wither the power threshold settings, or the extreme loads threshold might allow to decrease the loads on the blade by controlling the flap deflection [2].

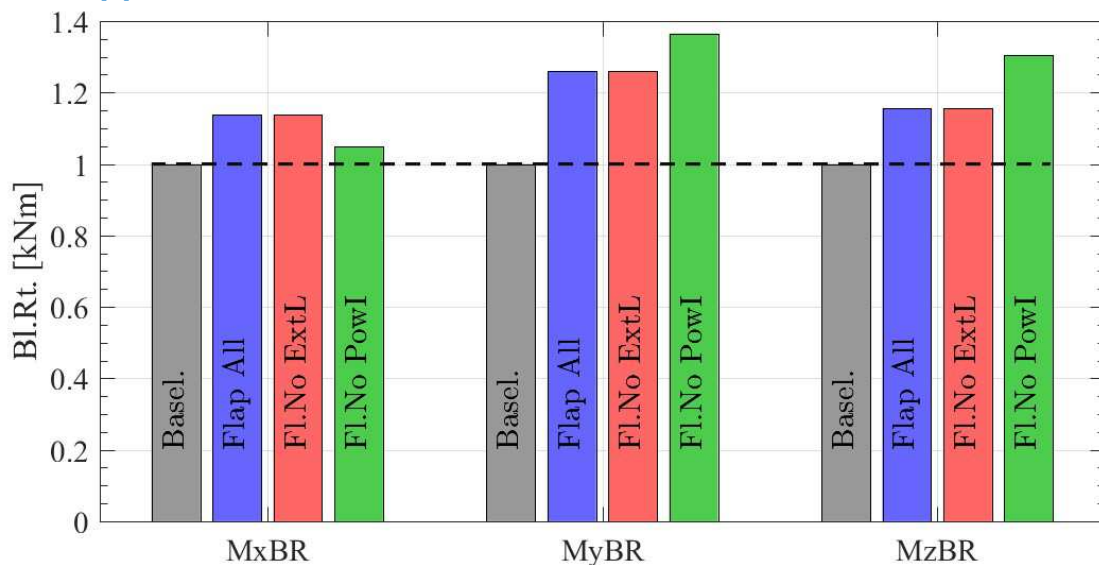


Figure 163 ultimate loads at the blades root. Flapwise (Mx), Edgewise (My), and Torsion (Mz)

In spite of the increase of the flapwise bending moment, the flap operational control allows to increase the minimum tower.blade tip clearance, by nearly 30 %, Figure 164 . On the contrary, as the thrust force is increased by the power increase flap control mode, the minimum tower clearance is reduced.

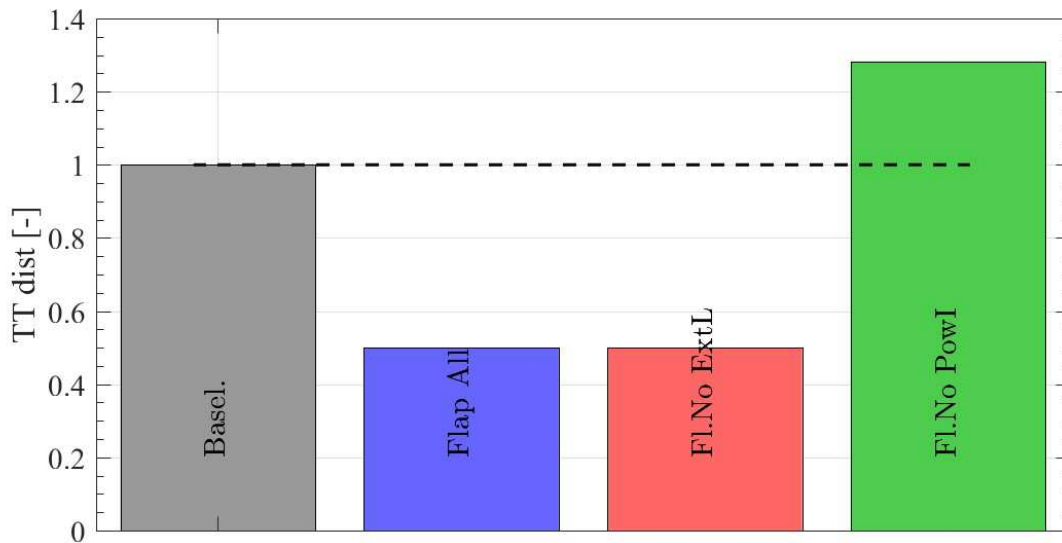


Figure 164 Tower-Blade Tip minimum clearance. The clearance is normalized by the minimum clearance from the baseline case, thus an increase of the clearance indicates a smaller deflection of the blade towards the tower.

The ultimate loads at the tower bottom fore-aft bending moment is slightly decreased by the flap load alleviation mode, and significantly increased by power increase control mode, Figure 165. For all simulation sets, the ultimate loads on the tower side-to-side moment ( $M_{yTB}$ ) are registered in the idling rotor case (DLC 6.1), where the chosen flap deflection angle decreases the idling rotational speed giving rise to larger oscillatory loads. The loads from DLC 6.1 should hence be taken as indicative, as on the limits of the modelling possibility of a standard aeroelastic code.

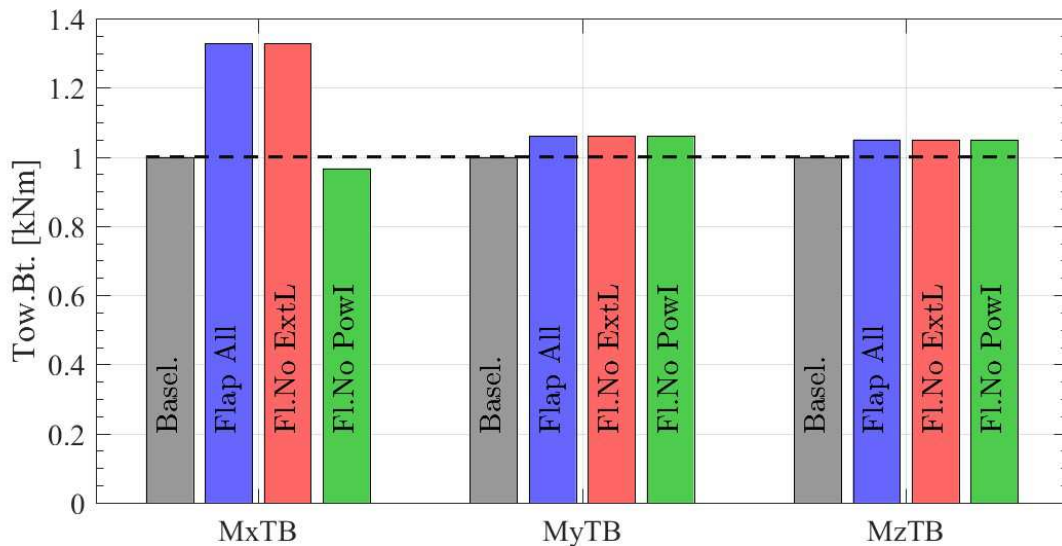


Figure 165 ultimate loads at the tower base flange. Fore-Aft moment ( $M_x$ ), Side-To-Side ( $M_y$ ), and Torsion ( $M_z$ )

The loads on the main bearing are decreased in the tilt direction and slightly increased in the yaw. The maximum torsion loads on the shaft among the simulated series is increased, Figure 166, but that is also reported in the idling case DLC 6.1.

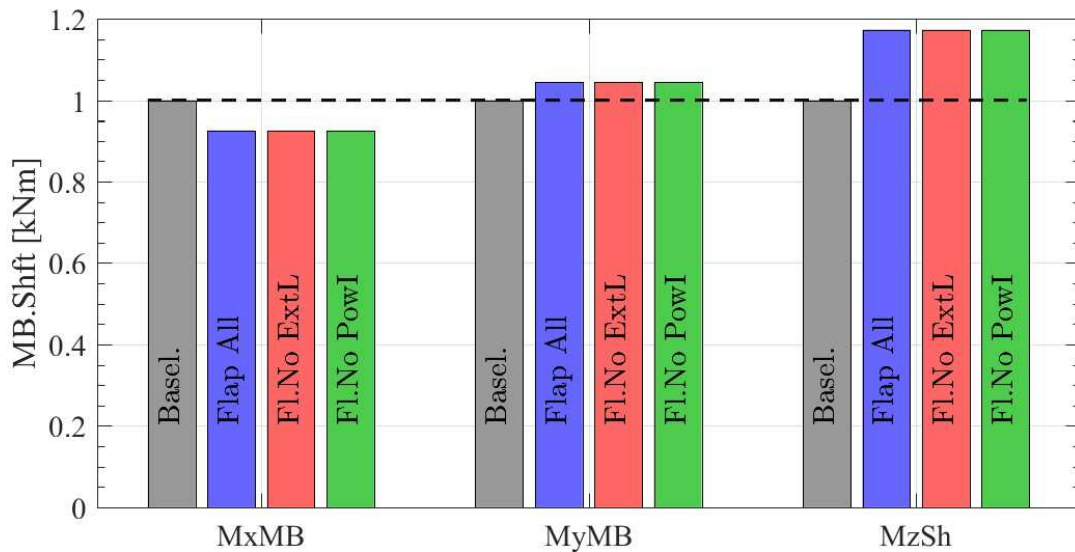


Figure 166 Ultimate loads on main bearing Tilt (Mx) and Yaw (My) moment, and Shaft Torsion (Mz)

### 9.5.3 AEP improvement

Setting the collective flap angles as function of the low pass filtered wind speed below rated power to increase the rotor power coefficient effectively increase the power output of the wind turbine below rated power. Increasing the power output below rated power also increases the thrust forces on the rotor, and its variation, thus increasing fatigue and ultimate loads, as observed in the previous sections.

The power increase is quantified by simulating the wind turbine power output in turbulent wind conditions, similar to what is prescribed by the IEC standard for the DLC 1.2 (or 1.1) for a class A wind turbine. The only differences being that no yaw misalignment in the wind field is considered here, 4 turbulence seeds per wind speed are considered, and to increase the resolution of the power curve, simulation for each 1 m/s variation of the average wind speed (instead of 2 m/s) are considered between 4 and 10 m/s.

The average power output among the 4 seeds of each wind speed bins is used to compare the turbulent power curves of the baseline case with no flap, and the case with the flaps Power Output increase mode activated below rated power, Figure 167. The power decrease at 4 m/s although appearing as relatively large is in fact rather small, and it is probably a consequence of a non-accurate flap deflection angles for wind speeds below 4 m/s, which were not considered in the flap deflection angle tuning, but do occur due to the turbulence in the wind.

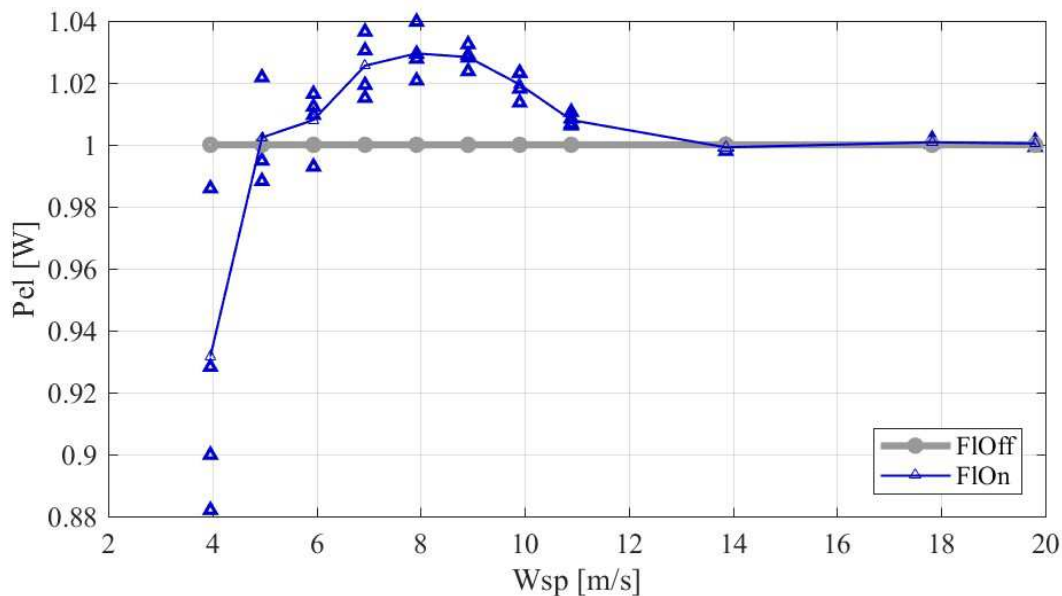


**Figure 167 Power increase obtained by setting the collective flap deflection angle according to the low passed filter wind speed**

The difference between the two power curves shows that with the flap a power increase close to 3 % can be on average achieved around 8 m/s. The overall AEP increase, considering a site with a Rayleigh wind distribution with average wind speed 7.5 m/s, is close to 1.3 %.

## 9.6 Conclusion

The individual flap controller developed at DTU [1,2,9] has been included in the aero-servo-elastic model of the Suzlon's wind turbine S111, and tuned to the turbine characteristics. Aeroelastic simulations of the turbine with and without Adaptive Trailing Edge Flaps, and considering different flap control modes are performed reproducing the IEC operational load cases (1.1 to 1.5) and the idling rotor case (1.6). The effects of the ATEF control are quantified in terms of fatigue and ultimate load variations, as well as increase in the AEP:

- The increase of turbine power below rated wind speed obtained with the flaps yields to an AEP increase of 1.7 % (Rayleigh distribution with 7.5 m/s average).
- The increase in power output yields also to a significant increase of thrust loads, causing higher fatigue and ultimate loads. The collective flap deflection for power increase brings the rotor induction level closer to the optimal one, and thus also increases the thrust coefficient, counteracting the thrust peak shaving efforts from the turbine standard controller.
- As a Class III A turbine is considered, the increase of fatigue loads below rated power caused by the power increase flap control mode has a relatively large impact on the overall lifetime fatigue DEL: the blade fatigue DEL are brought back to baseline level, and the fatigue loads on the tower fore-aft moment is significantly increased (+40 %).
- Excluding the power control mode, the flap control allows for a reduction of the blade flapwise fatigue lifetime DEL of 9 %. The tower fore-aft DEL is also reduced by 4 %, whereas the fatigue loads on the shaft are increased by about 14 %.
- The increase of pitch activity indicates a negative interaction between the turbine standard controller and the flap controller. A more careful tuning of either flap or standard control parameters and filter frequencies could probably limit such interaction.
- The ultimate loads observed among the simulated cases are generally increased by the flap control, especially so as the power increase flap control mode is active, imposing

- higher thrust levels on the rotor. The tower fore-aft and main-bearing tilt ultimate bending moments are slightly decreased by the flap load alleviation control mode.
- No significant changes in either fatigue or ultimate loads are observed by enabling or disabling the control mode with the flaps reacting to an extreme load threshold. Maybe a more careful tuning and selection of the parameters for this control mode might allow for further reduction on the simulated ultimate loads.
- In spite of the slight increase of ultimate blade flapwise moment, the flap load control leads to an increase of the minimum tower-blade tip clearance of about 25 % for the simulated DLB. The clearance increase is significant, but should be verified in a full design load bases, considering also cases of faults on the controlled flaps.

Overall the flap control achieves its main objective of alleviating the blade root flapwise fatigue loads, whereas the power increase control mode yields to an increase of both fatigue and ultimate loads, which the observed increase in AEP is probably not sufficient to justify.

A more carefully tuned control system, or maybe a more sophisticated control algorithm would probably allow to achieve higher load reduction with the ATEF, especially considering the ultimate loads.

Whether the load alleviations achieved with the flaps in the simulated cases would ultimately be sufficient to justify the increase in complexity for a class III A turbine remains an open question. The answer would require a redesign of the rotor considering the modification to the loads constraints given by the active flaps, and an estimation of the costs of rotor, other turbine components, and also of the flap system.

## 9.7 References

- [1] Barlas, Athanasios, Leonardo Bergami, Morten Hartvig Hansen, Mads Mølgaard Pedersen, David Verelst, Kenneth Thomsen, and Helge Aagaard Madsen. "Load Alleviation Potential of Active Flaps and Individual Pitch Control in a Full Design Load Basis." In *Proceedings of the EWEA Annual Event and Exhibition 2015*, 7. Paris, France: EWEA, 2015.
- [2] Barlas, Athanasios, Vasilis Pettas, Drew Patrick Gertz, and Helge Aagaard Madsen. "Extreme Load Alleviation Using Industrial Implementation of Active Trailing Edge Flaps in a Full Design Load Basis." In *Journal of Physics: Conference Series (Online)*, Vol. 753, 2016. doi:10.1088/1742-6596/753/4/042001.
- [3] Bergami, Leonardo. *Smart Rotor Modeling: Aero-Servo-Elastic Modeling of a Smart Rotor with Adaptive Trailing Edge Flaps*. Research Topics in Wind Energy 3. Heidelberg, Germany: Springer, 2014. doi:10.1007/978-3-319-07365-1.
- [4] Bergami, Leonardo, and Morten H. Hansen. "High-Fidelity Linear Time-Invariant Model of a Smart Rotor with Adaptive Trailing Edge Flaps." *Wind Energy* 20, no. 3 (March 1, 2017): 431–47. doi:10.1002/we.2014.
- [5] Bergami, Leonardo, Vasilis A. Riziotis, and Mac Gaunaa. "Aerodynamic Response of an Airfoil Section Undergoing Pitch Motion and Trailing Edge Flap Deflection: A Comparison of Simulation Methods." *Wind Energy* 18, no. 7 (July 2015): 1273–90. doi:10.1002/we.1759.
- [6] Hansen, M. H. "Aeroelastic Stability Analysis of Wind Turbines Using an Eigenvalue Approach." *Wind Energy* 7, no. 2 (2004): 133–143. doi:10.1002/we.116.
- [7] International Electrotechnical Commission. "IEC 61400-1: Wind Turbines Part 1: Design Requirements." International Electrotechnical Commission, 2005.
- [8] Larsen, Torben Juul. "How 2 HAWC2 the User's Manual." Risø National Laboratory. Technical University of Denmark, 2009.
- [9] Pettas, Vasilis, Athanasios Barlas, Drew Patrick Gertz, and Helge Aagaard Madsen. "Power Performance Optimization and Loads Alleviation with Active Flaps Using Individual Flap

Control.” In *Journal of Physics: Conference Series (Online)*, Vol. 749, 2016.  
doi:10.1088/1742-6596/749/1/012010.

- [10] Website: <http://www.suzlon.com/products/S111> . Suzlon S111 wind Generator. Last accessed on 11-07-2017.
- [11] Larsen, Torben Juul. “How 2 HAWC2 the User’s Manual.” Risø National Laboratory. Technical University of Denmark, 2009.
- [12] Pettas, Vasilis, Athanasios Barlas, Drew Patrick Gertz, and Helge Aagaard Madsen. “Power Performance Optimization and Loads Alleviation with Active Flaps Using Individual Flap Control.” In *Journal of Physics: Conference Series (Online)*, Vol. 749, 2016.  
doi:10.1088/1742-6596/749/1/012010.

## 10 CONCLUSIONS

Since the proof of the pudding is in the eating the objective of this deliverable was on the experimental proof-of-concept of the trailing-edge control concept. The main conclusion of this deliverable is that trailing edge flaps provide another degree of freedom to the wind turbine designers which make it possible to distribute the evitable structural loading over all the wind turbine components. Field experiments on a MW rotor is the next big step towards large scale implementation.

Each individual chapter contains valuable conclusions. Below you can find a summary of the main conclusions of the individual chapters.

- Through the experimental investigation of **novel load sensors** on a laboratory scale blade, the feasibility of using those types of sensors as load sensor has been proven. Especially the low frequency range down to 0.1Hz has not been investigated in a systematic manner before. By appropriate selection of sensor dimension and effect type (d31, d33) along with careful design of sensor signal conditioning, quasi-static load measurements down to **0.1 Hz could be achieved** in a laboratorial setting.
- **Free-floating flaps** were **designed for the first time** for the application of wind turbine load control. Numerical aeroelastic analysis concluded that such flaps show significant control authority in the desired frequency band (2P and beyond). However, the additional degree of freedom couples aerodynamically with the flapwise flexible mode of the blade and causes flutter at low wind speeds, just outside the design envelope. Using a data-driven feedback controller, the blade can be stabilized in the post-flutter region. Both of these results **were validated experimentally** in the wind tunnel.
- During the wind tunnel tests, the concept of **Subspace Predictive Repetitive Control** (SPRC), a dedicated data-driven control technique, was introduced to achieve blade load reductions. The pitch control action was composed of a superposition of 1P and 2P sinusoidal basis functions where the gains are automatically adapted to the time-varying wind conditions. It was **shown that significant rejection of 1P and 2P loads** in the blade load spectrum could be achieved with combined pitch and flap control.
- A **morphing trailing edge (MTE) flap** has been developed for the alleviation of unsteady loads within Task 2.3. It consists of an inner, printed cell structure which allows a deflection of the flap. On the suction side, the flap is covered with a Carbon Fiber Reinforced Polyester (CFRP) skin and on the pressure side with a pre-stressed silicone skin. The flap is actuated with a carbon rod attached to the trailing edge of the flap.
- In the testing campaign utilizing a **rotating rig**, the **morphing trailing edge** technology developed has been evaluated and successfully demonstrated. It is shown that the morphing wing achieves good performance in terms of aerodynamic load response, close to numerical estimations. Moreover, simple controller implementations show promising results in terms of dynamic load alleviation. In addition, the aerodynamic performance of ECN's new aerofoil has been evaluated in atmospheric conditions
- The individual flap controller developed in the INN WIND project has been included in the aero-servo-elastic model of the **Suzlon's wind turbine S111**, and tuned to the turbine characteristics. Overall the flap control achieves its main

objective of **alleviating the blade root flapwise fatigue loads with 9%**, whereas the power increase control mode yields a **1.7% increase in AEP**.

- Fatigue and extreme load reduction capabilities of IPC and IPC&IFC are assessed on the **10 MW and 20 MW Inwind.EU** RWT. Blade flapwise fatigue load reductions of about **25% are attained with both control strategies** tested in the present study (i.e. IPC and combined IPC&IFC), independent of the turbine size.